Takahiro Numai

# Fundamentals of Semiconductor Lasers

Second Edition



# **Springer Series in Optical Sciences**

Volume 93

## Founded by

H.K.V. Lotsch

#### **Editor-in-Chief**

William T. Rhodes, Georgia Institute of Technology, Atlanta, USA

#### **Editorial Board**

Ali Adibi, Georgia Institute of Technology, Atlanta, USA Toshimitsu Asakura, Hokkai-Gakuen University, Sapporo, Japan Theodor W. Hänsch, Max-Planck-Institut für Quantenoptik, Garching, Germany Ferenc Krausz, Ludwig-Maximilians-Universität München, Garching, Germany Bo A.J. Monemar, Linköping University, Linköping, Sweden Herbert Venghaus, Fraunhofer Institut für Nachrichtentechnik, Berlin, Germany Horst Weber, Technische Universität Berlin, Berlin, Germany Harald Weinfurter, Ludwig-Maximilians-Universität München, München, Germany

## **Springer Series in Optical Sciences**

The Springer Series in Optical Sciences, under the leadership of Editor-in-Chief William T. Rhodes, Georgia Institute of Technology, USA, provides an expanding selection of research monographs in all major areas of optics: lasers and quantum optics, ultrafast phenomena, optical spectroscopy techniques, optoelectronics, quantum information, information optics, applied laser technology, industrial applications, and other topics of contemporary interest.

With this broad coverage of topics, the series is of use to all research scientists and engineers who need up-to-date reference books.

The editors encourage prospective authors to correspond with them in advance of submitting a manuscript. Submission of manuscripts should be made to the Editor-in-Chief or one of the Editors. See also www.springer.com/series/624

Editor-in-Chief
William T. Rhodes
School of Electrical and Computer Engineering
Georgia Institute of Technology
Atlanta, GA 30332-0250
USA
e-mail: bill.rhodes@ece.gatech.edu

Editorial Board

Ali Adibi School of Electrical and Computer Engineering Georgia Institute of Technology Atlanta GA 30332-0250

USA

e-mail: adibi@ee.gatech.edu

Toshimitsu Asakura Faculty of Engineering Hokkai-Gakuen University 1-1, Minami-26, Nishi 11, Chuo-ku Sapporo, Hokkaido 064-0926 Japan e-mail: asakura@eli.hokkai-s-u.ac.jp

Theodor W. Hänsch Max-Planck-Institut für Quantenoptik Hans-Kopfermann-Straße 1 85748 Garching, Germany e-mail: t.w.haensch@physik.uni-muenchen.de

Ferenc Krausz Ludwig-Maximilians-Universität München Lehrstuhl für Experimentelle Physik Am Coulombwall 1 85748 Garching, Germany and Max-Planck-Institut für Quantenoptik Hans-Kopfermann-Straße 1 85748 Garching Germany

e-mail: ferenc.krausz@mpq.mpg.de

Bo A.J. Monemar

Department of Physics and Measurement Technology Materials Science Division Linköping University 58183 Linköping, Sweden e-mail: bom@ifm.liu.se

Herbert Venghaus Fraunhofer Institut für Nachrichtentechnik Heinrich-Hertz-Institut Einsteinufer 37 10587 Berlin, Germany e-mail: venghaus@hhi.de

Horst Weber Optisches Institut Technische Universität Berlin Straße des 17. Juni 135 10623 Berlin, Germany e-mail: weber@physik.tu-berlin.de

Harald Weinfurter Sektion Physik Ludwig-Maximilians-Universität München Schellingstraße 4/III 80799 München, Germany

e-mail: harald.weinfurter@physik.uni-muenchen.de

More information about this series at http://www.springer.com/series/624

# Takahiro Numai

# Fundamentals of Semiconductor Lasers

Second Edition



Takahiro Numai Department of Electrical and Electronic Engineering Ritsumeikan University Kusatsu Japan

ISSN 0342-4111 ISBN 978-4-431-55147-8 DOI 10.1007/978-4-431-55148-5 ISSN 1556-1534 (electronic) ISBN 978-4-431-55148-5 (eBook)

Library of Congress Control Number: 2014945137

Springer Tokyo Heidelberg New York Dordrecht London

#### © Springer Japan 2004, 2015

This work is subject to copyright. All rights are reserved by the Publisher, whether the whole or part of the material is concerned, specifically the rights of translation, reprinting, reuse of illustrations, recitation, broadcasting, reproduction on microfilms or in any other physical way, and transmission or information storage and retrieval, electronic adaptation, computer software, or by similar or dissimilar methodology now known or hereafter developed. Exempted from this legal reservation are brief excerpts in connection with reviews or scholarly analysis or material supplied specifically for the purpose of being entered and executed on a computer system, for exclusive use by the purchaser of the work. Duplication of this publication or parts thereof is permitted only under the provisions of the Copyright Law of the Publisher's location, in its current version, and permission for use must always be obtained from Springer. Permissions for use may be obtained through RightsLink at the Copyright Clearance Center. Violations are liable to prosecution under the respective Copyright Law. The use of general descriptive names, registered names, trademarks, service marks, etc. in this publication does not imply, even in the absence of a specific statement, that such names are exempt from the relevant protective laws and regulations and therefore free for general use.

While the advice and information in this book are believed to be true and accurate at the date of publication, neither the authors nor the editors nor the publisher can accept any legal responsibility for any errors or omissions that may be made. The publisher makes no warranty, express or implied, with respect to the material contained herein.

Printed on acid-free paper

Springer is part of Springer Science+Business Media (www.springer.com)

Dedicated to my grandparents in the USA, Kenichiro and Asano Kanzaki

# **Preface to the Second Edition**

The book *Fundamentals of Semiconductor Lasers* is a bridge between textbooks and journal papers on laser diodes (LDs). In the second edition, misprints in the first edition are corrected, and a multiple-layer model is added in Chap. 3 to analyze antiguiding. Based on the multiple-layer model, the basics of antiguiding and several journal papers on single horizontal transverse mode operations in LDs with antiguiding structures are explained in Chap. 5. In Chap. 6, a journal letter on single longitudinal mode operations in the first manufactured phase-shifted DFB-LD is described. The entire manuscript was written using the Système International d'Unités (SI). As a result, Appendix E in the second edition looks rather more complicated than Appendix E in the first edition. It should be noted that the manuscripts for the first edition were written in SI units except for Appendix E, which was written in CGS Gaussian units to express wave equations in simple formulas. In Appendix H, two definitions of photon density are compared and the rate equations with each definition are derived in order to avoid confusion when reading journal papers.

Finally, I am very grateful to Dr. Hisako Niko, Springer Japan, for providing an opportunity for publication of the second edition.

Kusatsu, Japan Takahiro Numai

# **Preface to the First Edition**

Semiconductor lasers have been actively studied since the first laser oscillation in 1962. Through continuing efforts based on physics, characteristics of semiconductor lasers have been extensively improved. As a result, they are now widely used. For example, they are used as the light sources for bar-code readers, compact disks (CDs), CD-ROMs, magneto-optical disks (MOs), digital video disks (DVDs), DVD-ROMs, laser printers, lightwave communication systems, and pumping sources of solid-state lasers. From these facts, it may be said that semiconductor lasers are indispensable for our contemporary life.

This textbook explains the physics and fundamental characteristics of semiconductor lasers with regard to system applications. It is aimed at senior undergraduates, graduate students, engineers, and researchers. The features of this book are as follows:

- The required knowledge to read this book is electromagnetism and introductory quantum mechanics taught in undergraduate courses. After reading this book, students will be able to understand journal papers on semiconductor lasers without difficulty.
- To solve problems in semiconductor lasers, sometimes opposite approaches are adopted according to system applications. These approaches are compared and explained.
- 3. In the research of semiconductor lasers, many ideas have been proposed and tested. Some ideas persist, and others have faded out. These ideas are compared and the key points of the persisting technologies are revealed.
- 4. The operating principles are often the same, although the structures seem to be different. These common concepts are essential and important; they allow us to deeply understand the physics of semiconductor lasers. Therefore, common concepts are emphasized in several examples, which lead to both a qualitative and a quantitative understanding of semiconductor lasers.

This book consists of two parts. The first part, Chapters 1–4 and reviews fundamental subjects such as the band structures of semiconductors, optical transitions, optical waveguides, and optical resonators. Based on these fundamentals, the

Preface to the First Edition

second part, Chapters 5–8 explains semiconductor lasers. The operating principles and basic characteristics of semiconductor lasers are discussed in Chapter 5 More advanced topics, such as dynamic single-mode lasers, quantum well lasers, and control of spontaneous emission, are described in Chapters 6–8.

Finally, the author would like to thank Professor emeritus of the University of Tokyo, Koichi Shimoda (former professor at Keio University), Professor Kiyoji Uehara of Keio University, Professor Tomoo Fujioka of Tokai University (former professor at Keio University), and Professor Minoru Obara of Keio University for their warm encouragement and precious advice since he was a student. He is also indebted to NEC Corporation, where he started research on semiconductor lasers soon after graduation from Keio University. Thanks are extended to the entire team at Springer-Verlag, especially Mr. Frank Ganz, Mr. Frank McGuckin, Ms. Margaret Mitchell, Mr. Timothy Taylor, and Dr. Hans Koelsch, for their kind help.

Kusatsu, Japan, September 2003

Takahiro Numai

# **Contents**

1	Band	Structures	1
	1.1	Introduction	1
	1.2	Bulk Structures	2
		1.2.1 $k \cdot p$ Perturbation Theory	2
		1.2.2 Spin-Orbit Interaction	6
	1.3		12
		1.3.1 Potential Well	12
		1.3.2 Quantum Well, Wire, and Box	14
	1.4	Super Lattices	19
		1.4.1 Potential	20
		1.4.2 Period	21
		1.4.3 Other Features in Addition to Quantum Effects	21
	Refere	ences	22
2	Optic	ral Transitions	23
	2.1	Introduction	23
	2.2	Light Emitting Processes	24
		2.2.1 Lifetime	25
		2.2.2 Excitation	25
		2.2.3 Transition States	25
	2.3	Spontaneous Emission, Stimulated Emission,	
		and Absorption	26
	2.4	Optical Gains	27
		2.4.1 Lasers	27
		2.4.2 Optical Gains	28
	Refere	ences	40
3	Optic	al Waveguides	11
	3.1	•	11
	3.2		13
			13

xii Contents

		3.2.2	Three-Layer Model to Analyze Guided Modes	44
		3.2.3	Multiple-Layer Model to Analyze	
			Guided Modes	52
	3.3	Three-l	Dimensional Optical Waveguides	56
		3.3.1	Effective Refractive Index Method	57
		3.3.2	Marcatili's Method	58
	Refer	ences		58
4	Optio	al Reson	nators	61
	4.1	Introdu	action	61
	4.2	Fabry-l	Perot Cavity	61
		4.2.1	Resonance Condition	65
		4.2.2	Free Spectral Range	65
		4.2.3	Spectral Linewidth	66
		4.2.4	Finesse	67
		4.2.5	Electric Field Inside Fabry-Perot Cavity	67
	4.3	DFB at	nd DBR	68
		4.3.1	Coupled Wave Theory	68
		4.3.2	Discrete Approach	72
		4.3.3	Comparison of Coupled Wave Theory	
			and Discrete Approach	74
		4.3.4	Category of Diffraction Gratings	76
		4.3.5	Phase-Shifted Grating	77
		4.3.6	Fabrication of Diffraction Gratings	81
	Refer	ences		86
_	E J	4-1-	of Construction In April 1	0.0
5			s of Semiconductor Lasers	89
	5.1	•	lements in Semiconductor Lasers	89
		5.1.1	Fabry-Perot Cavity	89
		5.1.2	pn-Junction.	90
	<i>5</i> 2	5.1.3	Double Heterostructure	91
	5.2		old Gain	92
		5.2.1	Resonance Condition	92
	<b>7</b> 0	5.2.2	Gain Condition	93
	5.3		ion Efficiency	94
		5.3.1	Slope Efficiency	94
		5.3.2	External Differential Quantum Efficiency	95
	<i>-</i> .	5.3.3	Light Output Ratio from Facets	96
	5.4		t Versus Light Output ( <i>I–L</i> ) Characteristics	97
		5.4.1	Rate Equations	97
		5.4.2	Threshold Current Density	99
		5.4.3	Current Versus Light Output ( <i>I–L</i> ) Characteristics	40.
			in CW Operation	101
		5.4.4	Dependence of <i>I–L</i> on Temperature	104

Contents xiii

	5.5	Current	Versus Voltage $(I-V)$ Characteristics	106
	5.6	Derivati	ive Characteristics	107
		5.6.1	Derivative Light Output	108
		5.6.2	Derivative Electrical Resistance	109
	5.7	Polariza	tion of Light	110
	5.8		ters and Specifications	111
	5.9		ode Operation	111
	5.10	Transve	rse Modes	114
		5.10.1	Vertical Transverse Modes	115
		5.10.2	Horizontal Transverse Modes	118
		5.10.3	Antiguiding	123
		5.10.4	Transverse Diffraction Grating	136
	5.11		dinal Modes	137
		5.11.1	Static Characteristics of Fabry-Perot LDs	139
		5.11.2	Dynamic Characteristics of Fabry-Perot LDs	141
	5.12	Modula	tion Characteristics	147
		5.12.1	Lightwave Transmission Systems	
			and Modulation	147
		5.12.2	Direct Modulation	150
	5.13	Noises.		156
		5.13.1	Quantum Noises	156
		5.13.2	Relative Intensity Noise (RIN)	169
		5.13.3	RIN with No Carrier Fluctuations	170
		5.13.4	RIN with Carrier Fluctuations	171
		5.13.5	Noises on Longitudinal Modes	175
		5.13.6	Optical Feedback Noise	177
	5.14		ations and Lifetime	182
		5.14.1	Classification of Degradations	183
		5.14.2	Lifetime	185
	Refere	ences		185
6	Dynai	mic Singl	e-Mode LDs	187
U	6.1	_	ction	187
	6.2		Os and DBR-LDs	187
	0.2	6.2.1	DFB-LDs	188
		6.2.2	DBR-LDs.	197
	6.3		Emitting LDs	198
	0.5	6.3.1	Vertical Cavity Surface Emitting LDs	198
		6.3.2	Horizontal Cavity Surface Emitting LDs	198
	6.4			199
			1 Cavity LDs	200
	Keiere	inces		∠00

xiv Contents

7	Quanti	um Well LDs	201
	7.1	Introduction	201
	7.2	Features of Quantum Well LDs	201
		7.2.1 Configurations of Quantum Wells	201
		7.2.2 Characteristics of QW-LDs	202
	7.3	Strained Quantum Well LDs	212
		7.3.1 Effect of Strains	212
		7.3.2 Band-Structure Engineering	213
		7.3.3 Analysis	216
	7.4	Requirements for Fabrication	224
	Referer	nces	224
8	Contro	ol of Spontaneous Emission	227
	8.1	Introduction	227
	8.2	Spontaneous Emission	227
		8.2.1 Fermi's Golden Rule	227
		8.2.2 Spontaneous Emission in a Free Space	229
		8.2.3 Spontaneous Emission in a Microcavity	229
		8.2.4 Fluctuations in the Vacuum Field	230
	8.3	Microcavity LDs	231
	8.4	Photon Recycling	232
	Referer	nces	234
Apj	pendix A	A: Cyclotron Resonance	235
Apj	pendix E	3: Time-Independent Perturbation Theory	239
Apj	oendix (	C: Time-Dependent Perturbation Theory	245
Apj	pendix I	D: TE Mode and TM Mode	253
Apj	pendix E	E: Characteristic Matrix in Discrete Approach	259
Anı	oendix F	F: Free Carrier Absorption and Plasma Effect	267
		•	
App	pendix (	G: Relative Intensity Noise (RIN)	269
App	pendix F	I: Rate Equations: Comparison of Two Definitions of the Photon Density	277
Ind	077		202

# Chapter 1 Band Structures

### 1.1 Introduction

Optical transitions, such as the *emission* and *absorption* of light, are closely related to the energies of electrons, as shown in Table 1.1. When electrons transit from high energy states to lower ones, lights are emitted, and in the reverse process, lights are absorbed. Note that *nonradiative transitions*, which do not emit lights, also exist when electrons transit from high energy states to lower ones. Light emissions, however, always accompany the transitions of electrons from high energy states to lower ones, which are referred to as *radiative transitions*.

Let us consider electron energies, which are the bases of the optical transitions. Figure 1.1 shows a relationship between atomic spacing and electron energies. When the atomic spacing is large, such as in gases, the electron energies are *discrete* and the *energy levels* are formed. With a decrease in the atomic spacing, the wave functions of the electrons start to overlap. Therefore, the energy levels begin to split so as to satisfy the *Pauli exclusion principle*. With an increase in the number of neighboring atoms, the number of split energy levels is enhanced, and the energy differences in the adjacent energy levels are reduced. In the semiconductor crystals, the number of atoms per cubic centimeter is of the order of  $10^{22}$ , where the lattice constant is approximately 0.5 nm and the atomic spacing is about 0.2 nm. As a result, the spacing of energy levels is of the order of  $10^{-18}$  eV. This energy spacing is much smaller than the *bandgap*, which is of the order of electron volts. Therefore, the constituent energy levels, which are known as the *energy bands*, are considered to be almost *continuous*.

**Table 1.1** Relationship between electron energies and optical transitions

Energy of the electrons	Optical transition
$High \rightarrow low$	Emission
Low → high	Absorption

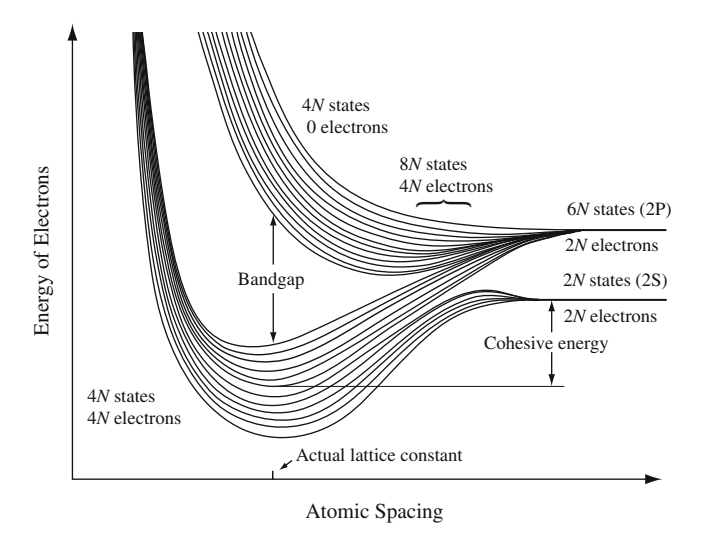


Fig. 1.1 Relationship between atomic spacing and electron energies for the diamond structure with N atoms

#### 1.2 Bulk Structures

# 1.2.1 $k \cdot p$ Perturbation Theory

We study the band structures of the *bulk* semiconductors, in which constituent atoms are periodically placed in a sufficiently long range compared with the lattice spacing.

Semiconductors have carriers, such as free electrons and holes, only in the vicinity of the band edges. As a result, we would like to know the band shapes and the effective masses of the carriers near the band edges, and they often give us enough information to understand fundamental characteristics of the optical transitions. When we focus on the neighbor of the band edges, it is useful to employ the  $k \cdot p$  perturbation theory [1–4] whose wave vectors ks are near the band edge wave vector  $k_0$  inside the Brillouin zone. The wave functions and energies of the bands are calculated with  $\Delta k = k - k_0$  as a perturbation parameter. For brevity, we put  $k_0 = 0$  in the following.

The Schrödinger equation in the steady state is written as [5, 6]

$$\left[ -\frac{\hbar^2}{2m} \nabla^2 + V(\mathbf{r}) \right] \psi_{n\mathbf{k}}(\mathbf{r}) = E_n(\mathbf{k}) \psi_{n\mathbf{k}}(\mathbf{r}), \tag{1.1}$$

1.2 Bulk Structures 3

where  $\hbar = h/2\pi = 1.0546 \times 10^{-34} \, \text{J} \, \text{s}$  is *Dirac's constant*,  $h = 6.6261 \times 10^{-34} \, \text{J} \, \text{s}$  is *Planck's constant*,  $m = 9.1094 \times 10^{-31} \, \text{kg}$  is the electron mass in a vacuum,  $V(\mathbf{r})$  is a potential,  $\psi_{n\mathbf{k}}(\mathbf{r})$  is a wave function,  $E_n(\mathbf{k})$  is an *energy eigenvalue*, n is a *quantum number*, and  $\mathbf{k}$  is a wave vector. In the *single crystals* where the atoms are placed *periodically*, the potential  $V(\mathbf{r})$  is spatially periodic. Therefore, as a solution of (1.1), we can consider the *Bloch function* given by

$$\psi_{nk}(\mathbf{r}) = e^{i \mathbf{k} \cdot \mathbf{r}} u_{nk}(\mathbf{r}), \tag{1.2}$$

$$u_{nk}(\mathbf{r}) = u_{nk}(\mathbf{r} + \mathbf{R}), \tag{1.3}$$

where R is a vector indicating the periodicity of the crystal. The theorem that (1.2) and (1.3) satisfy (1.1) is called the *Bloch theorem*, which indicates that the wave function  $u_{nk}(r)$  depends on the wave vector k and has the same periodicity as that of the crystal. Substituting (1.2) into (1.1) results in

$$\left[ -\frac{\hbar^2}{2m} \nabla^2 + V(\mathbf{r}) + \mathcal{H}' \right] u_{n\mathbf{k}}(\mathbf{r}) = E_n(\mathbf{k}) u_{n\mathbf{k}}(\mathbf{r}), \tag{1.4}$$

where

$$\mathcal{H}' = \frac{\hbar^2 \mathbf{k}^2}{2m} + \frac{\hbar}{m} \mathbf{k} \cdot \mathbf{p},\tag{1.5}$$

$$\mathbf{p} = -\mathrm{i}\,\hbar\nabla.\tag{1.6}$$

In the  $k \cdot p$  perturbation theory, which is only valid for small k, we solve (1.4) by regarding (1.5) as the *perturbation*. Note that the name of the  $k \cdot p$  perturbation stems from the second term on the right-hand side of (1.5).

When we consider the energy band with n = 0, the wave equation for the unperturbed state with k = 0 is expressed as

$$\left[ -\frac{\hbar^2}{2m} \nabla^2 + V(\mathbf{r}) \right] u_{00}(\mathbf{r}) = E_0(0) u_{00}(\mathbf{r}). \tag{1.7}$$

In the following, for simplicity, the wave function  $u_{nk}(\mathbf{r})$  and the energy  $E_0(0)$  are represented as  $u_n(\mathbf{k}, \mathbf{r})$  and  $E_0$ , respectively.

At first, we consider a nondegenerate case, in which the energy of the state n is always different from that of the other state n' ( $\neq n$ ). From the *first-order* perturbation theory (see Appendix B), the wave function  $u_0(k, r)$  is given by

$$u_0(\mathbf{k}, \mathbf{r}) = u_0(0, \mathbf{r}) + \sum_{\alpha \neq 0} \frac{-\mathrm{i} \left(\hbar^2 / m\right) \mathbf{k} \cdot \langle \alpha | \nabla | 0 \rangle}{E_0 - E_\alpha} u_\alpha(0, \mathbf{r}), \tag{1.8}$$

$$\langle \alpha | \nabla | 0 \rangle = \int u_{\alpha}^{*}(0, \mathbf{r}) \nabla u_{0}(0, \mathbf{r}) d^{3} \mathbf{r}, \qquad (1.9)$$

where  $u_n(k, r)$  is assumed to be an orthonormal function. Here,  $\langle \alpha |$  and  $|0 \rangle$  are the *bra vector* and the *ket vector*, respectively, which were introduced by Dirac. In the *second-order perturbation theory*, an energy eigenvalue is obtained as

$$E(\mathbf{k}) = E_0 + \frac{\hbar^2 k^2}{2m} + \frac{\hbar^2}{m^2} \sum_{i,j} k_i k_j \sum_{\alpha \neq 0} \frac{\langle 0 | p_i | \alpha \rangle \langle \alpha | p_j | 0 \rangle}{E_0 - E_\alpha}.$$
 (1.10)

From (1.10), the reciprocal effective mass tensor is defined as

$$\left(\frac{1}{m}\right)_{ij} \equiv \frac{1}{\hbar^2} \frac{\partial^2 E}{\partial k_i \partial k_j} = \frac{1}{m} \left(\delta_{ij} + \frac{2}{m} \sum_{\alpha \neq 0} \frac{\langle 0 | p_i | \alpha \rangle \langle \alpha | p_j | 0 \rangle}{E_0 - E_\alpha}\right).$$
(1.11)

With the help of (1.11), (1.10) reduces to

$$E(\mathbf{k}) = E_0 + \frac{\hbar^2}{2} \sum_{i,j} \left(\frac{1}{m}\right)_{ij} k_i k_j.$$
 (1.12)

This equation includes the periodicity of the crystal (potential) in the mass of the electron as the effective mass. This effective mass is useful to make analysis easier. For example, in the quantum well (QW) structures, the electrons see both the periodic potential of the crystal and the quantum well potential. If we express equations using the effective mass, we have only to consider the quantum well potential, because the periodic potential of the crystal is already included in the effective mass. This approximation is referred to as the *effective mass approximation*.

In the following, we will consider the band structures of semiconductor crystals. Most semiconductor crystals for semiconductor lasers have a *zinc-blende structure*, in which the bottom of the conduction bands is *s*-orbital-like and the tops of the valence bands are *p*-orbital-like. In zinc-blende or diamond structures, the atomic bonds are formed via  $sp^3$  hybrid orbitals as follows:

C: 
$$(2s)^2(2p)^2 \to (2s)^1(2p)^3$$
  
Si:  $(3s)^2(3p)^2 \to (3s)^1(3p)^3$   
ZnS: Zn:  $(3d)^{10}(4s)^2 \to \text{Zn}^{2-}: (3d)^{10}(4s)^1(4p)^3$   
S:  $(3s)^2(3p)^4 \to \text{S}^{2+}: (3s)^1(3p)^3$ 

Therefore, the wave functions for the electrons in the zinc-blende or diamond structures are expressed as superpositions of the *s*-orbital function and *p*-orbital functions.

Let us calculate the wave functions and energies of the bands in the zinc-blende structures. We assume that both the bottom of the conduction band and the tops of the valence bands are placed at k = 0, as in the direct transition semiconductors, which will be elucidated in Sect. 2.1. When the spin-orbit interaction is neglected, the tops of the valence bands are threefold *degenerate* corresponding to the three p-orbitals  $(p_x, p_y, p_z)$ . Here, the wave functions are written as

1.2 Bulk Structures 5

the *s*-orbital function for the bottom of the conduction band :  $u_s(\mathbf{r})$ , the *p*-orbital functions for the tops of the valence bands :

$$u_x = xf(\mathbf{r}), \ u_y = yf(\mathbf{r}), \ u_z = zf(\mathbf{r}), \ f(\mathbf{r})$$
: a spherical function.

When the energy bands are degenerate, a perturbed wave equation is given by a linear superposition of  $u_s(\mathbf{r})$  and  $u_i(\mathbf{r})$  (j = x, y, z) as

$$u_n(\mathbf{k}, \mathbf{r}) = Au_s(\mathbf{r}) + Bu_x(\mathbf{r}) + Cu_y(\mathbf{r}) + Du_z(\mathbf{r}),$$
 (1.13)

where A, B, C, and D are coefficients.

To obtain the energy eigenvalues, we rewrite (1.4) as

$$\left[ -\frac{\hbar^2}{2m} \nabla^2 + V(\mathbf{r}) + \mathcal{H}'_{\mathrm{d}} \right] u_n(\mathbf{k}, \mathbf{r}) = \left[ E_n(\mathbf{k}) - \frac{\hbar^2 k^2}{2m} \right] u_n(\mathbf{k}, \mathbf{r}), \tag{1.14}$$

$$\mathcal{H}'_{d} = \frac{\hbar}{m} \, \mathbf{k} \cdot \mathbf{p} = -\frac{\mathrm{i} \, \hbar^{2}}{m} \mathbf{k} \cdot \nabla. \tag{1.15}$$

Note that the unperturbed equation is obtained by setting k = 0 in (1.14), where  $E_n(0) = E_c$  and  $u_0(0, \mathbf{r}) = u_s(\mathbf{r})$  for the conduction band, while  $E_n(0) = E_v$  and  $u_0(0, \mathbf{r}) = u_j(\mathbf{r})$  (j = x, y, z) for the valence bands. Here,  $E_c$  is the energy of the bottom of the conduction band, and  $E_v$  is the energy of the tops of the valence bands.

Substituting (1.13) into (1.14); multiplying  $u_s^*(r)$ ,  $u_x^*(r)$ ,  $u_y^*(r)$ , and  $u_z^*(r)$  from the left-hand side; and then integrating with respect to a volume over the space leads to

$$(\mathcal{H}'_{ss} + E_{c} - \lambda)A + \mathcal{H}'_{sx}B + \mathcal{H}'_{sy}C + \mathcal{H}'_{sz}D = 0, 
\mathcal{H}'_{xs}A + (\mathcal{H}'_{xx} + E_{v} - \lambda)B + \mathcal{H}'_{xy}C + \mathcal{H}'_{xz}D = 0, 
\mathcal{H}'_{ys}A + \mathcal{H}'_{yx}B + (\mathcal{H}'_{yy} + E_{v} - \lambda)C + \mathcal{H}'_{yz}D = 0, 
\mathcal{H}'_{zs}A + \mathcal{H}'_{zx}B + \mathcal{H}'_{zy}C + (\mathcal{H}'_{zz} + E_{v} - \lambda)D = 0,$$
(1.16)

where

$$\mathcal{H}'_{ij} = \langle u_i | \mathcal{H}'_{d} | u_j \rangle = \int u_i^*(\mathbf{r}) \mathcal{H}'_{d} u_j(\mathbf{r}) d^3 \mathbf{r}(i, j = s, x, y, z),$$

$$\lambda = E_n(\mathbf{k}) - \frac{\hbar^2 k^2}{2m}.$$
(1.17)

Note that the orthonormality of  $u_s(\mathbf{r})$  and  $u_j(\mathbf{r})$  (j = x, y, z) were used to derive (1.16).

In (1.16), only when the determinant for the coefficients A, B, C, and D is zero, we have solutions A, B, C, and D other than A = B = C = D = 0. From (1.16) and (1.17), the determinant is given by

$$\begin{vmatrix} E_{c} - \lambda & Pk_{x} & Pk_{y} & Pk_{z} \\ P^{*}k_{x} & E_{v} - \lambda & 0 & 0 \\ P^{*}k_{y} & 0 & E_{v} - \lambda & 0 \\ P^{*}k_{z} & 0 & 0 & E_{v} - \lambda \end{vmatrix} = 0,$$
(1.18)

$$P = -i \frac{\hbar^2}{m} \int u_s^* \frac{\partial u_j}{\partial r_j} d^3 \mathbf{r}, \quad P^* = -i \frac{\hbar^2}{m} \int u_j^* \frac{\partial u_s}{\partial r_j} d^3 \mathbf{r}$$

$$(j = x, y, z, \quad r_x = x, \quad r_y = y, \quad r_z = z).$$
(1.19)

The solutions of (1.18) are obtained as

$$E_{1,2}(\mathbf{k}) = \frac{E_{\rm c} + E_{\rm v}}{2} + \frac{\hbar^2 k^2}{2m} \pm \left[ \left( \frac{E_{\rm c} - E_{\rm v}}{2} \right)^2 + k^2 |P|^2 \right]^{1/2},\tag{1.20}$$

$$E_{3,4}(\mathbf{k}) = E_{\rm v} + \frac{\hbar^2 k^2}{2m},\tag{1.21}$$

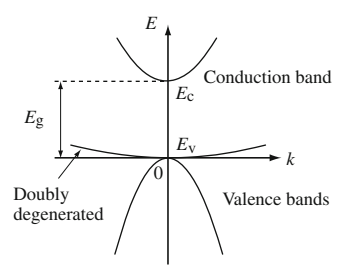
where (1.17) was used. Figure 1.2 shows the calculated results of (1.20) and (1.21). It should be noted that the spin-orbit interaction has been neglected and only the first-order perturbation has been included to derive these equations.

# 1.2.2 Spin-Orbit Interaction

We consider the band structures by introducing the spin-orbit interaction and the second-order perturbation. First, let us treat the *spin-orbit interaction* semiclassically. As shown in Fig. 1.3, the electron with the electric charge  $-e = -1.6022 \times 10^{-19}$  C rotates about the nucleus with the electric charge +Ze. The velocity of the electron is v, and the distance between the electron and the nucleus is |r|.

If the origin of the reference system is placed at the electron, the nucleus seems to rotate about the electron with the velocity -v. As a result, due to *Biot-Savart's law*, a *magnetic flux density B* is produced at the electron, which is written as

Fig. 1.2 Energy of the conduction and valence bands. Here, only the first-order perturbation is included; the spin-orbit interaction is neglected



1.2 Bulk Structures 7

$$\mathbf{B} = \frac{\mu_0}{4\pi} Z e^{\frac{\mathbf{r} \times \mathbf{v}}{r^3}} = \frac{\mu_0}{4\pi} \frac{Ze}{m} \frac{1}{r^3} \mathbf{l}.$$
 (1.22)

Here,  $\mu_0$  is magnetic permeability in a vacuum, and  $\boldsymbol{l}$  is the *orbital angular momentum* given by

$$l = r \times p = r \times mv. \tag{1.23}$$

The *spin magnetic moment*  $\mu_s$  is expressed as

$$\mu_{\rm s} = -\frac{e}{m}s = -\frac{2\mu_{\rm B}}{\hbar}s,\tag{1.24}$$

where s is the spin angular momentum and  $\mu_B$  is the Bohr magneton defined as

$$\mu_{\rm B} \equiv \frac{e\hbar}{2m} = 9.2740 \times 10^{-24} \,\mathrm{A}\,\mathrm{m}^2.$$
 (1.25)

As a result, the *interaction energy*  $\mathcal{H}_{SO}$  between the *spin magnetic moment*  $\mu_s$  and the magnetic flux density  $\boldsymbol{B}$  is obtained as

$$\mathcal{H}_{SO} = -\boldsymbol{\mu}_{s} \cdot \boldsymbol{B} = \frac{\mu_{0}}{4\pi} \frac{Ze^{2}}{m^{2}} \frac{1}{r^{3}} \boldsymbol{l} \cdot \boldsymbol{s}. \tag{1.26}$$

From Dirac's relativistic quantum mechanics, the interaction energy  $\mathcal{H}_{SO}$  is given by

$$\mathcal{H}_{SO} = \frac{\mu_0}{4\pi} \frac{Ze^2}{2m^2} \frac{1}{r^3} \mathbf{l} \cdot \mathbf{s}, \tag{1.27}$$

which is half of (1.26). As explained earlier, the spin-orbit interaction generates a magnetic field at the electron due to the orbital motions of the nucleus, and this field interacts with the electron's spin magnetic moment.

Introducing *Pauli's spin matrices*  $\sigma$  such as

$$s = \frac{\hbar}{2}\sigma,\tag{1.28}$$

$$\sigma_x = \begin{bmatrix} 0 & 1 \\ 1 & 0 \end{bmatrix}, \quad \sigma_y = \begin{bmatrix} 0 & -i \\ i & 0 \end{bmatrix}, \quad \sigma_z = \begin{bmatrix} 1 & 0 \\ 0 & -1 \end{bmatrix},$$
 (1.29)

we can write the *spin-orbit interaction Hamiltonian*  $\mathcal{H}_{SO}$  as

**Fig. 1.3** Motions of the electron



$$\mathcal{H}_{SO} = \frac{\mu_0}{4\pi} \frac{Ze^2}{2m^2} \frac{1}{r^3} \frac{\hbar}{2} \mathbf{l} \cdot \mathbf{\sigma}.$$
 (1.30)

If we express the *up-spin*  $\uparrow$   $(s_z = \hbar/2)$  as  $\alpha$  and the *down-spin*  $\downarrow$   $(s_z = -\hbar/2)$  as  $\beta$ , they are written in matrix form as

$$\alpha = \begin{bmatrix} 1 \\ 0 \end{bmatrix}, \quad \beta = \begin{bmatrix} 0 \\ 1 \end{bmatrix}. \tag{1.31}$$

Using  $\alpha$  and  $\beta$ , we obtain the following relations:

$$\sigma_{\tau}\alpha = \alpha, \quad \sigma_{\tau}\beta = -\beta.$$
 (1.32)

To treat the spin-orbit interaction, it is convenient to use the *spherical polar* coordinate systems. Therefore, we rewrite the spin-orbit interaction Hamiltonian  $\mathcal{H}_{SO}$  as

$$\mathcal{H}_{SO} = \frac{\hbar}{2} \, \xi(\mathbf{r}) \, \mathbf{l} \cdot \mathbf{\sigma} = \frac{\hbar}{2} \, \xi(\mathbf{r}) \left( l_z \sigma_z + \frac{l_+ \sigma_- + l_- \sigma_+}{2} \right), \tag{1.33}$$

where

$$\xi(\mathbf{r}) = \frac{\mu_0}{4\pi} \frac{Ze^2}{2m^2} \frac{1}{r^3},$$

$$l_{+} = l_x + i l_y, \quad l_{-} = l_x - i l_y,$$

$$\sigma_{+} = \sigma_x + i \sigma_y, \quad \sigma_{-} = \sigma_x - i \sigma_y.$$
(1.34)

When this  $\mathcal{H}_{SO}$  is added to the perturbation term, the wave equation (1.14) is modified as

$$\left[ -\frac{\hbar^2}{2m} \nabla^2 + V(\mathbf{r}) + \mathcal{H}'_{d} + \mathcal{H}_{SO} \right] u_n(\mathbf{k}, \mathbf{r}) = \left[ E_n(\mathbf{k}) - \frac{\hbar^2 k^2}{2m} \right] u_n(\mathbf{k}, \mathbf{r}). \quad (1.35)$$

It should be noted that l operates on  $e^{i k \cdot r}$  in the Bloch function, but this operation is neglected because the result is much smaller than the other terms.

To solve (1.35), it is useful to represent the wave functions  $u_n(\mathbf{k}, \mathbf{r})$  in the spherical polar coordinate systems such as

$$u_{s} = u_{s},$$

$$u_{+} = -\frac{u_{x} + i u_{y}}{\sqrt{2}} \sim -\frac{x + i y}{\sqrt{2}},$$

$$u_{-} = \frac{u_{x} - i u_{y}}{\sqrt{2}} \sim \frac{x - i y}{\sqrt{2}},$$

$$u_{z} \sim z.$$

$$(1.36)$$

1.2 Bulk Structures 9

In (1.36), the spherical function f(r) is omitted after  $\sim$  to simplify expressions. Note that  $\sqrt{2}$  in the denominators is introduced to normalize the wave functions. Using the spherical harmonic function  $Y_l^m$ , the wave functions  $u_+$ ,  $u_-$ , and  $u_z$  are also expressed as

$$u_{+} = Y_{1}^{1} = -\frac{1}{2}\sqrt{\frac{3}{2\pi}} \frac{x + iy}{\sqrt{x^{2} + y^{2} + z^{2}}} = -\frac{1}{2}\sqrt{\frac{3}{2\pi}} e^{i\phi} \sin\theta,$$

$$u_{-} = Y_{1}^{-1} = \frac{1}{2}\sqrt{\frac{3}{2\pi}} \frac{x - iy}{\sqrt{x^{2} + y^{2} + z^{2}}} = \frac{1}{2}\sqrt{\frac{3}{2\pi}} e^{-i\phi} \sin\theta,$$

$$u_{z} = Y_{1}^{0} = \frac{1}{2}\sqrt{\frac{3}{\pi}} \frac{z}{\sqrt{x^{2} + y^{2} + z^{2}}} = \frac{1}{2}\sqrt{\frac{3}{\pi}} \cos\theta,$$
(1.37)

where  $x = r \sin \theta \cos \phi$ ,  $y = r \sin \theta \sin \phi$ , and  $z = r \cos \theta$ .

When we consider the up- and down-spins  $\alpha$  and  $\beta$ , we have eight wave functions as follows:

$$u_s\alpha$$
,  $u_s\beta$ ,  $u_+\alpha$ ,  $u_+\beta$ ,  $u_z\alpha$ ,  $u_z\beta$ ,  $u_-\alpha$ ,  $u_-\beta$ .

Therefore, we have to calculate the elements of the  $8 \times 8$  matrix to obtain the energy eigenvalues from (1.35).

For brevity, we assume that k is directed in the z-direction and put

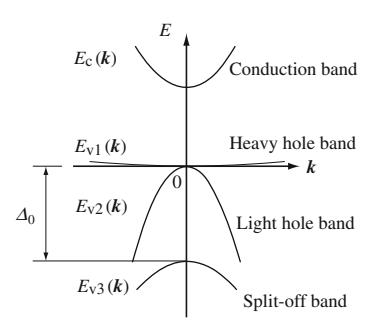
$$k_z = k, \ k_x = k_y = 0.$$
 (1.38)

In this case, however, we have only to solve the determinant for the  $4 \times 4$  matrix on  $(u_s\alpha, u_+\beta, u_z\alpha, u_-\beta)$  or  $(u_s\beta, u_-\alpha, u_z\beta, u_+\alpha)$  because of the symmetry in the  $8 \times 8$  matrix. This determinant for the  $4 \times 4$  matrix is written as

$$\begin{vmatrix} E_{c} - \lambda & 0 & Pk & 0 \\ 0 & E_{v} - \lambda - \frac{\Delta_{0}}{3} & \frac{\sqrt{2}}{3} \Delta_{0} & 0 \\ P^{*}k & \frac{\sqrt{2}}{3} \Delta_{0} & E_{v} - \lambda & 0 \\ 0 & 0 & 0 & E_{v} - \lambda + \frac{\Delta_{0}}{3} \end{vmatrix} = 0, \quad (1.39)$$

where the terms including  $\Delta_0$  are the matrix elements of  $\mathcal{H}_{SO}$ , and the other terms are those of  $\mathcal{H}'_d$ . Here, using  $\xi(\mathbf{r})$  in (1.34),  $\Delta_0$  is defined as

**Fig. 1.4** Energy bands when the spin-orbit interaction is considered under the first-order perturbation



$$\frac{\Delta_0}{3} = \frac{\hbar^2}{2} \int u_+^* u_+ \xi(\mathbf{r}) \, \mathrm{d}^3 \mathbf{r} = \frac{\hbar^2}{2} \int u_-^* u_- \xi(\mathbf{r}) \, \mathrm{d}^3 \mathbf{r} 
= \frac{\hbar^2}{4} \int (u_x^2 + u_y^2) \xi(\mathbf{r}) \, \mathrm{d}^3 \mathbf{r} = \frac{\hbar^2}{2} \int u_z^2 \xi(\mathbf{r}) \, \mathrm{d}^3 \mathbf{r}.$$
(1.40)

From (1.39), the energy of valence band 1 is obtained as

$$E_{\rm v1}(\mathbf{k}) = E_{\rm v} + \frac{\Delta_0}{3} + \frac{\hbar^2 k^2}{2m}.$$
 (1.41)

When  $|P|^2k^2$  is small enough, the energy of the conduction band  $E_c$  reduces to

$$E_{\rm c}(\mathbf{k}) = E_{\rm c} + \frac{\hbar^2 k^2}{2m} + \frac{|P|^2 k^2}{3} \left( \frac{2}{E_{\rm g}} + \frac{1}{E_{\rm g} + \Delta_0} \right),$$
 (1.42)

where

$$E_{\rm g} = E_{\rm c} - E_{\rm v} - \frac{\Delta_0}{3}.$$
 (1.43)

Similarly, the energies of valence bands 2 and 3 are given by

$$E_{v2}(\mathbf{k}) = E_{v} + \frac{\Delta_0}{3} + \frac{\hbar^2 k^2}{2m} - \frac{2|P|^2 k^2}{3E_{g}},$$
(1.44)

$$E_{v3}(\mathbf{k}) = E_{v} - \frac{2}{3}\Delta_{0} + \frac{\hbar^{2}k^{2}}{2m} - \frac{|P|^{2}k^{2}}{3(E_{g} + \Delta_{0})}.$$
 (1.45)

These results, which were obtained under the first-order  $k \cdot p$  perturbation, are shown in Fig. 1.4. From the definition of effective mass in (1.11), the band with energy  $E_{v1}(k)$  is referred to as the *heavy hole band*, and that with  $E_{v2}(k)$  is called the *light hole band*. It should be noted that the heavy hole band and the light hole band are degenerate at a point k = 0. The band with energy  $E_{v3}(k)$  is designated as the *split-off band*, and  $\Delta_0$  is called the *split-off energy*.

1.2 Bulk Structures 11

If we consider the second-order perturbation, the energies of the valence bands are given by

$$E_{v1,2}(\mathbf{k}) = E_v + \frac{\Delta_0}{3} + A_2 k^2$$

$$\pm \left[ B_2^2 k^4 + C_2^2 \left( k_x^2 k_y^2 + k_y^2 k_z^2 + k_z^2 k_x^2 \right) \right]^{1/2}$$

$$(1.46)$$

$$(1 \to +, 2 \to -)$$

$$E_{v3}(\mathbf{k}) = E_{v} - \frac{2}{3}\Delta_0 + A_2k^2. \tag{1.47}$$

The coefficients  $A_2$ ,  $B_2$ , and  $C_2$  in (1.46) and (1.47) are experimentally determined by the *cyclotron resonance* (see Appendix A). When the second-order perturbation is included, all the valence bands become upward-convex, as shown in Fig. 1.5, but degeneracy of the heavy hole band and the light hole band at k = 0 remains.

The preceding analysis treats the *direct transition* semiconductors where both the bottom of the conduction band and the tops of the valence bands are placed at k = 0. In the *indirect transition* semiconductors, k of the bottom of the conduction band and that of the tops of the valence bands are different. It should also be noted that the effective masses depend on the direction of k. Therefore, the band structures are more complicated.

Let us consider the wave functions of the valence bands under the second-order perturbation. Due to the spin-orbit interaction, the quantum states are indicated by j = l + s where l is the angular momentum operator and s is the spin operator. Therefore, as indexes of the wave functions, we use the quantum numbers j and  $m_j$ , which represent the eigenvalues of the operators j and  $j_z$ , respectively. The relation between the operators and the eigenvalues is summarized in Table 1.2.

When we express the wave functions as  $|j,m_j\rangle$ , the wave functions are expressed as

Fig. 1.5 Energy bands when the spin-orbit interaction is considered under the second-order perturbation

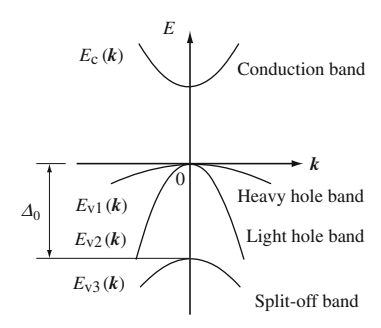


**Table 1.2** Relation between the operators and eigenvalues

Operator	Eigenvalue
$l^2$	$l(l+1)\hbar^2$ $(l=0:s ext{-orbital},\ l=1:p ext{-orbitals})$
$l_z$	$m_l \hbar, \ m_l = 1, 0, -1$
$s^2$	$s(s+1)\hbar^2, \ s=1/2$
$s_z$	$m_s \hbar, m_s = 1/2, -1/2$
$j^2$	$j(j+1)\hbar^2$ , $j = 3/2, 1/2$
$j_z$	$m_j \hbar, \ m_{j=3/2} = 3/2, 1/2, -1/2, -3/2,$
	$m_{j=1/2} = 1/2, -1/2$

for the heavy hole band

$$\left| \frac{3}{2}, \frac{3}{2} \right\rangle = \frac{1}{\sqrt{2}} \left| (x + i y) \alpha \right\rangle,$$

$$\left| \frac{3}{2}, -\frac{3}{2} \right\rangle = \frac{1}{\sqrt{2}} \left| (x - i y) \beta \right\rangle,$$
(1.48)

for the light hole band

$$\left| \frac{3}{2}, \frac{1}{2} \right\rangle = \frac{1}{\sqrt{6}} |2z\alpha + (x + iy)\beta\rangle,$$

$$\left| \frac{3}{2}, -\frac{1}{2} \right\rangle = \frac{1}{\sqrt{6}} |2z\beta - (x - iy)\alpha\rangle,$$
(1.49)

and for the split-off band

$$\left| \frac{1}{2}, \frac{1}{2} \right\rangle = \frac{1}{\sqrt{3}} |z\alpha - (x + iy)\beta\rangle,$$

$$\left| \frac{1}{2}, -\frac{1}{2} \right\rangle = \frac{1}{\sqrt{3}} |z\beta + (x - iy)\alpha\rangle.$$
(1.50)

# 1.3 Quantum Structures

# 1.3.1 Potential Well

The semiconductor structures whose sizes are small enough that their *quantum effects* may be significant are called *quantum structures*.

The electrons in the quantum structures see both the *periodic potential*, corresponding to the periodicity of the crystals, and the quantum well potential. Before studying the energy bands in the quantum structures, we will review the energies and wave functions of a particle in a square well potential.

Here, we assume that a carrier exists in a square potential well, as shown in Fig. 1.6. The square potential V(r) is

$$V(r) = 0$$
 inside the well  $V(r) = \infty$  outside the well. (1.51)

Note that the potential V(r) is not periodic. When the potential well is a cube with a side L, the boundary conditions for a wave function  $\phi(x, y, z)$  are given by

$$\phi(0, y, z) = \phi(L, y, z) = 0 
\phi(x, 0, z) = \phi(x, L, z) = 0 
\phi(x, y, 0) = \phi(x, y, L) = 0$$
(1.52)

Under these boundary conditions, the wave function  $\phi(x, y, z)$  and the energy E are obtained as

$$\phi(x, y, z) = \sqrt{\frac{8}{L^3}} \sin k_x x \cdot \sin k_y y \cdot \sin k_z z, \ E = \frac{\hbar^2}{2m} (k_x^2 + k_y^2 + k_z^2),$$

$$k_x = \frac{n_x \pi}{L}, \ k_y = \frac{n_y \pi}{L}, \ k_z = \frac{n_z \pi}{L} \quad (n_x, n_y, n_z = 1, 2, 3, \ldots). \tag{1.53}$$

Figure 1.7 shows the wave functions  $\phi$ s and the energies Es for a one-dimensional square well potential. As found in (1.53), the energies E are discrete and their values are proportional to a square of the quantum number  $n_x$ . Also, with a decrease in L, an energy separation between the energy levels increases. The wave functions can take negative values as well as positive ones. The squares of absolute values of the wave functions show possibilities of existence, so negative values are also allowed for the wave functions.

**Fig. 1.6** Square well potential

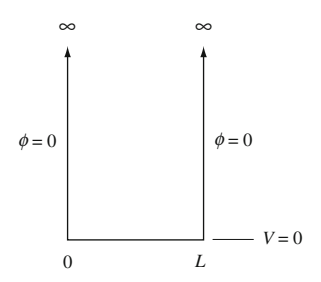
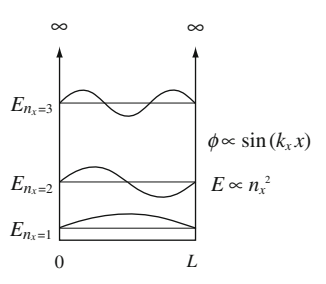


Fig. 1.7 Wave functions  $\phi$ s and energies Es in a one-dimensional square well potential



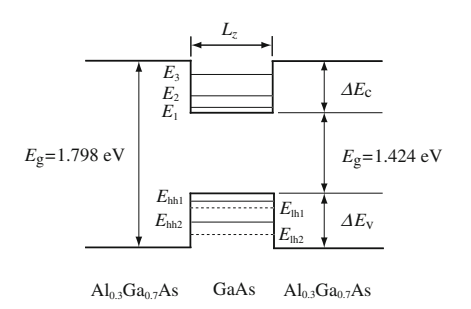
# 1.3.2 Quantum Well, Wire, and Box

First, we define some technical terms. Figure 1.8 shows the energies of the conduction band and valence bands for GaAs sandwiched by AlGaAs at a point k = 0.

The low energy regions for the electrons in the conduction band and the holes in the valence band are called *potential wells*. Note that, in Fig. 1.8, the vertical line shows the energy of the electrons, and the energy of the holes decreases with an increase in the height of the vertical line. In this figure, the potential well for the electrons in the conduction band and that for the holes in the valence band are both GaAs. When the width of this potential well  $L_z$  is of the order of less than several tens of nanometers, this well is referred to as the *quantum well*. The bandgaps of AlGaAs layers placed at both sides of GaAs are higher than that of GaAs. As a result, these AlGaAs layers function as the energy barriers for GaAs, and they are designated as the *energy barrier layers*. At the interfaces of the quantum well and the barriers, there are the energy difference in the conduction bands  $\Delta E_c$  and that in the valence bands  $\Delta E_v$ , which are called the *band offsets*.

The periods of the potential for the semiconductor crystals are the lattice constants, which are of the order of 0.5 nm. In contrast, the thickness of the potential wells or the barriers in the quantum structures is between the order of nanometers and several tens of nanometers. Hence, in the quantum structures, the electrons and the holes see both the *periodic potential* and the *quantum potential*. If we use the *effective mass*, the effect of the periodic potential is included in the effective mass, as shown

Fig. 1.8 Quantum well structure



in (1.12), and we have only to consider the quantum potential, which is referred to as the *effective mass approximation*.

Under the effective mass approximation, a wave function in the quantum structure is obtained by a product of the *base function*  $\psi$  and the *envelope function*  $\phi$ . As the base function, we use a wave function for the periodic potential

$$\psi_{nk}(\mathbf{r}) = e^{i \mathbf{k} \cdot \mathbf{r}} u_{nk}(\mathbf{r}), \quad u_{nk}(\mathbf{r}) = u_{nk}(\mathbf{r} + \mathbf{R}). \tag{1.54}$$

As the envelope function, we use a wave function for the quantum potential. For example, for a cube with the potential shown in Fig. 1.6,  $\phi$  is given by

$$\phi(x, y, z) = \sqrt{\frac{8}{L^3}} \sin k_x x \cdot \sin k_y y \cdot \sin k_z z. \tag{1.55}$$

#### 1.3.2.1 One-Dimensional Quantum Well

Let us consider a sheet with side lengths of  $L_x$ ,  $L_y$ , and  $L_z$ . As shown in Fig. 1.9, we assume that only  $L_z$  is a quantum size, which satisfies  $L_z \ll L_x$ ,  $L_y \approx L$ . Such a structure is called a *one-dimensional quantum well*.

The energies of the carriers are written as

$$E = E_{xy} + E_z,$$

$$E_{xy} = \frac{\hbar^2}{2m^*} \frac{\pi^2}{L^2} (n_x^2 + n_y^2), \quad E_z = \frac{\hbar^2}{2m^*} \frac{\pi^2}{L_z^2} n_z^2.$$
(1.56)

Here,  $\hbar$  is Dirac's constant;  $m^*$  is the effective mass of the carrier; and  $n_x$ ,  $n_y$ , and  $n_z$  are quantum numbers. If  $n_x$ ,  $n_y$ , and  $n_z$  are of the same order, we have  $E_{xy} \ll E_z$ .

Figure 1.10 schematically shows the energies of the valence bands in the onedimensional quantum well. In this figure,  $E_{\rm hh1}$  and  $E_{\rm hh2}$  (solid lines) represent the heavy hole bands, and  $E_{\rm lh1}$  and  $E_{\rm lh2}$  (broken lines) express the light hole bands. Here, subscripts 1 and 2 are the quantum numbers  $n_z$ s. As shown in Fig. 1.10, the quantum well structures remove degeneracy of the heavy hole band and the light hole band at a point k=0, because the potential symmetry of the quantum wells is lower than that of the bulk structures.

Let us calculate the *density of states* in the one-dimensional quantum well. As an example, we treat the density of states for  $n_z = 1$ . The density of states is determined by combinations of  $n_x$  and  $n_y$ . When  $n_x$  and  $n_y$  are large enough, the combinations  $(n_x, n_y)$  for a constant energy  $E_{xy}$  are represented by the points on the circumference of a circle with a radius r, which is given by

**Fig. 1.9** One-dimensional quantum well

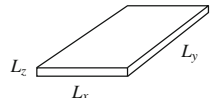
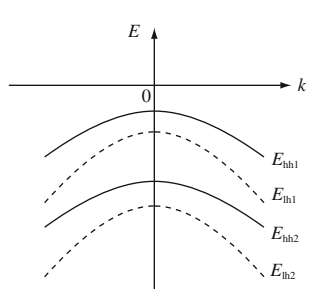


**Fig. 1.10** Valence bands in a one-dimensional quantum well



$$r^{2} = n_{x}^{2} + n_{y}^{2} = \frac{2m^{*}L^{2}}{\pi^{2}\hbar^{2}}E_{xy}.$$
 (1.57)

Because both  $n_x$  and  $n_y$  are positive numbers, the number S of the combinations  $(n_x, n_y)$  is given by the area of the quarter circle with the radius r, as shown in Fig. 1.11.

From Fig. 1.11, S is expressed as

$$S = \frac{1}{4}\pi r^2 = \frac{\pi}{4}(n_x^2 + n_y^2) = \frac{\pi}{4}\frac{2m^*L^2}{\pi^2\hbar^2}E_{xy} = \frac{m^*L^2}{2\pi\hbar^2}E_{xy}.$$
 (1.58)

Considering the up- and down-spins, the number of states N is written as

$$N = 2S = \frac{m^* L^2}{\pi \hbar^2} E_{xy}.$$
 (1.59)

Substituting  $E_{xy} = E - E_{z=1}$  into (1.59), the electron concentration n for the energy between zero and E is obtained as

$$n = \frac{N}{L^2 L_z} = \frac{m^*}{\pi \hbar^2 L_z} (E - E_{z=1}).$$
 (1.60)

When we define the density of states for the energy between E and E + dE as  $\rho_1(E)$ , we have

$$\int \rho_1(E) \, \mathrm{d}E \equiv n. \tag{1.61}$$

**Fig. 1.11** Combinations of  $n_x$  and  $n_y$ 

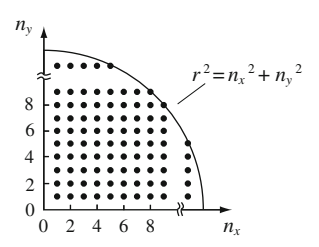
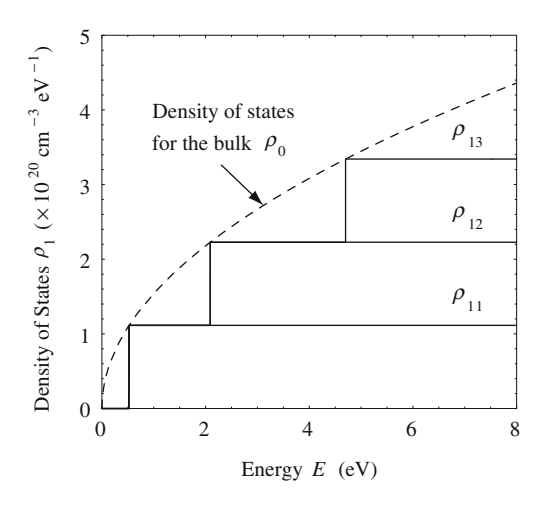


Fig. 1.12 Density of states for the one-dimensional quantum well for  $L_z = 3$  nm and  $m^* = 0.08 m$  (solid line) and that for the bulk structures (broken line)



**Fig. 1.13** Two-dimensional quantum well (quantum wire)



From (1.60) and (1.61), we obtain

$$\rho_1(E) \equiv \frac{\mathrm{d}n}{\mathrm{d}E} = \frac{m^*}{\pi \hbar^2 L_z}.$$
 (1.62)

Similarly, the densities of states for  $n_z = 2, 3, ...$  are calculated, and the results are shown in Fig. 1.12.

In Fig. 1.12,  $L_z$  is 3 nm,  $m^*$  is 0.08 m where m is the electron mass in a vacuum, and  $\rho_1(E)$  for  $n_z = 1$ , 2, 3 are indicated as  $\rho_{11}$ ,  $\rho_{12}$ ,  $\rho_{13}$ , respectively. It should be noted that the density of states for the one-dimensional quantum well is a *step function*. In contrast, the bulk structures have the density of states such as

$$\rho_0(E) = \frac{(2m^*)^{3/2}}{2\pi^2\hbar^3} E^{1/2},\tag{1.63}$$

which is proportional to  $E^{1/2}$  as shown by a broken line, because the number of states is the volume of 1/8 of the sphere with the radius r.

### 1.3.2.2 Two-Dimensional Quantum Well (Quantum Wire)

A stripe with  $L_x \gg L_y$ ,  $L_z$ , shown in Fig. 1.13, is designated the *two-dimensional* quantum well or the quantum wire. Note that  $L_y$  and  $L_z$  are quantum sizes.

For brevity, if we put  $L_y = L_z = L$ , the energies are written as

**Fig. 1.14** Density of states for the two-dimensional quantum well (quantum wire)

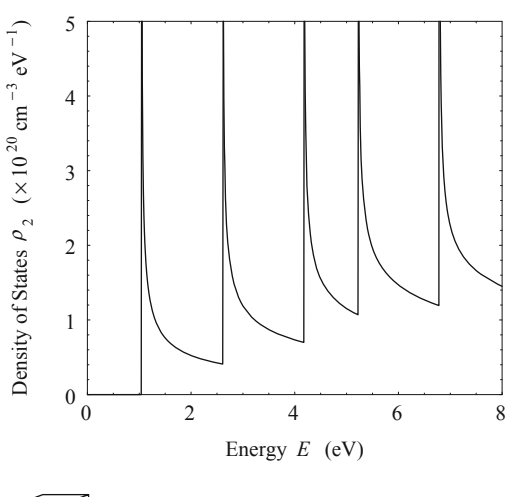




**Fig. 1.15** Three-dimensional quantum well (quantum box)

$$E = E_x + E_{yz},$$

$$E_x = \frac{\hbar^2}{2m^*} \frac{\pi^2}{L_x^2} n_x^2, \quad E_{yz} = \frac{\hbar^2}{2m^*} \frac{\pi^2}{L^2} (n_y^2 + n_z^2).$$
(1.64)

For a pair of quantum numbers  $(n_y, n_z)$ , the density of states  $\rho_2(E)$  is obtained as

$$\rho_2(E) = \frac{\sqrt{2m^*}}{\pi\hbar L^2} E_x^{-1/2} = \frac{\sqrt{2m^*}}{\pi\hbar L^2} (E - E_{yz})^{-1/2}.$$
 (1.65)

Figure 1.14 shows the calculated result of (1.65) with  $L_z = 3$  nm and  $m^* = 0.08 m$ , which are the same as in Fig. 1.12. When the energy E is equal to  $E_{yz}$ , the density of states  $\rho_2(E)$  is infinity. When E exceeds  $E_{yz}$ ,  $\rho_2(E)$  decreases in proportion to  $(E - E_{yz})^{-1/2}$ . As a result, the density of states  $\rho_2(E)$  has a saw-toothed shape.

#### 1.3.2.3 Three-Dimensional Quantum Well (Quantum Box)

As shown in Fig. 1.15, a box whose  $L_x$ ,  $L_y$ , and  $L_z$  are all quantum sizes, is named the *three-dimensional quantum well* or the *quantum box*.

For brevity, if we put  $L_x = L_y = L_z = L$ , the energies are written as

$$E = E_x + E_y + E_z,$$

$$E_x = \frac{\hbar^2}{2m^*} \frac{\pi^2}{L^2} n_x^2, \quad E_y = \frac{\hbar^2}{2m^*} \frac{\pi^2}{L^2} n_y^2, \quad E_z = \frac{\hbar^2}{2m^*} \frac{\pi^2}{L^2} n_z^2.$$
(1.66)

It should be noted that the energies are completely discrete. The density of states  $\rho_3(E)$  is a *delta function*, which is written as

$$\rho_3(E) = 2\sum_{n_x, n_y, n_z} \delta(E - E_x - E_y - E_z). \tag{1.67}$$

Figure 1.16 shows the number of states per volume and the density of states in the three-dimensional quantum well.

The energy distributions of the electrons are given by the product of the densities of states and the Fermi-Dirac distribution functions. With an increase in the dimension of the quantum wells, the energy bandwidths of the densities of states decrease. Therefore, the energy distribution of the electron concentrations narrows with an increase in the dimension of the quantum wells, as shown in Fig. 1.17.

As explained earlier, the energy distribution of the electrons in the quantum structures is narrower than that in the bulk structures. Therefore, the optical gain concentrates on a certain energy (wavelength). As a result, in the quantum well lasers, a low threshold current, a high speed modulation, a low chirping, and a narrow spectral linewidth are expected, which will be described in Chap. 7.

# 1.4 Super Lattices

In the previous section, we studied quantum structures. Here, we consider *super lattices*, which include array quantum structures and solitary ones. From the viewpoints of the potential and the period, super lattices are classified as follows.

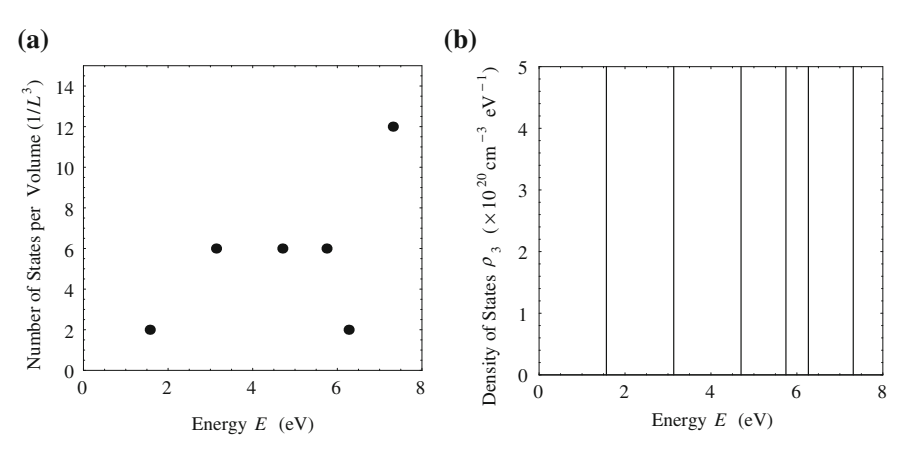


Fig. 1.16 a Number of states per unit volume and b the density of states for the three-dimensional quantum well (quantum box)

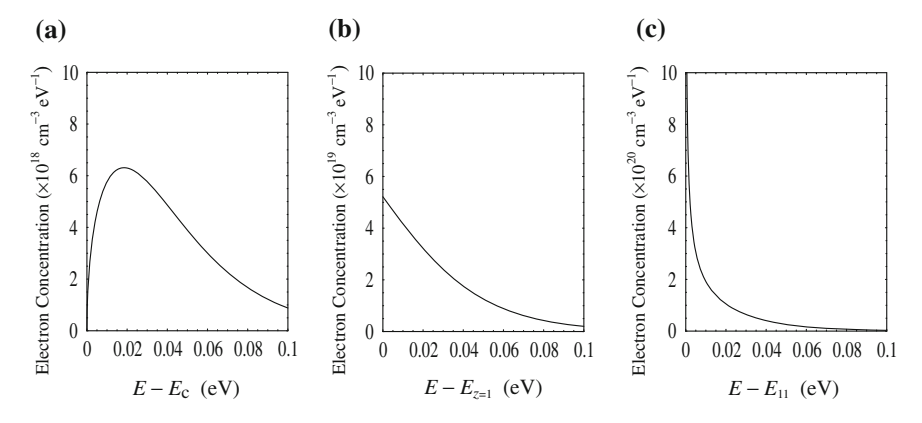
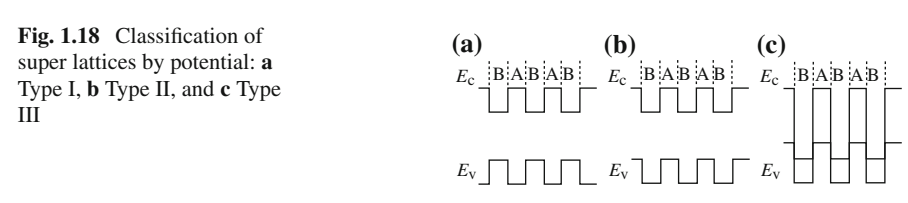


Fig. 1.17 Energy distribution of electron concentrations in quantum wells. a Bulk structure, b 1-D quantum structure, and c 2-D quantum structure

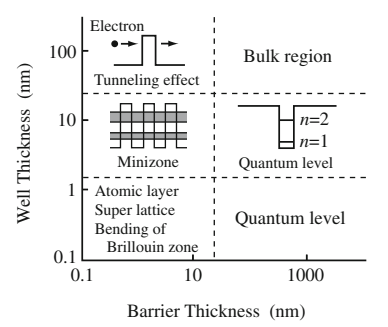


# 1.4.1 Potential

Figure 1.18 shows three kinds of super lattices. In this figure, the horizontal direction indicates the position of the layers, and the vertical direction represents the energy of the electrons. As a result, with an increase in the height of the vertical direction, the energy of electrons increases and that of the holes decreases. As shown in Fig. 1.18a, in *Type I* super lattice, a spatial position of the potential well for the electrons in the conduction band is the same as that for the holes in the valence band. Therefore, both electrons and the holes are confined to semiconductor layer B, which has a narrower bandgap than layer A. In *Type II* super lattice in Fig. 1.18b, the electrons in the conduction band are confined to semiconductor layer B, and the holes in the valence band are confined to semiconductor layer A. In *Type III* super lattice in Fig. 1.18c, the energy of the conduction band of semiconductor layer B overlaps that of the valence band of layer A, which results in the *semimetal*. Note that in some articles, Type II and Type III are called Type I' and Type II, respectively. The names other than Type I may be different, but the important point is that the characteristics of the super lattices are highly dependent on the shapes of the potentials.

1.4 Super Lattices 21

**Fig. 1.19** Classification of super lattices by period



#### 1.4.2 Period

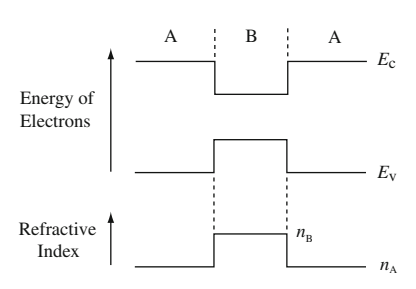
The characteristics of the super lattices also depend on the periods of the constituent layers. Figure 1.19 shows the relationships between the characteristics of the super lattices and the thickness of the barriers and wells. When each layer thickness is larger than several tens of nanometers, only the bulk characteristics are observed. If the barrier thickness is less than several tens of nanometers, the quantum mechanical tunneling effect appears, which leads to tunnel diodes (Esaki diodes) or devices using the resonant tunneling effect. Although the barriers are thick and only the wells are thin, quantum energy levels are formed in the wells. If such wells are used as the active layers in the light emitting devices, narrow light emission spectra are obtained. When both the barriers and the wells are thinner than the order of 10 nm, the wave functions of a well start to penetrate adjacent wells. As a result, the wave functions of each well overlap with each other, which produces the *minizones* and induces the Bloch oscillations or the negative resistances. As the thickness of both the barriers and the wells decreases further down to the order of atomic layers, bending of the Brillouin zones appears, which will transform the indirect transition materials into the direct transition ones.

# 1.4.3 Other Features in Addition to Quantum Effects

In order to fabricate the quantum structures, barriers and wells are required. Because the barriers and wells must have different bandgaps, different kinds of semiconductor materials are needed. Therefore, the quantum structures are inevitably *heterostructures*.

To achieve a low threshold current and a high light emission efficiency in *semiconductor lasers*, both the carriers and the light should be confined to the active layers where the light is generated and amplified. Therefore, the *double heterostructure*, in which the heterostructures are placed at both sides of the active layer, is adopted in semiconductor lasers. Figure 1.20 shows the electron energies and refractive indexes of the double heterostructure. Because the energy barriers exist in the junction boundaries, the carriers are confined to well layer B. In addition, the semiconductors with larger bandgaps generally have smaller refractive indexes. Therefore, light is

**Fig. 1.20** Energies and refractive indexes of the double heterostructure



confined to well layer B. As a result, both the carriers and the light are confined to well layer B, which is used as the active layer.

Finally, we consider a layer epitaxially grown on the semiconductor substrate whose lattice constant is different from that of the grown layer. When the layer thickness exceeds the *critical thickness*, the grown layer is plastically deformed and the *dislocations* are induced in it. If the dislocations are generated, the carriers are dissipated without emitting light. Consequently, characteristics of light emitting devices become extremely low.

Although the layer thickness is thinner than the critical thickness, the grown layers are elastically deformed and the dislocations are not generated in the grown layers. Due to the *elastic strains*, the atomic spacings of the grown layers change, which modifies the band structure of the grown layer. This technology is referred to as *band-structure engineering* and attracts a lot of attention. Because the quantum structures have thin layers, they are suitable for band-structure engineering using elastic strains, and they improve characteristics of semiconductor lasers, which will be explained in Chap. 7.

#### References

- 1. Kane, E.O.: Band structure of indium antimonide. J. Phys. Chem. Solids 1, 249 (1957)
- 2. Kittel, C.: Quantum Theory of Solids, 2nd edn. John Wiley and Sons, New York (1987)
- Bastard, G.: Wave Mechanics Applied to Semiconductor Heterostructures. Halsted Press, New York (1988)
- 4. Datta, S.: Quantum Phenomena. Addison-Wesley, Reading (1989)
- 5. Schiff, L.I.: Quantum Mechanics, 3rd edn. McGraw-Hill, New York (1968)
- 6. Messiah, A.: Quantum Mechanics, vol. 1, vol. 2. North-Holland, Amsterdam (1961)

# **Chapter 2 Optical Transitions**

## 2.1 Introduction

Among energy states, the state with the lowest energy is most stable. Therefore, the electrons in semiconductors tend to stay in low energy states. If they are excited by thermal energy, light, or electron beams, the electrons absorb these energies and transit to high energy states. These *transitions* of the electrons from low energy states to high energy states are called *excitations*. High energy states, however, are unstable. As a result, to take stable states, the electrons in high energy states *transit* to low energy states in certain *lifetimes*. These transitions of the excited electrons from high energy states to low energy states are referred to as *relaxations*. The excitation and relaxation processes between the valence band and the conduction band are shown in Fig. 2.1.

In semiconductors, the transitions of electrons from high energy states to low energy states are designated *recombinations* of the electrons and the holes. In the recombinations of the electrons and the holes, there are *radiative recombinations* and *nonradiative recombinations*. The radiative recombinations emit *photons*, and the energies of the photons correspond to a difference in the energies between the initial and final energy states related to the transitions. In contrast, in the nonradiative recombinations, the *phonons* are emitted to crystal lattices or the electrons are trapped in the defects, and the transition energy is transformed into forms other than light. The *Auger processes* are also categorized as nonradiative recombinations. To obtain high efficiency semiconductor light emitting devices, we have to minimize the nonradiative recombinations. However, to enhance modulation characteristics, the nonradiative recombination centers may be intentionally induced in the active layers, because they reduce the carrier lifetimes (see Sect. 5.1).

Let us consider the transitions of the electrons from the bottom of the conduction band to the top of the valence band. A semiconductor, in which the bottom of the conduction band and the top of the valence band are placed at a common wave vector k, is the *direct transition* semiconductor. A semiconductor, in which the bottom of the conduction band and the top of the valence band have different k-values,

24 2 Optical Transitions

Fig. 2.1 Excitation and relaxation

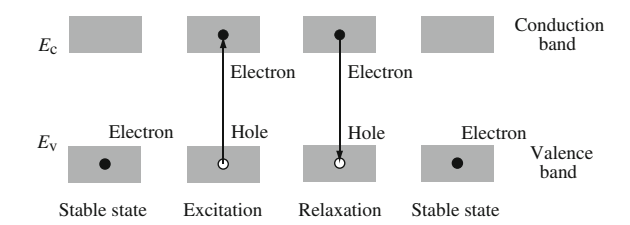
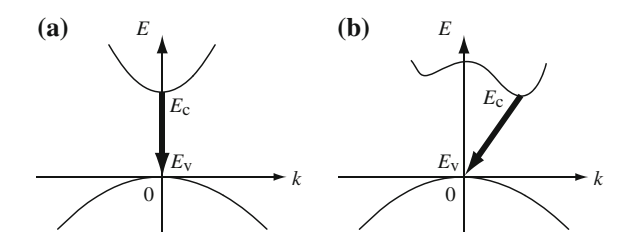


Fig. 2.2 a Direct and b indirect transition semiconductors



is the *indirect transition* semiconductor. These direct and indirect transitions are schematically shown in Fig. 2.2. In transitions of the electrons, the energy and the momentum are conserved, respectively. Therefore, the phonons do not take part in direct transitions. Because the wave vector k of the phonons is much larger than that of the photons, the phonon transitions accompany the indirect transitions to satisfy the momentum conservation law. Hence, in the direct transitions, the transition probabilities are determined by only the electron transition probabilities. In contrast, in the indirect transitions, the transition probabilities are given by a product of the electron transition probabilities and the phonon transition probabilities. As a result, the transition probabilities of the direct transitions are much higher than those of the indirect transitions. Consequently, the direct transition semiconductors are superior to the indirect ones for light emitting devices.

# 2.2 Light Emitting Processes

Light emission due to the radiative recombinations is called the *luminescence*. According to the lifetime, the excitation methods, and the energy states related to the transitions, light emitting processes are classified as follows.

## 2.2.1 Lifetime

With regard to the lifetime, there are two light emissions: *fluorescence*, with a short lifetime of  $10^{-9}$ – $10^{-3}$  s, and *phosphorescence*, with a long lifetime of  $10^{-3}$  s to one day.

## 2.2.2 Excitation

Luminescence due to optical excitation (pumping) is *photoluminescence*, which is widely used to characterize materials. Optical excitation is also used to pump dye lasers (for example, Rhodamine 6G and Coumalin) and solid-state lasers (e.g., YAG and ruby). When the photon energy of the pumping light is  $\hbar\omega_1$  and that of the luminescence is  $\hbar\omega_2$ , the luminescence with  $\hbar\omega_2 < \hbar\omega_1$  is called *Stokes lumines*cence and that with  $\hbar\omega_2 > \hbar\omega_1$  is designated anti-Stokes luminescence. Luminescence caused by electrical excitation is *electroluminescence*, which has been used for panel displays. In particular, luminescence by current injection is called *injection*type electroluminescence; it has been used for light emitting diodes (LEDs) and semiconductor lasers or laser diodes (LDs). In such injection-type optical devices, the carriers are injected into the active layers by forward bias across the pn junctions. Note that the current (carrier) injection is also considered the excitation, because it generates a lot of high energy electrons. The luminescence due to electron beam irradiation is *cathodoluminescence*, which has been adopted to characterize materials. The luminescence induced by mechanical excitation using stress is triboluminescence, and that by thermal excitation is thermoluminescence. Luminescence during a chemical reaction is referred to chemiluminescence; it has not been reported in semiconductors.

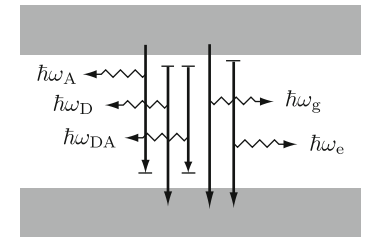
## 2.2.3 Transition States

Figure 2.3 shows light emission processes between various energy states. They are classified into impurity recombinations, interband recombinations, and exciton recombinations.

In *impurity recombinations*, there is recombination between the electron in the conduction band and the empty acceptor level with the photon energy of  $\hbar\omega_A$ , recombination between the electron in the donor level and the hole in the valence band with the photon energy of  $\hbar\omega_D$ , and recombination between the electron in the donor level and the empty acceptor level with the photon energy of  $\hbar\omega_{DA}$ . By observing light emissions due to these recombinations at extremely low temperatures, information on doping characteristics is obtained.

26 2 Optical Transitions

Fig. 2.3 Light emission processes



In *interband recombinations* between the conduction and valence bands, light emission in the vicinity of the band edges with the photon energy of  $\hbar\omega_{\rm g}$  is dominant. This *band edge emission* is used in most LEDs and LDs composed of III–V group semiconductors.

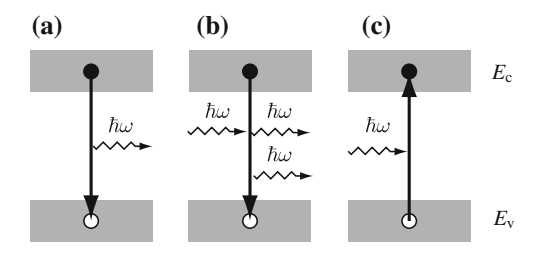
The *exciton recombination*, with the photon energy of  $\hbar\omega_e$ , is the recombination of the electron generated by decay of an exciton and the hole in the valence band.

## 2.3 Spontaneous Emission, Stimulated Emission, and Absorption

Figure 2.4 schematically shows radiations and absorption. In the radiations, there are spontaneous emission and stimulated emission (or induced emission). As shown in Fig. 2.4a, spontaneous emission is a radiative process in which an excited electron decays in a certain lifetime and a photon is emitted. Note that spontaneous emission takes place irrespective of incident lights. In contrast, in the stimulated emission illustrated in Fig. 2.4b, an incident light induces a radiative transition of an excited electron. The emitted light due to the stimulated emission has the same wavelength, phase, and direction as the incident light. Therefore, the light generated by the stimulated emission is highly monochromatic, coherent, and directional. In the stimulated emission, one incident photon generates two photons; one is the incident photon itself, and the other is an emitted photon due to the stimulated emission. As a result, the incident light is amplified by the stimulated emission. The absorption depicted in Fig. 2.4c is a process that the electron transits from a lower energy state to a higher one by absorbing energy from the incident light. Because this transition is induced by the incident light, it is sometimes called *induced absorption*. It should be noted that spontaneous absorption does not exist; this will be explained in Chap. 8.

When a light is incident on a material, the stimulated emission and the absorption simultaneously take place. In *thermal equilibrium*, there are more electrons in a lower energy state than in a higher one, because the lower energy state is more stable than the higher one. Therefore, in thermal equilibrium, only the absorption is observed when a light is incident on a material. In order to obtain a net optical gain, we have to make the number of electrons in a higher energy state larger than in the lower one. This condition is referred to as *inverted population*, or, *population inversion* because the electron population is inverted compared with that in thermal equilibrium. In

**Fig. 2.4** Radiation and absorption: **a** spontaneous emission, **b** stimulated emission, and **c** absorption



semiconductors, the population inversion is obtained only in the vicinity of the band edges by excitation of the electrons through optical pumping or electric current injection. The population inversion generates many electrons at the bottom of the conduction band and many holes at the top of the valence bands.

The laser oscillators use fractions of the spontaneous emission as the optical input and amplify the fractions by the stimulated emission under population inversion. Once the optical gains exceed the optical losses in the laser oscillators, *laser oscillations* take place. The term *laser* is an acronym for "light amplification by stimulated emission of radiation" and is used as a noun in a *laser oscillator*. Note that an emitted light from a laser oscillator is not a laser but a *laser light* or a *laser beam*. As a back formation from laser, "lase" is used as a verb meaning "to emit coherent light."

Among semiconductor light emitting devices, LEDs use spontaneous emission and are applied to remote-control transmitters, switch lights, brake lights, displays, and traffic signals. In contrast, LDs are oscillators of lights using stimulated emission and are used as light sources for lightwave communications, compact discs (CDs), magneto-optical discs (MOs), digital video discs (DVDs), laser beam printers, laser pointers, bar-code readers, and so on.

# 2.4 Optical Gains

## **2.4.1** *Lasers*

Let us consider the relationships between *laser oscillators* and *optical gains*. First, we review a general oscillator, as shown in Fig. 2.5. An oscillator has a *gain* and amplifies an input. Also, the oscillator returns a fraction of an output to an input port through a *feedback* loop. The returned one is repetitively amplified, and oscillation starts when a net gain exceeds an internal loss of the oscillator.

Figure 2.6 shows a laser oscillator where a fraction of the spontaneous emission is used as the input and the *optical gain* is produced by the stimulated emission. To feed back light, *optical resonators* or *optical cavities*, which are composed of *reflectors* or *mirrors*, are adopted. Due to this configuration, characteristics of lasers (for brevity,

28 2 Optical Transitions

Fig. 2.5 Oscillator

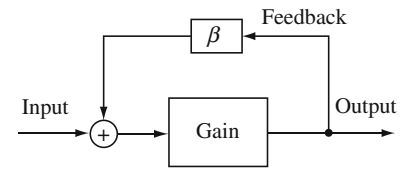
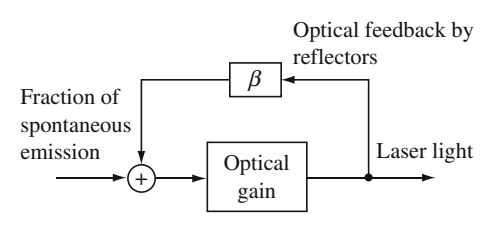


Fig. 2.6 Laser oscillator



*lasers* are used for laser oscillators here) are affected by the optical gains and optical resonators. Many lasers use optical resonators, but nitrogen lasers, whose optical gains are very large, can start laser oscillations even without optical resonators. It should be noted that all semiconductor lasers use optical resonators.

As explained earlier, a fraction of the spontaneous emission is used as the input of a laser. Note that all the spontaneously emitted lights cannot be used as the input, because they have different wavelengths, phases, and propagation directions. Among these lights, only the lights, which have wavelengths within the optical gain spectrum and satisfy the resonance conditions of the optical resonators, can be the sources of laser oscillations. Other spontaneous emissions, which do not satisfy the resonance conditions of optical resonators, are readily emitted outward without obtaining sufficient optical gains for laser oscillations. The lights amplified by the stimulated emission have the same wavelength, phase, and propagation direction as those of the input lights. Therefore, the laser lights are highly monochromatic, bright, coherent, and directional.

# 2.4.2 Optical Gains

#### 2.4.2.1 Carrier Distribution

We derive equations for the optical gains of semiconductor lasers. We suppose that many electrons are excited to the conduction band by optical pumping or electrical current injection. In this condition, the *carrier distribution* is in *nonthermal equilibrium*, and there are many electrons in the conduction band and many holes in the valence band. As a result, one *Fermi level E*<sub>F</sub> cannot describe the distribution functions of the electrons and holes. In this case, it is useful to determine the distribution functions by assuming that the electrons in the conduction band and the holes in the

2.4 Optical Gains 29

valence band are separately governed by Fermi–Dirac distribution. For this purpose, we introduce quasi-Fermi levels  $E_{Fc}$  and  $E_{Fv}$  defined as

$$n = N_{c} \exp\left(-\frac{E_{c} - E_{Fc}}{k_{B}T}\right),$$

$$p = N_{v} \exp\left(-\frac{E_{Fv} - E_{v}}{k_{B}T}\right),$$

$$N_{c} = 2\left(\frac{2\pi m_{e} * k_{B}T}{h^{2}}\right)^{3/2},$$

$$N_{v} = 2\left(\frac{2\pi m_{h} * k_{B}T}{h^{2}}\right)^{3/2}.$$
(2.1)

Here, n and p are the electron concentration and the hole concentration, respectively;  $E_{\rm c}$  and  $E_{\rm v}$  are the energy of the bottom of the conduction band and that of the top of the valence band, respectively;  $k_{\rm B}=1.3807\times 10^{-23}\,{\rm J/K}$  is Boltzmann constant; T is an absolute temperature;  $N_{\rm c}$  and  $N_{\rm v}$  are the effective density of states for the electrons and that for the holes, respectively;  $m_{\rm e}^*$  and  $m_{\rm h}^*$  are the effective mass of the electrons and that of the holes, respectively; and h is Planck's constant.

From (2.1), these quasi-Fermi levels  $E_{Fc}$  and  $E_{Fv}$  are written as

$$E_{Fc} = E_{c} + k_{B}T \ln \left(\frac{n}{N_{c}}\right),$$

$$E_{Fv} = E_{v} - k_{B}T \ln \left(\frac{p}{N_{v}}\right).$$
(2.2)

We express a distribution function for the electrons in the valence band with the energy  $E_1$  as  $f_1$  and that for the electrons in the conduction band with the energy  $E_2$  as  $f_2$ . Using  $E_{Fc}$  and  $E_{Fv}$ , we can express  $f_1$  and  $f_2$  as

$$f_{1} = \frac{1}{\exp\left[\left(E_{1} - E_{Fv}\right) / \left(k_{B}T\right)\right] + 1},$$

$$f_{2} = \frac{1}{\exp\left[\left(E_{2} - E_{Fc}\right) / \left(k_{B}T\right)\right] + 1}.$$
(2.3)

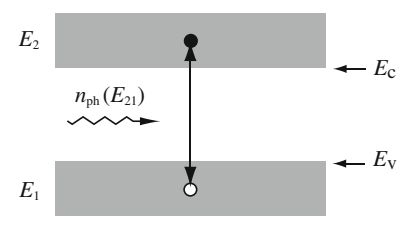
It should be noted that the distribution function for the holes in the valence band is given by  $[1 - f_1]$ .

## 2.4.2.2 Optical Transition Rates

As shown in Fig. 2.7, we assume that a light, which has a photon energy of  $E_{21}=E_2-E_1$  and a photon density of  $n_{\rm ph}(E_{21})$ , interacts with a direct-transition

30 2 Optical Transitions

**Fig. 2.7** Schematic model for radiation and absorption



semiconductor. Under this assumption, we calculate the *transition rates* for the stimulated emission, the absorption, and the spontaneous emission. In Fig. 2.7,  $E_c$  is the energy for the bottom of the conduction band, and  $E_v$  is the energy for the top of the valence band. Note that this figure shows the energy bands for a certain value of k, and the horizontal line has no physical meaning.

#### (i) Stimulated Emission Rate

The stimulated emission rate per unit volume  $r_{21}(stim)$  is given by a product of

the transition probability per unit time from  $E_2$  to  $E_1$ :  $B_{21}$ , the electron concentration in a state with the energy  $E_2$ :  $n_2$ , the hole concentration in a state with the energy  $E_1$ :  $p_1$ , the photon density:  $n_{\rm ph}(E_{21})$ .

The concentration  $n_2$  of the electron, which occupies a state with the energy  $E_2$  in the conduction band, is expressed as

$$n_2 = \rho_{\rm c}(E_2 - E_{\rm c}) f_2, \tag{2.4}$$

where  $\rho_c(E_2 - E_c)$  is the density of states, which is a function of  $E_2 - E_c$ , and  $f_2$  is the distribution function in (2.3).

The concentration  $p_1$  of the hole, which occupies a state with the energy  $E_1$  in the valence band, is written as

$$p_1 = \rho_{\rm v}(E_{\rm v} - E_1)[1 - f_1], \tag{2.5}$$

where  $\rho_v(E_v - E_1)$  is the density of states, which is a function of  $E_v - E_1$ , and  $f_1$  is the distribution function in (2.3).

Therefore, the stimulated emission rate  $r_{21}$  (stim) is obtained as

$$r_{21}(\text{stim}) = B_{21}n_2p_1n_{\text{ph}}(E_{21})$$
  
=  $B_{21}n_{\text{ph}}(E_{21})\rho_{\text{c}}(E_2 - E_{\text{c}})\rho_{\text{v}}(E_{\text{v}} - E_1)f_2[1 - f_1].$  (2.6)

2.4 Optical Gains 31

## (ii) Absorption Rate

The absorption rate per unit volume  $r_{12}$  (abs) is given by a product of

the transition probability per unit time from  $E_1$  to  $E_2$ :  $B_{12}$ , the concentration of an empty state with the energy  $E_2$ :  $p_2$ , the electron concentration in a state with the energy  $E_1$ :  $n_1$ , the photon density:  $n_{\rm ph}(E_{21})$ .

The concentration  $p_2$  of an empty state, which is not occupied by the electrons with the energy  $E_2$  in the conduction band, is expressed as

$$p_2 = \rho_{\rm c}(E_2 - E_{\rm c})[1 - f_2]. \tag{2.7}$$

The concentration  $n_1$  of the electron, which occupies a state with the energy  $E_1$  in the valence band, is written as

$$n_1 = \rho_{\rm v}(E_{\rm v} - E_1) f_1. \tag{2.8}$$

As a result, the absorption rate  $r_{12}$  (abs) is obtained as

$$r_{12}(abs) = B_{12}p_2n_1n_{ph}(E_{21})$$
  
=  $B_{12}n_{ph}(E_{21})\rho_c(E_2 - E_c)\rho_v(E_v - E_1)f_1[1 - f_2].$  (2.9)

## (iii) Spontaneous Emission Rate

The spontaneous emission rate per unit volume  $r_{21}$  (spon) is independent of the incident photon density and given by a product of

the transition probability per unit time from  $E_2$  to  $E_1$ :  $A_{21}$ , the electron concentration in a state with the energy  $E_2$ :  $n_2$ , the hole concentration in a state with the energy  $E_1$ :  $p_1$ .

Using (2.4) and (2.5), the spontaneous emission rate  $r_{21}$  (spon) is obtained as

$$r_{21}(\text{spon}) = A_{21}n_2p_1$$
  
=  $A_{21}\rho_c(E_2 - E_c)\rho_v(E_v - E_1)f_2[1 - f_1].$  (2.10)

## 2.4.2.3 Optical Transition in Thermal Equilibrium

In thermal equilibrium, the carrier distributions are described by one Fermi level  $E_{\rm F}$ , and the radiations balance the absorption. In other words, a sum of the stimulated

emission rate and the spontaneous emission rate is equal to the absorption rate. Using the optical transition rates for the stimulated emission, the spontaneous emission, and the absorption, we obtain

$$r_{21}(\text{stim}) + r_{21}(\text{spon}) = r_{12}(\text{abs}),$$
  
 $E_{\text{Fc}} = E_{\text{Fv}} = E_{\text{F}}.$  (2.11)

Substituting (2.6), (2.9), and (2.10) into (2.11), we have

$$n_{\rm ph}(E_{21}) = \frac{A_{21}}{B_{12} \exp[E_{21}/(k_{\rm B}T)] - B_{21}},$$
 (2.12)

while the blackbody radiation theory gives

$$n_{\rm ph}(E_{21}) = \frac{8 \pi n_{\rm r}^3 E_{21}^2}{h^3 c^3 \exp[E_{21}/(k_{\rm B}T)] - h^3 c^3}.$$
 (2.13)

Here,  $n_{\rm r}$  is the effective refractive index of a material, h is Planck's constant, and  $c = 2.99792458 \times 10^8 \,\mathrm{m/s}$  is the speed of light in a vacuum.

Comparison of (2.12) and (2.13) results in

$$A_{21} = Z(E_{21})B, \quad B_{21} = B_{12} = B,$$
  
 $Z(E_{21}) = \frac{8 \pi n_r^3 E_{21}^2}{h^3 c^3},$  (2.14)

which is known as *Einstein's relation*, and  $A_{21}$  is called *Einstein's A coefficient*; and B is called *Einstein's B coefficient*. It should be noted that  $B_{21} = B_{12} = B$ , and  $A_{21}$  is proportional to B.

We consider the physical meaning of  $Z(E_{21})$  in (2.14) in the following. We suppose that a light field  $E_{\rm L}$  is written as

$$E_{\rm L} = A_0 \exp[i(\omega t - \mathbf{k} \cdot \mathbf{r})], \tag{2.15}$$

where  $A_0$  is a complex amplitude,  $\omega$  is an angular frequency, t is a time, k is a wave vector, and r is a position vector. We also suppose that the periodic boundary condition is satisfied on the surfaces of a cube with a side length L. Because the electric fields at x = 0 and x = L are the same, an eigenmode is given by

$$\exp(0) = \exp(i k_x L) = 1, \quad \therefore \quad k_x = \frac{2 \pi}{L} n_x,$$
 (2.16)

where  $k_x$  is an x-component of the wave vector  $\mathbf{k}$  and  $n_x$  is an integer. Similarly, we obtain

$$k_y = \frac{2\pi}{L} n_y, \quad k_z = \frac{2\pi}{L} n_z,$$
 (2.17)

2.4 Optical Gains 33

where  $n_y$  and  $n_z$  are integers. Hence,  $k^2 = k_x^2 + k_y^2 + k_z^2$  is expressed as

$$k^{2} = \left(\frac{2\pi}{L}\right)^{2} (n_{x}^{2} + n_{y}^{2} + n_{z}^{2}). \tag{2.18}$$

Using the effective refractive index  $n_r$  of the material, the angular frequency  $\omega$  is given by

$$\omega = \frac{kc}{n_{\rm r}}.\tag{2.19}$$

Therefore, the energy  $E = \hbar \omega$  is written as

$$E = \hbar\omega = \frac{2\pi\hbar c}{n_{\rm r}L}(n_{\rm x}^2 + n_{\rm y}^2 + n_{\rm z}^2)^{1/2} = \frac{hc}{n_{\rm r}L}(n_{\rm x}^2 + n_{\rm y}^2 + n_{\rm z}^2)^{1/2}, \quad (2.20)$$

which takes discrete values, because  $n_x$ ,  $n_y$ , and  $n_z$  are integers. However, when L is much larger than the wavelength of the light,  $n_x^2 + n_y^2 + n_z^2$  becomes a huge number, and many modes exist near each other. When we consider a sphere with a radius of  $R = (n_x^2 + n_y^2 + n_z^2)^{1/2}$ , the number of combinations  $(n_x, n_y, n_z)$  is equal to a volume of the sphere  $4 \pi R^3/3$ . For each combination  $(n_x, n_y, n_z)$ , there exist two modes corresponding to their polarizations, which are perpendicular to each other. As a result, the number of modes whose energy is placed between 0 and E is given by

$$2 \times \frac{4\pi}{3} \left( \frac{n_{\rm r} E L}{hc} \right)^3 = \frac{8\pi n_{\rm r}^3 E^3}{3h^3 c^3} L^3.$$
 (2.21)

The number of modes with their energies between E and E + dE is obtained as a derivative of (2.21) with respect to E, which is expressed as

$$\frac{8\pi n_{\rm r}^3 E^2}{h^3 c^3} L^3 dE. (2.22)$$

Because a volume of the cube is  $L^3$ , dividing (2.22) by  $L^3$  gives the number of modes per unit volume, that is, the *mode density* m(E) dE as

$$m(E) dE = \frac{8 \pi n_{\rm r}^3 E^2}{h^3 c^3} dE.$$
 (2.23)

From (2.23) and the third equation in (2.14), it is found that we have  $m(E_{21}) = Z(E_{21})$ . This relation suggests that the spontaneous emission takes place for all the modes with their energy placed between E and E + dE while the stimulated emission and absorption occur only for the mode corresponding to the incident light.

Note that the derivation of A and B assumes that both  $r_{21}(\text{stim})$  and  $r_{12}(\text{abs})$  are proportional to the photon density  $n_{\text{ph}}(E_{21})$ . If we assume that both  $r_{21}(\text{stim})$  and  $r_{12}(\text{abs})$  are proportional to the energy density of the photons as Einstein did [1], other formulas for A and B will be obtained.

## 2.4.2.4 Definitions of the Mode Density

In the preceding discussion, we explained the mode density m(E) dE with the energies placed between E and E+dE. Here, we will derive mode densities  $m(\omega)$  d $\omega$  with the angular frequencies of a light between  $\omega$  and  $\omega+d\omega$ , and  $m(\nu)$  d $\nu$  with the light frequencies between  $\nu$  and  $\nu+d\nu$ . Using the (effective) refractive index of the material  $n_{\Gamma}$  and the speed of light in a vacuum c, we have

$$k = \frac{n_{\rm r}\omega}{c} = \frac{2\,\pi\,n_{\rm r}\nu}{c}.\tag{2.24}$$

Substituting (2.24) into (2.18) and then calculating a volume  $4 \pi R^3/3$  of a sphere with the radius  $R = (n_x^2 + n_y^2 + n_z^2)^{1/2}$  results in

$$2 \times \frac{4\pi}{3} R^3 = \frac{n_r^3 \omega^3}{3\pi^2 c^3} L^3 = \frac{8\pi n_r^3 \nu^3}{3c^3} L^3, \tag{2.25}$$

where a factor 2 corresponds to the directions of the polarizations. As a result, dividing (2.25) by  $L^3$  and then differentiating with respect to  $\omega$  or  $\nu$  leads to

$$m(\omega) d\omega = \frac{n_{\rm r}^3 \omega^2}{\pi^2 c^3} d\omega, \quad m(\nu) d\nu = \frac{8 \pi n_{\rm r}^3 \nu^2}{c^3} d\nu.$$
 (2.26)

## 2.4.2.5 Net Stimulated Emission

Let us consider the excited conditions where many free carriers exist. In these non-thermal equilibrium conditions, radiations do not balance with absorption anymore. When a light is incident on a material, the stimulated emission and the absorption simultaneously take place. Therefore, the net stimulated emission rate  $r^0$ (stim) is given by

$$r^{0}(\text{stim}) = r_{21}(\text{stim}) - r_{12}(\text{abs})$$

$$= Bn_{\text{ph}}(E_{21})\rho_{\text{c}}(E_{2} - E_{\text{c}})\rho_{\text{v}}(E_{\text{v}} - E_{1})[f_{2} - f_{1}]$$

$$= \frac{A_{21}}{Z(E_{21})}n_{\text{ph}}(E_{21})\rho_{\text{c}}(E_{2} - E_{\text{c}})\rho_{\text{v}}(E_{\text{v}} - E_{1})[f_{2} - f_{1}]. \tag{2.27}$$

From (2.27), to obtain the *net stimulated emission*  $r^0(\text{stim}) > 0$ , we need

$$f_2 > f_1,$$
 (2.28)

which indicates the population inversion in the semiconductors. With the help of (2.3), (2.28) reduces to

2.4 Optical Gains 35

$$E_{\rm Fc} - E_{\rm Fy} > E_2 - E_1 = E_{21},$$
 (2.29)

which is known as the *Bernard–Duraffourg relation*. In semiconductor lasers, a typical carrier concentration for  $r^0(\text{stim}) > 0$  is of the order of  $10^{18} \, \text{cm}^{-3}$ .

## 2.4.2.6 Net Stimulated Emission Rate and Optical Gains

The optical power gain coefficient per unit length g is defined as

$$\frac{\mathrm{d}I}{\mathrm{d}z} = gI,\tag{2.30}$$

where I is the light intensity per unit area and z is a coordinate for a propagation direction of the light. Because the light intensity is proportional to the square of the electric field, the amplitude gain coefficient  $g_E$ , which is the gain coefficient for the electric field, is given by  $g_E = g/2$ . From the definition, I is expressed as

$$I = v E_{21} n_{\text{ph}}(E_{21}) = v \hbar \omega n_{\text{ph}}(E_{21}),$$

$$v = \frac{d\omega}{dk} = \frac{c}{n_{\text{r}}},$$

$$\frac{dI}{dt} = v E_{21} \frac{dn_{\text{ph}}(E_{21})}{dt} = v E_{21} r^{0}(\text{stim}),$$
(2.31)

where v is a group velocity of the light in the material,  $E_{21} = \hbar \omega$  is the photon energy, and  $n_{\rm ph}(E_{21})$  is the photon density.

Here we consider a relationship between the derivatives of I with respect to a position and a time. Because the position z is a function of the time t, we have

$$\frac{\mathrm{d}I}{\mathrm{d}z} = \frac{\mathrm{d}t}{\mathrm{d}z} \frac{\mathrm{d}I}{\mathrm{d}t} = \left(\frac{\mathrm{d}z}{\mathrm{d}t}\right)^{-1} \frac{\mathrm{d}I}{\mathrm{d}t} = \frac{1}{v} \frac{\mathrm{d}I}{\mathrm{d}t},$$

$$\frac{\mathrm{d}I}{\mathrm{d}z} = gI = gv E_{21} n_{\mathrm{ph}}(E_{21}).$$
(2.32)

From (2.31) and (2.32), we have the relation

$$r^0(\text{stim}) = v g n_{\text{ph}}(E_{21}).$$
 (2.33)

As a result, it is found that a large  $r^0$ (stim) leads to a large g. Using (2.27), (2.31), and (2.33), we can also express g as

$$g = \frac{r^0(\text{stim})}{n_{\text{ph}}(E_{21})} \frac{n_{\text{r}}}{c} = \frac{n_{\text{r}}}{c} B \rho_{\text{c}}(E_2 - E_{\text{c}}) \rho_{\text{v}}(E_{\text{v}} - E_1) [f_2 - f_1]. \tag{2.34}$$

From the *time-dependent quantum mechanical perturbation theory* (see Appendix C), Einstein's *B* coefficient in (2.14), which is the transition rate due to the stimulated emission for a photon in a free space, is given by

$$B = \frac{e^2 h}{2m^2 \varepsilon_0 n_{\rm r}^2 E_{21}} |\langle 1 | \mathbf{p} | 2 \rangle|^2.$$
 (2.35)

Here, e is the elementary charge; h is Planck's constant; m is the electron mass;  $\varepsilon_0$  is permittivity in a vacuum;  $n_r$  is the refractive index of the material;  $E_{21}$  is the photon energy; p is the momentum operator; and  $|1\rangle$  and  $|2\rangle$  are the wave functions of the valence band and the conduction band in a steady state, respectively.

Substituting (2.35) into (2.14), we can write Einstein's A coefficient as

$$A_{21} = \frac{4\pi e^2 n_{\rm r} E_{21}}{m^2 \varepsilon_0 h^2 c^3} |\langle 1|\mathbf{p}|2\rangle|^2.$$
 (2.36)

Using the *dipole moment*  $\mu$ , (2.35) and (2.36) can be rewritten as follows: The momentum operator p is expressed as

$$p = m \frac{\mathrm{d}r}{\mathrm{d}t}.\tag{2.37}$$

As a result, we obtain

$$\frac{1}{m} \langle 1 | \boldsymbol{p} | 2 \rangle = \frac{\mathrm{d}}{\mathrm{d}t} \langle 1 | \boldsymbol{r} | 2 \rangle = \mathrm{i} \,\omega \langle 1 | \boldsymbol{r} | 2 \rangle, \tag{2.38}$$

where  $r \propto e^{i\omega t}$  was assumed. With the help of (2.38), Einstein's A and B coefficients are written as

$$B = \frac{\pi e^2 \omega}{\varepsilon_0 n_{\rm r}^2} |\langle 1|\mathbf{r}|2\rangle|^2 = \frac{\pi \omega}{\varepsilon_0 n_{\rm r}^2} |\mu|^2,$$

$$A_{21} = \frac{2n_r \omega^3}{\varepsilon_0 h c^3} |\mu|^2,$$

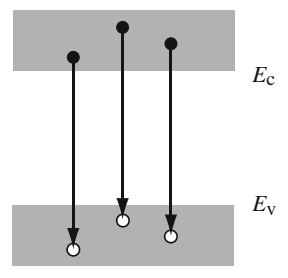
$$|\mu|^2 = |\langle 1|e\mathbf{r}|2\rangle|^2.$$
(2.39)

Note that many textbooks on quantum electronics use (2.39) as Einstein's A coefficient. Expressions on Einstein's B coefficient depend on the definitions of the stimulated emission rate whether it is proportional to the photon density or to the energy density. In the preceding explanations, Einstein's B coefficient is defined to be in proportion to the photon density. Therefore, the quantum mechanical transition rate for the stimulated emission is equal to Einstein's B coefficient.

In semiconductors, due to the energy band structures, transitions take place between various energy states, as shown in Fig.2.8. If we put  $E_{21} = E$  and  $E_2 - E_c = E''$ , the electron energy in the valence band E' for the allowed transition

2.4 Optical Gains 37

**Fig. 2.8** Transition with a constant photon energy



is given by E' = E'' - E. Therefore, by integrating (2.27) with respect to E'', the net stimulated emission rate  $r^0$  (stim) in the semiconductors is obtained as

$$r^{0}(\text{stim}) = \frac{e^{2}h \, n_{\text{ph}}(E)}{2m^{2} \varepsilon_{0} n_{\text{r}}^{2} E} \, \int_{0}^{\infty} |\langle 1 | \boldsymbol{p} | 2 \rangle|^{2} \rho_{\text{c}}(E'') \rho_{\text{v}}(E') [f_{2}(E'') - f_{1}(E')] \, dE'',$$
(2.40)

where (2.35) was used. Similarly, the optical power gain coefficient g(E) is given by

$$g(E) = \frac{e^2 h}{2m^2 \varepsilon_0 n_{\rm r} cE} \int_0^\infty |\langle 1| \mathbf{p} | 2 \rangle|^2 \rho_{\rm c}(E'') \rho_{\rm v}(E') [f_2(E'') - f_1(E')] dE''. \tag{2.41}$$

From (2.10) and (2.36), the spontaneous emission rate  $r_{21}$  (spon) is expressed as

$$r_{21}(\text{spon}) = \frac{4\pi e^2 n_{\rm r} E}{m^2 \varepsilon_0 h^2 c^3} \int_0^\infty |\langle 1| \boldsymbol{p} | 2\rangle|^2 \rho_{\rm c}(E'') \rho_{\rm v}(E') f_2(E'') [1 - f_1(E')] \, \mathrm{d}E''.$$
(2.42)

When the excitation is weak, the absorption is observed, and the net absorption rate  $r^0$  (abs) is written as

$$r^{0}(abs) = r_{12}(abs) - r_{21}(stim) = -r^{0}(stim).$$
 (2.43)

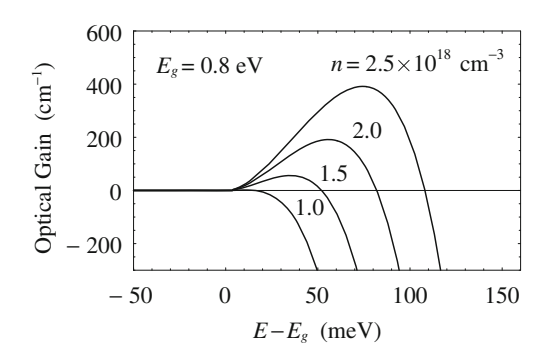
Therefore, the optical power absorption coefficient  $\alpha(E)$  and the optical power gain coefficient g(E) are related as

$$\alpha(E) = -g(E). \tag{2.44}$$

Figure 2.9 shows the calculated optical power gain coefficient g(E) in (2.41) as a function of  $E-E_{\rm g}$  for the bulk structures with the bandgap energy of  $E_{\rm g}=0.8\,{\rm eV}$ . With an increase in the carrier concentration n, the gain peak shifts toward a higher energy (shorter wavelength). This shift of the gain peak is caused by the *band filling effect* [2], in which the electrons in the conduction band and the holes in the valence band occupy each band from the band edges. Because higher energy states are more dense than lower energy states, the optical gain in higher energy states is larger than that in lower energy ones.

38 2 Optical Transitions

Fig. 2.9 Optical power gain coefficient



Here, let us consider the optical power gain coefficient g(E) from other viewpoints. In (2.41),  $\rho_c(E'')\rho_v(E')$  is considered to be the density of state pairs related to the optical transitions. The density of state pairs is also expressed using the law of momentum conservation (k-selection rule) and the law of energy conservation ( $E_{21} = E_2 - E_1$ ). Under the k-selection rule, optical transitions take place only for  $k = k_1 = k_2$ . Therefore, we can define the density of state pairs or the reduced density of states  $\rho_{red}(E_{21})$  as

$$\rho_{\text{red}}(E_{21}) dE_{21} \equiv \rho_{\text{v}}(E_1) dE_1 = \rho_{\text{c}}(E_2) dE_2,$$
 (2.45)

where

$$dE_{21} = dE_1 + dE_2. (2.46)$$

From (2.45) and (2.46), we have

$$\rho_{\text{red}}(E_{21}) = \left[\frac{1}{\rho_{\text{v}}(E_1)} + \frac{1}{\rho_{\text{c}}(E_2)}\right]^{-1}.$$
 (2.47)

If the conduction and valence bands are parabolic, the energies  $E_1$  and  $E_2$  are written as

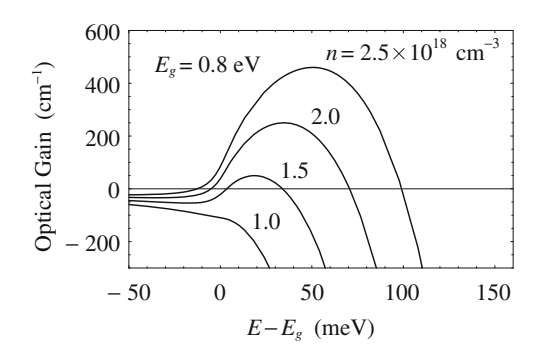
$$E_1 = E_{\rm v} - \frac{\hbar^2 k^2}{2m_{\rm h}^*},\tag{2.48}$$

$$E_2 = E_c + \frac{\hbar^2 k^2}{2m_e^*},\tag{2.49}$$

where  $m_h^*$  and  $m_e^*$  are the effective masses of the holes and the electrons, respectively. As a result,  $E_1$  and  $E_2$  are rewritten as

2.4 Optical Gains 39

**Fig. 2.10** Optical power gain coefficient under the *k*-selection rule



$$E_1 = E_{\rm v} - \frac{m_{\rm e}^*}{m_{\rm e}^* + m_{\rm b}^*} (E_{21} - E_{\rm g}),$$
 (2.50)

$$E_2 = E_c + \frac{m_h^*}{m_e^* + m_h^*} (E_{21} - E_g).$$
 (2.51)

Also, once the initial state of the optical transitions is given, the final state is determined by  $E_{21}$  and k. Hence, the number of state pairs per volume associated with the optical transitions for the photon energies between  $E_{21}$  and  $E_{21} + dE_{21}$  is given by

$$\rho_{\text{red}}(E_{21}) [f_2(E_{21}) - f_1(E_{21})] dE_{21}.$$
 (2.52)

We assume that the energy states related to optical transitions have an energy width of  $\hbar/\tau_{in}$ , and the spectral shape of Lorentzian such as

$$L(E_{21}) = \frac{1}{\pi} \frac{\hbar/\tau_{\text{in}}}{(E_{21} - E)^2 + (\hbar/\tau_{\text{in}})^2},$$
 (2.53)

where  $\tau_{in}$  is the relaxation time due to electron scatterings and transitions. In this case, the optical power gain coefficient g(E) is expressed as

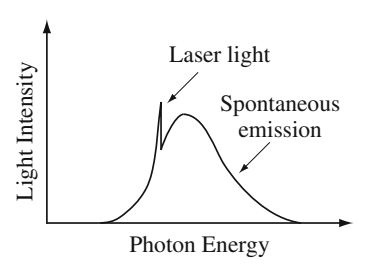
$$g(E) = \frac{e^2 h}{2m^2 \varepsilon_0 n_{\rm r} c E} \int_0^\infty |\langle 1 | \boldsymbol{p} | 2 \rangle|^2 \rho_{\rm red}(E_{21}) \left[ f_2(E_{21}) - f_1(E_{21}) \right] L(E_{21}) \, dE_{21}, \tag{2.54}$$

which is plotted in Fig. 2.10 for the bulk structures with  $\tau_{\rm in}=10^{-13}\,\rm s$ . It is found that relaxation is equivalent to band tailing, which contributes to optical transitions in  $E < E_{\rm g}$ .

Because  $f_2$  and  $[1 - f_1]$  are always positive, spontaneously emitted lights distribute in a higher energy than the gain peak. Figure 2.11 schematically shows spectra for the stimulated emission (laser light) and the spontaneously emitted lights; its horizontal line indicates photon energy. Note that the photon energies increase due to the band filling effect with enhancement of the excitation, irrespective of spontaneous emission or stimulated emission.

40 2 Optical Transitions

**Fig. 2.11** Stimulated emission and spontaneous emission



## References

- 1. Einstein, A.: Zur Quantentheorie der Strahlung. Phys. Z. 18, 121 (1917)
- 2. Pankove, J.I.: Optical Processes in Semiconductors. Dover, New York (1975)

# **Chapter 3 Optical Waveguides**

## 3.1 Introduction

An optical beam propagating in a *free space* expands in beam width with an increase in propagation distance. The beam divergence angle  $\theta$  in radians is expressed as

$$\theta \simeq \frac{\lambda}{d},$$
 (3.1)

where  $\lambda$  is a light wavelength and d is a beam diameter. For example, if a laser beam with  $\lambda = 1 \,\mu\text{m}$  and  $d = 1 \,\text{mm}$  propagates by 100 m, its beam width expands to about 10 cm. In contrast, the *optical waveguide* confines lights to itself during propagation of the lights [1–5].

In typical bulk (double heterostructure) semiconductor lasers, the active layer thickness is  $0.1\,\mu m$ , the beam width is  $0.3\,\mu m$ , and the cavity length is  $300\,\mu m$ . If there are no optical waveguides, this beam width expands up to  $500\,\mu m$  by a single-way propagation, where  $\lambda$  is assumed to be  $0.5\,\mu m$ . In semiconductor lasers, only the *active layer* has optical gain, and it is extremely inefficient to amplify a beam with the width of  $500\,\mu m$  by the active layer with the thickness of only  $0.1\,\mu m$ . Therefore, to amplify lights efficiently, optical waveguides are indispensable for semiconductor lasers. It should be noted that *optical fibers* are also representative optical waveguides.

Figure 3.1 shows cross-sectional views of the optical waveguides. According to the operating principles, optical waveguides are divided into *index guiding* waveguides and *gain guiding* ones. In index guiding waveguides, a light is confined to a high-refractive index region, which is surrounded by low-refractive index regions. In Fig. 3.1a, only if the *refractive indexes*  $n_f$ ,  $n_c$ , and  $n_s$  satisfy  $n_f > n_c$ ,  $n_s$ , a light is confined to a region with  $n_f$ . The gain guiding waveguides use the property that only a gain region amplifies a light, and a light seems to propagate in the gain region. In Fig. 3.1b, a light is confined to a region with the *optical gain*  $g_f$ , which is larger than  $g_c$  and  $g_s$ .

To consider optical gain, we introduce the *complex refractive index* 

$$\tilde{n} = n_{\rm r} - \mathrm{i}\,\kappa,\tag{3.2}$$

**Fig. 3.1** Cross sections of optical waveguides: **a** index guiding and **b** gain guiding

(a) $n_{\rm f} > n_{\rm c}, n_{\rm s}$	<b>(b)</b> $g_{\rm f} > g_{\rm c}, g_{\rm s}$
$n_{\rm c}$	g <sub>c</sub>
$n_{ m f}$	$g_{ m f}$
$n_{\rm s}$	$g_{s}$

where  $n_r$  is a so-called refractive index and  $\kappa$  is the *extinction coefficient*. Here, we express the electric field E of a light as

$$E = E_0 \exp[i(\omega t - kz)], \tag{3.3}$$

where  $E_0$  is an amplitude,  $\omega$  is an angular frequency of the light, t is a time, k is a wave number, and z is a coordinate for a propagation direction of the light. Using the complex refractive index  $\tilde{n}$  in (3.2), the angular frequency  $\omega$ , and the speed of light in a vacuum c, we can write the wave number k as

$$k = \frac{\tilde{n}\omega}{c} = \frac{n_{\rm r} - i\kappa}{c}\omega. \tag{3.4}$$

Substituting (3.4) into (3.3), we have

$$E = E_0 \exp\left[i\left(\omega t - \frac{n_r \omega}{c}z\right)\right] \cdot \exp\left(-\frac{\omega \kappa}{c}z\right),\tag{3.5}$$

where  $\kappa > 0$  shows the optical loss and  $\kappa < 0$  indicates the optical gain. As a result, the *optical amplitude gain coefficient*  $g_{\rm E}$  and the extinction coefficient  $\kappa$  are related as

$$g_{\rm E} = -\frac{\omega}{c}\kappa. \tag{3.6}$$

Note that the optical power gain coefficient g is equal to  $2g_E$ , because the light intensity is proportional to  $|E|^2$ .

From the viewpoint of shape, optical waveguides are classified into a *two-dimensional optical waveguide*, or a *planar optical waveguide*, and a *three-dimensional optical waveguide*, or a *strip optical waveguide*. The two-dimensional waveguide has a plane, which is much larger than a wavelength of light and confines a light one-dimensionally. Only the size of its confinement direction is of the order of a light wavelength or less. The three-dimensional waveguide confines a light two-dimensionally, and the sizes along these two confinement directions are of the order of a light wavelength or less. The remaining direction is the propagation direction of a light.

## 3.2 Two-Dimensional Optical Waveguides

## 3.2.1 Propagation Modes

Let us consider a two-dimensional waveguide where the *guiding layer* is sandwiched by the *cladding layer* and the *substrate*, as shown in Fig. 3.2. The refractive indexes of the guiding layer, the cladding layer, and the substrate are  $n_f$ ,  $n_c$ , and  $n_s$ , respectively. To confine a light in the guiding layer, we need  $n_f > n_s \ge n_c$ , and  $n_f - n_s$  is usually of the order of from  $10^{-3}$  to  $10^{-1}$ .

Figure 3.3 shows propagation directions of a light when the light enters from the substrate to the cladding layer through the guiding layer. From *Snell's law*, the angles  $\theta_s$ ,  $\theta_f$ , and  $\theta_c$ , which are formed by the interface normals and the directions of the light, are related to the refractive indexes  $n_s$ ,  $n_f$ , and  $n_c$  as

$$n_{\rm s}\sin\theta_{\rm s} = n_{\rm f}\sin\theta_{\rm f} = n_{\rm c}\sin\theta_{\rm c}.$$
 (3.7)

When  $\theta_s$  is equal to  $\pi/2$ , a light cannot propagate in the substrate, and the *total reflection* takes place at the interface of the substrate and the guiding layer. In this case, the power reflectivity (reflectance) is 100 %. When  $\theta_c$  is equal to  $\pi/2$ , the total reflection takes place at the interface of the cladding layer and the guiding layer. The minimum value of  $\theta_f$  to obtain the total reflection is called the *critical angle*. According to  $\theta_s = \pi/2$ , and  $\theta_c = \pi/2$ , we have two critical angles  $\theta_{fs}$  and  $\theta_{fc}$ , which are expressed as

$$\theta_{\rm fs} = \sin^{-1}\left(\frac{n_{\rm s}}{n_{\rm f}}\right), \theta_{\rm fc} = \sin^{-1}\left(\frac{n_{\rm c}}{n_{\rm f}}\right). \tag{3.8}$$

Here,  $\theta_{\rm fs} \geq \theta_{\rm fc}$  is satisfied under the assumption of  $n_{\rm f} > n_{\rm s} \geq n_{\rm c}$ .

Corresponding to a value of  $\theta_f$ , there are three *propagation modes*, as shown in Fig. 3.4.

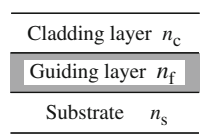


Fig. 3.2 Cross section of a two-dimensional optical waveguide

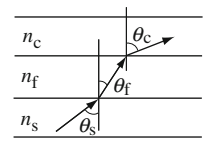


Fig. 3.3 Snell's law

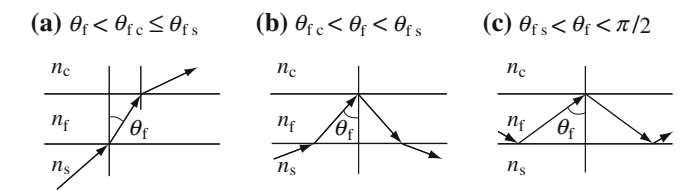


Fig. 3.4 Propagation modes: a radiation mode, b substrate radiation mode, and c guided mode

## (a) $\theta_f < \theta_{fc} \le \theta_{fs}$ : Radiation Mode

44

The light is not confined to the optical waveguide at all.

## (b) $\theta_{fc} < \theta_{f} < \theta_{fs}$ : Substrate Radiation Mode

Total reflection occurs at the interface of the cladding layer and the guiding layer, while refraction takes place at the interface of the guiding layer and the substrate. As a result, there exists a light propagating in the substrate.

## (c) $\theta_{fs} < \theta_f < \pi/2$ : Guided Mode

At both the interfaces, total reflections occur. A light is completely confined to the optical waveguide.

Among (a), (b), and (c), the guided mode in (c) is the most important for semi-conductor lasers and photonic integrated circuits. In (a) and (b), the guided mode does not exist, and such a condition is referred to as the *cutoff*. Therefore, in the following, we examine the guided mode in detail.

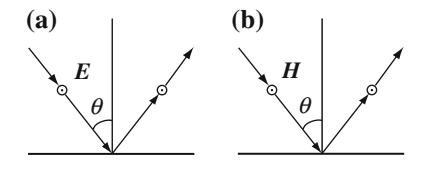
# 3.2.2 Three-Layer Model to Analyze Guided Modes

## 3.2.2.1 Total Reflection

The total reflection is the reflection with  $|r|^2 = 1$ , where r is the amplitude reflectivity. It should be noted that r depends on the angle of incidence and the direction of polarization.

Here, we consider a *plane wave*, and we define the *plane of incidence* as a plane on which all the directions of *incident light*, *reflected light*, and *refracted light* coexist. The *transverse electric* (TE) mode is a *linearly polarized light* whose *electric field E* is normal to the plane of incidence. The *transverse magnetic* (TM) mode is a linearly polarized light whose *magnetic field H* is normal to the plane of incidence. Figure 3.5

**Fig. 3.5** a TE mode and b TM mode



shows the TE mode and the TM mode, where the plane of incidence is placed on the face of the page and only the incident and reflected lights are illustrated.

From the Fresnel formulas, the amplitude reflectivities are given by

$$r_{\text{TE,c}} = \frac{n_{\text{f}} \cos \theta_{\text{f}} - \sqrt{n_{\text{c}}^2 - n_{\text{f}}^2 \sin^2 \theta_{\text{f}}}}{n_{\text{f}} \cos \theta_{\text{f}} + \sqrt{n_{\text{c}}^2 - n_{\text{f}}^2 \sin^2 \theta_{\text{f}}}},$$

$$r_{\text{TE,s}} = \frac{n_{\text{f}} \cos \theta_{\text{f}} - \sqrt{n_{\text{s}}^2 - n_{\text{f}}^2 \sin^2 \theta_{\text{f}}}}{n_{\text{f}} \cos \theta_{\text{f}} + \sqrt{n_{\text{s}}^2 - n_{\text{f}}^2 \sin^2 \theta_{\text{f}}}},$$
(3.9)

$$r_{\text{TM,c}} = \frac{n_{\text{c}}^2 \cos \theta_{\text{f}} - n_{\text{f}} \sqrt{n_{\text{c}}^2 - n_{\text{f}}^2 \sin^2 \theta_{\text{f}}}}{n_{\text{c}}^2 \cos \theta_{\text{f}} + n_{\text{f}} \sqrt{n_{\text{c}}^2 - n_{\text{f}}^2 \sin^2 \theta_{\text{f}}}},$$

$$r_{\text{TM,s}} = \frac{n_{\text{s}}^2 \cos \theta_{\text{f}} - n_{\text{f}} \sqrt{n_{\text{s}}^2 - n_{\text{f}}^2 \sin^2 \theta_{\text{f}}}}{n_{\text{s}}^2 \cos \theta_{\text{f}} + n_{\text{f}} \sqrt{n_{\text{s}}^2 - n_{\text{f}}^2 \sin^2 \theta_{\text{f}}}}.$$
(3.10)

Here, subscripts TE and TM show the TE mode and the TM mode, respectively; subscripts c and s correspond to the reflection at the interface of the cladding layer and guiding layer and at the interface of the substrate and guiding layer, respectively.

When the total reflections take place,  $|r|^2 = 1$  is satisfied, and the amplitude reflectivities in (3.9) and (3.10) take complex numbers. As a result, we can write the amplitude reflectivity r as

$$r = \exp(i\,2\phi),\tag{3.11}$$

where  $\phi$  is the *phase shift* added to the reflected wave at the interface. In other words, due to the total reflection, the phase of the reflected wave is shifted at the interface of the reflection. When we rewrite (3.9) and (3.10) in the form of (3.11), the phase shifts are expressed as

$$\tan \phi_{\text{TE,c}} = \frac{\sqrt{n_{\text{f}}^2 \sin^2 \theta_{\text{f}} - n_{\text{c}}^2}}{n_{\text{f}} \cos \theta_{\text{f}}},$$

$$\tan \phi_{\text{TE,s}} = \frac{\sqrt{n_{\text{f}}^2 \sin^2 \theta_{\text{f}} - n_{\text{s}}^2}}{n_{\text{f}} \cos \theta_{\text{f}}},$$
(3.12)

$$\tan \phi_{\text{TM,c}} = \frac{n_{\text{f}} \sqrt{n_{\text{f}}^2 \sin^2 \theta_{\text{f}} - n_{\text{c}}^2}}{n_{\text{c}}^2 \cos \theta_{\text{f}}},$$

$$\tan \phi_{\text{TM,s}} = \frac{n_{\text{f}} \sqrt{n_{\text{f}}^2 \sin^2 \theta_{\text{f}} - n_{\text{s}}^2}}{n_{\text{s}}^2 \cos \theta_{\text{f}}},$$
(3.13)

where the subscripts are the same as in (3.9) and (3.11).

## 3.2.2.2 Guiding Condition

We consider a monochromatic coherent plane wave, which propagates in an optical waveguide as shown in Fig. 3.6. Here, the x-axis is normal to the layer interfaces, the y-axis is parallel to the layer interfaces, and the z-axis is along the propagation direction of the light. The thickness of the guiding layer is h.

Neglecting a time-dependent factor, we can express the propagating electric field E as

$$E = E_0 \exp[-ik_0 n_f(\pm x \cos\theta_f + z \sin\theta_f)], \tag{3.14}$$

where  $k_0 = \omega/c$  is a wave number in a vacuum, and a sign in front of x corresponds to the propagation direction of the light (+: toward positive x and -: toward negative x). The *propagation constant*  $\beta$  and the *phase velocity*  $v_p$  along the z-axis are defined as

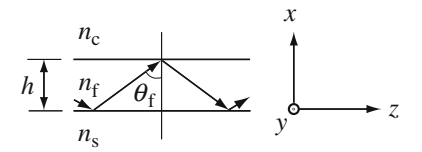
$$\beta \equiv k_0 n_{\rm f} \sin \theta_{\rm f} \equiv \frac{\omega}{v_{\rm p}},\tag{3.15}$$

as shown in Fig. 3.7.

If we see a light in a reference system which moves toward the positive z-axis with a phase velocity  $v_p$ , we observe that a light is multireflected along the x-axis. Changes in the phase during a roundtrip of the light along the x-axis are given by

 $x = 0 \rightarrow h$  (the first half)  $: k_0 n_f h \cos \theta_f,$  x = h (at the interface of the reflection)  $: -2\phi_c,$   $x = h \rightarrow 0$  (the second half)  $: k_0 n_f h \cos \theta_f,$ x = 0 (at the interface of the reflection)  $: -2\phi_s.$ 

**Fig. 3.6** Coordinate system for a guided mode



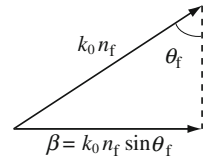
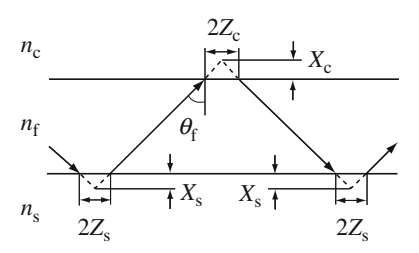


Fig. 3.7 Propagation constant

Fig. 3.8 Goos-Hänchen shift



Because the phase of the wave front shifts after a roundtrip, the lightwave intensity is modified by interference. Therefore, to obtain a propagating lightwave without decay, a total phase change in the roundtrip must satisfy

$$2k_0 n_f h \cos \theta_f - 2\phi_c - 2\phi_s = 2m\pi \quad (m = 0, 1, 2, ...), \tag{3.16}$$

where *m* is the *mode number*. Equation (3.16) shows a resonance condition normal to the *z*-axis, which is called the *transverse resonance condition*. From (3.16), it is found that the angle of incidence  $\theta_f$  for the guided mode takes discrete values.

In summary, the guiding condition is characterized by simultaneously satisfying the transverse resonance condition (3.16) and the total reflection condition  $\theta_{fs} < \theta_f < \pi/2$ .

#### 3.2.2.3 Goos-Hänchen Shift

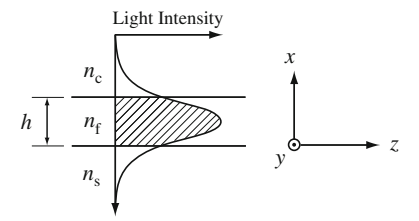
When the total reflection takes place, a phase of a lightwave shifts by  $-2\phi$  at the interface of the reflection. Due to this phase shift, an optical path changes at the reflection interfaces, as shown in Fig. 3.8. This shift in the optical path Z is called the *Goos-Hänchen shift*, which is given by

$$Z = \frac{\mathrm{d}\phi}{\mathrm{d}\beta},\tag{3.17}$$

where  $\beta$  is the propagation constant along the z-axis.

At each reflection interface, a lightwave propagates along the interface and has a component with a decay constant 1/X along the x-axis where X is the *penetration depth*. This exponentially decaying wave is designated the *evanescent wave*, and the energy does not flow along the x-axis.

**Fig. 3.9** Distribution of light intensity



With the help of (3.12) and (3.13), the Goos-Hänchen shifts and the penetration depths are expressed as

$$k_{0}Z_{\text{TE,c}} = (n_{f}^{2} \sin^{2}\theta_{f} - n_{c}^{2})^{-1/2} \cdot \tan\theta_{f},$$

$$k_{0}Z_{\text{TE,s}} = (n_{f}^{2} \sin^{2}\theta_{f} - n_{s}^{2})^{-1/2} \cdot \tan\theta_{f},$$

$$X_{\text{TE,c}} = \frac{Z_{\text{TE,c}}}{\tan\theta_{f}}, \quad X_{\text{TE,s}} = \frac{Z_{\text{TE,s}}}{\tan\theta_{f}},$$
(3.18)

$$k_0 Z_{\text{TM,c}} = (n_f^2 \sin^2 \theta_f - n_c^2)^{-1/2} \cdot \tan \theta_f \cdot \left(\frac{N^2}{n_c^2} + \frac{N^2}{n_f^2} - 1\right)^{-1},$$

$$k_0 Z_{\text{TM,s}} = (n_f^2 \sin^2 \theta_f - n_s^2)^{-1/2} \cdot \tan \theta_f \cdot \left(\frac{N^2}{n_s^2} + \frac{N^2}{n_f^2} - 1\right)^{-1},$$

$$X_{\text{TM,c}} = \frac{Z_{\text{TM,c}}}{\tan \theta_f}, \quad X_{\text{TM,s}} = \frac{Z_{\text{TM,s}}}{\tan \theta_f}.$$
(3.19)

#### 3.2.2.4 Effective Refractive Index

Using a wave number  $k_0 = \omega/c$  in a vacuum and the propagation constant  $\beta$  along the z-axis, we define the effective refractive index N as

$$N \equiv \frac{\beta}{k_0} = n_{\rm f} \sin \theta_{\rm f}. \tag{3.20}$$

This effective refractive index N is considered to be a refractive index of a material for a plane wave propagating along the z-axis. Because the semiconductor lasers have optical waveguides within themselves, the effective refractive index N is important to determine the resonance conditions. Note that the value of N for the guided modes satisfies

$$n_{\rm S} < N < n_{\rm f},\tag{3.21}$$

where  $n_{\rm f} > n_{\rm s}$  was used.

## 3.2.2.5 Optical Confinement Factor

We define the *optical confinement factor*  $\Gamma$  as a ratio of the intensity of the light existing in the relevant layer to the total light intensity.

Because the light intensity distributes as shown in Fig. 3.9, the optical confinement factor  $\Gamma_f$  for the guiding layer (hatched area) is given by

$$\Gamma_{\rm f} = \frac{\int_0^h |E(x)|^2 dx}{\int_{-\infty}^\infty |E(x)|^2 dx}.$$
 (3.22)

Similarly, the optical confinement factors  $\Gamma_c$  for the cladding layer and  $\Gamma_s$  for the substrate are written as

$$\Gamma_{c} = \frac{\int_{h}^{\infty} |E(x)|^{2} dx}{\int_{-\infty}^{\infty} |E(x)|^{2} dx}, \quad \Gamma_{s} = \frac{\int_{-\infty}^{0} |E(x)|^{2} dx}{\int_{-\infty}^{\infty} |E(x)|^{2} dx}.$$
 (3.23)

The optical confinement factor  $\Gamma$  is important to design optical losses or optical gains in the optical waveguides. Using  $\Gamma$ , we can approximately express the effective refractive index N as

$$N \approx \Gamma_{\rm s} n_{\rm s} + \Gamma_{\rm f} n_{\rm f} + \Gamma_{\rm c} n_{\rm c}. \tag{3.24}$$

## 3.2.2.6 Normalized Expressions for Eigenvalue Equation

The equation for the transverse resonance condition (3.16) is called an *eigenvalue equation*. By solving (3.16) numerically, we can examine propagation characteristics of the guided modes. Furthermore, normalizing (3.16) leads to *dispersion curves*, which are common to all step-like two-dimensional optical waveguides. To obtain a normalized expression of the eigenvalue equation, we define the *normalized frequency*, or the *normalized waveguide thickness V*, and the *normalized waveguide refractive index b* as

$$V = k_0 h \sqrt{n_{\rm f}^2 - n_{\rm s}^2},\tag{3.25}$$

$$b = \frac{N^2 - n_s^2}{n_f^2 - n_s^2}. (3.26)$$

In addition, we introduce the asymmetry measure a as

$$a = \frac{n_s^2 - n_c^2}{n_r^2 - n_s^2}. (3.27)$$

Substituting (3.12), (3.13), and (3.25)–(3.27) into (3.16), we obtain the normalized eigenvalue equation as

$$V\sqrt{1-b} = m\pi + \tan^{-1}\chi_{\rm s}\sqrt{\frac{b}{1-b}} + \tan^{-1}\chi_{\rm c}\sqrt{\frac{a+b}{1-b}},$$
 (3.28)

where

$$\chi_i = \begin{cases} 1 & \text{: TE mode} \\ (n_f/n_i)^2 & \text{: TM mode } (i = s, c). \end{cases}$$
 (3.29)

It should be noted that the guided modes for the gain guiding waveguides can be calculated from (3.16) or (3.28), if we replace the refractive index  $n_i$  (i = s, f, c) with the complex refractive index  $\tilde{n}_i$ .

Figure 3.10 shows the normalized dispersion curves for the guided TE modes. If the waveguide parameters, such as the refractive indexes and the layer thickness, are given, we can design the optical waveguides using Fig. 3.10. For the design of the optical waveguides, the *cutoff condition*, in which the guided modes do not exist, is important. When the angle of incidence  $\theta_f$  is equal to the critical angle  $\theta_{fs}$ , the lightwave is not confined to the guiding layer anymore, and a fraction of the optical power is emitted to the substrate. In this case, we have  $N = n_s$ , which results in b = 0 from (3.26). Hence, from (3.28), a normalized frequency for the cutoff condition  $V_m$  is given by

$$V_m = m\pi + \tan^{-1} \chi_c \sqrt{a}. \tag{3.30}$$

For  $V_m < V < V_{m+1}$ , the guided modes from the zeroth order to the mth order exist as shown in Fig. 3.10, and a lower-order mode has a larger b for a common V value. Therefore, from (3.26), a lower-order mode has a larger effective refractive index, and the fundamental mode (m = 0) has the largest N among the guided modes.

Figure 3.11 shows the electric fields E(x) for fundamental (m = 0), first-order (m = 1), and second-order (m = 2) TE modes, in which the *m*th-order TE mode is indicated by TE<sub>m</sub>. See Appendix D for the relationship between the eigenvalue equations and the light fields.

For symmetric optical waveguides with  $n_s = n_c$ , by using V and b, the optical confinement factor  $\Gamma_f$  is also expressed as

$$\Gamma_{\rm f} = \frac{V\sqrt{b} + 2b}{V\sqrt{b} + 2}.\tag{3.31}$$

## 3.2.2.7 Coupling of Light into Optical Waveguides

When the total reflections occur at the interfaces, we cannot couple a light into the guiding layer from the cladding layer or the substrate. Therefore, we introduce the light from a *facet* of the optical waveguide, as shown in Fig. 3.12. It should be noted that the angle of incidence in the guiding layer  $\theta_f$  must satisfy the guiding conditions.

**Fig. 3.10** Normalized dispersion curves for guided TE modes

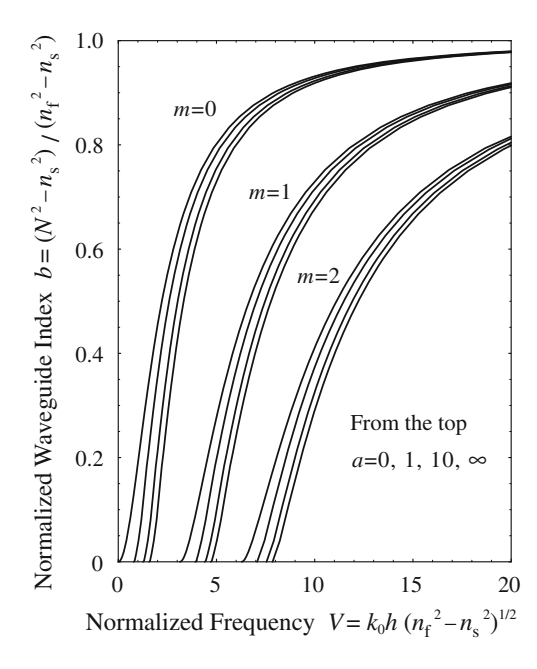


**Fig. 3.11** Distributions of electric fields

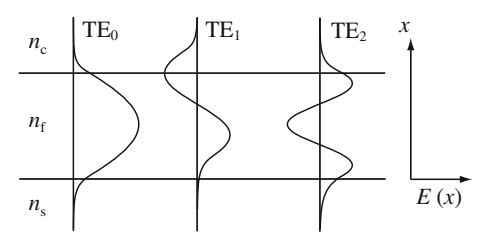
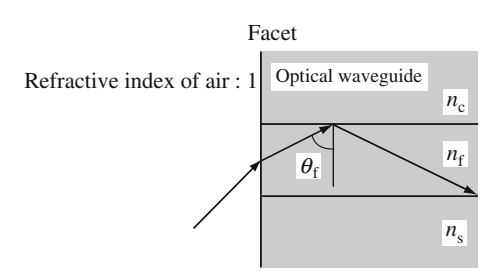


**Fig. 3.12** Coupling of a light into an optical waveguide



In semiconductor lasers, lights are generated in the active layers, and we do not have to couple a light from outside. However, when semiconductor lasers are used as optical amplifiers by biasing below threshold, or they are controlled by an incident light such as in *injection locking*, lights are introduced from the facets of semiconductor lasers.

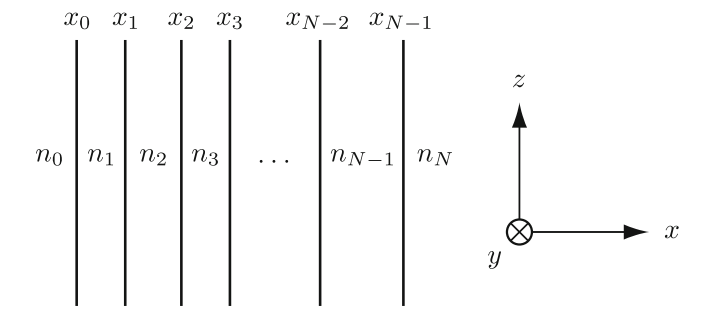


Fig. 3.13 Multiple layer optical waveguide

## 3.2.3 Multiple-Layer Model to Analyze Guided Modes

We consider the light, which propagates along the z-axis in the multiple layer optical waveguide shown in Fig. 3.13. From Maxwell equations, the light fields  $\psi_y(x)$  and  $\psi_z(x)$  at the position x and the light fields  $\psi_y(x_i)$  and  $\psi_z(x_i)$  at the position  $x_i$  are related by the following equation

$$\begin{bmatrix} \psi_{y}(x) \\ \psi_{z}(x) \end{bmatrix} = \mathbf{G}(x - x_{i}) \begin{bmatrix} \psi_{y}(x_{i}) \\ \psi_{z}(x_{i}) \end{bmatrix}, \tag{3.32}$$

where  $G(x - x_i)$  is a matrix.

If we assume that an electric field E and a magnetic field H of the light are expressed by a separation-of-variables procedure, we have  $\psi_y(x) = E_y(x)$ ,  $\psi_z(x) = iZ_0H_z(x)$  for the TE mode; and  $\psi_y(x) = Z_0H_y(x)$ ,  $\psi_z(x) = -iE_z(x)$  for the TM mode. Here, a subscript indicates a component along each coordinate and  $Z_0 = \sqrt{\mu_0/\varepsilon_0}$  is the *impedance of vacuum*.

To define the matrix  $G(x - x_i)$ , we introduce parameters such as

$$\kappa_i = \sqrt{k_0^2 n_i^2 - \beta^2},\tag{3.33}$$

$$\gamma_i = \sqrt{\beta^2 - k_0^2 n_i^2},\tag{3.34}$$

$$\zeta_i = \begin{cases} 1 & \text{TE mode} \\ n_i^2 & \text{TM mode} \end{cases}$$
 (3.35)

where  $k_0$  is the wave number of the light in a vacuum,  $n_i$  is the refractive index of the ith layer, and  $\beta$  is the propagation constant. It should be noted that the propagation constant  $\beta$  is calculated by solving the eigenvalue equation described below.

For the *i*th layer with  $\beta < k_0 n_i$ , the matrix  $G(x - x_i)$  is written as

(3.42)

$$G(x - x_i) = \begin{bmatrix} \cos \kappa_i (x - x_i) & -\frac{k_0 \zeta_i}{\kappa_i} \sin \kappa_i (x - x_i) \\ \frac{\kappa_i}{k_0 \zeta_i} \sin \kappa_i (x - x_i) & \cos \kappa_i (x - x_i) \end{bmatrix}.$$
 (3.36)

For the *i*th layer with  $\beta > k_0 n_i$ , the matrix  $G(x - x_i)$  is expressed as

$$G(x - x_i) = \begin{bmatrix} \cosh \gamma_i (x - x_i) & -\frac{k_0 \zeta_i}{\gamma_i} \sinh \gamma_i (x - x_i) \\ -\frac{\gamma_i}{k_0 \zeta_i} \sinh \gamma_i (x - x_i) & \cosh \gamma_i (x - x_i) \end{bmatrix}.$$
(3.37)

In (3.36) and (3.37), dependence of the light fields on time t is assumed to be  $\exp(i\omega t)$  where  $\omega$  is the angular frequency of the light, and  $\det G(x - x_i) = 1$  is satisfied.

Since  $\psi_y(x)$  and  $\psi_z(x)$  are tangential components of the light fields,  $\psi_y(x)$  and  $\psi_z(x)$  are continuous at the boundaries, respectively. By using these boundary conditions,  $\psi_y(x_0)$ ,  $\psi_z(x_0)$ ,  $\psi_y(x_{N-1})$ , and  $\psi_z(x_{N-1})$  are related as

$$\begin{bmatrix} \psi_{y}(x_{0}) \\ \psi_{z}(x_{0}) \end{bmatrix} = \prod_{i}^{N-1} G(-d_{i}) \begin{bmatrix} \psi_{y}(x_{N-1}) \\ \psi_{z}(x_{N-1}) \end{bmatrix} = \begin{bmatrix} A & B \\ C & D \end{bmatrix} \begin{bmatrix} \psi_{y}(x_{N-1}) \\ \psi_{z}(x_{N-1}) \end{bmatrix}, \quad (3.38)$$

where  $d_i = x_i - x_{i-1}$  is the thickness of the *i*th layer.

The propagation modes should have field distributions of  $\exp \left[ \gamma_0(x - x_0) \right]$  in  $x \le x_0$  and  $\exp \left[ -\gamma_N(x - x_{N-1}) \right]$  in  $x \ge x_{N-1}$ . Here, we assume that dependence of the light fields on time t is expressed as  $\exp(i\omega t)$  where  $\omega$  is the angular frequency of the light.

The electromagnetic fields  $E_y(x,t)$  and  $H_z(x,t)$  for the TE mode are assumed as follows:

$$E_{y}(x,t) = E_{y}(x) \exp(i\omega t) = E_{0} \exp\left[\gamma_{0}(x-x_{0})\right] \exp(i\omega t) \quad (x \leq x_{0}),$$
(3.39)  

$$H_{z}(x,t) = H_{z}(x) \exp(i\omega t) = H_{0} \exp\left[\gamma_{0}(x-x_{0})\right] \exp(i\omega t) \quad (x \leq x_{0}),$$
(3.40)  

$$E_{y}(x,t) = E_{y}(x) \exp(i\omega t) = E_{N} \exp\left[-\gamma_{N}(x-x_{N-1})\right] \exp(i\omega t) \quad (x \geq x_{N-1}),$$
(3.41)  

$$H_{z}(x,t) = H_{z}(x) \exp(i\omega t) = H_{N} \exp\left[-\gamma_{N}(x-x_{N-1})\right] \exp(i\omega t) \quad (x \geq x_{N-1}),$$

where  $E_0$ ,  $H_0$ ,  $E_N$ , and  $H_N$  are amplitudes, which are independent of position x and time t.

In a uniform optical material, which has magnetic permeability in a vacuum  $\mu_0$  usually, one of Maxwell's equations is written as

$$\nabla \times \mathbf{E} = -\mu_0 \, \frac{\partial \mathbf{H}}{\partial t}.\tag{3.43}$$

By inserting (3.39)–(3.42) into (3.43), we obtain

$$\gamma_0 E_0 = -i \,\mu_0 \omega H_0 \quad (x \le x_0), \tag{3.44}$$

$$-\gamma_N E_N = -i \,\mu_0 \omega H_N \ (x \ge x_{N-1}). \tag{3.45}$$

From (3.44) and (3.45),  $iZ_0H_0$  and  $iZ_0H_N$  are given by

$$iZ_0 H_0 = \sqrt{\frac{\mu_0}{\varepsilon_0}} \left( -\frac{\gamma_0}{\mu_0 \omega} E_0 \right) = -\frac{\gamma_0}{\sqrt{\varepsilon_0 \mu_0} \omega} E_0$$

$$= -\frac{c\gamma_0}{\omega} E_0 = -\frac{\gamma_0}{k_0} E_0 \quad (x \le x_0),$$
(3.46)

$$iZ_0 H_N = \sqrt{\frac{\mu_0}{\varepsilon_0}} \left( \frac{\gamma_N}{\mu_0 \omega} E_N \right) = \frac{\gamma_N}{\sqrt{\varepsilon_0 \mu_0}} \omega E_N$$

$$= \frac{c\gamma_N}{\omega} E_N = \frac{\gamma_N}{k_0} E_N \quad (x \ge x_{N-1}),$$
(3.47)

where  $c=1/\sqrt{\varepsilon_0\mu_0}$  is the speed of light in a vacuum, and  $k_0=\omega/c$  is the wave number of the light in a vacuum. Therefore, the light fields  $\psi_y(x)$  and  $\psi_z(x)$  for the TE mode are written as

$$\psi_{\nu}(x) = E_{\nu}(x) = E_0 \exp\left[\gamma_0(x - x_0)\right] \quad (x \le x_0), \tag{3.48}$$

$$\psi_z(x) = iZ_0 H_z(x) = -\frac{\gamma_0}{k_0} E_0 \exp\left[\gamma_0(x - x_0)\right] \quad (x \le x_0), \tag{3.49}$$

$$\psi_{y}(x) = E_{y}(x) = E_{N} \exp\left[-\gamma_{N}(x - x_{N-1})\right] \quad (x \ge x_{N-1}), \tag{3.50}$$

$$\psi_{z}(x) = iZ_{0}H_{z}(x) = \frac{\gamma_{N}}{k_{0}}E_{N}\exp\left[-\gamma_{N}(x - x_{N-1})\right] \quad (x \ge x_{N-1}). \tag{3.51}$$

The electromagnetic fields  $H_y(x, t)$  and  $E_z(x, t)$  for the TM mode are assumed as follows:

$$H_y(x,t) = H_y(x) \exp(i\omega t) = H_0 \exp[\gamma_0(x - x_0)] \exp(i\omega t) \quad (x \le x_0),$$
 (3.52)

$$E_z(x,t) = E_z(x) \exp(i\omega t) = E_0 \exp\left[\gamma_0(x - x_0)\right] \exp(i\omega t) \quad (x \le x_0), \tag{3.53}$$

$$H_{y}(x,t) = H_{y}(x) \exp(i\omega t) = H_{N} \exp\left[-\gamma_{N}(x - x_{N-1})\right] \exp(i\omega t) \quad (x \ge x_{N-1}),$$
(3.54)

$$E_z(x,t) = E_z(x) \exp(i\omega t) = E_N \exp\left[-\gamma_N(x - x_{N-1})\right] \exp(i\omega t) \quad (x \ge x_{N-1}).$$
(3.55)

When the electric current does not flow, one of Maxwell's equations in a uniform optical material with the refractive index  $n_i$  is written as

$$\nabla \times \boldsymbol{H} = \varepsilon_0 n_i^2 \frac{\partial \boldsymbol{E}}{\partial t}.$$
 (3.56)

By inserting (3.52)–(3.55) into (3.56), we obtain

$$\gamma_0 H_0 = i \,\varepsilon_0 n_0^2 \omega E_0 = i \,\varepsilon_0 \zeta_0 \omega E_0 \quad (x \le x_0), \tag{3.57}$$

$$-\gamma_N H_N = i \varepsilon_0 n_N^2 \omega E_N = i \varepsilon_0 \zeta_N \omega E_N \quad (x \ge x_{N-1}). \tag{3.58}$$

From (3.57) and (3.58),  $iE_0$  and  $iE_N$  are given by

$$iE_0 = \frac{\gamma_0}{\varepsilon_0 \zeta_0 \omega} H_0 \quad (x \le x_0), \tag{3.59}$$

$$iE_N = -\frac{\gamma_N}{\varepsilon_0 \zeta_N \omega} H_N \quad (x \ge x_{N-1}). \tag{3.60}$$

Therefore, the light fields  $\psi_{\nu}(x)$  and  $\psi_{\tau}(x)$  for the TM mode are written as

$$\psi_{y}(x) = Z_{0}H_{y}(x) = Z_{0}H_{0} \exp\left[\gamma_{0}(x - x_{0})\right] \quad (x \le x_{0}), \tag{3.61}$$

$$\psi_{z}(x) = -iE_{z}(x) = -\frac{\gamma_{0}}{\varepsilon_{0}\zeta_{0}\omega}H_{0}\exp\left[\gamma_{0}(x - x_{0})\right] \quad (x \le x_{0}), \tag{3.62}$$

$$\psi_{y}(x) = Z_{0}H_{y}(x) = Z_{0}H_{N} \exp\left[-\gamma_{N}(x - x_{N-1})\right] \quad (x \ge x_{N-1}), \tag{3.63}$$

$$\psi_z(x) = -iE_z(x) = \frac{\gamma_N}{\varepsilon_0 \zeta_N \omega} H_N \exp\left[-\gamma_N (x - x_{N-1})\right] \quad (x \ge x_{N-1}). \tag{3.64}$$

Inserting (3.48)–(3.51)and (3.61)–(3.64) into (3.38), we have a following eigenvalue equation

$$\frac{k_0 \zeta_N}{\gamma_N} A + B + \frac{k_0^2 \zeta_0 \zeta_N}{\gamma_0 \gamma_N} C + \frac{k_0 \zeta_0}{\gamma_0} D = 0.$$
 (3.65)

As dependence of the light fields on time t,  $\exp(-i\omega t)$  is also often used as well as  $\exp(i\omega t)$ . If we assume that dependence of the light fields on time t is expressed as  $\exp(-i\omega t)$ , the light fields  $\psi_v(x)$  and  $\psi_z(x)$  are expressed as

for the TE mode

$$\psi_{\nu}(x) = E_{\nu}(x) = E_0 \exp\left[\gamma_0(x - x_0)\right] \quad (x \le x_0), \tag{3.66}$$

$$\psi_z(x) = iZ_0 H_z(x) = \frac{\gamma_0}{k_0} E_0 \exp\left[\gamma_0(x - x_0)\right] \quad (x \le x_0), \tag{3.67}$$

$$\psi_{y}(x) = E_{y}(x) = E_{N} \exp\left[-\gamma_{N}(x - x_{N-1})\right] \quad (x \ge x_{N-1}), \tag{3.68}$$

$$\psi_z(x) = iZ_0 H_z(x) = -\frac{\gamma_N}{k_0} E_N \exp\left[-\gamma_N (x - x_{N-1})\right] \quad (x \ge x_{N-1}), \quad (3.69)$$

and for the TM mode

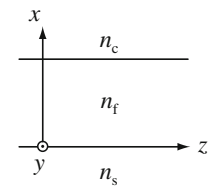


Fig. 3.14 Coordinates for a three-dimensional optical waveguide

$$\psi_{y}(x) = Z_{0}H_{y}(x) = Z_{0}H_{0} \exp\left[\gamma_{0}(x - x_{0})\right] \quad (x \le x_{0}), \tag{3.70}$$

$$\psi_{z}(x) = -iE_{z}(x) = \frac{\gamma_{0}}{\varepsilon_{0}\zeta_{0}\omega}H_{0}\exp\left[\gamma_{0}(x - x_{0})\right] \quad (x \le x_{0}), \tag{3.71}$$

$$\psi_{y}(x) = Z_{0}H_{y}(x) = Z_{0}H_{N} \exp\left[-\gamma_{N}(x - x_{N-1})\right] \quad (x \ge x_{N-1}), \tag{3.72}$$

$$\psi_z(x) = -iE_z(x) = -\frac{\gamma_N}{\varepsilon_0 \zeta_N \omega} H_N \exp\left[-\gamma_N (x - x_{N-1})\right] \quad (x \ge x_{N-1}). \quad (3.73)$$

As a result, the eigenvalue equation is given by

$$\frac{k_0 \zeta_N}{\gamma_N} A - B - \frac{k_0^2 \zeta_0 \zeta_N}{\gamma_0 \gamma_N} C + \frac{k_0 \zeta_0}{\gamma_0} D = 0.$$
 (3.74)

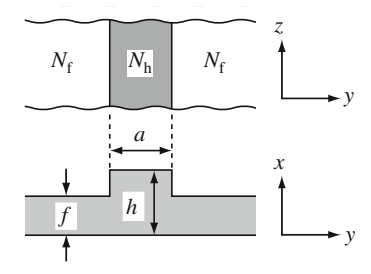
By solving (3.65) or (3.74), we can obtain the propagation constant  $\beta$  of the multiple layer optical waveguide and the filed distribution. If we use complex refractive index, we can consider optical gain or loss in the optical waveguide. When  $\beta$ 's are real, the guided modes for the index guiding waveguides exist. When  $\beta$ 's are complex, the guided modes might exist when the optical waveguides have optical gain. Therefore, in the semiconductor lasers, we have to consider the modes for complex  $\beta$ 's as well as the guided modes for real  $\beta$ 's.

# 3.3 Three-Dimensional Optical Waveguides

As shown in Fig. 3.14, we select a coordinate system in which the propagation direction of the light is the z-axis, the layer interfaces are normal to the x-axis, and the layer planes are parallel to the y-axis.

The two-dimensional optical waveguides can confine lights only along the x-axis, and not along the y-axis. In contrast, the *three-dimensional optical waveguides* confine lights along both the x- and y-axes. When these three-dimensional optical waveguides are adopted in semiconductor lasers, the guided modes are efficiently amplified, which results in low-threshold, high-efficiency laser operations. However, analysis of the three-dimensional optical waveguides is more complicated than that of two-dimensional ones, and we cannot obtain exact analytical solutions. As a result,

**Fig. 3.15** Effective refractive index method



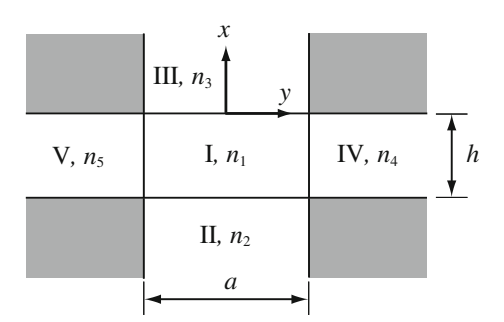
approximate analytical methods or numerical analyses are used to design the three-dimensional optical waveguides. As approximate analytical methods, we explain the *effective refractive index method* and *Marcatili's method*. These approximate methods can be applied to the guided modes, only when an *aspect ratio* a/h > 1 where h is the guiding layer thickness and a is the waveguide width, and the guiding condition is far from the cutoff conditions. If these two conditions are not satisfied, accuracy of the approximations degrades.

## 3.3.1 Effective Refractive Index Method

Figure 3.15 shows a ridge+ optical waveguide where an upper figure is a top view and a lower one is a cross-sectional view. Here, a is the waveguide width, h is the film thickness of the core region, and f is the film thickness of the surrounding regions.

At first, we treat the core region and the surrounding regions separately, and we regard each region as the two-dimensional optical waveguide. Therefore, the normalized frequency V and the normalized waveguide refractive index b for each region are defined as

Fig. 3.16 Marcatili's method



$$V_{\rm h} = k_0 h \sqrt{n_{\rm f}^2 - n_{\rm s}^2}, \quad V_{\rm f} = k_0 f \sqrt{n_{\rm f}^2 - n_{\rm s}^2},$$
 (3.75)

$$b_{\rm h} = \frac{N_{\rm h}^2 - n_{\rm s}^2}{n_{\rm f}^2 - n_{\rm s}^2}, \quad b_{\rm f} = \frac{N_{\rm f}^2 - n_{\rm s}^2}{n_{\rm f}^2 - n_{\rm s}^2}, \tag{3.76}$$

where subscripts h and f correspond to the core region and the surrounding regions, respectively; and  $N_h$  and  $N_f$  are the effective refractive indexes for each region.

Secondly, we consider that the guiding layer with the refractive index  $N_h$  and thickness a is sandwiched by the layers with the refractive index  $N_f$ , as shown in the upper figure of Fig. 3.15. As a result, the normalized frequency  $V_y$  of the three-dimensional optical waveguide is defined as

$$V_y = k_0 a \sqrt{N_h^2 - N_f^2}. (3.77)$$

If we express the effective refractive index of the three-dimensional optical waveguide as  $N_s$ , the normalized waveguide refractive index  $b_s$  of the three-dimensional optical waveguide is given by

$$b_{\rm s} = \frac{N_{\rm s}^2 - N_{\rm f}^2}{N_{\rm h}^2 - N_{\rm f}^2}.$$
 (3.78)

Substituting  $V_y$  and  $b_s$  into (3.28) leads to the dispersion curves for the three-dimensional optical waveguide.

## 3.3.2 Marcatili's Method

Figure 3.16 shows a cross-sectional view of the three-dimensional optical waveguide, which is seen toward the positive direction of the *z*-axis. If most of the guided modes are confined to region I, light field amplitudes drastically decay with an increase in distance from the interfaces. Therefore, the light intensities distributed in the shaded areas in Fig. 3.16 are neglected, which is referred to as Marcatili's method [6]. Under this assumption, light fields are obtained by solving wave equations.

## References

- 1. Tamir, T. (ed.): Integrated Optics, 2nd edn. Springer, Berlin (1979)
- 2. Tamir, T. (ed.): Guided-Wave Optoelectronics, 2nd edn. Springer, Berlin (1990)
- 3. Hunsperger, R.G.: Integrated Optics: Theory and Technology, 3rd edn. Springer, Berlin (1991)

References 59

- 4. Marcuse, D.: Theory of Dielectric Waveguides, 2nd edn. Academic Press, San Diego (1991)
- 5. Ebeling, K.J.: Integrated Optoelectronics. Springer, Berlin (1992)
- 6. Marcatili, E.A.J.: Dielectric rectangular waveguide and directional coupler for integrated optics. Bell Syst. Tech. J. **48**, 2071 (1969)

# **Chapter 4 Optical Resonators**

#### 4.1 Introduction

As shown in Fig. 4.1, the lasers use a fraction of spontaneously emitted lights as the input and amplify the fraction by the stimulated emission. To feed back the light, the *optical resonators*, or the *optical cavities*, which consist of reflectors, are adopted. The resonance conditions of the optical resonators determine lasing conditions such as a threshold and an oscillation wavelength.

In this chapter, we focus on the optical resonators that are used in the semiconductor lasers and explain the *Fabry-Perot cavity*, the *distributed feedback* (DFB) cavity, and the *distributed Bragg reflector* (DBR), which is a component of a resonator.

The optical resonators are divided into three groups whose constituent components are *mirrors*, *diffraction gratings*, and hybrid of mirrors and diffraction gratings.

Figure 4.2 shows the optical resonators comprising the mirrors: the *Fabry-Perot cavity* and the *ring cavity*. The Fabry-Perot cavity consists of two parallel mirrors in which lights experience repetitive roundtrips. The ring cavity, in contrast, has three or more mirrors, in which lights propagate clockwise or counterclockwise. These two optical cavities are also widely used in gas, solid, and dye lasers as well as in semiconductor lasers. One of the mirrors is often replaced by the diffraction grating in order to select an oscillation mode. Note that a *cleaved facet* is used as a mirror in semiconductor lasers.

Figure 4.3 shows the optical resonators, which use diffraction gratings: the *DFB* cavity and the *DBR*. The DFB cavity has an active layer, which generates a light, and the optical gain, in its corrugated region, and functions as the optical resonator by itself. In contrast, the DBR does not have an active layer in its corrugated region and functions as a reflector, not a resonator. Therefore, the DBR is combined with other DBRs or the cleaved facets to form optical resonators.

## 4.2 Fabry-Perot Cavity

The Fabry-Perot laser has an active material inside the Fabry-Perot cavity, as shown in Fig. 4.4a. In the semiconductor lasers, cleaved facets are used as mirrors, as illustrated in Fig. 4.4b, because lights are reflected at the interface of the air and the

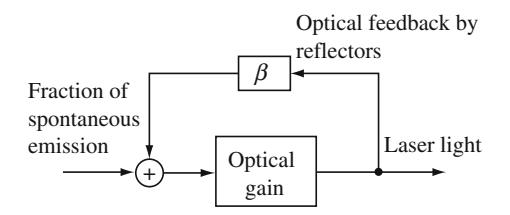


Fig. 4.1 Laser

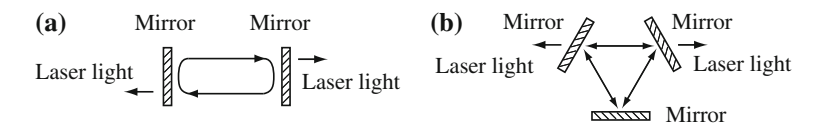


Fig. 4.2 Optical resonators with reflectors: a Fabry-Perot cavity and b ring cavity

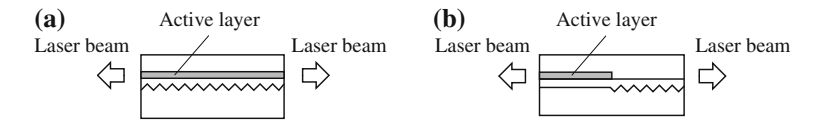


Fig. 4.3 a DFB and b DBR

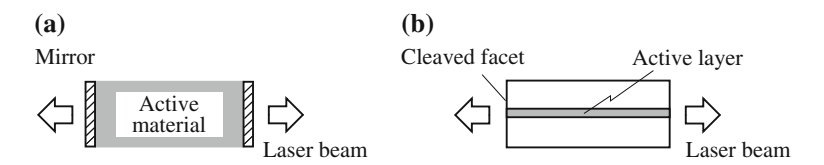


Fig. 4.4 Fabry-Perot lasers: a laser and b LD

semiconductor due to a difference in refractive indexes. Note that the cleaved facets are very flat with the order of atomic layers, and they are much smoother than light wavelengths. These cleaved facets are often coated with *dielectric films* to control the reflectivities or protect the facets from degradation.

Let us consider *transmission characteristics* of the Fabry-Perot cavity. We assume that the amplitude reflectivities of the two mirrors are  $r_1$  and  $r_2$ ; the amplitude transmissivities of the two mirrors are  $t_1$  and  $t_2$ , as shown in Fig. 4.5. As explained in Chap. 3, these reflectivities and transmissivities depend on the angle of incidence and the polarization of the light. Here, we suppose that the angle of incidence  $\theta_0$  is small enough, and we regard  $r_1$ ,  $r_2$ ,  $t_1$ , and  $t_2$  as constant.

If we neglect a time-dependent factor, we can write the incident electric field  $E_i$  through the surface at z=0 as

$$E_{\rm i} = t_1 E_0 \exp\left[-\frac{{\rm i}\,n_{\rm rt}\omega}{c}(x\sin\theta + z\cos\theta)\right] \times \exp[g_{\rm E}(x\sin\theta + z\cos\theta)]. \quad (4.1)$$

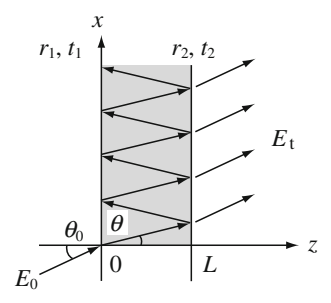


Fig. 4.5 Analytical model for the Fabry-Perot cavity

Here,  $E_0$  is an amplitude of the electric field of the incident light,  $n_{\rm rt}$  is a real part of the complex refractive index of the material placed between the two mirrors,  $\omega$  is an angular frequency of the light, c is the speed of light in a vacuum, and  $g_{\rm E}$  is the optical amplitude gain coefficient defined in (3.6).

The transmitted electric field  $E_t$  through the Fabry-Perot cavity is expressed as

$$E_{t} = t_{1}t_{2}E_{0} \exp\left[-\frac{i n_{rt}\omega}{c}(x \sin \theta + L \cos \theta) + \frac{g_{E}L}{\cos \theta}\right]$$

$$\times \left\{1 + r_{1}r_{2} \exp\left(-i \delta + \frac{2g_{E}L}{\cos \theta}\right) + (r_{1}r_{2})^{2} \exp\left[2\left(-i \delta + \frac{2g_{E}L}{\cos \theta}\right)\right] + \cdots\right\}$$

$$= \frac{t_{1}t_{2}E_{0} \exp\left[-\frac{i n_{rt}\omega}{c}(x \sin \theta + L \cos \theta) + \frac{g_{E}L}{\cos \theta}\right]}{1 - r_{1}r_{2} \exp\left(-i \delta + \frac{2g_{E}L}{\cos \theta}\right)},$$
(4.2)

where

$$\delta = \frac{2n_{\rm rt}\omega L\cos\theta}{c} \tag{4.3}$$

was introduced.

The incident light intensity  $I_0$  and the transmitted light intensity  $I_t$  are related to the electric fields  $E_0$  and  $E_t$  as

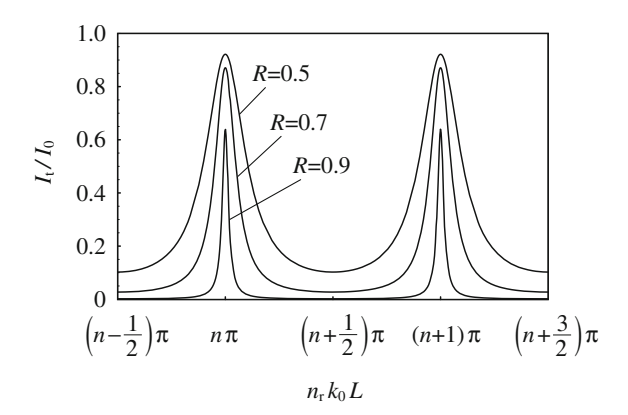
$$I_0 \propto E_0^* E_0, \quad I_t \propto E_t^* E_t.$$
 (4.4)

Therefore, with the help of (4.2), we obtain

$$I_{t} = \frac{(t_{1}t_{2})^{2}G_{s}}{1 + (r_{1}r_{2})^{2} \cdot G_{s}^{2} - 2r_{1}r_{2}G_{s}\cos\delta} I_{0},$$

$$G_{s} = \exp\left(\frac{2g_{E}L}{\cos\theta}\right).$$
(4.5)

**Fig. 4.6** Transmission characteristics for the Fabry-Perot cavity



Because the power reflectivities  $R_1$ ,  $R_2$  and the power transmissivities  $T_1$ ,  $T_2$  are given by

$$R_1 = r_1^* r_1, \quad R_2 = r_2^* r_2, \quad T_1 = t_1^* t_1, \quad T_2 = t_2^* t_2,$$
 (4.6)

we can rewrite (4.5) as

$$I_{\rm t} = \frac{T_1 T_2 G_{\rm s}}{1 + G_{\rm s}^2 R_1 R_2 - 2G_{\rm s} \sqrt{R_1 R_2} \cos \delta} I_0. \tag{4.7}$$

The angle  $\theta$  is given by  $\theta = \pi/2 - \theta_f$ , where  $\theta_f$  was defined in Fig. 3.6. Hence, we have  $\cos \theta = \sin \theta_f$  and (4.3) reduces to

$$\delta = \frac{2n_{\rm r}\omega L}{c} = 2n_{\rm r}k_0L, \quad k_0 = \frac{\omega}{c},\tag{4.8}$$

where the effective refractive index  $N = n_{\rm rt} \sin \theta_{\rm f} \equiv n_{\rm r}$  was used. When the angle of incidence  $\theta_0$  is small, as in a fundamental mode, (4.7) results in

$$I_{t} = \frac{T_{1}T_{2}G_{s0}}{(1 - G_{s0}\sqrt{R_{1}R_{2}})^{2} + 4G_{s0}\sqrt{R_{1}R_{2}}\sin^{2}(n_{r}k_{0}L)} I_{0},$$

$$G_{s0} = \exp(2g_{E}L) = \exp(gL),$$

$$(4.9)$$

where (4.8) was used and g is the optical power gain coefficient. Figure 4.6 shows a plot of (4.9) where  $G_{s0} = 1$ , and  $R_1 = R_2 = R$ ,  $T_1 = T_2 = T = 0.98 - R$  by assuming that the optical power loss at each mirror is 2 %. The transmissivities have maximum values at  $n_r k_0 L = n\pi$  (n: a positive integer) and minimum values at (n + 1/2) $\pi$ . With an increase in R, the transmission spectra narrow and the transmissivities decrease. If the optical power loss at the mirror is null, we have T = 1 - R, which results in a maximum power transmissivity of 1 (100 %) irrespective of R.

#### 4.2.1 Resonance Condition

When the *resonance condition* is satisfied, the power transmissivity has a peak. From (4.9), the resonance condition is given by

$$n_{\rm r}k_0L = \frac{n_{\rm r}\omega L}{c} = \frac{n_{\rm rt}\omega L}{c}\cos\theta = n\pi,\tag{4.10}$$

where n is a positive integer. From this equation, it is found that the effective refractive index  $n_r$  is useful to express the resonance condition. At *normal incidence* with  $\theta_0 = \theta = 0$ , the resonance condition is written as

$$\frac{n_{\rm rt}\omega L}{c} = n_{\rm rt}k_0 L = n\pi. \tag{4.11}$$

Using a wavelength in a vacuum  $\lambda_0$ , (4.11) reduces to

$$L = n \frac{\lambda_0}{2n_{\rm rt}}. (4.12)$$

Because  $\lambda_0/n_{\rm rt}$  is a wavelength in a material, a product of a positive integer and a half-wavelength in a material is equal to the cavity length L at the resonance condition.

## 4.2.2 Free Spectral Range

The Fabry-Perot cavity is used as a *spectrometer*, because its transmissivity depends on a light wavelength. However, two lights whose  $n_r k_0 L$  values are different by  $n\pi$  (n: a positive integer) cannot be resolved by the Fabry-Perot cavity, because there is a common transmissivity for the two lights. When  $(n-1/2)\pi < n_r k_0 L < (n+1/2)\pi$  is satisfied, a light is not confused by other lights. This region of  $n_r k_0 L$  is called the *free spectral range*, because the light is resolved free from other lights. The free spectral range in an angular frequency  $\omega_{\rm FSR}$  is given by

$$\omega_{\rm FSR} = \frac{c}{n_{\rm r}L}\pi. \tag{4.13}$$

Using the free spectral range  $\lambda_{FSR}$  in a wavelength,  $\omega_{FSR}$  is written as

$$\omega_{\text{FSR}} = 2\pi c \left( \frac{1}{\lambda_0} - \frac{1}{\lambda_0 + \lambda_{\text{FSR}}} \right). \tag{4.14}$$

As a result, we have

$$\lambda_{\rm FSR} \simeq \frac{{\lambda_0}^2}{2n_{\rm r}L} = \frac{{\lambda_0}^2}{2\pi c} \,\omega_{\rm FSR}.$$
 (4.15)

#### 4.2.3 Spectral Linewidth

The half width at half maximum (HWHM) is a difference between the wavelength or the frequency for the maximum transmissivity and that for the half of the maximum transmissivity. The full width at half maximum (FWHM), which is twice as large as the HWHM, is a difference between the two wavelengths or frequencies for the half of the maximum transmissivity.

Let us calculate the *spectral linewidth* using (4.9). When the transmissivity takes a maximum value, the resonance condition (4.11) is satisfied. As a result, the denominator in (4.9) reduces to

$$(1 - G_{s0}\sqrt{R_1R_2})^2. (4.16)$$

When the transmissivity is half-maximum, the denominator in (4.9) is twice (4.16), and we have

$$(1 - G_{s0}\sqrt{R_1R_2})^2 + 4G_{s0}\sqrt{R_1R_2}\sin^2(n_rk_0L) = 2(1 - G_{s0}\sqrt{R_1R_2})^2, \quad (4.17)$$

which results in

$$\sin(n_{\rm r}k_0L) = \pm \frac{1}{2\sqrt[4]{G_{\rm s0}^2 R_1 R_2}} (1 - G_{\rm s0}\sqrt{R_1 R_2}). \tag{4.18}$$

Expressing  $k_0 = k_m$  on resonance and  $k_0 = k_m \pm \Delta k_0$  at half-maximum and then substituting  $k_0 = k_m \pm \Delta k_0$  into (4.18) leads to

$$\sin(n_{\rm r}\Delta k_0 L) = \frac{1}{2\sqrt[4]{G_{\rm s0}^2 R_1 R_2}} (1 - G_{\rm s0} \sqrt{R_1 R_2}). \tag{4.19}$$

For the spectra in Fig. 4.6,  $n_r \Delta k_0 L \ll 1$  is satisfied. Hence, (4.19) reduces to

$$\Delta k_0 = \frac{1 - G_{s0}\sqrt{R_1 R_2}}{2n_r L \sqrt[4]{G_{s0}^2 R_1 R_2}}.$$
(4.20)

Using  $k_0 = \omega/c$ , we can express the HWHM in an angular frequency  $\Delta\omega_{\rm H}$  as

$$\Delta\omega_{\rm H} = c\Delta k_0 = \frac{c(1 - G_{\rm s0}\sqrt{R_1R_2})}{2n_rL\sqrt[4]{G_{\rm s0}^2R_1R_2}}.$$
 (4.21)

Therefore, the FWHM  $\Delta\omega_{\rm F}$ , which is twice the HWHM, is given by

$$\Delta\omega_{\rm F} = 2\Delta\omega_{\rm H} = \frac{c(1 - G_{\rm s0}\sqrt{R_1R_2})}{n_{\rm r}L\sqrt[4]{G_{\rm s0}^2R_1R_2}}.$$
 (4.22)

Using a wavelength in a vacuum, we can write the FWHM in a wavelength  $\Delta \lambda_{\rm F}$  as

$$\Delta \lambda_{\rm F} \simeq \frac{{\lambda_0}^2}{2\pi c} \, \Delta \omega_{\rm F} = \frac{{\lambda_0}^2 (1 - G_{\rm s0} \sqrt{R_1 R_2})}{2\pi n_{\rm r} L \sqrt[4]{G_{\rm s0}}^2 R_1 R_2}.\tag{4.23}$$

#### 4.2.4 Finesse

When we measure a wavelength or a frequency of light, an index of resolution is given by the *finesse*. The finesse F is defined as a ratio of the free spectral range to the FWHM, which is given by

$$F = \frac{\omega_{\text{FSR}}}{\Delta \omega_{\text{F}}} = \frac{\lambda_{\text{FSR}}}{\Delta \lambda_{\text{F}}} = \frac{\pi \sqrt[4]{G_{\text{s0}}^2 R_1 R_2}}{1 - G_{\text{s0}} \sqrt{R_1 R_2}},$$
(4.24)

where (4.13), (4.15), (4.22) and (4.23) were used. With an increase in F, the resolution of a wavelength or a frequency is improved.

#### 4.2.5 Electric Field Inside Fabry-Perot Cavity

Earlier, we considered a relationship between the incident light and the transmitted light in the Fabry-Perot cavity. In this section, we study the light inside the Fabry-Perot cavity. When the amplitude reflectivities are  $r_1 = r_2 = r$  and the amplitude transmissivities are  $t_1 = t_2 = t$ , the electric field E inside the Fabry-Perot cavity is written as

$$E = tE_0 \exp(k_{\text{eff}} x \sin \theta) \left\{ \exp(k_{\text{eff}} z \cos \theta) + r \exp[k_{\text{eff}} (2L - z) \cos \theta] \right\}$$
$$\times \left[ 1 + r^2 \exp(2k_{\text{eff}} L \cos \theta) + r^4 \exp(4k_{\text{eff}} L \cos \theta) + \cdots \right]$$

$$= \frac{tE_0 \exp(k_{\text{eff}} x \sin \theta) \left\{ \exp(k_{\text{eff}} z \cos \theta) + r \exp[k_{\text{eff}} (2L - z) \cos \theta] \right\}}{1 - r^2 \exp(2k_{\text{eff}} L \cos \theta)}, \quad (4.25)$$

where

$$k_{\text{eff}} = -\frac{\mathrm{i}\,n_{\text{rt}}\omega}{c} + g_{\text{E}}.\tag{4.26}$$

In (4.25),  $\exp(k_{\rm eff} z \cos \theta)$  exhibits a forward running wave toward a positive direction along the z-axis, and  $\exp[k_{\rm eff} (2L - z) \cos \theta]$  expresses a backward running wave after reflection at a plane with z = L. If we introduce  $a = r \exp(2k_{\rm eff} L \cos \theta)$ , (4.25) reduces to

$$E = tE_0 \exp(k_{\text{eff}} x \sin \theta) \frac{(1-a) \exp(k_{\text{eff}} z \cos \theta) + 2a \cosh(k_{\text{eff}} z \cos \theta)}{1 - r^2 \exp(2k_{\text{eff}} L \cos \theta)} . \quad (4.27)$$

**Fig. 4.7** Feedback points of lights: **a** Fabry-Perot cavity and **b** DFB cavity and DBR

In (4.27), the first term in the numerator represents a forward *running wave*, and the second term shows a *standing wave*. From (4.25)–(4.27), the light intensity inside the Fabry-Perot cavity takes a maximum value when

$$\frac{n_{\rm rt}\omega L}{c}\cos\theta = \frac{n_{\rm r}\omega L}{c} = n_{\rm r}k_0L = n\pi. \tag{4.28}$$

Here, n is a positive integer, which shows the number of *nodes* existing between z = 0 and z = L for a standing wave. Note that (4.28) is the same as the resonance condition (4.10), which indicates that both the transmissivity and the internal light intensity of the Fabry-Perot cavity have the largest values at the resonance condition.

#### 4.3 DFB and DBR

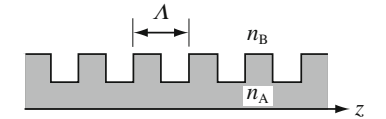
The *DFB* cavity and the *DBR* are the optical waveguides, which have diffraction gratings in them. They feed back lights by spatially modulating the complex refractive indexes of the optical waveguides. In the Fabry-Perot cavity, the reflection points of lights are only the facets. In contrast, in the DFB cavity and the DBR, reflection points of lights are distributed in the optical waveguide as shown in Fig. 4.7. The difference in the DFB cavity and the DBR is that the former has the optical gain in the corrugated region, and the latter does not. As described earlier, the DFB cavity functions as the optical resonator, and the DBR forms the optical resonator with other DBRs or cleaved facets.

## 4.3.1 Coupled Wave Theory

Because only the difference in the DFB cavity and the DBR is whether there is optical gain, their characteristics can be analyzed by a common method. In order to treat the optical gains or losses, we consider an optical waveguide with a complex dielectric constant  $\tilde{\varepsilon}$ 

When a lightwave is assumed to propagate along the z-axis, a propagation constant k in the optical waveguide is given by

Fig. 4.8 Diffraction grating



$$k^{2} = \omega^{2} \mu \tilde{\varepsilon} = \omega^{2} \mu (\varepsilon_{r} - i \varepsilon_{i}) \simeq k_{0}^{2} n_{r}(z)^{2} \left[ 1 + i \frac{2\alpha(z)}{k_{0} n_{r}(z)} \right],$$
  

$$\tilde{\varepsilon} = \varepsilon_{r} - i \varepsilon_{i} = \varepsilon_{0} \left[ n_{r}(z) + i \frac{\alpha(z)}{k_{0}} \right]^{2},$$
(4.29)

where  $\omega$  is an angular frequency of the light;  $\mu$  is magnetic permeability of a material;  $k_0 = \omega/c$  is a wave number in a vacuum;  $\varepsilon_0 = 8.854 \times 10^{-12}$  F/m is permittivity in a vacuum;  $n_r(z)$  is a real part of a complex refractive index; and  $\alpha(z) = g_E$  is an optical amplitude gain coefficient. For the usual optical materials,  $\mu$  is almost equal to magnetic permeability in a vacuum  $\mu_0 = 4\pi \times 10^{-7}$  H/m. Because of  $|\alpha(z)| \ll k_0$ , a second-order term of  $\alpha(z)$  was neglected in (4.29). Figure 4.8 shows a schematic cross section of the diffraction gratings. The effective refractive index of the optical waveguide is periodically modulated with a pitch of  $\Lambda$  by the corrugations formed at the interface between the two layers with the refractive indexes  $n_A$  and  $n_B$  ( $n_A \neq n_B$ ).

Here, we assume that  $n_r(z)$  and  $\alpha(z)$  are sinusoidal functions of z, which are written as

$$n_{\rm r}(z) = n_{\rm r0} + n_{\rm r1}\cos(2\beta_0 z + \Omega),$$
  
 $\alpha(z) = \alpha_0 + \alpha_1\cos(2\beta_0 z + \Omega),$  (4.30)

where  $\Omega$  is a phase at z=0 and  $\beta_0$  is related to the grating pitch  $\Lambda$  as

$$\beta_0 = \frac{\pi}{4}.\tag{4.31}$$

Under the assumption of  $n_{\rm rl} \ll n_{\rm r0}$  and  $\alpha_{\rm l} \ll \alpha_{\rm 0}$ , substituting (4.30) into (4.29) leads to

$$k(z)^{2} = k_{0}^{2} n_{r0}^{2} + i 2k_{0} n_{r0} \alpha_{0} + 4k_{0} n_{r0} \left(\frac{\pi n_{r1}}{\lambda_{0}} + i \frac{\alpha_{1}}{2}\right) \cos(2\beta_{0}z + \Omega). \quad (4.32)$$

Here,  $k_0 = 2\pi/\lambda_0$ , where  $\lambda_0$  is a wavelength in a vacuum.

When the refractive index is constant  $(n_{r1} = 0)$  and the material is *transparent*  $(\alpha_0 = \alpha_1 = 0)$ , the propagation constant k(z) in (4.32) is given by

$$k(z) = \beta = k_0 n_{\rm r0}.$$
 (4.33)

In the optical waveguides with corrugations, reflections in Fig. 4.7b couple a forward running wave and a backward one. To express this coupling, we define the *coupling coefficient*  $\kappa$  of the diffraction gratings as

$$\kappa = \frac{\pi n_{\rm rl}}{\lambda_0} + i \frac{\alpha_1}{2},\tag{4.34}$$

which is important to describe the resonance characteristics of the DFB cavity and the DBR.

With the help of (4.33) and (4.34), (4.32) reduces to

$$k(z)^{2} = \beta^{2} + i 2\beta\alpha_{0} + 4\beta\kappa\cos(2\beta_{0}z + \Omega). \tag{4.35}$$

Substituting (4.35) into a wave equation for the electric field E given by

$$\frac{d^2E}{dz^2} + k(z)^2E = 0, (4.36)$$

we obtain

$$\frac{\mathrm{d}^2 E}{\mathrm{d}z^2} + \left[\beta^2 + \mathrm{i}\,2\beta\alpha_0 + 4\beta\kappa\cos(2\beta_0 z + \Omega)\right]E = 0. \tag{4.37}$$

The electric field E(z), which is a solution of (4.37), is represented by a superposition of a forward running field  $E_r(z)$  and a backward one  $E_s(z)$  such as

$$E(z) = E_{\rm r}(z) + E_{\rm s}(z),$$
  
 $E_{\rm r}(z) = R(z) \exp(-i\beta_0 z),$  (4.38)  
 $E_{\rm s}(z) = S(z) \exp(i\beta_0 z),$ 

where R(z) and S(z) are the field amplitudes of the forward running wave and the backward one, respectively, and both are functions of z. Inserting (4.38) into (4.37) gives the wave equations for R and S as follows:

$$-\frac{\mathrm{d}R}{\mathrm{d}z} + (\alpha_0 - \mathrm{i}\,\delta)R = \mathrm{i}\,\kappa S \exp(-\mathrm{i}\Omega),$$

$$\frac{\mathrm{d}S}{\mathrm{d}z} + (\alpha_0 - \mathrm{i}\,\delta)S = \mathrm{i}\,\kappa R \exp(\mathrm{i}\Omega),$$
(4.39)

where  $\delta$  is defined as

$$\delta \equiv \frac{\beta^2 - {\beta_0}^2}{2\beta_0} \simeq \beta - \beta_0. \tag{4.40}$$

Here, R and S were assumed to be slowly varying functions of z, and the second derivatives with respect to z were neglected. Because the forward running wave R and the backward one S are coupled by the coupling coefficient  $\kappa$ , (4.39) is called the *coupled wave equation*, and a theory based on (4.39) is referred to as the *coupled wave theory* [1].

As a wavelength for  $\delta = 0$ , we define Bragg wavelength  $\lambda_B$  in a vacuum as

$$\lambda_{\rm B} = \frac{2n_{\rm r0}\Lambda}{m},\tag{4.41}$$

where (4.31), (4.33), and (4.40) were used and m is a positive integer designated the order of diffraction.

Using constants a and b, which are determined by the boundary conditions, general solutions of (4.37) are given by

$$E_{r}(z) = [a \exp(\gamma z) + \rho \exp(-i\Omega) \cdot b \exp(-\gamma z)] \exp(-i\beta_{0}z),$$
  

$$E_{s}(z) = [\rho \exp(i\Omega) \cdot a \exp(\gamma z) + b \exp(-\gamma z)] \exp(i\beta_{0}z),$$
(4.42)

where

$$\gamma^{2} = (\alpha_{0} - i \delta)^{2} + \kappa^{2},$$

$$\rho = \frac{-\gamma + (\alpha_{0} - i \delta)}{i \kappa}.$$
(4.43)

To continue analyzing, it is useful to introduce a *transfer matrix*  $F_i$  [2], which is defined as

$$\begin{bmatrix} E_{\rm r}(0) \\ E_{\rm s}(0) \end{bmatrix} = \mathbf{F}_i \begin{bmatrix} E_{\rm r}(L_i) \\ E_{\rm s}(L_i) \end{bmatrix}. \tag{4.44}$$

Here,  $L_i$  is the length of a corrugated region and  $F_i$  is written as

$$\boldsymbol{F}_i = \begin{bmatrix} F_{11} & F_{12} \\ F_{21} & F_{22} \end{bmatrix},$$

$$F_{11} = \left[ \cosh(\gamma L_i) - \frac{\alpha_0 - \mathrm{i} \, \delta}{\gamma} \sinh(\gamma L_i) \right] \exp(\mathrm{i} \, \beta_0 L_i),$$

$$F_{12} = \frac{\mathrm{i} \, \kappa}{\gamma} \sinh(\gamma L_i) \exp[-\mathrm{i} \, (\beta_0 L_i + \Omega)],$$

$$F_{21} = -\frac{\mathrm{i} \, \kappa}{\gamma} \sinh(\gamma L_i) \exp[\mathrm{i} \, (\beta_0 L_i + \Omega)],$$

$$F_{22} = \left[ \cosh(\gamma L_i) + \frac{\alpha_0 - \mathrm{i} \, \delta}{\gamma} \sinh(\gamma L_i) \right] \exp(-\mathrm{i} \, \beta_0 L_i).$$
(4.45)

When multiple regions are connected in series, as shown in Fig. 4.9, the total transfer matrix F is given by a product of transfer matrixes in all regions such as

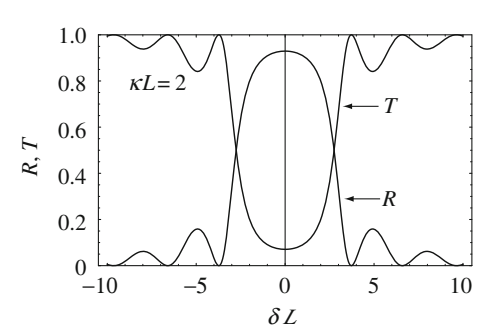
$$F = \prod_{i} F_{i}. \tag{4.46}$$

If both facets have the power reflectivity of  $R_1$  and  $R_2$ , the total transfer matrix  $F_R$  is given by

$$E_{r} \stackrel{R_{1}}{\longleftrightarrow} F_{1} \stackrel{F_{2}}{\longleftrightarrow} F_{r} \stackrel{R_{2}}{\longleftrightarrow} E_{r} \stackrel{E_{r}}{\longleftrightarrow} (L)$$

Fig. 4.9 Analytical model for a diffraction grating

**Fig. 4.10** Calculated transmission and reflection spectra of a diffraction grating



$$F_{R} = \frac{1}{\sqrt{(1 - R_{1})(1 - R_{2})}} \begin{bmatrix} 1 & -\sqrt{R_{1}} \\ -\sqrt{R_{1}} & 1 \end{bmatrix} \times F \times \begin{bmatrix} 1 & \sqrt{R_{2}} \\ \sqrt{R_{2}} & 1 \end{bmatrix}. \quad (4.47)$$

Let us calculate the power transmissivity T and the power reflectivity R. When we assume that the corrugated region length is L and the input is  $E_{\rm r}(0)$  with  $E_{\rm s}(L)=0$ , the output for the transmission is  $E_{\rm r}(L)$  and that for the reflection is  $E_{\rm s}(0)$ . From the definition of the transfer matrix, the power transmissivity T and the power reflectivity R are given by

$$T = \frac{1}{F_{11}^* F_{11}}, \quad R = \frac{F_{21}^* F_{21}}{F_{11}^* F_{11}}.$$
 (4.48)

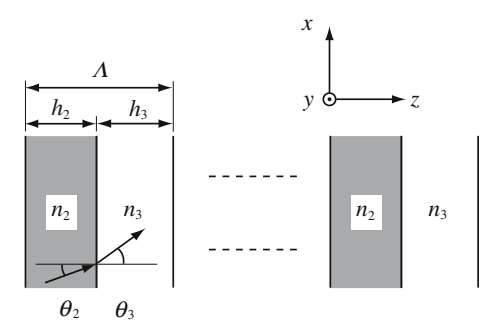
Figure 4.10 shows calculated transmission and reflection spectra of a diffraction grating. The horizontal line is  $\delta L = \delta \times L$ , and the vertical line is the power transmissivity T and the power reflectivity R. Here, it is assumed that the optical waveguide is transparent ( $\alpha_0 = \alpha_1 = 0$ ),  $\kappa L = 2$ , and  $R_1 = R_2 = 0$ . In these spectra, there is a low-transmissivity (high-reflectivity) region that is symmetrical about  $\delta L = 0$ . This region is called the *stop band*, because the transmission is stopped.

## 4.3.2 Discrete Approach

In the DFB cavity and the DBR, the complex refractive indexes are periodically modulated along the propagation direction of lights. Therefore, they can be analyzed by the *discrete approach*, which has been applied to the *periodic multilayers*.

Figure 4.11 shows a model for analysis where a region with a complex refractive index  $n_2$  and length  $h_2$  and a region with  $n_3$  and  $h_3$  are alternately placed. The angles

**Fig. 4.11** Analytical model in a discrete approach



formed by the interface normal and the light propagation directions are supposed to be  $\theta_2$  and  $\theta_3$  in the former region and the latter region, respectively.

The relationship between the input and output lights is expressed by a *characteristic matrix*  $M_2$ , which is defined as

$$\begin{bmatrix} U(0) \\ V(0) \end{bmatrix} = \mathbf{M}_2 \begin{bmatrix} U(z) \\ V(z) \end{bmatrix}. \tag{4.49}$$

Here, an electric field E and a magnetic field H are assumed to be expressed by a separation-of-variables procedure. Hence, U(z) and V(z) show dependence of E and E on E and E on E and the plane of incidence as an E are sult, we have E of the propagation direction as a positive E-axis and the plane of incidence as an E-plane. As a result, we have E of the propagation direction as a positive E-axis and the plane of incidence as an E-plane. As a result, we have E of the propagation of the propagation E of the p

When we introduce parameters such as

$$\beta_2 = \frac{2\pi}{\lambda_0} n_2 h_2 \cos \theta_2, \quad \beta_3 = \frac{2\pi}{\lambda_0} n_3 h_3 \cos \theta_3,$$

$$p_2 = n_2 \cos \theta_2, \quad p_3 = n_3 \cos \theta_3,$$
(4.50)

the characteristic matrix  $M_2$  for the TE mode is written as

$$\mathbf{M}_{2} = \begin{bmatrix} \cos \beta_{2} & -\frac{\mathrm{i}}{p_{2}} \sin \beta_{2} \\ -\mathrm{i} p_{2} \sin \beta_{2} & \cos \beta_{2} \end{bmatrix} \begin{bmatrix} \cos \beta_{3} & -\frac{\mathrm{i}}{p_{3}} \sin \beta_{3} \\ -\mathrm{i} p_{3} \sin \beta_{3} & \cos \beta_{3} \end{bmatrix}. \tag{4.51}$$

If the number of periods is N, the total characteristic matrix of the optical waveguide M is given by

$$\mathbf{M} = \mathbf{M}_2{}^{N} = \begin{bmatrix} m_{11} & m_{12} \\ m_{21} & m_{22} \end{bmatrix}. \tag{4.52}$$

To analyze the DFB cavity and the DBR by the discrete approach, it is useful to put

$$n_2 = n_{\rm r0} + \Delta n, \quad n_3 = n_{\rm r0} - \Delta n,$$
  
 $h_2 = h_3 = \frac{\Lambda}{2}, \quad \theta_2 = \theta_3 = 0,$  (4.53)

where  $n_{r0}$  is an average refractive index of a material;  $\Delta n$  is a shift of refractive index from  $n_{r0}$ ;  $\Lambda$  is the grating pitch; and  $L = N\Lambda$  is the corrugated region length. If  $\theta_2 = \theta_3 = 0$ , we have common characteristic matrixes for the TE mode and the TM mode. With the help of (4.52), when the outside of the DFB cavity and the DBR is the air, the power transmissivity T and the power reflectivity R are obtained as

$$T = \left| \frac{2}{(m_{11} + m_{12}) + (m_{21} + m_{22})} \right|^{2},$$

$$R = \left| \frac{(m_{11} + m_{12}) - (m_{21} + m_{22})}{(m_{11} + m_{12}) + (m_{21} + m_{22})} \right|^{2},$$
(4.54)

where the boundary conditions at the interfaces for E and H were used. Note that the obtained T and R are derived from Maxwell's equations. In this process, we have assumed that E and H are expressed by a separation-of-variables procedure, and approximations have not been used. For more detailed explanations on the characteristic matrix, see Appendix E.

## 4.3.3 Comparison of Coupled Wave Theory and Discrete Approach

To clarify the application limits of the coupled wave theory and the discrete approach, we will compare the results of these two theories. For brevity, we assume that a material is transparent ( $\alpha_0 = \alpha_1 = 0$ ) and consider the reflectivity at Bragg wavelength ( $\delta = 0$ ) in the first-order diffraction gratings (m = 1).

#### 4.3.3.1 Coupled Wave Theory

74

From (4.43), the assumption of  $\alpha_0 - i \delta = 0$  leads to  $\gamma = \pm \kappa$ . Substituting this result into (4.45) and (4.48), we obtain the power reflectivity R as

$$R = \tanh^2(\kappa L),\tag{4.55}$$

where L is the corrugated region length. From (4.55), it is found that  $\kappa$  and L are important to determine the reflectivity of the diffraction gratings.

#### 4.3.3.2 Discrete Approach

When  $\Delta n \ll n_{\rm r0}$  is satisfied, the power reflectivity R is obtained as

$$R = \left[1 - \left(\frac{n_{\rm r0} - \Delta n}{n_{\rm r0} + \Delta n}\right)^{2N}\right]^{2} \left[1 + \left(\frac{n_{\rm r0} - \Delta n}{n_{\rm r0} + \Delta n}\right)^{2N}\right]^{-2},\tag{4.56}$$

where (4.51)–(4.54) were used. The second terms in both brackets are approximated as

$$\left(\frac{n_{\rm r0} - \Delta n}{n_{\rm r0} + \Delta n}\right)^{2N} \simeq \left(1 - \frac{\Delta n}{n_{\rm r0}}\right)^{4N} = \left[\left(1 - \frac{\Delta n}{n_{\rm r0}}\right)^{n_{\rm r0}/\Delta n}\right]^{4N\Delta n/n_{\rm r0}}$$

$$= \exp\left(-4N\frac{\Delta n}{n_{\rm r0}}\right). \tag{4.57}$$

With the help of  $N\Lambda = L$  and (4.41), the exponent of the right-hand side in (4.57) is written as

$$4N\frac{\Delta n}{n_{\rm r0}} = \frac{8\Delta n}{2n_{\rm r0}\Lambda} L = \frac{8\Delta n}{\lambda_{\rm B}} L. \tag{4.58}$$

If we put

$$8\Delta n = 2\pi n_{\rm rl} \tag{4.59}$$

and substitute (4.59) into (4.58), we have

$$4N\frac{\Delta n}{n_{\rm r0}} = 2\frac{\pi n_{\rm r1}}{\lambda_{\rm B}} L = 2\kappa L,$$
 (4.60)

where (4.34) and the assumption of  $\alpha_1 = 0$  were used. Substituting (4.60) into (4.57) results in

$$\left(\frac{n_{\rm r0} - \Delta n}{n_{\rm r0} + \Delta n}\right)^{2N} \simeq e^{-2\kappa L}.\tag{4.61}$$

Inserting (4.61) into (4.56) leads to

$$R \simeq \left[\frac{1 - e^{-2\kappa L}}{1 + e^{-2\kappa L}}\right]^2 = \tanh^2(\kappa L). \tag{4.62}$$

From (4.55) and (4.62), it is found that the result of the coupled wave theory agrees with that of the discrete approach when  $\Delta n \ll n_{\rm r0}$  is satisfied.

**Fig. 4.12** a Uniform grating and **b** periodic multilayer

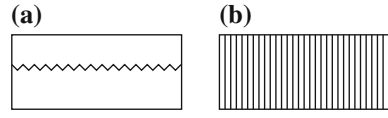
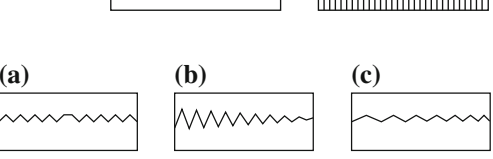


Fig. 4.13 Diffraction gratings used for the DFB cavity and the DBR: a phase-shifted, b tapered, and c chirped



It should be noted that the coupled wave theory assumes that complex refractive indexes vary sinusoidally, while the discrete approach presumes that complex refractive indexes change abruptly. Also, in the example for the discrete approach, two layers were alternately placed. Therefore, with an increase in  $\Delta n$ , the results of the coupled wave theory and the discrete approach differ from each other. However, with an increase in the number of layers in one period so that the complex refractive indexes may change sinusoidally in one period, the results of the two theories agree even when  $\Delta n$  is large. Also, the discrete approach can easily analyze any corrugation shape, because one period can be decomposed into many layers. However, because  $\Delta n$  in the DFB cavity and the DBR is of the order of  $10^{-3}$ , the coupled wave theory is widely used to analyze or design the DFB cavity and the DBR.

As shown in Fig. 4.12, a uniform grating in the DFB cavity or the DBR and a periodic multilayer seem different in shape. However, they can be analyzed by a common theory, because the operating principle is common. We should always focus on the essentials, irrespective of superficial differences.

## 4.3.4 Category of Diffraction Gratings

From the viewpoint of the pitch and depth, the diffraction gratings are divided into four groups.

The diffraction grating with uniform pitch and depth, which is shown in Fig. 4.12a, is a *uniform grating*. Other diffraction gratings are shown in Fig. 4.13. Figure 4.13a is a *phase-shifted grating* [3, 4] whose corrugations shift in its optical waveguide, and this grating is especially important for longitudinal single-mode operations in the DFB-LDs. Figure 4.13b is a *tapered grating* whose corrugation depth is spatially modulated along the propagation direction of the lights. Figure 4.13c is a *chirped grating* whose pitch varies along the propagation direction.

**Fig. 4.14** Phase-shifted grating

Pitch  $\Lambda$  Phase shift  $-\Delta \Omega$  Z  $E_{r}(0)$   $\theta_{1}$   $\theta_{2}$   $\theta_{3}$   $\theta_{4}$   $F_{1}$   $F_{2}$ 

 $E_{\rm s}(L)$ 

z = L

 $E_{\rm s}(0)$ 

z = 0

**Fig. 4.15** Analytical model for the phase-shifted grating

## 4.3.5 Phase-Shifted Grating

The refractive indexes of the optical fibers change according to the wavelengths of lights, and propagation velocities of lights vary with their wavelengths, which is referred to as *chromatic dispersion*. Hence, if semiconductor lasers show multimode operations, optical pulses broaden in the time domain, and finally adjacent optical pulses overlap each other to limit the transmission of signals. This overlap of adjacent pulses becomes serious with increases in the transmission distance and the signal speed. Therefore, longitudinal single-mode semiconductor lasers are required for long-haul, large-capacity optical fiber communication systems. To achieve stable single-mode operations, DFB-LDs with phase-shifted gratings or gain-coupled gratings have been developed. In the following, we will explain the phase-shifted gratings, which have been used commercially.

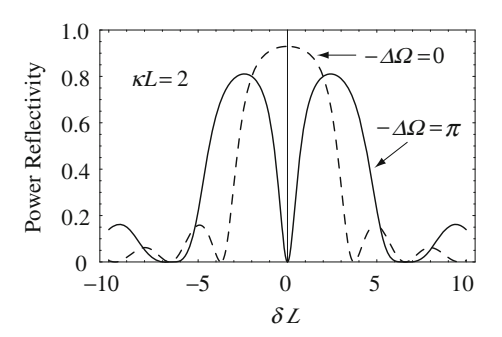
#### 4.3.5.1 Transmission and Reflection Characteristics

Figure 4.14 shows a schematic structure of the phase-shifted grating, in which the corrugation phase is shifted by  $-\Delta\Omega$  along the z-axis, and the corrugations in the uniform gratings are illustrated by a broken line. It should be noted that the negative sign of the phase shift is related to the definition of the spatial distribution of the complex refractive index in (4.30).

Let us analyze the phase-shifted gratings using the coupled wave theory. We suppose that both the pitch and the depth are uniform except in the phase-shifted region. Figure 4.15 shows an analytical model, where the diffraction gratings consist of two regions, and the phase shift is introduced as a phase jump at the interface of the two regions.

The transfer matrixes of Regions 1 and 2 are expressed as  $F_1$  and  $F_2$ , respectively. The phase  $\Omega$  at the left edge of Region 1 is written as  $\theta_1$ . Then the phase  $\theta_2$  at the

**Fig. 4.16** Reflection spectrum



right edge of Region 1 is given by

$$\theta_2 = \theta_1 + 2\beta_0 L_1. \tag{4.63}$$

Due to the phase shift  $\Delta\Omega$ , the phase  $\theta_3$  at the left edge of Region 2 is obtained as

$$\theta_3 = \theta_2 + \Delta\Omega = \theta_1 + 2\beta_0 L_1 + \Delta\Omega. \tag{4.64}$$

With the help of (4.48), the transmission and reflection characteristics of the phase-shifted gratings are given by the transfer matrix  $F = F_1 \times F_2$ .

Figure 4.16 shows calculated reflection spectra for  $\kappa L=2$ , where the horizontal line is  $\delta L=\delta \times L$  and the vertical line is the power reflectivity. Here, it has been assumed that a material is transparent and the facet reflectivity is null. The solid line and broken line correspond to the phase-shifted grating with  $-\Delta\Omega=\pi$  and the uniform grating with  $-\Delta\Omega=0$ , respectively. The characteristic feature of the phase-shifted grating is that it has a pass band within the stop band, and the phase-shifted DFB-LDs oscillate at this transmission wavelength. The transmission wavelength located within the stop band depends on the phase shift. When the phase shift is  $\pi$ , the transmission wavelength agrees with Bragg wavelength.

## **4.3.5.2** Comparison of the Phase-Shifted Grating and the Fabry-Perot Cavity [5]

Comparing the phase-shifted gratings with the Fabry-Perot cavity, we can understand a physical meaning of the relationship between the transmission wavelength and the phase shift.

Figure 4.17 schematically shows the Fabry-Perot cavity where the power reflectivity of the mirror is  $R_0$  and the cavity length is L. From (4.12), the resonance condition of the Fabry-Perot cavity is given by

$$L = n \frac{\lambda_0}{2n_r}. (4.65)$$

Fig. 4.17 Fabry-Perot cavity

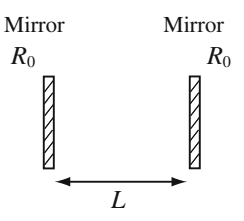
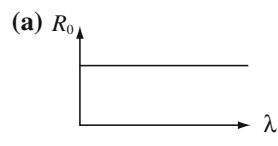
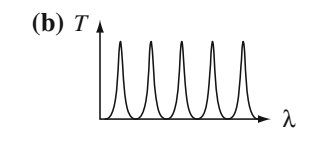
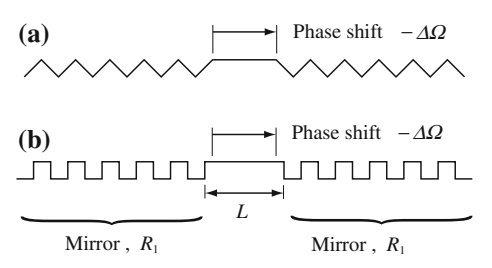


Fig. 4.18 Resonance characteristics of the Fabry-Perot cavity: a reflectance of a mirror and b transmittance of a cavity





**Fig. 4.19** Phase-shifted grating: **a** saw-toothed grating and **b** rectangular grating

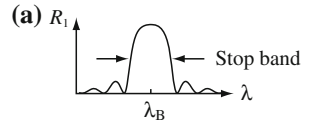


Here, n is a positive integer,  $n_{\rm r}$  is the effective refractive index of a material, and  $\lambda_0$  is a light wavelength in a vacuum. Figure 4.18 shows the power reflectivity (reflectance)  $R_0$  of the *mirror* and the power transmissivity (transmittance) T of the *Fabry-Perot cavity* as a function of a wavelength  $\lambda$ . It should be noted that  $R_0$  is independent of  $\lambda$  if the dispersions are neglected, and there are sharp peaks for all the wavelengths satisfying the resonance condition (4.65).

Figure 4.19 schematically shows the phase-shifted gratings with a saw-toothed shape and a rectangular shape. Grating shapes affect the value of  $\kappa$ , but the concepts on the grating pitch are common to both structures. Therefore, to focus on only the grating pitch, we will consider the rectangular shape in the following.

The phase shift  $-\Delta\Omega$  is defined as illustrated in Fig. 4.19. Such a phase-shifted grating is regarded as the Fabry-Perot cavity with length L and the two mirrors, which have wavelength-dependent reflectivities. In this case, a relation between L and  $\Delta\Omega$  is expressed as

$$L = \frac{\Lambda}{2} + \frac{|\Delta\Omega|}{2\beta_0} = \frac{\Lambda}{2} \left( 1 + \frac{|\Delta\Omega|}{\pi} \right),\tag{4.66}$$



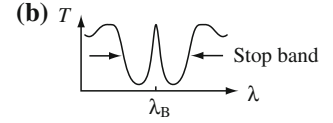


Fig. 4.20 Resonance characteristics of the phase-shifted grating: a reflectance of a mirror and b transmittance of a cavity

where (4.31) was used. From (4.66), it is found that the cavity length L changes with the phase shift  $-\Delta\Omega$ , which varies a resonance (transmission) wavelength according to (4.12). For example, when the phase shift is  $\pi$ , (4.41) and (4.66) give

$$L = \Lambda = m \frac{\lambda_{\rm B}}{2n_{\rm r0}},\tag{4.67}$$

where m is a positive integer called the order of diffraction and  $n_{r0}$  is the averaged refractive index. From (4.67), it is found that the resonance wavelength for  $-\Delta\Omega = \pi$  is a product of Bragg wavelength and a positive integer. For the first-order grating (m=1), the resonance wavelength is Bragg wavelength.

Figure 4.20 shows the power reflectivity  $R_1$  of the *mirror* in Fig. 4.19 and the power transmissivity T of the *phase-shifted grating* (cavity) with  $-\Delta\Omega = \pi$  as a function of a wavelength. The power reflectivity  $R_1$  of the mirror depends on a wavelength  $\lambda$ , and only the selected wavelength region has high reflectivity. Therefore, only a resonance wavelength located in the high reflectivity region is selectively multireflected in the cavity. Also, because the cavity length L is of the order of a wavelength, the mode spacing (free spectral range) is so large that only one transmission peak exists within the stop band.

As described earlier, the phase-shifted grating can be qualitatively explained as the Fabry-Perot cavity. The only difference between the phase-shifted grating and the Fabry-Perot cavity is the dependence of the mirror reflectivities on a wavelength.

#### 4.3.5.3 Definition of the Phase Shift [6]

There are two definitions of the phase shift in the phase-shifted grating, as shown in Fig. 4.21. In Fig. 4.21a, Region 1 (z < 0) and Region 2 (z > 0) shift symmetrically with respect to z = 0, while in Fig. 4.21b, Region 1 does not move and Region 2 (z > 0) shifts at z = 0.

Using the definition in Fig. 4.21a, the refractive index  $n_r(z)$  in Region 1 is expressed as

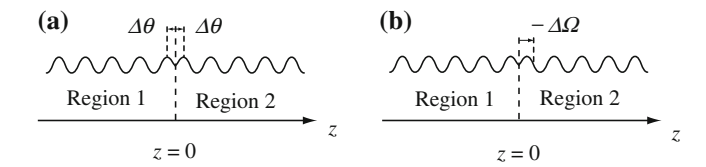


Fig. 4.21 Definition of the phase shift: a Two common phase shifts are introduced in both of Region 1 and Region 2, and b one phase shift is introduced in Region 2 only

$$n_{\rm r}(z) = n_{\rm r0} + n_{\rm r1}\cos(2\beta_0 z + \Delta\theta),$$
 (4.68)

whereas the refractive index in Region 2 is written as

$$n_{\rm r}(z) = n_{\rm r0} + n_{\rm r1}\cos(2\beta_0 z - \Delta\theta).$$
 (4.69)

When we use the definition in Fig. 4.21b, the refractive index in Region 2 is written as

$$n_{\rm r}(z) = n_{\rm r0} + n_{\rm r1}\cos(2\beta_0 z + \Delta\theta + \Delta\Omega),\tag{4.70}$$

where (4.68) was used. Because (4.69) and (4.70) represent the same refractive index, the two phase shifts  $\Delta\Omega$  and  $\Delta\theta$  are related as

$$\Delta\theta + \Delta\Omega = 2m\pi - \Delta\theta,\tag{4.71}$$

which reduces to

$$2\Delta\theta + \Delta\Omega = 2m\pi,\tag{4.72}$$

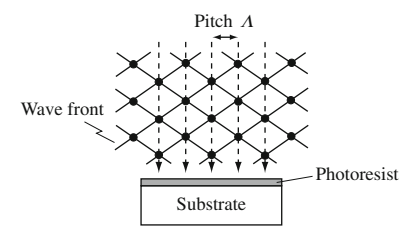
where m is an integer.

These two definitions of the phase shift are used in various journal papers or books. Therefore, we should be careful in discussing a value of the phase-shift.

## 4.3.6 Fabrication of Diffraction Gratings

In DFB-LDs and DBR-LDs, oscillation wavelengths are just or in the vicinity of Bragg wavelengths. The oscillation wavelength for the light sources of the optical fiber transmission systems is  $1.3 \,\mu m$  in which the *dispersion* of the optical fiber is the smallest, or  $1.55 \,\mu m$  where the *absorption loss* of the optical fiber is the lowest. Because the effective refractive index  $n_{r0}$  of the semiconductor lasers is nearly 3.2, pitches of the first-order grating  $\Lambda$  are approximately  $0.2 \,\mu m$  for a wavelength of  $1.3 \,\mu m$  and  $0.24 \,\mu m$  for  $1.55 \,\mu m$  from (4.41). Corrugation depth is about  $0.1 \,\mu m = 100 \,nm$  just after the grating fabrication and is reduced to several tens of nanometers after epitaxial growth of semiconductor layers on the diffraction grating.

**Fig. 4.22** Principle of holographic exposure



This reduction in the grating depth is caused by thermal decomposition of the grating surface during heating prior to the epitaxial growth.

To fabricate such fine diffraction gratings with high accuracy, *holographic exposure* [7–15], *electron-beam exposure* [16], and *X-ray exposure* [17] systems have been developed.

#### 4.3.6.1 Holographic Exposure

Holographic exposure systems use interference of two coherent laser beams to make *interference fringe patterns*. The obtained interference fringe patterns are transferred to the *photoresists* coated on the substrates via developing the photoresists. Finally, the substrates are etched with the patterned photoresists as the *etching masks*.

Figure 4.22 shows a principle of the holographic exposure, where solid lines show wave fronts of two lightwaves and closed circles indicate the points in which the light intensity is enhanced due to interference. As the wave fronts propagate toward the substrate, the closed circles propagate along the broken lines. Consequently, the photoresist regions indicated by arrows are exposed. The grating pitch  $\Lambda$  is determined by the spacing of the broken lines.

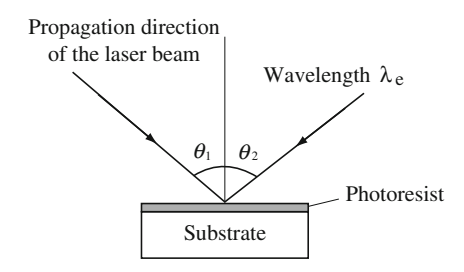
Figure 4.23 shows the angles of incidence  $\theta_1$  and  $\theta_2$ , which are formed by the normals of the substrate plane and the propagation directions of the two laser beams. The grating pitch  $\Lambda$  is given by

$$\Lambda = \frac{\lambda_{\rm e}}{\sin \theta_1 + \sin \theta_2},\tag{4.73}$$

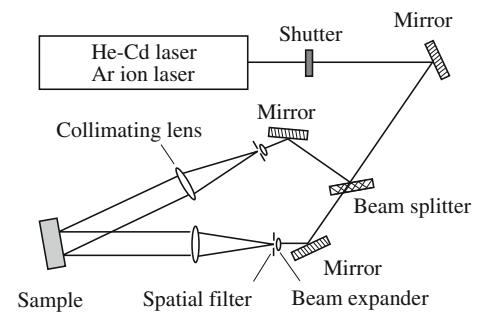
where  $\lambda_e$  is a wavelength of the incident laser beams.

Figure 4.24 shows an example of the holographic exposure systems. As the light sources, He-Cd lasers ( $\lambda_e=441.6\,\mathrm{nm}$ , 325 nm) or Ar ion lasers ( $\lambda_e=488\,\mathrm{nm}$ ) are widely used. A single laser beam emitted from the light source is divided into two laser beams by a beam splitter, and these two laser beams are expanded. These expanded beams are collimated and are finally incident on the photoresists coated on the substrates. To achieve fine patterns with high accuracy, we need high uniformity in the wave fronts; low fluctuations in the optical paths; high stability in the wavelength, the phase, and the light intensity of the laser beams; and precise control

**Fig. 4.23** Angle of incidence in holographic exposure



**Fig. 4.24** Holographic exposure system



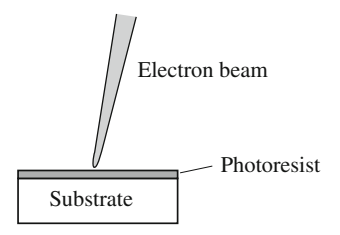


Fig. 4.25 Electron beam exposure

of the angle of incidence. For these purposes, the holographic exposure systems must be isolated from mechanical vibrations and air flow.

#### 4.3.6.2 Electron Beam Exposure

The electron beam exposure systems scan electron beams on the photoresist in a vacuum, as shown in Fig. 4.25. Scanning of the electron beams and transfer of the samples are controlled by computers, which results in flexible patterns. The problem is that exposure time is long. For example, it takes about 10 h to draw patterns of the diffraction grating on a 1 cm<sup>2</sup> substrate.

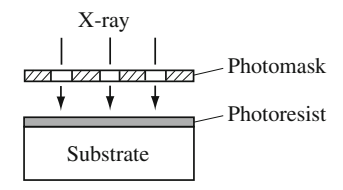
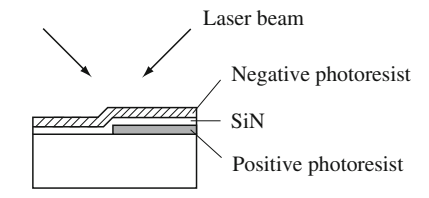


Fig. 4.26 X-ray exposure

**Fig. 4.27** Holographic exposure using positive and negative photoresists



#### 4.3.6.3 X-ray Exposure

Wavelengths of X-rays are short, which leads to small diffraction angles. Hence, X-rays are suitable to transfer fine patterns of a photomask to the photoresist, as shown in Fig. 4.26. To obtain sufficient X-ray intensity for exposure, *synchrotron radiation* is often used, which needs a huge plant. Also, highly reliable photomasks for the X-ray exposure systems have not yet been developed.

#### 4.3.6.4 Fabrication of Phase-Shifted Grating

The electron beam and X-ray exposure systems are suitable to fabricate various patterns. These systems, however, have problems on costs and productivity. As a result, the holographic exposure systems, which have high productivity with low cost, have attracted a lot of interest. As will be explained in Chap. 6, the most stable single-mode operations are obtained when the phase-shift is  $|\Delta\Omega|=\pi$ , which corresponds to a shift in the length  $\Lambda/2$  in the first-order grating. In other words, the top and bottom of the corrugations are reversed in the optical waveguide.

From the viewpoint of the *reverse* of the corrugations, *positive* and *negative* photoresists are simultaneously exposed. In a positive photoresist, exposed areas are removed by development, whereas in a negative photoresist, unexposed areas are removed. Therefore, by selectively forming the positive photoresist and the negative photoresist on the substrate, we can obtain a pattern and its reverse on the same plane. Figure 4.27 shows an example of this method, where SiN is used to prevent chemical reactions between the positive photoresist and the negative one [8].

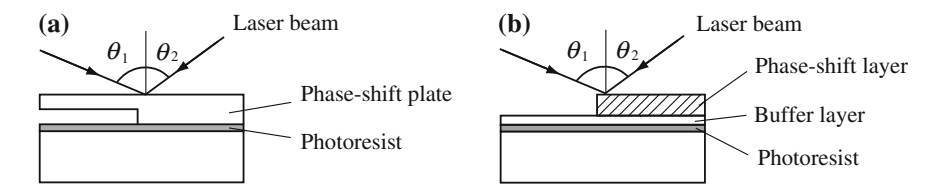


**Fig. 4.28** Holographic exposure shifting both wavefronts of the two incident laser beams by using **a** a phase-shift plate and **b** a phase-shift layer with a buffer layer

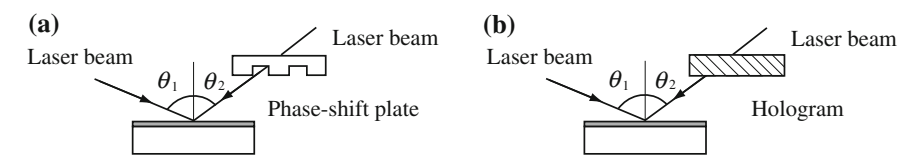


**Fig. 4.29** Holographic exposure shifting one of the wavefronts of the two incident laser beams by using **a** a phase-shift plate and **b** a hologram

From the viewpoint of the *shift in the pitch*, wave fronts of the laser beams are shifted, as shown in Figs. 4.28 and 4.29.

In Fig. 4.28, a material with a larger refractive index than air is selectively placed on the surface of the photoresist to shift both wave fronts of the two incident laser beams. The lights incident on this material are refracted by Snell's law, which leads to a change in the exposed positions. In Fig. 4.28a [10], the phase-shift plate is put on the photoresist. If there is a tiny air gap such as the order of  $1\,\mu m$  between the phase-shift plate and the photoresist, exposed patterns are heavily degraded due to multireflections of the laser beams. Hence, precise position control of the phase-shift plate and the photoresist is required. In Fig. 4.28b [11], in contrast, the phase-shift layer is coated on a buffer layer, which automatically results in no air gap between the phase-shift layer and the buffer layer.

In Fig. 4.29, an optical element such as a phase-shift plate or a hologram is inserted in the optical path for one laser beam to shift one of the wave fronts of the two incident laser beams. In Fig. 4.29a [12], the wave fronts are disturbed due to diffractions at steps in the phase-shift plate, which reduces the grating formed area. Figure 4.29b [13] uses a hologram to generate a required phase shift on the photoresist, and there are no distortions in the wave fronts. However, a highly reliable hologram has not yet been developed.

Figure 4.30 shows a replica method [14] where one laser beam is incident on a replica of a master phase-shifted grating. The fringe patterns, which are formed by interference of the transmitted light and the diffracted light from the replica, are transferred to a photoresist.

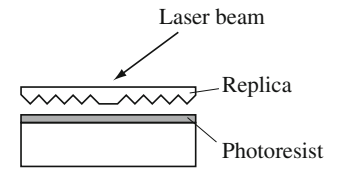


Fig. 4.30 Replica method

Because of reproducibility, productivity, a large tolerance in lithography conditions, and costs, the phase-shift method in Fig. 4.28b was first applied to manufacture phase-shifted gratings. Later, the replica method in Fig. 4.30 was also commercially used. Recently, electron beam exposure systems have been used in some factories.

#### References

- Kogelnik, H., Shank, C.V.: Coupled-wave theory of distributed feedback lasers. J. Appl. Phys. 43, 2327 (1972)
- 2. Yamada, M., Sakuda, K.: Analysis of almost-periodic distributed feedback slab waveguides via a fundamental matrix approach. Appl. Opt. 26, 3474 (1987)
- 3. Haus, H.A., Shank, C.V.: Antisymmetric taper of distributed feedback lasers. IEEE J. Quantum Electron. **QE-12**, 532 (1976)
- 4. Haus, H.A.: Waves and Fields in Optoelectronics. Prentice-Hall, Englewood Cliffs (1984)
- Numai, T.: A study on semiconductor wavelength tunable optical filters and lasers. Ph.D. thesis, Keio University, Yokohama (1992)
- Numai, T.: 1.5-μm wavelength tunable phase-shift-controlled distributed feedback laser. IEEE/OSA J. Lightwave Technol. 10, 199 (1992)
- 7. Utaka, K., Akiba, S., Sakai, K., et al.:  $\lambda/4$ -shifted InGaAsP/InP DFB lasers by simultaneous holographic exposure of positive and negative photoresists. Electron. Lett. **20**, 1008 (1984)
- Utaka, K., Akiba, S., Sakai, K., et al.: λ/4-shifted InGaAsP/InP DFB lasers. IEEE J. Quantum Electron. QE-22, 1042 (1986)
- 9. Okai, M., Tsuji, S., Hirao, M., et al.: New high resolution positive and negative photoresist method for  $\lambda/4$ -shifted DFB lasers. Electron. Lett. **23**, 370 (1987)
- Shirasaki, M., Soda, H., Yamakoshi, S., et al.: λ/4-shifted DFB-LD corrugation formed by a novel spatial phase modulating mask. Eur. Conf. Opt. Commun./Integr. Opt. Opt. Communi. 1, 25–28 (1985)
- Numai, T., Yamaguchi, M., Mito, I., et al.: A new grating fabrication method for phase-shifted DFB LDs. Jpn. J. Appl. Phys. Part 2 26, L1910 (1987)
- 12. Tsuji, S., Ohishi, A., Okai, M., et al.: Quarter lambda shift DFB lasers by phase image projection method. 10th International Semiconductor Laser Conference, p. 58 (1986)
- 13. Ono, Y., Takano, S., Mito, I., et al.: Phase-shifted diffraction-grating fabrication using holographic wavefront reconstruction. Electron. Lett. 23, 57 (1987)
- 14. Okai, M., Tsuji, S., Chinone, N., et al.: Novel method to fabricate corrugation for a  $\lambda/4$ -shifted distributed feedback laser using a grating photomask. Appl. Phys. Lett. **55**, 415 (1989)

References 87

15. Sugimoto, H., Abe, Y., Matsui, T., et al.: Novel fabrication method of quarter-wave-shifted gratings using ECR-CVD SiN<sub>x</sub> films. Electron. Lett. **23**, 1260 (1987)

- Sekartedjo, K., Eda, N., Furuya, K., et al.: 1.5-μm phase-shifted DFB lasers for single-mode operation. Electron. Lett. 20, 80 (1984)
- 17. Nishida, T., Nakao, M., Tamamura, T., et al.: Synchrotron radiation lithography for DFB laser gratings. Jpn. J. Appl. Phys. **28**, 2333 (1989)

## Chapter 5

## **Fundamentals of Semiconductor Lasers**

#### 5.1 Key Elements in Semiconductor Lasers

As shown in Fig. 5.1, a laser is composed of an active material, which has optical gain; and an optical resonator, which feeds back light by its reflectors. In *semi-conductor lasers*, the *active layers* generate spontaneous emission and amplify a fraction of the spontaneous emission by stimulated emission. As optical resonators, Fabry-Perot cavities, ring cavities, DFB cavities, and DBRs are used. In this chapter, we study the fundamental characteristics of semiconductor lasers using Fabry-Perot LDs, which are shown in Fig. 5.2. Dynamic single-mode lasers such as the DFB-LDs are discussed in Chap. 6.

In the following, we explain the *optical resonator*, the *pn-junction*, and the *double heterostructure* (DH), which are indispensable elements in semiconductor lasers.

## 5.1.1 Fabry-Perot Cavity

As explained in Chap. 4, the Fabry-Perot cavity comprises two parallel mirrors. In semiconductor lasers, cleaved facets such as  $\{011\}$  or  $\{0\overline{1}1\}$  surfaces are used as mirrors, as shown in Fig. 5.2. When a light is normally incident on a facet, the power reflectivity  $R_0$  is given by

$$R_0 = \left(\frac{n_{\rm rt} - 1}{n_{\rm rt} + 1}\right)^2,\tag{5.1}$$

where  $n_{\rm rt}$  and 1 are the refractive indexes of the semiconductors and the air, respectively.

When  $n_{\rm rt}$  is 3.5,  $R_0$  is about 31 %. It should be noted that the cleaved facets are flat of the order of atomic layers, and the surface is smoother than the wavelengths of lights. Therefore, cleaved facets function as mirrors with high accuracy. To control the reflectivities or to protect the facets, dielectric films are often coated on the cleaved facets.

© Springer Japan 2015

89

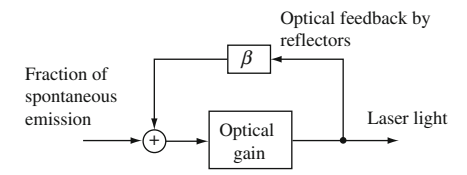


Fig. 5.1 Key elements in the lasers

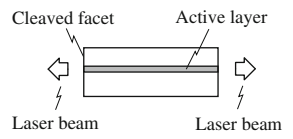


Fig. 5.2 Fabry-Perot LD

#### 5.1.2 pn-Junction

In semiconductor lasers, in order to inject the carriers into the active layers, the active layers are placed inside the pn-junctions. Therefore, the active layer is sandwiched by the *p-cladding layer* and the *n-cladding layer*, as shown in Fig. 5.3. Applying a *forward bias* voltage, which is positive on the p-side and negative on the n-side, across this pn-junction, the electrons are injected from the n-cladding layer to the active layer and the holes are injected from the p-cladding layer to the active layer as shown in Fig. 5.4. As explained in Chap. 2, when the population inversion is generated by the carrier injection, net stimulated emission is obtained.

Note that the impurities are often *undoped* in the active layers to achieve high radiation efficiency. However, in the active layers there are background carriers whose concentrations depend on epitaxial growth methods. Therefore, the active layers are not ideal *intrinsic* semiconductors.

If the impurities are doped in the active layers, the injected carriers combine with the impurities. Therefore, the *carrier lifetime* is reduced and the modulation speed is enhanced (see Sects. 5.11 and 5.12). However, the recombinations of the injected carriers and impurities do not contribute to laser transitions, which decreases the radiation efficiency. Thus, active layers are sometimes intentionally doped to achieve high-speed modulations so long as the radiation efficiency is not highly degraded.



Fig. 5.3 Cross section of a pn-junction in semiconductor lasers

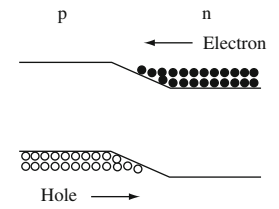


Fig. 5.4 Carrier injection in a pn-junction under a forward bias

#### 5.1.3 Double Heterostructure

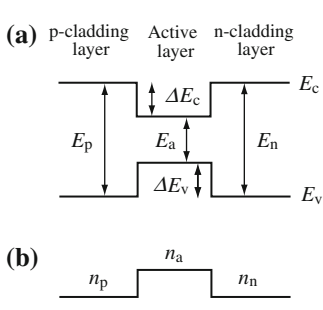
The *heterojunction* is a junction consisting of different materials in which materials with different compositions are also categorized. In contrast, the junction composed of common material is called the *homojunction*.

The bandgap energies in semiconductors depend on the constituent elements and compositions. As a result, the heterostructures have the *energy barriers* at the junction interfaces, and these energy barriers confine the carriers to the well layers. To achieve efficient recombination of the electrons and holes, these carriers have to be confined to the active layers. Therefore, the heterostructures are formed at both interfaces of the active layer. Such a structure is designated the *double heterostructure* because there are double heterojunctions.

Figure 5.5 shows the distributions of the energy and refractive index of the double heterostructure. At the junction interfaces, there are the band offsets  $\Delta E_{\rm c}$  for the conduction band and  $\Delta E_{\rm v}$  for the valence band, as shown in Fig. 5.5a. Under a forward bias, the holes are injected from the p-cladding layer to the active layer, and the electrons are injected from the n-cladding layer to the active layer. The energy barrier for the holes is  $\Delta E_{\rm v}$  at the interface of the n-cladding layer and the active layer; that for the electrons is  $\Delta E_{\rm c}$  at the interface of the p-cladding layer and the active layer. In many semiconductors, their refractive indexes increase with a decrease in bandgap energies. Hence, the refractive index of the active layer  $n_{\rm a}$  is usually greater than that of the p-cladding layer  $n_{\rm p}$  and that of the n-cladding layer  $n_{\rm n}$ . As a result, a light is efficiently confined to the active layer, which results in a high light amplification rate.

As described earlier, the double heterostructure confines both the carriers and the light to the active layer. Therefore, the double heterostructure is indispensable to achieve excellent characteristics in semiconductor lasers. It should be noted that the first continuous wave (CW) laser oscillation at room temperature was achieved by the double heterostructure [1, 2].

**Fig. 5.5** Double heterostructure: **a** Energy of electrons and **b** distribution of refractive index



#### 5.2 Threshold Gain

We explain the *threshold gain*, which is the optical gain required for laser oscillation. From (4.9), the transmitted light intensity  $I_t$  and the incident light intensity  $I_0$  are related as

$$\frac{I_{\rm t}}{I_0} = \frac{T_1 T_2 G_{\rm s0}}{(1 - G_{\rm s0} \sqrt{R_1 R_2})^2 + 4G_{\rm s0} \sqrt{R_1 R_2} \sin^2(n_{\rm r} k_0 L)},$$

$$G_{\rm s0} = \exp(2g_{\rm E} L) = \exp(gL),$$
(5.2)

where  $g_{\rm E}$  is the amplitude gain coefficient for the electric field and g is the optical power gain coefficient.

Oscillation is a state in which there is an output without an input from outside. As a result, the oscillation condition is given by  $I_0 = 0$  and  $I_t > 0$  in (5.2). Therefore, at the oscillation condition, the denominator in (5.2) is 0, and (5.2) goes to infinity. Hence, the oscillation condition for the Fabry-Perot LDs is expressed as

Resonance condition: 
$$\sin(n_1 k_0 L) = 0$$
,  
Gain condition:  $1 - G_{s0} \sqrt{R_1 R_2} = 0$ . (5.3)

#### 5.2.1 Resonance Condition

From (5.3), the resonance condition is written as

$$\frac{n_{\rm r}\omega L}{c} = n_{\rm r}k_0L = n\pi,\tag{5.4}$$

where *n* is a positive integer. Using a wavelength in a vacuum  $\lambda_0$ , (5.4) reduces to

$$L = n \frac{\lambda_0}{2n_{\rm r}},\tag{5.5}$$

5.2 Threshold Gain 93

which is the same as the resonance condition of the Fabry-Perot cavity explained in Chap. 4. Note that laser oscillation starts at the resonance wavelength nearest to the gain peak.

#### 5.2.2 Gain Condition

From (5.3), the *gain condition* is obtained as

$$1 - G_{s0}\sqrt{R_1R_2} = 1 - \sqrt{R_1R_2}\exp(gL) = 0.$$
 (5.6)

As a result, the optical power gain coefficient g is written as

$$g = \frac{1}{L} \ln \frac{1}{\sqrt{R_1 R_2}},\tag{5.7}$$

where the right-hand side is called the mirror loss.

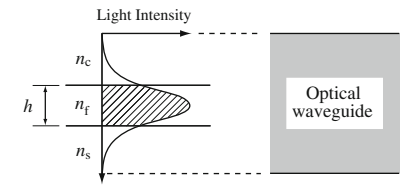
As described in Chap. 3, the guided modes propagate in the optical waveguides while confined to the guiding layer (active layer), and the fields of the guided modes penetrate into the p-cladding layer and the n-cladding layer, as shown in Fig. 5.6. Hence, the light sees optical losses in the p-cladding and n-cladding layers. Therefore, we have to consider the optical power gain coefficient g for the entire region where the lights exist.

Using the optical confinement factors, the optical power gain coefficient, and the optical power loss coefficients of the layers in the optical waveguide, we can approximately write the optical power gain coefficient g of the optical waveguide as

$$g = \Gamma_{a}g_{a} - \Gamma_{a}\alpha_{a} - \Gamma_{p}\alpha_{p} - \Gamma_{n}\alpha_{n}. \tag{5.8}$$

Here,  $\Gamma_a$ ,  $\Gamma_p$ , and  $\Gamma_n$  are the optical confinement factors of the active layer, the p-cladding layer, and the n-cladding layer, respectively;  $g_a$  is the optical power gain coefficient of the active layer; and  $\alpha_a$ ,  $\alpha_p$ , and  $\alpha_n$  are the optical power loss coefficients of the active layer, the p-cladding layer, and the n-cladding layer, respectively. It should be noted that the exact g value is obtained by solving eigenvalue equations, which include complex refractive indexes.

**Fig. 5.6** Distribution of light intensity in the optical waveguide



Introducing the internal loss as

$$\alpha_{i} = \Gamma_{a}\alpha_{a} + \Gamma_{p}\alpha_{p} + \Gamma_{n}\alpha_{n} \tag{5.9}$$

and substituting (5.9) into (5.8), we have

$$g = \Gamma_{\rm a} g_{\rm a} - \alpha_{\rm i},\tag{5.10}$$

where  $\Gamma_a g_a$  is the modal gain. Inserting (5.10) into (5.7) results in

$$\Gamma_{a}g_{a} = \alpha_{i} + \frac{1}{L} \ln \frac{1}{\sqrt{R_{1}R_{2}}} = \alpha_{i} + \frac{1}{2L} \ln \frac{1}{R_{1}R_{2}},$$
(5.11)

which is the threshold gain of the Fabry-Perot LDs. In this equation, the left-hand side is the threshold gain and the right-hand side is the total loss. Therefore, (5.11) indicates that laser oscillation takes place when optical gain is equal to total loss, which is the sum of the internal loss and mirror loss. In InGaAsP/InP LDs for lightwave communications,  $\Gamma_a g_a$  is 50–60 cm<sup>-1</sup> because of  $R_1 = R_2 = 32$  %, L = 250–300  $\mu$ m, and  $\alpha_i = 10$ –20 cm<sup>-1</sup>. When electric currents are injected into semiconductor lasers, laser oscillation starts at the threshold current  $I_{th}$ , which satisfies (5.11).

#### 5.3 Radiation Efficiency

Figure 5.7 schematically shows the current versus light output (I-L) characteristics of the semiconductor lasers. As shown in Fig. 5.7, when the injection current I exceeds the threshold current  $I_{th}$ , laser beams are emitted outward. To evaluate radiation efficiency of the semiconductor lasers, the *slope efficiency* and the *external differential quantum efficiency* are used.

## 5.3.1 Slope Efficiency

The slope efficiency  $S_{dj}$  (in units of mW/mA or W/A) per facet is defined as the ratio of the increase in light intensity  $\Delta P_j$  (j=1,2) to the increase in injection current  $\Delta I$ , which is given by

$$S_{\rm dj} = \frac{\Delta P_j}{\Delta I}.\tag{5.12}$$

The slope efficiency for the total light output is obtained as

$$S_{\text{d,tot}} = \frac{\Delta P_1 + \Delta P_2}{\Delta I} = \frac{\Delta P}{\Delta I},\tag{5.13}$$

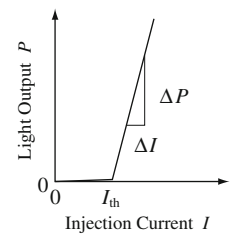


Fig. 5.7 Current versus light output characteristics

where  $\Delta P$  is an increase in the total light intensity.

#### 5.3.2 External Differential Quantum Efficiency

The external differential quantum efficiency  $\eta_d$  (in no units) is defined as the number of photons emitted outward per injected carrier. The external differential quantum efficiency  $\eta_d$  for the total light output is given by

$$\eta_{\rm d} = \frac{\Delta P}{\hbar \omega} / \left(\frac{\Delta I}{e}\right) = \frac{\Delta P}{\Delta I} \frac{e}{\hbar \omega} = S_{\rm d,tot} \frac{e}{\hbar \omega} ,$$
(5.14)

where  $\omega$  is an angular frequency of the light,  $\hbar$  is Dirac's constant, and e is the elementary charge.

As shown in (5.11), the total loss is a sum of the internal loss and mirror loss. For a reference system placed outside the optical cavity, the mirror loss indicates the light emission rate from the optical cavity. As a result, using the *internal quantum efficiency*  $\eta_i$ , which is defined as the number of photons emitted inside the optical cavity per injected carrier, the external differential quantum efficiency  $\eta_d$  is expressed as

$$\eta_{\rm d} = \eta_{\rm i} \, \frac{(\text{Mirror Loss})}{(\text{Total Loss})} = \eta_{\rm i} \, \frac{\frac{1}{2L} \, \ln \frac{1}{R_1 R_2}}{\alpha_{\rm i} + \frac{1}{2L} \, \ln \frac{1}{R_1 R_2}} = \eta_{\rm i} \, \frac{\ln \frac{1}{R_1 R_2}}{2\alpha_{\rm i} L + \ln \frac{1}{R_1 R_2}}, \quad (5.15)$$

where the optical losses at the facets due to absorption or scattering were assumed to be negligible. For  $\eta_i=100$  %, L=300  $\mu m$ ,  $R_1=R_2=32$  %, and  $\alpha_i=20$  cm<sup>-1</sup>, we have  $\eta_d=66$  %.

#### 5.3.3 Light Output Ratio from Facets

We consider the light outputs  $P_1$  and  $P_2$  from the two facets. As shown in Fig. 5.8, we assume that the light intensities in the vicinity of the facets inside the optical cavity are  $P_a$ ,  $P_b$ ,  $P_c$ , and  $P_d$ ; the power reflectivities of the facets are  $R_1$  and  $R_2$ ; and the power transmissivities of the facets are  $T_1$  and  $T_2$ . Here, the arrows indicate the propagation directions of the lights. Among the light intensities in a steady state, we have a relationship such as

$$P_{\rm a} = R_1 P_{\rm d}, P_{\rm b} = {\rm e}^{gL} P_{\rm a}, P_{\rm c} = R_2 P_{\rm b}, P_{\rm d} = {\rm e}^{gL} P_{\rm c},$$
  
 $P_1 = T_1 P_{\rm d}, P_2 = T_2 P_{\rm b},$  (5.16)

where g is the optical power gain coefficient and L is the cavity length. Deleting  $P_k$  (k = a, b, c, d) from (5.16), we have

$$\frac{P_1}{P_2} = \frac{T_1 \sqrt{R_2}}{T_2 \sqrt{R_1}}. (5.17)$$

Substituting  $P = P_1 + P_2$  into (5.16) leads to

$$P_1 = \frac{T_1\sqrt{R_2}}{T_1\sqrt{R_2} + T_2\sqrt{R_1}} P, \ P_2 = \frac{T_2\sqrt{R_1}}{T_1\sqrt{R_2} + T_2\sqrt{R_1}} P.$$
 (5.18)

Hence, the external differential quantum efficiencies for each light output  $\eta_{d1}$  and  $\eta_{d2}$  are written as

$$\eta_{d1} = \frac{T_1 \sqrt{R_2}}{T_1 \sqrt{R_2} + T_2 \sqrt{R_1}} \eta_d, \quad \eta_{d2} = \frac{T_2 \sqrt{R_1}}{T_1 \sqrt{R_2} + T_2 \sqrt{R_1}} \eta_d, \quad (5.19)$$

where  $\eta_d$  is the external differential quantum efficiency for the total light output. When the optical losses at the facets are negligibly small, we have  $T_1 = 1 - R_1$  and  $T_2 = 1 - R_2$ .

Fig. 5.8 Light intensities inside and outside the Fabry-Perot cavity

#### 5.4 Current Versus Light Output (*I–L*) Characteristics

We study the current versus light output (I-L) characteristics above and below the threshold. With an increase in the injection current into semiconductor lasers, the carrier concentration in the active layer is enhanced. When the carrier concentration exceeds the threshold carrier concentration, laser oscillation starts and the light output drastically increases compared to below the threshold. This change in light output is considered to be a change in the photon density. Therefore, we analyze I-L characteristics by introducing the *rate equations* on the *carrier concentration* and the *photon density* in the active layer. Dependence of I-L on temperature is also briefly described.

#### 5.4.1 Rate Equations

The electron concentration n is defined as  $n = N/V_a$ ; the photon density S is defined as  $S = N_{\rm ph}/V_a$  where N is the number of the electrons in the active layer,  $N_{\rm ph}$  is the number of the photons, and  $V_a$  is the volume of the active layer. If we assume that the electron concentration n is equal to the hole concentration p, we can write the rate equations for the carrier concentration n and the photon density S of the laser light as

$$\frac{\mathrm{d}n}{\mathrm{d}t} = \frac{J}{ed} - G(n)S - \frac{n}{\tau_n},\tag{5.20}$$

$$\frac{\mathrm{d}S}{\mathrm{d}t} = G(n)S - \frac{S}{\tau_{\mathrm{ph}}} + \beta_{\mathrm{sp}} \frac{n}{\tau_{\mathrm{r}}}.$$
 (5.21)

Here, J is the injection current density, which is an electric current flowing through a unit area in the active layer; e is the elementary charge; d is the active layer thickness; G(n) is the amplification rate due to the stimulated emission;  $\tau_n$  is the *carrier lifetime*;  $\tau_{\text{ph}}$  is the *photon lifetime*;  $\beta_{\text{sp}}$  is the *spontaneous emission coupling factor*; and  $\tau_{\text{r}}$  is the *radiative recombination lifetime* due to spontaneous emission.

In (5.20), J/(ed) is an increased rate of the carrier concentration in the active layer; -G(n)S shows a consumption rate of the carrier concentration due to the stimulated emission and is proportional to the photon density S; and  $-n/\tau_n$  expresses a decay rate of the carrier concentration in the carrier lifetime  $\tau_n$ .

In (5.21), G(n)S shows an increased rate of photon density S due to stimulated emission;  $-S/\tau_{\rm ph}$  is a decreased rate of photon density inside the optical cavity due to absorption and light emission toward the outside of the optical cavity; and  $\beta_{\rm sp} \, n/\tau_{\rm r}$  represents a coupling rate of spontaneously emitted photons to the lasing mode, which is a resonance mode of the cavity.

Here, we explain G(n),  $\tau_n$ ,  $\tau_{ph}$ , and  $\beta_{sp}$  in detail. With the transparent carrier concentration  $n_0$ , in which a material is transparent, we can approximately write

$$G(n)$$
 as

$$G(n) = \Gamma_a g_0(n - n_0), \tag{5.22}$$

where  $g_0$  is the differential gain coefficient and  $\Gamma_a$  is the optical confinement factor of the active layer.

Using the radiative recombination lifetime  $\tau_r$  and the nonradiative recombination lifetime  $\tau_{nr}$ , we can express the carrier lifetime  $\tau_n$  as

$$\frac{1}{\tau_n} = \frac{1}{\tau_r} + \frac{1}{\tau_{nr}}. (5.23)$$

The radiative recombination lifetime  $\tau_r$  is determined by the spontaneous emission and is not affected by the stimulated emission. The nonradiative recombination lifetime  $\tau_{nr}$  is related to the recombinations of the injected carriers and the defects or impurities that do not emit lights.

The *photon lifetime*  $\tau_{ph}$  is the time during which the photons stay in the optical cavity; it is expressed as

$$\frac{1}{\tau_{\rm ph}} = \frac{c}{n_{\rm r}} \left( \alpha_{\rm i} + \frac{1}{2L} \ln \frac{1}{R_1 R_2} \right),$$
 (5.24)

where  $n_r$  is the effective refractive index and c is the speed of light in a vacuum. Here, let us derive (5.24). If we put

$$\alpha_{\rm t} = \alpha_{\rm i} + \frac{1}{2L} \ln \frac{1}{R_1 R_2},$$
(5.25)

we can write a differential equation for the photon density S with respect to a position z as

$$\frac{\mathrm{d}S}{\mathrm{d}z} = -\alpha_{\mathrm{t}} S,\tag{5.26}$$

where the light is assumed to propagate toward a positive z-axis. As a result, a derivative of the photon density S with respect to a time t is given by

$$\frac{\mathrm{d}S}{\mathrm{d}t} = \frac{\mathrm{d}z}{\mathrm{d}t} \frac{\mathrm{d}S}{\mathrm{d}z} = \frac{c}{n_{\mathrm{r}}} \frac{\mathrm{d}S}{\mathrm{d}z} = -\frac{c}{n_{\mathrm{r}}} \alpha_{\mathrm{t}} S \equiv -\frac{S}{\tau_{\mathrm{ph}}}.$$
 (5.27)

From (5.25) to (5.27), the photon lifetime  $\tau_{ph}$  in (5.24) is obtained. The *spontaneous emission coupling factor*  $\beta_{sp}$  is defined as

$$\beta_{\rm sp} = \frac{\text{(spontaneous emission coupling rate to the lasing mode)}}{\text{(total spontaneous emission rate)}}.$$
 (5.28)

When the spontaneous emission spectrum is assumed to be *Lorentzian* with the center angular frequency  $\omega_0$  and the FWHM  $\Delta\omega$ , the spontaneous emission coupling rate

to the lasing mode per unit time and unit volume  $r_{\rm sp}$  is given by

$$r_{\rm sp} = r_{\rm sp0} \frac{(\Delta \omega/2)^2}{(\omega - \omega_0)^2 + (\Delta \omega/2)^2},$$
 (5.29)

where  $r_{\rm sp0}$  is a coefficient.

To calculate the total spontaneous emission rate, we consider the number of modes  $dN_m$  with two polarizations that exist in a mode volume  $V_m$ ; a solid angle for propagation direction  $d\Omega$ ; and an angular frequency range  $d\omega$ . When the distribution of the modes is continuous, as in a free space,  $dN_m$  is given by

$$dN_{\rm m} = V_{\rm m} m(\omega) d\omega \frac{d\Omega}{4\pi} = V_{\rm m} \frac{n_{\rm r}^3 \omega^2}{\pi^2 c^3} d\omega \frac{d\Omega}{4\pi}, \qquad (5.30)$$

where (2.26) was used. From (5.29) to (5.30), the total spontaneous emission rate  $R_{\rm sp}$  is obtained as

$$R_{\rm sp} = \int r_{\rm sp} \, \mathrm{d}N_{\rm m} = r_{\rm sp0} \, \frac{V_{\rm m}}{2\pi} \left(\frac{n_{\rm r}}{c}\right)^3 \omega_0^2 \, \Delta\omega. \tag{5.31}$$

Using (5.28), (5.29), and (5.31), we can express the spontaneous emission coupling factor  $\beta_{sp}$  for the angular frequency  $\omega_0$  (a wavelength in a vacuum  $\lambda_0$ ) as

$$\beta_{\rm sp} = \frac{r_{\rm sp}}{R_{\rm sp}} = \frac{2\pi}{V_{\rm m}} \left(\frac{c}{n_{\rm r}}\right)^3 \frac{1}{\omega_0^2 \Delta \omega} = \frac{1}{4\pi^2 n_{\rm r}^3 V_{\rm m}} \frac{\lambda_0^4}{\Delta \lambda} = \frac{\Gamma_{\rm a}}{4\pi^2 n_{\rm r}^3 V_{\rm a}} \frac{\lambda_0^4}{\Delta \lambda}, \quad (5.32)$$

where  $\Gamma_{\rm a}=V_{\rm a}/V_{\rm m}$  is the optical confinement factor of the active layer and  $\Delta\lambda$  is the FWHM in units of wavelength. From (5.32), it is found that the spontaneous emission coupling factor  $\beta_{\rm sp}$  increases with a decrease in the mode volume  $V_{\rm m}$  and the spectral linewidth  $\Delta\lambda$ .

# 5.4.2 Threshold Current Density

Let us calculate the *threshold current density J\_{th}* using the rate equations.

First, we consider the rate equations below the threshold, where net stimulated emission is negligible and S = 0. Therefore, (5.20) reduces to

$$\frac{\mathrm{d}n}{\mathrm{d}t} = \frac{J}{ed} - \frac{n}{\tau_n}.\tag{5.33}$$

In a steady state (d/dt = 0), from (5.33), the carrier concentration n is given by

$$n = \frac{J}{ed} \tau_n. \tag{5.34}$$

When the carrier concentration n increases from 0 to the *threshold carrier concentration*  $n_{th}$ , we expect that (5.34) is still satisfied at the threshold. As a result, the threshold current density  $J_{th}$  is expressed as

$$J_{\rm th} = \frac{ed}{\tau_n} n_{\rm th}. \tag{5.35}$$

From (5.35), it is found that a small  $n_{\rm th}$  and a long  $\tau_n$  lead to a low  $J_{\rm th}$ . Because the optical confinement factor  $\Gamma_{\rm a}$  of the active layer depends on the active layer thickness d, the threshold current density  $n_{\rm th}$  is a function of d and there exists an optimum d value to achieve the lowest  $J_{\rm th}$ .

Secondly, we calculate the threshold carrier concentration  $n_{\rm th}$  using the rate equations above the threshold. In usual semiconductor lasers, the spontaneous emission coupling factor  $\beta_{\rm sp}$  is of the order of  $10^{-5}$ . Therefore, as the first approximation, we neglect the term  $\beta_{\rm SD} n / \tau_{\rm r}$ .

Because (5.21) is valid for any S value in a steady state, we have

$$G(n) = \Gamma_{\rm a} g_0(n - n_0) = \frac{1}{\tau_{\rm ph}},$$
 (5.36)

where (5.22) was used. Substituting (5.11) and (5.24) into (5.36), we also obtain

$$G(n) = \frac{c}{n_{\rm r}} \Gamma_{\rm a} g_{\rm a}. \tag{5.37}$$

From (5.36), the carrier concentration n in a steady state is given by

$$n = \frac{1}{\Gamma_a g_0 \tau_{\rm ph}} + n_0. \tag{5.38}$$

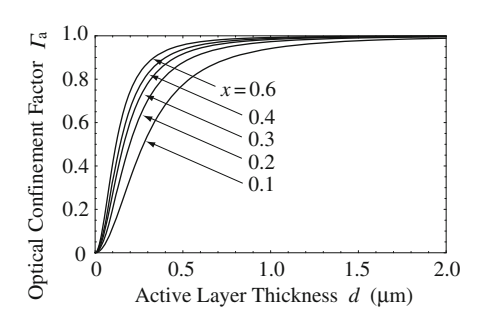
Because (5.38) is satisfied even at the threshold, the threshold carrier concentration  $n_{\text{th}}$  is written as

$$n_{\rm th} = \frac{1}{\Gamma_{\rm a} g_0 \tau_{\rm ph}} + n_0. \tag{5.39}$$

In semiconductor lasers, changes in the cavity length, facet reflectivities, and refractive indexes during laser operation are small, and the right-hand sides of (5.38) and (5.39) are considered to be constant. Therefore, above the threshold, the carrier concentration n is clamped on the threshold carrier concentration  $n_{\text{th}}$ . Hence, G(n) is constant above the threshold, as far as the gain saturation and coupling of spontaneous emission to the lasing mode are neglected.

Substituting (5.39) into (5.35), we have

**Fig. 5.9** Optical confinement factor



$$J_{\text{th}} = \frac{ed}{\tau_n} n_{\text{th}} = \frac{ed}{\tau_n} \left( \frac{1}{\Gamma_a g_0 \tau_{\text{ph}}} + n_0 \right),$$

$$A = \frac{ed}{\tau_n} n_0, \quad B = \frac{ed}{\tau_n} \frac{1}{\Gamma_a g_0 \tau_{\text{ph}}},$$
(5.40)

where it is clearly shown that the threshold current density  $J_{\rm th}$  depends on the optical confinement factor  $\Gamma_{\rm a}$ . Figure 5.9 shows calculated results of  $\Gamma_{\rm a}$  for  ${\rm Al}_x{\rm Ga}_{1-x}{\rm As}/{\rm Ga}{\rm As}$  double heterostructures. As shown in Fig. 5.9, with an increase in the active layer thickness d,  $\Gamma_{\rm a}$  is enhanced. Note that  $\Gamma_{\rm a}$  is proportional to  $d^2$  when d is small.

Figure 5.10 shows the threshold current density  $J_{th}$  as a function of the active layer thickness d. It is found that  $J_{th}$  takes a minimum value when d is approximately 0.1  $\mu$ m. In Fig. 5.10, A is a current density, which is required to obtain the population inversion and is proportional to the active layer thickness d as in (5.40). On the other hand, B is a current density, in which the optical gain balances the loss in the optical cavity. For a thin active layer, B is inversely proportional to d, because  $\Gamma_a$  is proportional to  $d^2$ . Because  $J_{th}$  is given by A + B, there exists an optimum d value to obtain a minimum  $J_{th}$ .

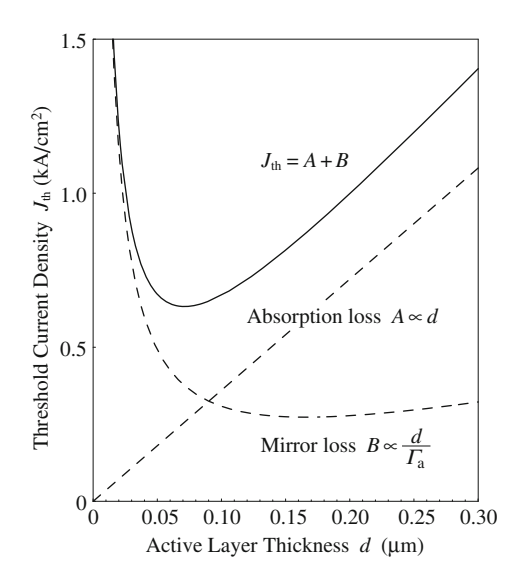
# 5.4.3 Current Versus Light Output (I-L) Characteristics in CW Operation

## 5.4.3.1 Without Coupling of Spontaneous Emission to the Lasing Mode

Let us examine changes in the carrier concentration n and photon density S with the injection current density J. When the spontaneous emission coupling factor  $\beta_{sp}$  is small, coupling of spontaneous emission to the lasing mode can be neglected.

Below the threshold, with an increase in J, the carrier concentration n increases according to (5.34), but the photon density S is 0. Above the threshold, n does not increase any more and remains at the threshold carrier concentration  $n_{\rm th}$ , while S drastically increases with J, because the excess carriers  $(n-n_{\rm th})$  are converted to photons.

Fig. 5.10 Dependence of the threshold current density  $J_{\text{th}}$  on the active layer thickness d



From (5.20), the steady-state photon density S above the threshold is obtained as

$$S = \frac{1}{G(n)} \left( \frac{J}{ed} - \frac{n_{\text{th}}}{\tau_n} \right). \tag{5.41}$$

Substituting (5.35) and (5.36) into (5.41) results in

$$S = \frac{\tau_{\rm ph}}{ed}(J - J_{\rm th}). \tag{5.42}$$

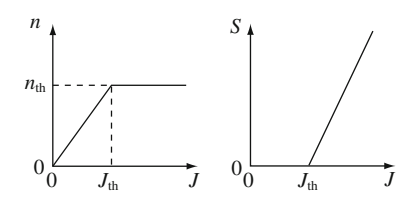
In summary, dependence of the carrier concentration n and photon density S on the injection current density J is expressed as

in 
$$J < J_{\text{th}}$$
: 
$$n = \frac{J}{ed} \tau_n, \quad S = 0; \tag{5.43}$$

in 
$$J \ge J_{\text{th}}$$
: 
$$n = \frac{J_{\text{th}}}{ed} \tau_n, \ S = \frac{\tau_{\text{ph}}}{ed} (J - J_{\text{th}}). \tag{5.44}$$

Figure 5.11 illustrates the calculated results of (5.43) and (5.44). It is clearly shown that the carrier concentration n is clamped on  $n_{\rm th}$  above the threshold current density  $J_{\rm th}$ .

**Fig. 5.11** Carrier concentration *n* and photon density *S* when coupling of the spontaneous emission to the lasing mode is neglected



## 5.4.3.2 With Coupling of Spontaneous Emission to the Lasing Mode

For brevity, we assume that nonradiative recombination is negligible, which leads to  $\tau_r \approx \tau_n$ . In a steady state, when the coupling of spontaneous emission to lasing mode is included, (5.20) and (5.21) reduce to

$$\frac{J}{ed} = \Gamma_{a} g_{0}(n - n_{0}) S + \frac{n}{\tau_{n}}, \tag{5.45}$$

$$\frac{S}{\tau_{\rm ph}} = \Gamma_{\rm a} g_0(n - n_0) S + \beta_{\rm sp} \frac{n}{\tau_n},\tag{5.46}$$

where (5.22) was used. Therefore, the carrier concentration n and photon density S are given by

$$n = \frac{n_{\rm th}}{2(1 - \beta_{\rm sp})} \left( X - \sqrt{X^2 - Y} \right),\tag{5.47}$$

$$S = \frac{\beta_{\rm sp}}{\Gamma_{\rm a} g_0 \tau_n} \frac{X - \sqrt{X^2 - Y}}{2(1 - \beta_{\rm sp}) - \left(X - \sqrt{X^2 - Y}\right)},\tag{5.48}$$

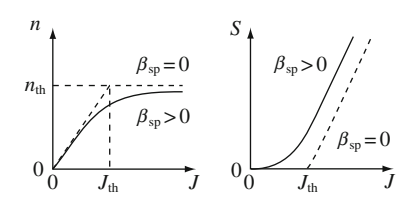
where

$$X = 1 + \frac{J}{J_{\text{th}}} - \beta_{\text{sp}} \frac{n_0}{n_{\text{th}}},\tag{5.49}$$

$$Y = 4(1 - \beta_{\rm sp}) \, \frac{J}{J_{\rm th}}.\tag{5.50}$$

Figure 5.12 shows the calculated results of (5.47) and (5.48), where solid and broken lines correspond to  $\beta_{\rm sp} > 0$  and  $\beta_{\rm sp} = 0$ , respectively. Coupling of the spontaneous emission to the lasing mode lowers n and enhances S, which results in a vague threshold. When  $\beta_{\rm sp} < 1$ , however, the emitted lights below the threshold are incoherent spontaneous emissions or amplified spontaneous emissions.

Fig. 5.12 Carrier concentration n and photon density S when coupling of spontaneous emission to the lasing mode is included



## 5.4.4 Dependence of I-L on Temperature

Generally, with a rise in temperature, the threshold current density  $J_{th}$  increases and external differential quantum efficiency  $\eta_d$  decreases, as shown in Fig. 5.13. Here, the horizontal line and the vertical line show the injection current and light output, respectively.

Dependence of the threshold current density  $J_{\rm th}$  on a temperature is empirically expressed as

$$J_{\rm th} = J_{\rm th0} \exp\left(\frac{T_{\rm j}}{T_0}\right),\tag{5.51}$$

where  $J_{\text{th0}}$  is a coefficient,  $T_{\text{j}}$  is the temperature in the active layer or the junction temperature, and  $T_{0}$  is the *characteristic temperature*, which indicates dependence of the threshold current density on the temperature.

A large characteristic temperature  $T_0$  seems to result in a small  $\mathrm{d}J_{\mathrm{th}}/\mathrm{d}T_{\mathrm{j}}$ , which indicates a good semiconductor laser. However, we must be careful about evaluating the temperature characteristics of semiconductor lasers by  $T_0$ , because a larger  $J_{\mathrm{th}}$  leads to a greater  $T_0$  when  $\mathrm{d}J_{\mathrm{th}}/\mathrm{d}T_{\mathrm{j}}$  is constant. Therefore, only when semiconductor lasers with a common  $J_{\mathrm{th}}$  at the same temperature are compared can  $T_0$  be an appropriate index.

**Fig. 5.13** Dependence of I-L on temperature

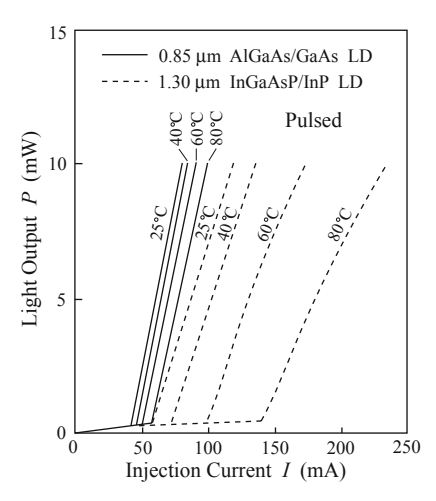


**Fig. 5.14** Characteristic temperature  $T_0$ 

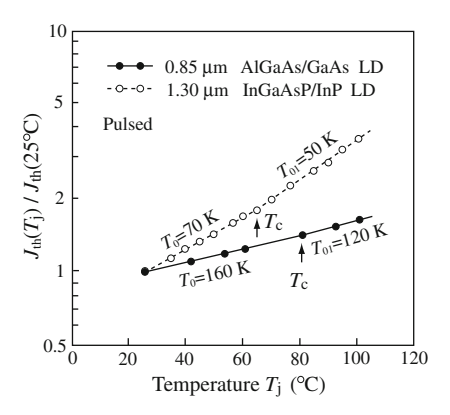


Figure 5.14 shows examples of the characteristic temperature  $T_0$  for an AlGaAs/GaAs LD and an InGaAsP/InP LD in pulsed operations. In an AlGaAs/GaAs LD with an oscillation wavelength of 0.85  $\mu$ m,  $T_0$  is approximately 160 K from 25 to 80 °C. It is considered that an increase in  $J_{th}$  with an increment in  $T_j$  is caused by broadening the gain spectrum and *overflow* of the carriers over the heterobarriers. To reduce the overflow of the carriers over the heterobarriers, we must increase the band offset  $\Delta E_g$  between the active and cladding layers. In general, the band offset  $\Delta E_g$  should be larger than 0.3 eV to suppress a drastic increase in  $J_{th}$  with a rise in  $T_j$ .

The external quantum efficiency  $\eta_d$  decreases with an increase in  $J_{th}$ , because the threshold carrier concentration  $n_{th}$  increases with  $J_{th}$ , which enhances the *free carrier absorption* (see Appendix F).

In an InGaAsP/InPLD with oscillation wavelength of 1.3  $\mu$ m,  $T_0$  is approximately 70 K from 25 to 65 °C. This  $T_0$  is lower than that of an AlGaAs/GaAs LD because of efficient overflow of the carriers due to the light effective mass of the electrons and nonradiative recombinations due to the *Auger processes* and the *valence band absorptions*.

The effective masses of the electrons are  $0.070 \, m$  for AlGaAs with a bandgap wavelength of  $0.85 \, \mu m$ , and  $0.059 \, m$  for InGaAsP with a bandgap wavelength of  $1.3 \, \mu m$ , where m is the electron mass in a vacuum.

The Auger processes are schematically shown in Fig. 5.15 where C, H, L, and S indicate the conduction band, heavy hole band, light hole band, and split-off band, respectively. In the Auger processes, there are two processes, CHSH and CHCC. In the CHSH process, the emitted energy due to a recombination of electron 1 in the conduction band (C) and hole 2 in the heavy hole band (H) excites electron 3 in the split-off band (S) to the heavy hole band (H). In the CHCC process, the energy emitted due to recombination of electron 1 in the conduction band (C) and hole 2 in the heavy hole band (H) pumps electron 3 in the conduction band (C) to a higher energy state 4 in the conduction band. These processes are three-body collision processes, and a recombination rate  $R_A$  for the Auger processes is given by

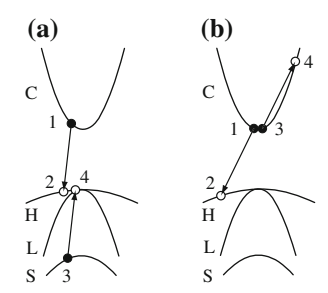


Fig. 5.15 Auger processes: a CHSH and b CHCC

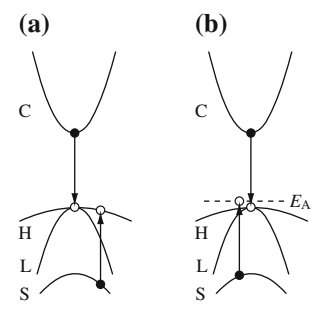


Fig. 5.16 Valence band absorption: electron excited to a heavy hole band and b the acceptor level

$$R_{\rm A} = C_{\rm p} n p^2 + C_{\rm n} n^2 p, (5.52)$$

where  $C_p$  and  $C_n$  are the Auger coefficients for the CHSH and CHCC processes, respectively.

In valence band absorptions, an electron in the split-off band absorbs a light generated by recombination of an electron in the conduction band and a hole in the heavy hole band. These absorption processes are shown in Fig. 5.16, where an electron is excited to the heavy hole band and the acceptor level.

With an increase in temperature, the internal quantum efficiency  $\eta_i$  decreases due to the Auger processes and the external quantum efficiency  $\eta_d$  is lowered due to the valence band absorptions and the free carrier absorption. Therefore, light emission efficiency is reduced with an increase in temperature.

# 5.5 Current Versus Voltage (I-V) Characteristics

In a steady state, (5.20) and (5.21) reduce to

$$S = -\beta_{\rm S} \frac{n}{\tau_{\rm r}} \frac{1}{G(n) - \tau_{\rm ph}^{-1}},\tag{5.53}$$

$$I = eV_{\mathcal{A}}\left[G(n)S + \frac{n}{\tau_n}\right]. \tag{5.54}$$

Here, I is the injection current and  $V_A = S_A d$  is the volume of the active layer in which  $S_A$  is the area of the active layer and d is the active layer thickness.

A flowing current in semiconductor lasers consists of the diffusion current, drift current, and recombination current. Here, it is assumed that the radiative recombination is dominant, and the diffusion and drift currents are neglected, as shown in (5.54).

The carrier concentration n is approximately given by

$$n = n_{\rm i} \exp\left(\frac{eV}{2k_{\rm B}T}\right),\tag{5.55}$$

where V is a voltage across the pn-junction and  $n_i$  is the intrinsic carrier concentration, which is expressed as

$$n_{\rm i} = 2\left(\frac{2\pi k_{\rm B}T}{h^2}\right)^{3/2} (m_{\rm e}m_{\rm h})^{3/4} \exp\left(-\frac{E_{\rm g}}{2k_{\rm B}T}\right).$$
 (5.56)

Here,  $k_{\rm B}$  is Boltzmann's constant, T is an absolute temperature, h is Planck's constant,  $m_{\rm e}$  and  $m_{\rm h}$  are the effective masses of the electron and the hole, respectively, and  $E_{\rm g}$  is the bandgap energy of the active layer.

From (5.53)–(5.55), a relation between the injection current I and the voltage V is given by

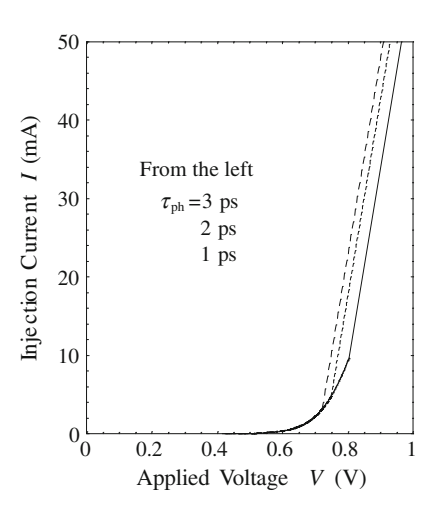
$$I = eV_{A} \left[ -\beta_{S} \frac{n_{i} e^{eV/2k_{B}T}}{\tau_{r}} \frac{G(n_{i} e^{eV/2k_{B}T})}{G(n_{i} e^{eV/2k_{B}T}) - \tau_{ph}^{-1}} + \frac{n_{i} e^{eV/2k_{B}T}}{\tau_{n}} \right], \quad (5.57)$$

which is illustrated in Fig. 5.17. In this figure, solid, dotted, and broken lines correspond to the photon lifetimes  $\tau_{\rm ph}=1$  ps, 2 ps, and 3 ps, respectively. Here, a sum of a contact resistance and a bulk resistance is assumed to be 4  $\Omega$ , which is typical in conventional semiconductor lasers. Other physical parameters that are used in this calculation are  $\beta_{\rm s}=10^{-5}$ ,  $n_{\rm i}=2.7\times10^{11}$  cm<sup>-3</sup>,  $\tau_{\rm r}=\tau_n=1$  ns, T=293.15 K (20 °C),  $(\partial G/\partial n)_{n=n_{\rm th}}=2.5\times10^{-6}$  cm<sup>3</sup>/s, and  $V_{\rm A}=40\,\mu{\rm m}^3=4\times10^{-11}$  cm<sup>3</sup>. It is also supposed that the transparent carrier concentration is  $n_0=0.6\,n_{\rm th}$ , the effective refractive index is 3.5, and the group velocity  $v_{\rm g}$  is 8.57  $\times$  10<sup>9</sup> cm/s.

## **5.6 Derivative Characteristics**

We can use *derivative measurements* to precisely detect the threshold current. In the following, relationships among the threshold current, the *derivative light output*, and the *derivative electrical resistance* are explained.

Fig. 5.17 Current versus voltage (I-V) characteristics



## 5.6.1 Derivative Light Output

Using photon density S in the active layer, we can write the internal light intensity P as

$$P = h \nu v_{\rm g} S_{\rm B} S, \tag{5.58}$$

where h is Planck's constant,  $\nu$  is an oscillation frequency,  $\nu_{\rm g}$  is a group velocity of the photons, and  $S_{\rm B}$  is beam area. From (5.58), the derivative light output with respect to the injection current  ${\rm d}P/{\rm d}I$  is written as

$$\frac{\mathrm{d}P}{\mathrm{d}I} = h\nu v_{\mathrm{g}} S_{\mathrm{B}} \frac{\mathrm{d}S}{\mathrm{d}I} = h\nu v_{\mathrm{g}} S_{\mathrm{B}} \frac{\partial S}{\partial n} \frac{\partial n}{\partial I}.$$
 (5.59)

Figure 5.18 shows calculated light output and derivative light output as a function of the injection current where (5.53), (5.54), (5.58), and (5.59) were used. The used

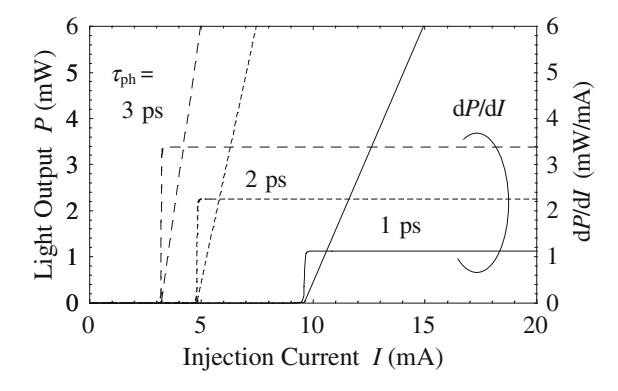


Fig. 5.18 Current versus light output and derivative light output

parameters are the same as in Fig. 5.17. A sharp rise in dP/dI clearly indicates the threshold current.

## 5.6.2 Derivative Electrical Resistance

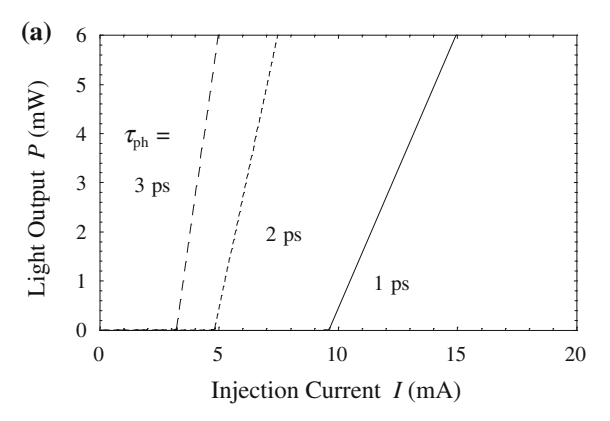
The derivative resistance dV/dI is expressed as

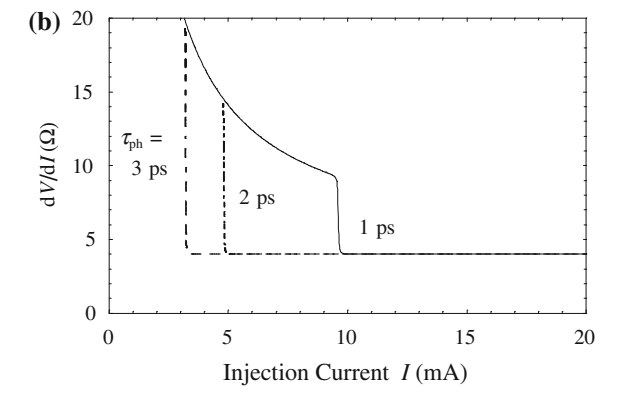
$$\frac{\mathrm{d}V}{\mathrm{d}I} = \frac{\partial V}{\partial n} \frac{\partial n}{\partial I}.\tag{5.60}$$

Figure 5.19 shows calculated I-L and I-dV/dI characteristics where (5.55)–(5.57) and (5.60) were used. The parameters used are the same as in Figs. 5.17 and 5.18.

As shown in Fig. 5.19a, b, the I-dV/dI curves have kinks at the threshold currents. Therefore, the threshold currents are determined by the derivative electrical resistance dV/dI, and this method is especially useful for semiconductor ring or disk lasers with extremely low light output.

Fig. 5.19 Current versus a light output and b derivative electrical resistance





## 5.7 Polarization of Light

Fabry-Perot LDs, which have *bulk* active layers, oscillate in the *TE mode*. As explained in Chap. 1, the bulk active layers do not have particular quantum mechanical axes. As a result, the optical gains for the bulk active layers have values averaged with respect to all angles and are independent of the polarization of lights. However, the facet reflectivities depend on the polarization of lights.

Figure 5.20a schematically shows reflection at a facet of a semiconductor laser in a zigzag model. We suppose that the effective refractive index of the optical waveguide is  $n'_{\rm A}$  and the refractive index of the outside of the optical waveguide is  $n_{\rm B}$ . This reflection is also considered as the reflection at the interface of a material with the refractive index  $n_{\rm A} = n'_{\rm A}/\cos\theta$  and that with the refractive index  $n_{\rm B}$ , as shown in Fig. 5.20b.

When the angle of incidence is  $\theta$ , *Fresnel formulas* give the power reflectivities  $R_{\text{TE}}$  and  $R_{\text{TM}}$  as

$$R_{\text{TE}} = \left| \frac{n_{\text{A}} \cos \theta - \sqrt{n_{\text{B}}^2 - n_{\text{A}}^2 \sin^2 \theta}}{n_{\text{A}} \cos \theta + \sqrt{n_{\text{B}}^2 - n_{\text{A}}^2 \sin^2 \theta}} \right|^2,$$
 (5.61)

$$R_{\text{TM}} = \left| \frac{n_{\text{B}}^2 \cos \theta - n_{\text{A}} \sqrt{n_{\text{B}}^2 - n_{\text{A}}^2 \sin^2 \theta}}{n_{\text{B}}^2 \cos \theta + n_{\text{A}} \sqrt{n_{\text{B}}^2 - n_{\text{A}}^2 \sin^2 \theta}} \right|^2, \tag{5.62}$$

where subscripts indicate the polarization of lights. Figure 5.21 shows the power reflectivity R when laser beams are emitted from GaAs with the refractive index  $n_{\rm A}=3.6$  to the air with  $n_{\rm B}=1$ . As found in Fig. 5.21, a relation  $R_{\rm TE}\geq R_{\rm TM}$  is kept for all values of  $\theta$ . Hence, from (5.11), the threshold gains for the TE modes are lower than those of the TM modes, which results in a start of lasing in the TE modes. With an increase in  $\theta$ , i.e., with an increase in the order of modes,  $R_{\rm TE}$  is enhanced. Therefore, the threshold gains of higher order modes are smaller than those of lower order modes. However, to minimize the threshold current density the active layer thickness d should be approximately  $0.1~\mu{\rm m}$ , as shown in Fig. 5.10. In such a small d, the higher order modes are cut off and only the fundamental mode oscillates.

Note that the light intensity ratio of the TE and TM modes is approximately 1: 1 below the threshold, because the light emitted below the threshold is the spontaneous emission.

**Fig. 5.20** Reflection at a facet: **a** A three-layer model and **b** a single-layer model

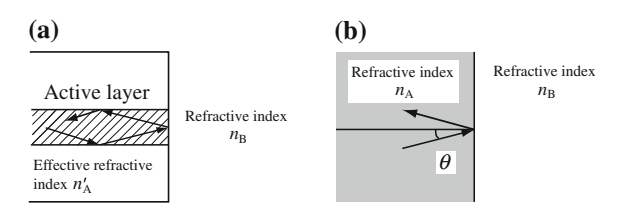
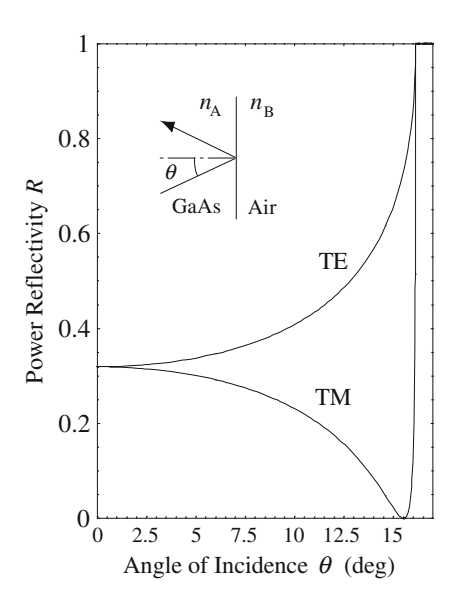


**Fig. 5.21** Reflectivity for TE and TM modes



## 5.8 Parameters and Specifications

There are trade-offs among characteristics of semiconductor lasers, which are determined by the internal loss  $\alpha_i$ , power reflectivity at a facet R, cavity length L, active layer thickness d, and so on. For example, a long L and a large R result in a low threshold gain  $\Gamma_a g_a$ , as shown in (5.11). However, a long L leads to a large volume of the active layer  $V_A$ , which results in a large threshold current  $I_{th} = J_{th} \times V_A$ . Also, a large R leads to a low power transmissivity T, which results in a low light output as found in (5.18). Therefore, we need to design semiconductor lasers to satisfy specifications according to applications.

# **5.9 Two-Mode Operation**

Up to now, for brevity, we have considered single-mode operations and have neglected the gain saturation. Here, we treat two-mode operations by including self-saturation and cross-saturation of the optical gains [3–8].

The rate equations for the photon densities  $S_1$  and  $S_2$  in two-mode operations are given by

$$\dot{S}_1 = (\alpha_1 - \beta_1 S_1 - \theta_{12} S_2) S_1, \tag{5.63}$$

$$\dot{S}_2 = (\alpha_2 - \beta_2 S_2 - \theta_{21} S_1) S_2, \tag{5.64}$$

where  $\alpha_i \equiv G_i - 1/\tau_{\text{ph}i}$  is the net amplification rate,  $G_i$  is the amplification rate,  $\tau_{\text{ph}i}$  is the photon lifetime for the *i*th mode,  $\beta_i$  is the self-saturation coefficient, and  $\theta_{ij}$  is the cross-saturation coefficient (i, j = 1, 2). In a steady state (d/dt = 0), we obtain

$$\beta_1 S_1 + \theta_{12} S_2 = \alpha_1 : L_1, \tag{5.65}$$

$$\beta_2 S_2 + \theta_{21} S_1 = \alpha_2 : L_2, \tag{5.66}$$

where  $L_1$  and  $L_2$  indicate lines in Fig. 5.22. From small variations analysis, the coupling constant C is defined as

$$C \equiv \frac{\theta_{12}\theta_{21}}{\beta_1\beta_2}.\tag{5.67}$$

According to the value of C, the coupling strengths are classified into three regions as

C < 1 weak coupling,

C = 1 neutral coupling,

C > 1 strong coupling.

Relationships between  $S_1$  and  $S_2$  are summarized in Fig. 5.22. As found in (5.63) and (5.64), we have  $\dot{S}_i < 0$  in a region above line  $L_i$  (i = 1, 2), and  $\dot{S}_i > 0$  in a region below line  $L_i$  (i = 1, 2). According to a sign of  $\dot{S}_i$ , a stable point of the photon density  $S_i$  is determined.

Figure 5.22a, b show the weak coupling (C < 1); in (a), for  $\beta_1\alpha_2/\theta_{21} < \alpha_1$  only mode 1 oscillates and oscillation of mode 2 is inhibited, and in (b), for  $\theta_{12}\alpha_2/\beta_2 < \alpha_1 < \beta_1\alpha_2/\theta_{21}$  mode 1 and mode 2 simultaneously oscillate, which is only allowed in the weak coupling. If  $\alpha_1 < \theta_{12}\alpha_2/\beta_2$ , only mode 2 oscillates to prevent mode 1 from oscillating.

Figure 5.22c, d show the neutral coupling (C=1), and lines  $L_1$  and  $L_2$  are parallel. For  $\beta_2\alpha_1/\theta_{12}=\theta_{21}\alpha_1/\beta_1>\alpha_2$ , as shown in Fig. 5.22c, d, only mode 1 oscillates and mode 2 cannot oscillate. If  $\beta_2\alpha_1/\theta_{12}=\theta_{21}\alpha_1/\beta_1<\alpha_2$ , only mode 2 oscillates oscillation of mode 1 suppressed.

Figure 5.22e, f show the strong coupling (C > 1); in (e), for  $\alpha_2 < \beta_2 \alpha_1/\theta_{12}$  only mode 1 oscillates, and in (f), for  $\beta_2 \alpha_1/\theta_{12} < \alpha_2 < \theta_{21}\alpha_1/\beta_1$ , mode 1 or mode 2 oscillates according to the initial values of  $S_1$  and  $S_2$ . For example, a change in the refractive index of the optical waveguide by an applied voltage or an injection current leads to a bistable operation between  $S_1$  and  $S_2$ , which is only observed in the strong coupling. If  $\theta_{21}\alpha_1/\beta_1 < \alpha_2$ , only mode 2 oscillates.

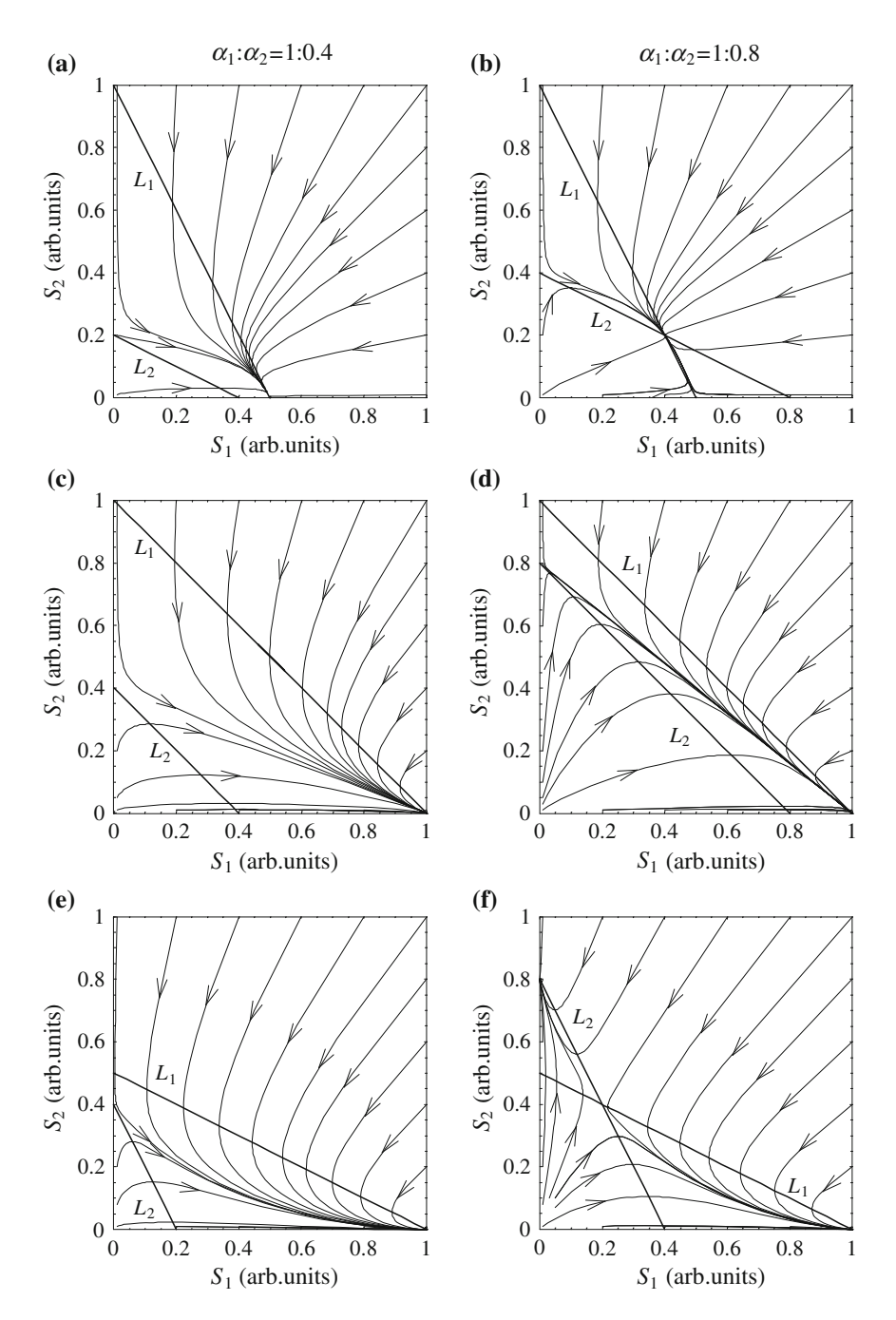


**Fig. 5.22** Relationships between  $S_1$  and  $S_2$ : **a** and **b** Weak coupling  $(\theta_{ij}/\beta_i = 0.5)$ , **c** and **d** neutral coupling  $(\theta_{ij}/\beta_i = 1)$ , and **e** and **f** strong coupling  $(\theta_{ij}/\beta_i = 2)$ 

The *transverse modes*, or *lateral modes*, show the light intensity distributions along the axes perpendicular to the cavity axis, which determine the shapes of the laser beams. The transverse modes are highly dependent on the structures of the optical waveguides, and the *vertical transverse modes* display the light intensity distributions along the axes perpendicular to the active layer plane, whereas the *horizontal transverse modes* exhibit the light intensity distributions along the axes parallel to the active layer plane.

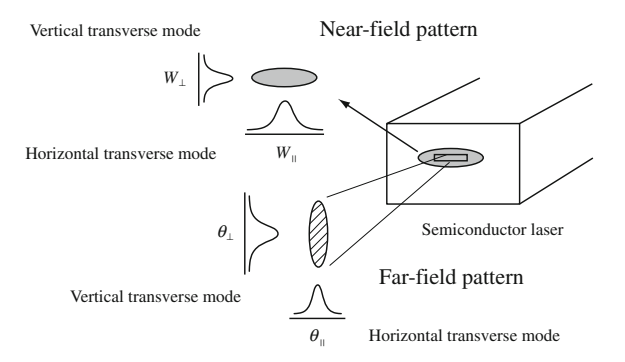
To evaluate the transverse modes, we usually use *near-field patterns* and *far-field patterns*, as shown in Fig. 5.23.

The near-field pattern is the light intensity distributions on a facet; its indexes are the length of the emission region  $W_{\parallel}$  and  $W_{\perp}$  illustrated in Fig. 5.23. Usually, the active layer thickness d is approximately 0.1  $\mu$ m or less to minimize the threshold current density, while the active layer width is of the order of  $2\,\mu$ m or more to achieve high reproducibility with high accuracy. As a result, the near-field pattern is asymmetric, which is long along the axis parallel to the active layer plane and short along the axis perpendicular to the active layer plane.

The far-field pattern is the light intensity distributions at a position that is far enough from the facet. As shown in Fig. 5.23, its indexes are the radiation angles  $\theta_{\parallel}$  and  $\theta_{\perp}$ , which are independent of the distance between the facet and the detector. This far-field pattern is considered to be a *diffracted pattern* of the near-field pattern if the near-field pattern is regarded as a *slit*. With a decrease in the size of the slit, the size of the diffracted patterns increases. Therefore, the far-field patterns are large for small near-field patterns and small for large near-field patterns. Because of asymmetry in the near-field patterns, the far-field patterns are also asymmetric with small horizontal transverse modes and large vertical ones.

When we couple a laser beam to an optical component such as a lens or an optical fiber, we would like to achieve a large coupling efficiency. For this purpose, a symmetric laser beam with a narrow radiation angle is required. In this respect, conventional semiconductor lasers are not optimized, and the optical coupling loss is minimized by optimizing the optical components or the optical coupling systems.

**Fig. 5.23** Near-field and far-field patterns



Recently, however, semiconductor lasers with optical waveguides whose thickness or width is graded along the cavity axes have been demonstrated to enhance the optical coupling efficiencies. Vertical cavity surface emitting lasers are also suitable to achieve high optical coupling efficiency because their emitted beams have symmetric circular shapes with narrow radiation angles (see Chap. 6).

### 5.10.1 Vertical Transverse Modes

#### 5.10.1.1 Guided Modes

The vertical transverse modes present light intensity distributions along the axes perpendicular to the active layer plane. Because the double heterostructures are adopted in semiconductor lasers, index guiding is established along the axis perpendicular to the active layer plane. The guiding condition is represented by the eigenvalue equation for the transverse resonance condition.

Here, we briefly review the key points of the eigenvalue equation, which was explained in Chap. 3. Figure 5.24 shows an optical waveguide, in which the guiding layer with the refractive index  $n_f$  and the thickness h is sandwiched by the cladding layer with the refractive index  $n_c$  and the substrate with the refractive index  $n_s$  where  $n_f > n_s \ge n_c$ .

Because Fabry-Perot LDs with bulk active layers oscillate in the TE modes, we consider the eigenvalue equation for the TE modes. Using a wave number in a vacuum  $k_0$ , the normalized frequency or the normalized waveguide thickness V is defined as

$$V = k_0 h \sqrt{n_{\rm f}^2 - n_{\rm s}^2}. ag{5.68}$$

With the help of the effective refractive index N, the normalized waveguide refractive index  $b_{TE}$  is defined as

$$b_{\rm TE} = \frac{N^2 - n_{\rm S}^2}{n_{\rm f}^2 - n_{\rm S}^2}.$$
 (5.69)

Also, we introduce the asymmetry measure  $a_{TE}$  as

$$a_{\rm TE} = \frac{n_{\rm s}^2 - n_{\rm c}^2}{n_{\rm f}^2 - n_{\rm s}^2}.$$
 (5.70)

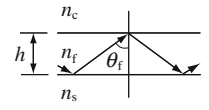


Fig. 5.24 Cross section of an optical waveguide

Using these normalized parameters, we can express the normalized eigenvalue equation for the TE modes as

$$V\sqrt{1 - b_{\text{TE}}} = m\pi + \tan^{-1}\sqrt{\frac{b_{\text{TE}}}{1 - b_{\text{TE}}}} + \tan^{-1}\sqrt{\frac{a_{\text{TE}} + b_{\text{TE}}}{1 - b_{\text{TE}}}},$$
 (5.71)

where m is a nonnegative integer, which is called the order of modes.

The important concept in designing optical waveguides is the cutoff condition in which the guided modes do not exist. When the angle of incidence (= angle of reflection) in the guiding layer  $\theta_f$  is equal to the critical angle  $\theta_{fs}$ , propagated lights are not confined to the guiding layer and a fraction of the lights are emitted to the substrate. In this case, we have  $N = n_s$ , which results in  $b_{TE} = 0$  from (5.69). As a result, from (5.71), the normalized frequency  $V_m$  for the mth-order mode to be cut off is obtained as

$$V_m = m\pi + \tan^{-1}\sqrt{a_{\rm TE}}.\tag{5.72}$$

For  $V_m < V < V_{m+1}$ , the guided modes from the zeroth- to the *m*th-order modes exist. In a symmetric optical waveguide with  $n_s = n_c$  where  $a_{TE} = 0$  in (5.70), (5.72) reduces to

$$V_m = m\pi. (5.73)$$

From (5.68) to (5.73), the cutoff guiding layer thickness  $h_c$  in a symmetric optical waveguide is expressed as

$$h_{\rm c} = \frac{m\pi}{k_0 \sqrt{n_{\rm f}^2 - n_{\rm s}^2}} = \frac{m\lambda_0}{2\sqrt{n_{\rm f}^2 - n_{\rm s}^2}}, \quad k_0 = \frac{2\pi}{\lambda_0},$$
 (5.74)

where  $\lambda_0$  is a wavelength of a light in a vacuum. From (5.74), with increases in  $h_c$  and  $n_f^2 - n_s^2$ , higher order modes with large ms can be guided in the optical waveguides.

Using V and b, the optical confinement factor  $\Gamma_f$  in the symmetric optical waveguide is given by

$$\Gamma_{\rm f} = \frac{V\sqrt{b} + 2b}{V\sqrt{b} + 2}.\tag{5.75}$$

## 5.10.1.2 Laser Oscillation in Higher Order Modes

## (i) Active Layer Thickness $d \gtrsim h_{\rm c}$

From (5.74) and (5.75), a relationship of the optical confinement factor  $\Gamma_m$  for the mth-order mode and  $\Gamma_{m-1}$  for the (m-1)th-order mode is written as

$$\Gamma_m < \Gamma_{m-1}. \tag{5.76}$$

When the active layer thickness d is slightly larger than  $h_c$ , a difference in the reflectivities between the adjacent higher order modes is small. Therefore, from (5.40), the threshold current density  $J_{\text{th},m}$  for the mth-order mode and  $J_{\text{th},m-1}$  for the (m-1)th-order mode are related as

$$J_{\text{th }m} > J_{\text{th }m-1},$$
 (5.77)

which leads to a laser oscillation in the (m-1)th-order mode, and not the mth-order mode.

## (ii) Active Layer Thickness $d \gg h_c$

As shown in Fig. 5.21, higher order TE modes have larger reflectivities than lower order ones. Therefore, when the active layer thickness d is much larger than  $h_c$ , a laser oscillation in the mth-order mode takes place. For an AlGaAs/GaAs LD with  $n_f = 3.6$ ,  $(n_f - n_s)/n_f = 5$ %, and  $\lambda_0 = 0.85 \,\mu\text{m}$ , the cutoff guiding layer thickness  $h_{cm}$  for the mth-order mode is obtained as

$$h_{c1} = 0.38 \,\mu\text{m}, \ h_{c2} = 0.76 \,\mu\text{m}, \ h_{c3} = 1.13 \,\mu\text{m}.$$

In this case, according to the active layer thickness *d*, the following laser oscillations in higher order modes take place:

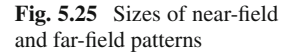
 $d > 0.66 \,\mu\text{m}$ : first-order mode  $d > 0.98 \,\mu\text{m}$ : second-order mode  $d > 1.30 \,\mu\text{m}$ : third-order mode

In conventional semiconductor lasers, to minimize the threshold current density, the active layer thickness d is approximately 0.1  $\mu$ m, as shown in Fig. 5.10. Therefore, the vertical transverse modes are fundamental modes (m = 0).

#### 5.10.1.3 Near-Field Pattern and Far-Field Pattern

Let us consider the vertical size of the near-field patterns  $W_{\perp}$  and of the far-field patterns  $\theta_{\perp}$ . When the active layer thickness d is larger than a light wavelength in a material,  $W_{\perp}$  shrinks with a decrease in d, because the light emission region narrows. However, when d is less than a light wavelength in a material,  $W_{\perp}$  increases with a decrease in d, because the guided lights highly penetrate into the cladding layer and the substrate.

As described before, the far-field pattern is considered to be a diffracted pattern of the near-field pattern. As a result, the far-field pattern is large for a small near-field pattern and is small for a large near-field pattern.



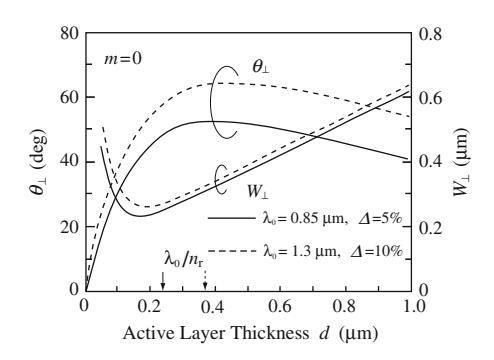


Figure 5.25 shows the calculated results of  $W_{\perp}$  and  $\theta_{\perp}$  for the fundamental TE mode (m=0). The horizontal line is the active layer thickness d, and  $\Delta$  in the inset is  $(n_{\rm f}-n_{\rm s})/n_{\rm f}$ . For  $d=0.1~\mu{\rm m}$ , the radiation angle  $\theta_{\perp}$  is approximately 30°, which is not good enough for optical coupling. However, this value is much smaller than those of LDs below the threshold or LEDs. This is because the mode for the laser light is the guided mode, while the spontaneously emitted lights include not only the guided modes but also the radiation modes, which have various polarizations and propagation directions. In LEDs, to achieve a relatively narrow radiation angle, monolithic or hybrid lenses are formed on their light emission surfaces.

## 5.10.2 Horizontal Transverse Modes

The horizontal transverse modes show the light intensity distributions along the axes parallel to the active layer plane. To control the horizontal transverse modes, gain guiding and index guiding, which were explained in Chap. 3, have been used. In gain guiding, lights propagate only in the optical gain region. In index guiding, lights propagate in a high refractive index region, which is surrounded by low index regions. As shown in Table 5.1, gain guiding is superior to index guiding in fabrication but inferior in lasing characteristics.

## 5.10.2.1 Gain Guiding

In gain guiding structures, optical gain regions are formed by restricting the current flowing area. For example, electrodes are selectively evaporated.

**Table 5.1** Comparison of gain guiding and index guiding

	Stability	Threshold current	Fabrication
Gain guiding	Unstable	Large	Simple
Index guiding	Stable	Small	Complicated

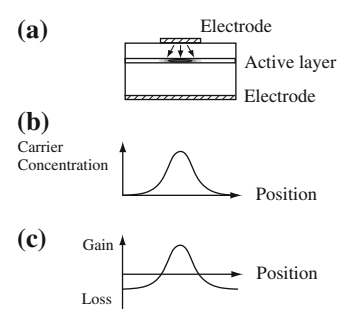


Fig. 5.26 Gain guiding LD: a Cross-sectional view, b distribution of the carrier concentration, and c distribution of the optical gain

Figure 5.26 shows (a) a cross-sectional view of a gain guiding LD seen from a facet, (b) distribution of the carrier concentration, and (c) distribution of the optical gain. The injection current flows from the selectively formed electrode along the arrows by diffusion. As a result, the carrier concentration is largest at the center of the stripe, and decreases with an increase in the distance from the center. Therefore, the center region of the stripe has optical gain and the stripe edges have optical losses.

Here, we consider distribution of the refractive index in the gain guiding structure. With an increase in injection current, the refractive index changes due to the *free carrier plasma effect*, Joule heating in the active layer, and the *spatial hole burning*.

When the free carriers are induced to vibrate with the frequency of a light, the phases of the free carrier vibrations shift and cancel out the electrical polarizations of the lattice atoms. This phenomenon is referred to as the free carrier plasma effect. A change in the refractive index  $\Delta n_{\rm rf}$  due to the free carrier plasma effect is given by

$$\Delta n_{\rm rf} = -\frac{e^2}{2m^*\omega^2\varepsilon_0 n_{\rm r}} n,\tag{5.78}$$

which is proportional to the injected carrier concentration n. Here, e is the elementary charge,  $m^*$  is the effective mass of the free carriers,  $\omega$  is the angular frequency of a light,  $\varepsilon_0$  is permittivity in a vacuum, and  $n_r$  is the refractive index when the carriers are not injected. On the derivation of (5.78), see Appendix F. When the carrier concentration n is of the order of  $10^{18}$  cm<sup>-3</sup>, a decrease in the refractive index is of the order of  $10^{-3}$ . Because the carrier concentration is large at the center of the stripe, the refractive index in the center is lower than the surrounding regions according to (5.78). As a result, the light is not completely confined to the active layer and is radiated to the surrounding regions, which is called the *antiguiding effect*.

With an increase in injection current, the active layer is heated by Joule heating. Therefore, the refractive index increases, and this change  $\Delta n_{rT}$  is expressed as

$$\Delta n_{\rm rT} = (2 \sim 5) \times 10^{-4} \Delta T$$
 (5.79)

where  $\Delta T$  is an increase in the temperature of the active layer, which is expressed in units of Kelvin. As opposed to the free carrier plasma effect, the increase in the refractive index due to Joule heating of the active layer contributes to confine the light to the active layer, which is referred to as the *guiding effect*.

When we further increase the injection current and have a large light output, a lot of carriers are consumed due to stimulated emission. Because stimulated emission efficiently takes places at a large optical gain region, the carrier concentration at the center of the stripe is lower than that of its surrounding regions. This phenomenon is known as spatial hole burning, which increases the refractive index at the center region, resulting in a large confinement of the light to the active layer.

As explained earlier, the horizontal distribution of the refractive index is determined by the free carrier plasma effect, Joule heating of the active layer, and the spatial hole burning. Hence, the horizontal transverse modes show complicated behaviors, such as changes in the positions or multiple peaks, according to a value of the injection current. When the horizontal transverse modes change, kinks are observed in I-L curves.

In gain guiding structures, wave fronts of the horizontal transverse modes bend convexly in the propagation direction, while those of the vertical transverse modes are close to plane waves. As a result, the *beam waist*, in which the beam diameter is minimum of the horizontal transverse modes is placed inside the optical cavity, while that of the vertical transverse modes is located on a facet of a semiconductor laser. Such a difference in the positions of the beam waists for the vertical and horizontal transverse modes is called *astigmatism*. When there is astigmatism, we cannot focus both the vertical and horizontal transverse modes on a common plane by a oneaxially symmetric convex lens, and we obtain only defocused images.

#### 5.10.2.2 Index Guiding

Index guiding structures have an intentionally formed refractive index distribution, as shown in Fig. 5.27. In the index guiding structures, both the horizontal and vertical transverse modes are close to plane waves, which do not generate astigmatism.

To obtain stable horizontal transverse modes, we need that (1)  $\Delta n_{\rm r} > |\Delta n_{\rm rf}|$  where  $\Delta n_{\rm r}$  is a difference in the refractive indexes between the active layer and its surround-

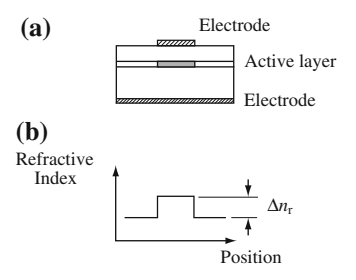
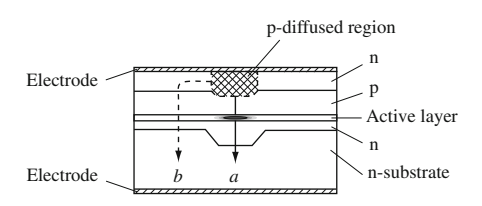


Fig. 5.27 Index guiding LD: a Cross-sectional view and b distribution of the refractive index

Fig. 5.28 Rib waveguide



ing layers and  $\Delta n_{\rm rf}$  is a change in the refractive index due to the free carrier plasma effect; (2) the cutoff condition for the higher order modes is satisfied; and (3) the active layer width is shorter than the *diffusion length* of the carriers. Condition (1) is required to achieve index guiding even in a high injection current. Condition (2) is introduced to obtain a single horizontal transverse mode. If there are multiple higher order horizontal transverse modes, *mode hopping* or the *mode competition* takes place between various modes according to operating conditions, which leads to unstable horizontal transverse modes. To avoid these unstable conditions, only the fundamental horizontal transverse mode should exist in the optical waveguides. Finally, condition (3) is needed to achieve uniform distributions of the carrier concentration in the active layer, which reduces spatial hole burning. The active layer width is usually about 2  $\mu$ m, because the diffusion length of the injected carriers is 2–3  $\mu$ m from the viewpoint of reproducibility. To satisfy conditions (1) and (2),  $\Delta n_{\rm r}/n_{\rm r}$  is approximately  $10^{-2}$ .

Up to now, many index guiding structures have been developed to efficiently confine both the carriers and the light to the active layer, and the structures are classified into three categories: rib waveguides, ridge waveguides, and buried heterostructures (BHs).

## (i) Rib Waveguide

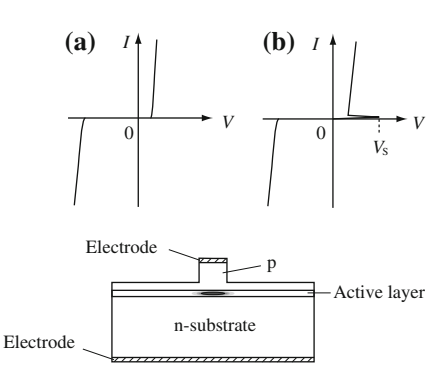
*Rib waveguides* are optical waveguides with convex or concave regions, which are suitable for semiconductor lasers whose active layers cannot be exposed to the air by etching. For example, AlGaAs active layers are easily oxidized in the air, and their emission efficiencies drastically decrease.

As an example of a rib waveguide, Fig. 5.28 shows a plano convex waveguide (PCW) structure, in which the semiconductor layers are grown on a preetched substrate. Here, solid line a and broken line b show the flowing paths of the electric currents. Path a is a direction of a forward current across the pn-junction, and the electrical resistance along this path is low. On the other hand, in path b, the electric current flows through a *pnpn structure* (*thyristor*).

Figure 5.29 shows I-V characteristics in the pn and pnpn structures. When the applied voltage is below a switching voltage  $V_s$ , a pn-junction inside the pnpn structure is reversely biased, and the electric current hardly flows. Once the applied voltage exceeds  $V_s$ , the pnpn structure shows similar I-V characteristics to those of the

**Fig. 5.29** Current versus voltage (I-V) characteristics in **a** pn and **b** pnpn structures

Fig. 5.30 Ridge waveguide



pn-junctions in forward bias. Therefore, by designing  $V_s$  to be larger than the applied voltage across the pn-junction, the electric current hardly flows through path b.

Note that the electric current flowing regions are broad, because a current constriction structure is not formed below the p-diffused region. In other words, rib waveguides are not optimized for confinement of the carriers to the active layers.

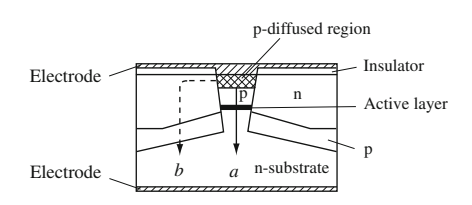
### (ii) Ridge Waveguide

*Ridge waveguides* are optical waveguides with a convex region. Because they are easily fabricated by etching after epitaxial growth, low-cost semiconductor lasers are expected. When the active layer materials cannot be exposed to the air, etching is stopped above the active layer, as shown in Fig. 5.30.

### (iii) Buried Heterostructure

Buried heterostructures (BHs), in which the active layer is surrounded by regrown regions, are fabricated as follows: At first, epitaxial layers are grown on a semiconductor substrate, which is followed by etching to form a stripe. This stripe is buried by the second epitaxial growth and the buried regions prevent the injection current from flowing. Although fabrication processes are complicated, low-threshold and high-efficiency operations are obtained because of efficient confinement of the carriers and light to the active layers. However, because the active layers are exposed to the air during fabrication, only the active layers insensitive to oxidization are suitable for buried heterostructures. For example, InGaAsP/InP LDs, which are the light sources of optical fiber communication systems, frequently adopt buried heterostructures. Figure 5.31 shows an example of a buried heterostructure. To constrict the current flowing region, the surrounding regions of the stripe are pnpn structures. Therefore, the electric current efficiently flows in path *a* but hardly flows along path *b*. Also, a current constriction structure is formed below the p-diffused region, and the carriers are efficiently injected into the active layer.

Fig. 5.31 Buried heterostructure (BH)



## 5.10.3 Antiguiding

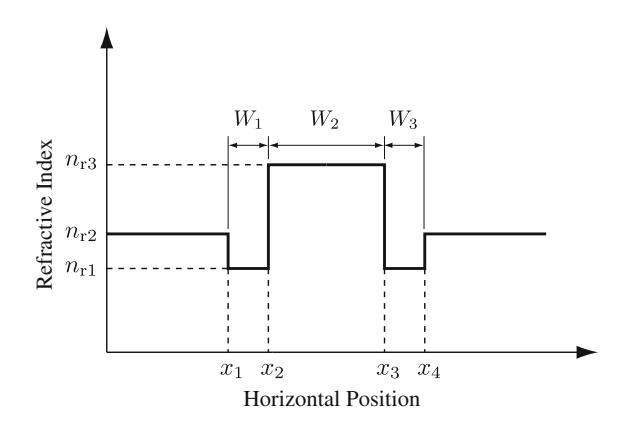
#### 5.10.3.1 Distribution of Refractive Index and Transverse Mode

In the air, AlGaAs layers are oxidized easily and the oxidized AlGaAs layers cause degradations in electrical and optical characteristics of semiconductor lasers. Because AlGaAs layers are oxidized during etching process before epitaxial regrowth to bury a mesa, it is difficult to fabricate buried heterostructures for semiconductor lasers with AlGaAs layers. Therefore, ridge structures are adopted often for semiconductor lasers with AlGaAs layers such as semiconductor lasers with the oscillation wavelength of  $0.98\,\mu\text{m}$ , which are used as pumping sources of Er-doped optical fiber amplifiers.

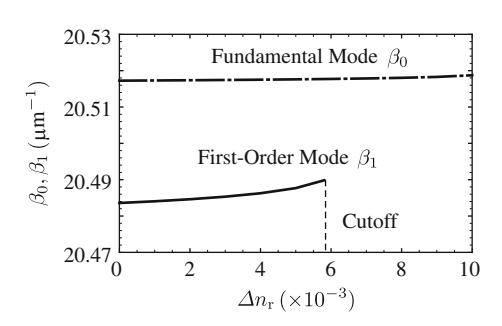
In the ridge structures, higher order horizontal transverse modes as well as fundamental horizontal transverse mode are confined. As a result, with an increase in injected current, higher order horizontal transverse modes lase; kinks appear in their current versus light-output (I-L) curves. The light output where a kink appears is called kink level. Below the kink level, the fundamental horizontal transverse mode is obtained; above the kink level, higher order horizontal transverse modes oscillate. To increase the kink levels, ridge structures with antiguiding layers have been proposed [9–16].

Figure 5.32 shows an example of a distribution of a refractive index for antiguiding. In the center, a region with the highest refractive index  $n_{r3}$  exists. Outside the region with the highest refractive index  $n_{r3}$ , two regions with a relatively high refractive

**Fig. 5.32** Distribution of a refractive index for antiguiding



**Fig. 5.33** Propagation constants for the fundamental and the first-order horizontal transverse modes



index  $n_{r2}$  are located via two regions with the lowest refractive index  $n_{r1}$ . Here,  $W_1$ ,  $W_2$ , and  $W_3$  are width of each region.

In Fig. 5.32, by assuming that  $n_{r1} = 3.190$ ,  $n_{r2} = n_{r1} + \Delta n_r$ ,  $n_{r3} = 3.202$ ,  $W_1 = W_3 = 0.5 \,\mu\text{m}$ ,  $W_2 = 3.3 \,\mu\text{m}$ , and the wavelength in the vacuum  $\lambda_0$  is 0.98  $\mu$ m, propagation constants  $\beta_0$  and  $\beta_1$  are calculated. Here,  $\beta_0$  is the propagation constant for the fundamental horizontal transverse mode and  $\beta_1$  is that for the first-order horizontal transverse mode. Figure 5.33 shows the propagation constants  $\beta_0$  and  $\beta_1$  as a function of the difference in the refractive index  $\Delta n_r$ . The dash-dotted and solid lines indicate  $\beta_0$  and  $\beta_1$ , respectively. Both  $\beta_0$  and  $\beta_1$  slightly increase with an increase in  $\Delta n_r$ . It should be noted that solutions of  $\beta_1$  exist only in  $0 \leq \Delta n_r \leq 0.58$ . In  $\Delta n_r > 0.58$ ,  $\beta_1$  does not exist and the first-order horizontal transverse mode is cut off due to antiguiding.

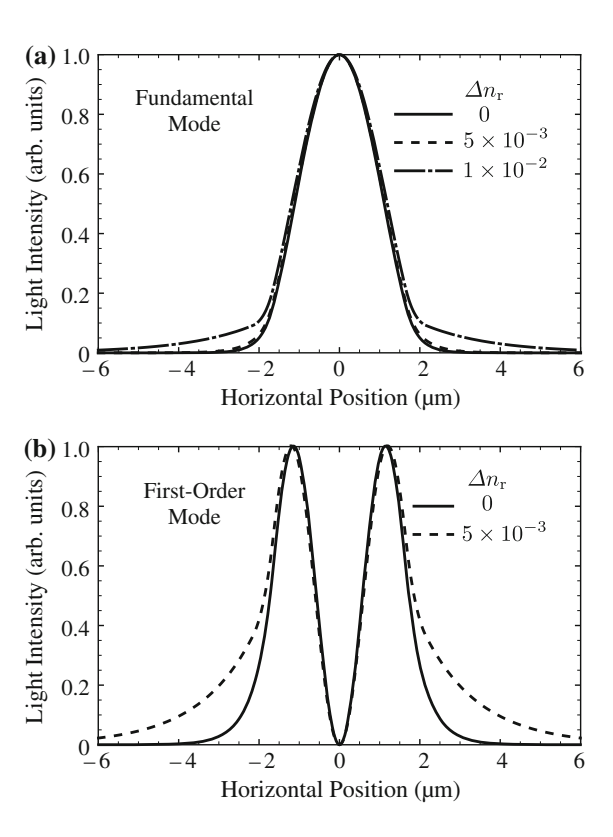
Figure 5.34 shows horizontal near field patterns (a) for the fundamental horizontal transverse mode and (b) for the first-order horizontal transverse mode with  $\Delta n_{\rm r}$  as a parameter. The other parameters are the same as those in Fig. 5.33. The solid, broken, and dash-dotted lines correspond to  $\Delta n_{\rm r} = 0$ ,  $5 \times 10^{-3}$ , and  $1 \times 10^{-2}$ , respectively. It should be noted that the first-order horizontal transverse mode does not exist for  $\Delta n_{\rm r} = 1 \times 10^{-2}$ . It is found that intensity of the side lobes increases with an increase in  $\Delta n_{\rm r}$ , which indicates that light tends to be antiguided with an increase in  $\Delta n_{\rm r}$ .

#### 5.10.3.2 Ridge LD with Antiguiding Layers

In the following, simulated laser characteristics for ridge LDs with antiguiding layers are explained. Figure 5.35 shows schematic cross-sectional views of (a) a ridge structure with steps in both the upper and lower guiding layers, (b) a ridge structure with steps in only the upper guiding layer, (c) a ridge structure with steps in only the lower guiding layer, and (d) a conventional ridge structure without steps in either guiding layer [11].

In Fig. 5.35,  $\Delta t_p$  is the thickness of the steps in the upper guiding layer,  $\Delta t_n$  is the thickness of the steps in the lower guiding layer,  $t_0$  is the thickness of the guiding layers without steps, and d is the distance from the bottom of the mesa to the bottom of the upper guiding layer. The width of the rectangular mesas is 3.3  $\mu$ m, the width

**Fig. 5.34** Horizontal near field patterns **a** for the fundamental horizontal transverse mode and **b** for the first-order horizontal transverse mode



of the bases is  $60\,\mu\text{m}$ , and the length of the cavities is  $1,200\,\mu\text{m}$ . The reflectivities of the front and rear facets are 2 and  $90\,\%$ , respectively. The refractive index and the thickness of the n-GaAs substrate are 3.54 and  $100\,\mu\text{m}$ , respectively. The refractive index of the p-Al<sub>0.2</sub>Ga<sub>0.8</sub>As cladding layer and the refractive index of the n-Al<sub>0.2</sub>Ga<sub>0.8</sub>As cladding layer are both 3.424. The refractive index and the thickness of the undoped Al<sub>0.15</sub>Ga<sub>0.85</sub>As guiding layers are 3.453 and  $200\,\text{nm}$ , respectively. The refractive index and the thickness of the undoped Al<sub>0.1</sub>Ga<sub>0.9</sub>As barrier layers are 3.482 and  $10\,\text{nm}$ , respectively. The refractive index and the thickness of the undoped Al<sub>0.03</sub>Ga<sub>0.97</sub>As barrier layer are 3.52 and  $10\,\text{nm}$ , respectively. The refractive index and the thickness of the undoped In<sub>0.2</sub>Ga<sub>0.8</sub>As strained quantum well (QW) active layers are 3.65 and  $10\,\text{nm}$ , respectively. The active region has a separate-confinement heterostructure (SCH) with Al<sub>0.1</sub>Ga<sub>0.9</sub>As barrier layers, an Al<sub>0.03</sub>Ga<sub>0.97</sub>As barrier layer, and double In<sub>0.2</sub>Ga<sub>0.8</sub>As strained QW active layers. The guiding layers, barrier layers, and active layers are undoped to suppress internal optical loss due to free-carrier absorption.

In Fig. 5.35a–c, the optical confinement of higher order transverses modes to the center of the mesa is weakened and the modal gain of higher order horizontal transverse modes decreases, owing to the antiguiding layers with thickness of  $t_0 + \Delta t_p$ 

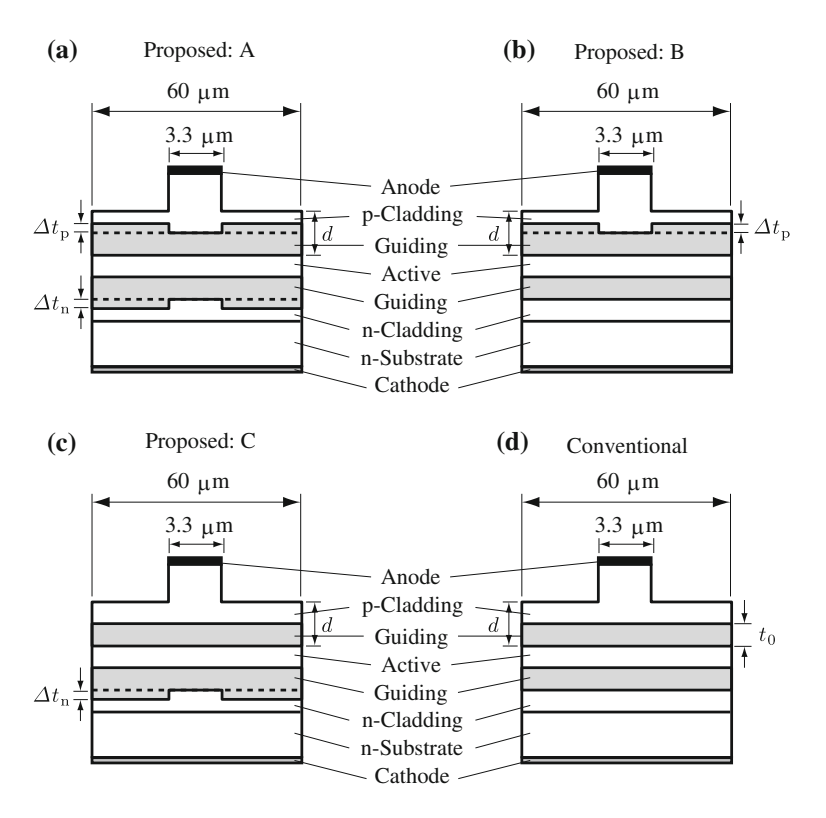
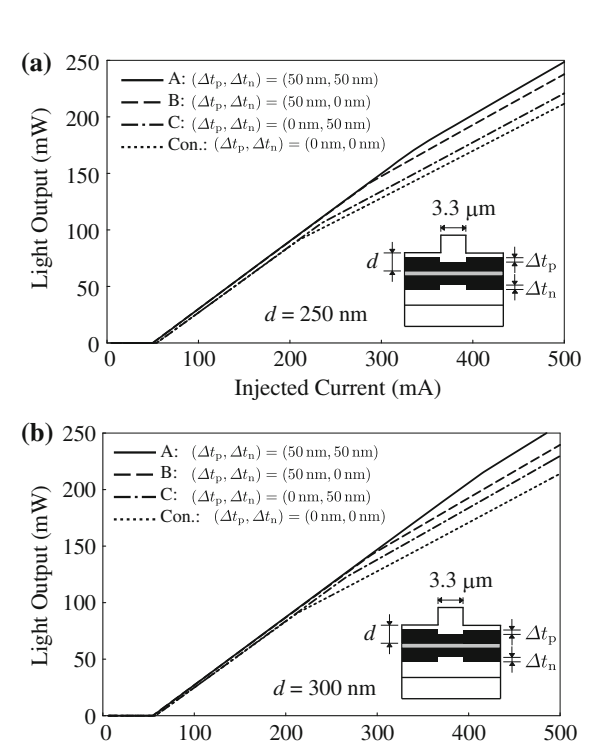


Fig. 5.35 Schematic cross-sectional views of  $\bf a$  a proposed ridge structure with steps in both the upper and lower guiding layers,  $\bf b$  a proposed ridge structure with steps in only the upper guiding layer,  $\bf c$  a proposed ridge structure with steps in only the lower guiding layer, and  $\bf d$  a conventional ridge structure without steps in either guiding layer. Here,  $\Delta t_p$  is thickness of the steps in the upper guiding layer,  $\Delta t_n$  is thickness of the steps in the lower guiding layer,  $t_0$  is thickness of the guiding layers without steps, and d is the distance from the bottom of the mesa to the bottom of the upper guiding layer [11] (Copyright © 2009 The Japan Society of Applied Physics)

or  $t_0 + \Delta t_n$  in both sides of the mesa. As a result, it is expected that oscillations of higher order horizontal transverse modes are suppressed even when the injected current is high. The undoped guiding layers below the mesa shown in Fig. 5.35a–c are thinner than those in the side regions. Therefore, it is expected that the injected current efficiently flows into the active region below the mesa, and spreading of the injected current into the side regions is suppressed for the ridge structures with antiguiding layers, which are shown in Fig. 5.35a–c.

Simulated I-L curves are shown in Fig. 5.36. The parameters are the steps in the guiding layers  $\Delta t_p$  and  $\Delta t_n$ , which have the value of 0 or 50 nm. It should be noted that  $\Delta t_p = \Delta t_n = 0$  nm corresponds to the conventional ridge structure, which is shown in Fig. 5.35d. The distances from the bottom of the mesa to the bottom of the upper guiding layer d's are (a) 250 and (b) 300 nm. The kink levels are defined as

Fig. 5.36 I-L curves for the proposed ridge structure. The parameters are  $\Delta t_{\rm p}$  and  $\Delta t_{\rm n}$ . The distances from the bottom of the mesa to the bottom of the upper guiding layer d's are a 250 and b 300 nm [11] (Copyright © 2009 The Japan Society of Applied Physics)

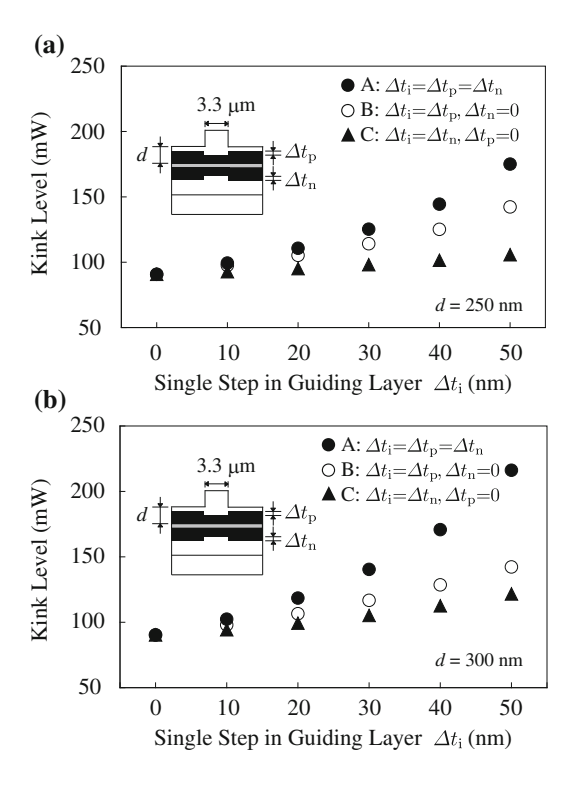


Injected Current (mA)

the light output at which the first-order horizontal transverse mode started to oscillate. Therefore, the kink levels seem to be relatively low. It should be noted that the first-order horizontal transverse mode started to oscillate and the second-order or higher order horizontal transverse modes did not oscillate at the kink levels in Fig. 5.36a, b. The kink levels increase with an increase in the number of steps in the guiding layers.

Figure 5.37 shows kink level as a function of  $\Delta t_i$  (i = p or n) for d = (a) 250 nm and (b) 300 nm. The closed circles, open circles, and closed triangles represent  $\Delta t_i = \Delta t_p = \Delta t_n$ ,  $\Delta t_i = \Delta t_p$  with  $\Delta t_n = 0$ , and  $\Delta t_i = \Delta t_n$  with  $\Delta t_p = 0$ , respectively. For d = 250 nm, the kink levels for  $(\Delta t_p, \Delta t_n)$  = (50 nm, 50 nm), (50 nm, 0 nm), (0 nm, 50 nm), and (0 nm, 0 nm) are 175, 142, 106 and 91 mW, respectively. For d = 300 nm, the kink levels for  $(\Delta t_p, \Delta t_n)$  = (50 nm, 50 nm), (50 nm, 0 nm), (0 nm, 50 nm), and (0 nm, 0 nm) are 216, 142, 122, and 90 mW, respectively. It is found that both  $\Delta t_p$  and  $\Delta t_n$  increase the kink levels and the contribution of  $\Delta t_p$  is higher than that of  $\Delta t_n$ . In addition, the kink level for d = 300 nm increased to a greater degree than that for d = 250 nm with increases in  $\Delta t_p$  and  $\Delta t_n$ . The reason for this is considered as follows: spreading of the injected current for d = 300 nm is larger than that for d = 250 nm. Therefore, spreading of the injected current for d = 300 nm is more sensitive to  $\Delta t_p$  and  $\Delta t_n$  than that for d = 250 nm.

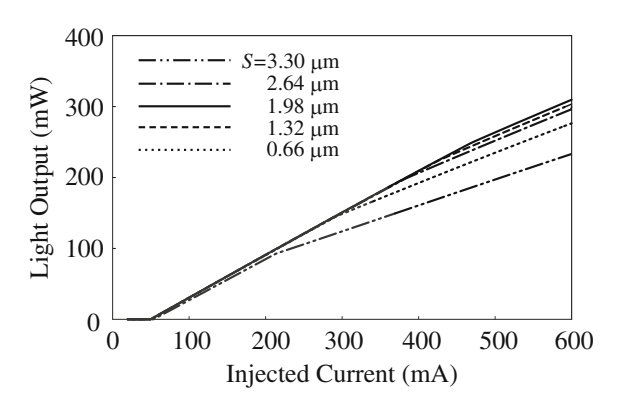
Fig. 5.37 Kink level as a function of  $\Delta t_i$  (i = p or n) for  $d = \mathbf{a}$  250 and  $\mathbf{b}$  300 nm. The closed circles, open circles, and closed triangles represent  $\Delta t_i = \Delta t_p = \Delta t_n$ ,  $\Delta t_i = \Delta t_p$  with  $\Delta t_n = 0$ , and  $\Delta t_i = \Delta t_n$  with  $\Delta t_p = 0$ , respectively [11] (Copyright © 2009 The Japan Society of Applied Physics)



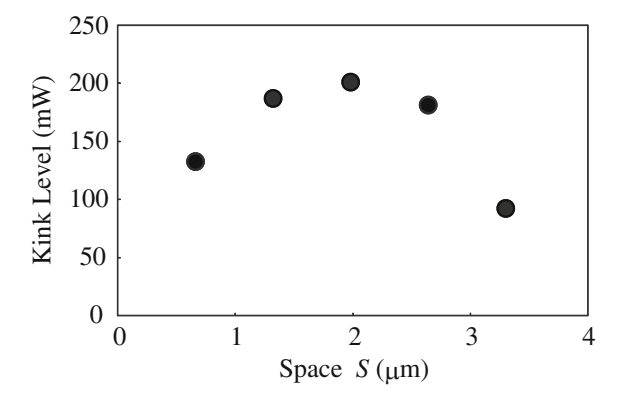
In the structure shown in Fig. 5.35a, the dependence of lasing characteristics on the space S in the antiguiding layers is theoretically investigated [13]. Here, the space S is the width of thin guiding layers below the mesa. Simulated I-L curves are shown in Fig. 5.38 with the space S in the antiguiding layers as a parameter. The dotted, broken, solid, dash-dotted, and dash-double-dotted lines correspond to S=0.66, 1.32, 1.98, 2.64, and  $3.30 \,\mu\text{m}$ , respectively. With a decrease in S, the threshold current decreases because the injected carriers concentrate to the region below the mesa. At the kink levels, the first-order horizontal transverse mode started to oscillate and the second-order or higher order horizontal transverse modes did not oscillate.

The threshold current  $I_{th}$  decreases with a decrease in S and saturates below  $S=1.98 \, \mu m$ , because injected carriers are confined to the space region in  $1.98 \, \mu m < S < 3.3 \, \mu m$ , and injected carriers overflowed to the steps in  $S < 1.98 \, \mu m$ . The threshold current  $I_{th}=49.1 \, \text{mA}$  at  $S=1.98 \, \mu m$  is  $0.92 \, \text{times}$  as large as  $I_{th}=53.2 \, \text{mA}$  at  $S=3.3 \, \mu m$ . When the mesa width is as narrow as  $2 \, \mu m$ , kinks in I-L curves are not obtained. However, the electrical resistance is large at such a narrow mesa width. To obtain low electrical resistance, the mesa width should be wider, but kinks in I-L curves tend to appear. In fact, kinks in I-L curves are obtained when the mesa width is larger than  $2.5 \, \mu m$ . From these simulated results, it can be said that

Fig. 5.38 I-L curves for the proposed ridge structure. A parameter is the space in the antiguiding layers S. The dotted, broken, solid, dash-dotted, and dash-double-dotted lines correspond to S=0.66, 1.32, 1.98, 2.64, and  $3.30 \,\mu\text{m}$ , respectively [13] (Copyright © 2009 The Japan Society of Applied Physics)



**Fig. 5.39** Kink level as a function of the space in the antiguiding layers *S* [13] (Copyright © 2009 The Japan Society of Applied Physics)



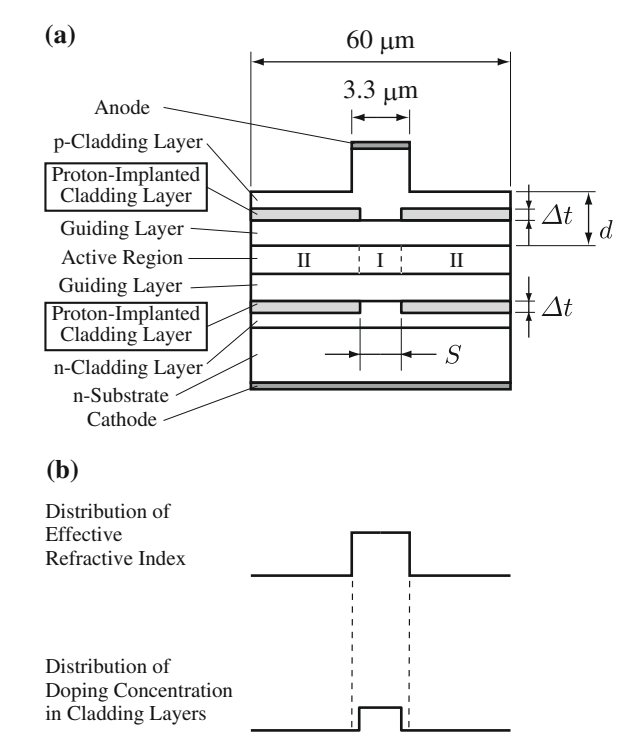
the proposed ridge structures with antiguiding layers are suitable for ridge structures with a relatively wide mesa.

Figure 5.39 shows the kink level as a function of the space S in the antiguiding layers. The kink level has a peak at  $S=1.98\,\mu\text{m}$ , and the kink level at  $S=1.98\,\mu\text{m}$  is 2.18 times as large as that at  $S=3.3\,\mu\text{m}$ . The reason for this is considered as follows: In  $1.98\,\mu\text{m} < S < 3.3\,\mu\text{m}$ , injected carriers are confined to the space region, but spatial hole burning appears. In  $S<1.98\,\mu\text{m}$ , injected carriers overflowed to the steps, but spatial hole burning is negligible because S is shorter than the carrier diffusion length of  $2\,\mu\text{m}$ .

## 5.10.3.3 Ridge LD with Proton-Implanted Antiguiding Layers

A ridge LD with selectively proton-implanted cladding layers is proposed to increase kink level and decrease threshold current [14]. In this laser, horizontal transverse modes are confined by the ridge structure; carrier distributions are con-

Fig. 5.40 a Schematic cross-sectional view of a proposed ridge structure with proton-implanted cladding layers and b distributions of the effective refractive index of the semiconductor laser and doping concentration of the cladding layers. Here,  $\Delta t$  is the thickness of the proton-implanted regions, S is the space between the proton-implanted regions, and d is the distance from the bottom of the mesa to the bottom of the upper guiding layer [14] (Copyright © 2010 The Japan Society of Applied Physics)

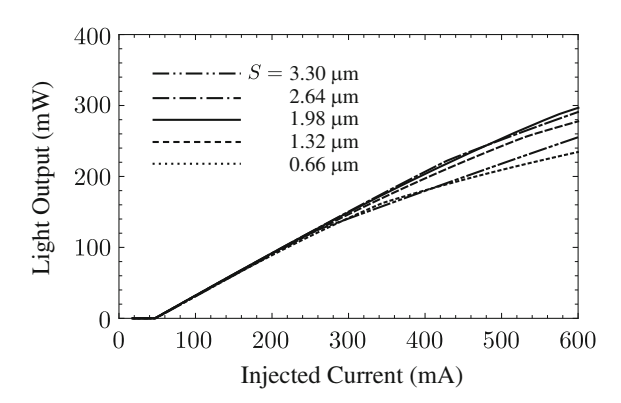


trolled by selectively proton-implanted cladding layers. From simulations of lasing characteristics, it is found that the kink level is higher and the threshold current is lower than those of the ridge-type semiconductor lasers with antiguiding layers for horizontal transverse modes [13].

Figure 5.40a shows a schematic cross-sectional view of a ridge structure with proton-implanted cladding layers; Fig. 5.40b shows distributions of the effective refractive index of the semiconductor laser and doping concentration of the cladding layers. The light is confined by the distribution of the effective refractive index of the semiconductor laser; the carriers are confined by the distribution of the doping concentration of the cladding layers because the flow path of the injected current is restricted to the doped region in the cladding layers.

In Fig. 5.40a, the shaded areas are the proton-implanted regions,  $\Delta t$  is the thickness of the proton-implanted regions, S is the space between the proton-implanted regions, and d is the distance from the bottom of the mesa to the bottom of the upper guiding layer. The height of the rectangular mesa is  $1.55 \,\mu\text{m}$ . Active region I has a width of S; active region II is located beside active region I. The width of the mesa is  $3.3 \,\mu\text{m}$ , the width of the base is  $60 \,\mu\text{m}$ , and the length of the cavity is  $1,200 \,\mu\text{m}$ . When S is fixed to  $3.3 \,\mu\text{m}$ ,  $d = 250 \,\text{nm}$  has resulted in the lowest threshold current. Therefore, for  $d = 250 \,\text{nm}$ , the dependences of kink level and threshold current on

Fig. 5.41 I-L curves for the proposed ridge structure. The parameter is the space between the proton-implanted regions (S). The *dotted*, *broken*, *solid*, *dash-dotted*, and *dash-double-dotted lines* correspond to S=0.66, 1.32, 1.98, 2.64, and  $3.30 \,\mu\text{m}$ , respectively [14] (Copyright © 2010 The Japan Society of Applied Physics)



the space S between the proton-implanted regions are examined. The thickness  $\Delta t$  of the proton-implanted regions is 50 nm. Reflectivities of the front and rear facets are 2 and 90%, respectively.

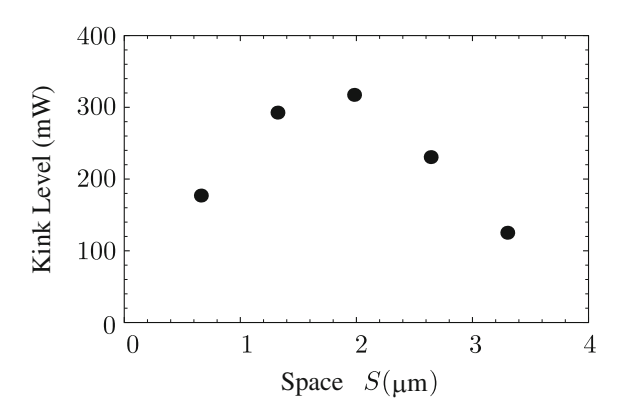
The refractive indexes and the thicknesses are as follows: The refractive index and the thickness of the n-GaAs substrate are 3.54 and 100  $\mu m$ , respectively. The refractive index of both the p-Al $_{0.2}$ Ga $_{0.8}$ As cladding layer and n-Al $_{0.2}$ Ga $_{0.8}$ As cladding layer is 3.424. It is assumed that the refractive index of the proton-implanted regions of the cladding layers is also 3.424 by controlling annealing condition after proton-implanted cladding layers. The residual carrier concentration in the proton-implanted regions is assumed to be  $10^{15}$  cm $^{-3}$ . The refractive index and the thickness of undoped Al $_{0.15}$ Ga $_{0.85}$ As guiding layers are 3.453 and 200 nm, respectively. The refractive index and the thickness of undoped Al $_{0.1}$ Ga $_{0.9}$ As barrier layers are 3.482 and 10 nm, respectively. The refractive index and the thickness of an undoped Al $_{0.03}$ Ga $_{0.97}$ As barrier layer are 3.52 and 10 nm, respectively. The refractive index and the thickness of In $_{0.2}$ Ga $_{0.8}$ As QW active layers are 3.65 and 10 nm, respectively.

The active regions have an SCH with  $Al_{0.1}Ga_{0.9}As$  barrier layers, an  $Al_{0.03}Ga_{0.97}As$  barrier layer, and two  $In_{0.2}Ga_{0.8}As$  strained QW active layers. The  $Al_{0.1}Ga_{0.9}As$  and  $Al_{0.03}Ga_{0.97}As$  barrier layers and the  $In_{0.2}Ga_{0.8}As$  QW active layers in the active regions as well as the  $Al_{0.15}Ga_{0.85}As$  guiding layers are undoped to reduce internal optical loss due to free-carrier absorption.

Simulated I-L curves are shown in Fig. 5.41 with the space S between the proton-implanted regions as a parameter. The dotted, broken, solid, dash-dotted, and dash-double-dotted lines correspond to  $S=0.66,\,1.32,\,1.98,\,2.64,\,$  and  $3.30\,\mu m$ , respectively. At the kink levels, the first-order horizontal transverse mode started to oscillate and the second-order or higher order horizontal transverse modes did not oscillate.

The threshold current  $I_{\text{th}}$  decreases and then increases with a decrease in S, which reflects the overlapping of the electron distribution below the threshold current and the horizontal near-field patters for the fundamental mode. The lowest threshold

Fig. 5.42 Kink level as a function of the space between the proton-implanted regions (S) [14] (Copyright © 2010 The Japan Society of Applied Physics)



current  $I_{th} = 46.8 \,\text{mA}$  at  $S = 1.98 \,\mu\text{m}$  is 0.975 times as large as the largest value of 48.0 mA at  $S = 3.3 \,\mu\text{m}$ ; 0.95 times as large as the lowest value of 49.1 mA in [13].

Figure 5.42 shows kink level as a function of the space S between the proton-implanted regions. With a decrease in S, the kink level increases and then decreases. The kink level peaks at  $S=1.98\,\mu\text{m}$ , and the kink level at  $S=1.98\,\mu\text{m}$  is 2.54 times as large as that at  $S=3.3\,\mu\text{m}$ ; 1.58 times as large as the highest value in [13].

## 5.10.3.4 Ridge LD with Modified Proton-Implanted Antiguiding Layers

In the ridge LD with selectively proton-implanted cladding layers, distributions of the refractive index and the doping concentrations are modified to increase kink level and decrease threshold current [15]. Light is confined by the proton-implanted  $n-Al_{0.2}Ga_{0.8}As$  cladding layer; carriers are confined by the proton-implanted  $p-Al_{0.2}Ga_{0.8}As$  cladding layer. From simulations, it is found that the kink level is higher and the threshold current is lower than those of the ridge-type semiconductor lasers with antiguiding layers for horizontal transverse modes [9–13]. In addition, it is revealed that they are optimal when the space between the proton-implanted regions in the p-cladding layer is  $1.3\,\mu m$ .

Figure 5.43a shows a schematic cross-sectional view of a ridge structure with selectively proton-implanted cladding layers and Fig. 5.43b shows distributions of the effective refractive index of the semiconductor laser and doping concentration of the cladding layers. The shaded areas are proton-implanted. Here,  $S_p$  is the space between the proton-implanted regions in the p-cladding layer;  $S_n$  is the space between the proton-implanted regions in the n-cladding layer.

The refractive index of the proton-implanted n-Al $_{0.2}$ Ga $_{0.8}$ As cladding layer is higher than that of n-Al $_{0.2}$ Ga $_{0.8}$ As cladding layer by  $1.5 \times 10^{-3}$  because of the free carrier plasma effect. The refractive index of the proton-implanted p-Al $_{0.2}$ Ga $_{0.8}$ As cladding layer is higher than that of p-Al $_{0.2}$ Ga $_{0.8}$ As cladding layer by only  $1.5 \times 10^{-4}$  because of large effective mass of hole. As a result, the distribution of the refrac-

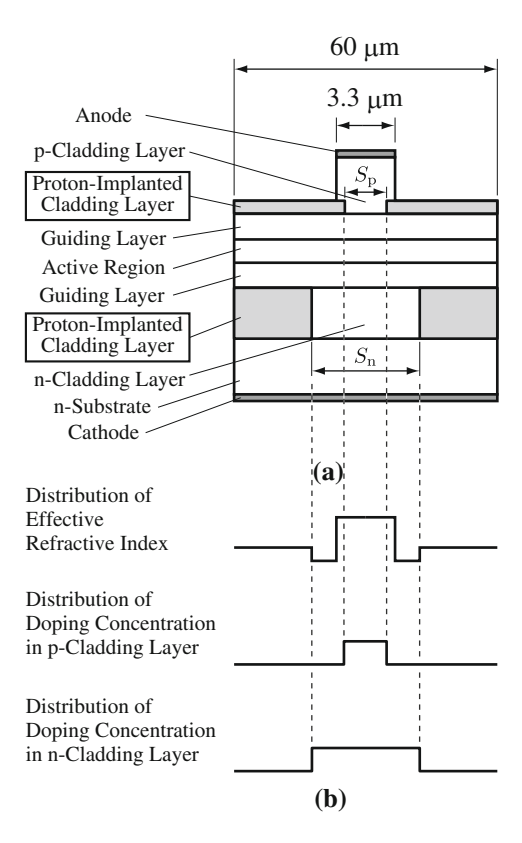


Fig. 5.43 a Schematic cross-sectional view of a proposed ridge structure with selectively proton-implanted cladding layers and **b** distributions of the effective refractive index of the semiconductor laser and doping concentration of the cladding layers. The shaded areas are undoped. Here,  $S_p$  is the space between the proton-implanted regions in the p-cladding layer;  $S_n$  is the space between the proton-implanted regions in the n-cladding layer. The distribution of the refractive index of the n-cladding layer contributes to the effective refractive index; the distribution of the refractive index of the p-cladding layer does not contribute to the effective refractive index. The proton-implanted p-Al<sub>0.2</sub>Ga<sub>0.8</sub>As cladding layer confines carriers [15] (Copyright © 2013 Springer "With kind permission of Springer Science + Business Media")

tive index of the n-cladding layer contributes to the effective refractive index; the distribution of the refractive index of the p-cladding layer does not contribute to the effective refractive index. The proton-implanted p-Al $_{0.2}$ Ga $_{0.8}$ As cladding layer confines carriers. The height of the rectangular mesa is  $1.55\,\mu m$  and the width of the rectangular mesa is  $3.3\,\mu m$ . The width of the base is  $60\,\mu m$ , and the length of the cavity is  $1,200\,\mu m$ . Reflectivities of the front and rear facets are 2 and 90%, respectively. This structure can be fabricated by two step proton-implantations after forming a ridge structure. By controlling accelerating voltage for each proton-implantation,

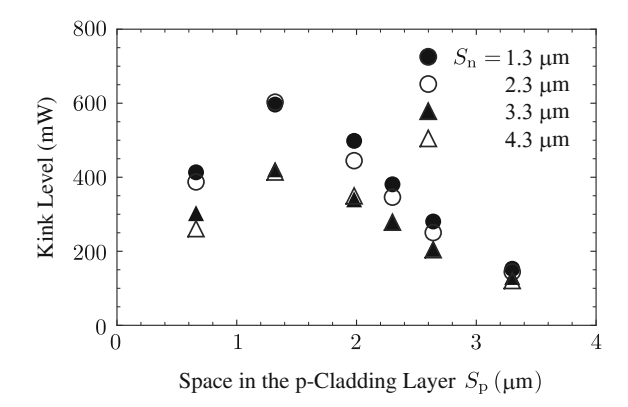


Fig. 5.44 Kink level as a function of the space  $S_p$  between the proton-implanted regions in the p-cladding layer. The kink level has a maximum value of  $603 \,\mathrm{mW}$  at  $S_p = 1.3 \,\mu\mathrm{m}$  and  $S_n = 2.3 \,\mu\mathrm{m}$ . This kink level is 1.9 times as high as the highest simulated value which was obtained previously [15] (Copyright © 2013 Springer "With kind permission of Springer Science + Business Media")

protons are implanted to the designed depth. After proton-implantations, annealing decreases optical damage, which were confirmed experimentally.

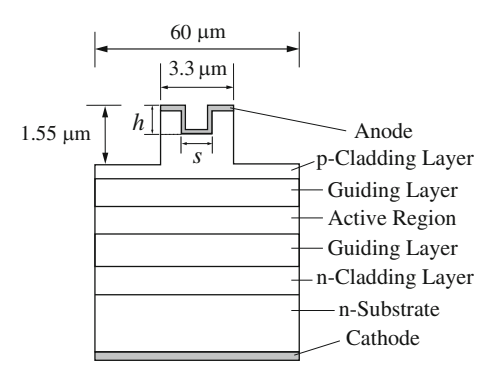
The threshold current  $I_{th}$  has a minimum value of 46.3 mA at  $S_p=1.3~\mu m$  and  $S_n=4.3~\mu m$ . This value of the threshold current is 99% of the lowest simulated value which was obtained in [14]. There is the optimum value for  $S_p$  to obtain the lowest threshold current. The reason for this is that the transverse spreading of the carriers is suppressed most efficiently at  $S_p=1.3~\mu m$ . It is considered that transverse spreading of the carriers is determined by the ambipolar transverse diffusion by the narrower space in the cladding layers  $S_p$ . The calculated ambipolar transverse diffusion length  $L_a=1.35~\mu m$  is quite similar to  $S_p=1.3~\mu m$ .

Figure 5.44 shows a kink level as a function of the space  $S_p$  between the proton-implanted regions in the p-cladding layer. The parameter is the space  $S_n$  between the proton-implanted regions in the n-cladding layer. The kink level has a maximum value of 603 mW at  $S_p = 1.3 \,\mu\text{m}$  and  $S_n = 2.3 \,\mu\text{m}$ . This kink level is 1.9 times as high as the highest simulated value in [14].

#### 5.10.3.5 Ridge LD with Horizontal Coupling

A ridge LD with horizontal coupling of horizontal transverse modes is proposed to make the fabrication process simple and achieve kink-free operation [16]. In this semiconductor laser, a groove is formed in the center of the mesa, and the horizontal transverse modes of the laser beams are determined by the coupling of the horizontal transverse modes confined by the two ridges, which are formed in the mesa. From simulations, it is found that kinks do not appear by optimizing the width and depth of the groove.

5.10 Transverse Modes 135



**Fig. 5.45** Schematic cross-sectional view of a proposed ridge structure with horizontal coupling of horizontal transverse modes. A groove is formed in the center of the mesa and two ridges are formed. Here, *S* is the width of the groove in the mesa and the space between the two ridges; *h* is the depth of the groove in the mesa and the height of the two ridges measured from the bottom of the groove [16] (Copyright © 2013 Springer "With kind permission of Springer Science + Business Media")

Figure 5.45 shows a schematic cross-sectional view of a ridge structure with horizontal coupling of horizontal transverse modes. A grove is formed in the center of the mesa and two ridges are formed. These two ridges confine horizontal transverse modes, and the horizontal transverse modes are coupled through the groove. It is expected that the coupling of the fundamental horizontal transverse modes for each ridge becomes higher than the coupling of the higher order horizontal transverse modes for each ridge. In Fig. 5.45, S is the width of the groove and the space between the two ridges; h is the depth of the groove and the height of the two ridges measured from the bottom of the groove. The height of the mesa is  $1.55 \,\mu$ m and the width of the mesa is  $3.3 \,\mu$ m. The width of the base is  $60 \,\mu$ m, and the length of the cavity is  $1,200 \,\mu$ m. Reflectivities of the front and rear facets are 2 and 90%, respectively.

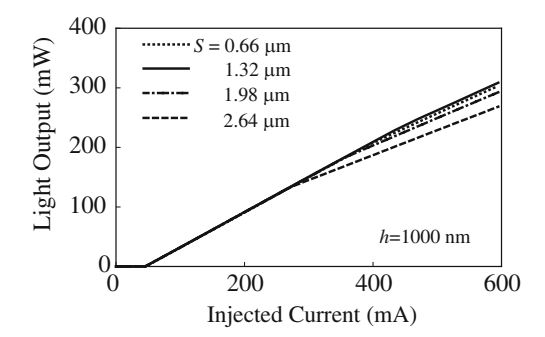


**Fig. 5.46** Injected current versus light output curves when the depth h of the groove in the mesa is 1,000 nm. The parameter is the width S of the groove in the mesa. The highest kink level is obtained at  $S = 1.32 \,\mu\text{m}$  [16] (Copyright © 2013 Springer "With kind permission of Springer Science + Business Media")

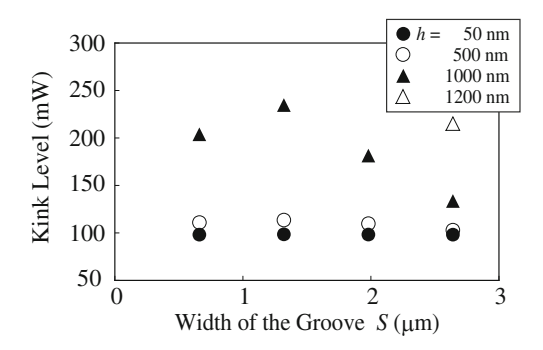


Fig. 5.47 Kink levels as a function of the width S of the groove in the mesa. With an increase in the depth h of the groove, the kink levels increase. For  $h=1,200\,\mathrm{nm}$ , kinks do not appear in  $S\leq 1.98\,\mu\mathrm{m}$  [16] (Copyright © 2013 Springer "With kind permission of Springer Science + Business Media")

Figure 5.46 shows injected current versus total light output characteristics. The parameter is the width S of the groove in the mesa. The depth h of the groove in the mesa is 1,000 nm. The kink is caused by lasing of the first-order horizontal transverse mode. The kink level depends on the width S of the groove, and the highest kink level is obtained at  $S = 1.32 \,\mu\text{m}$ .

The threshold current decreases with an increase in the depth h of the groove in the mesa. For  $h \ge 500$  nm, the threshold current decreases with an increase in the width S of the groove in the mesa. The lowest threshold current for kink-free operation is obtained at  $S = 1.98 \,\mu\text{m}$  and  $h = 1,200 \,\text{nm}$ , and its value is  $50.2 \,\text{mA}$ , which is slightly larger than the simulated lowest value of  $46.3 \,\text{mA}$  in [13]. It should be noted that kinks do not appear in the present paper while kinks appeared in [13].

Figure 5.47 shows the kink levels as a function of the width S of the groove in the mesa. The parameter is the depth h of the groove in the mesa. With an increase in the depth h of the groove, the kink levels increase. For  $h \le 1,000$  nm, the kink levels are the highest at  $S = 1.32 \, \mu \text{m}$ . For h = 1,200 nm, kinks do not appear in  $S \le 1.98 \, \mu \text{m}$  up to the injected current of 2 A. From this result, the horizontal transverse modes are coupled efficiently through the groove in  $S \le 1.98 \, \mu \text{m}$ .

# 5.10.4 Transverse Diffraction Grating

Diffraction gratings are usually utilized to control longitudinal mode in order to obtain stable single longitudinal mode operation in DFB-LDs and DBR-LDs. From the viewpoint that the propagation constant for the fundamental horizontal transverse mode and the propagation constant for the first-order horizontal transverse mode have different values, it is expected that the horizontal transverse mode is controlled by the transverse diffraction grating.

5.10 Transverse Modes 137

**Fig. 5.48** Cross-sectional view of a ridge LD with a transverse diffraction grating

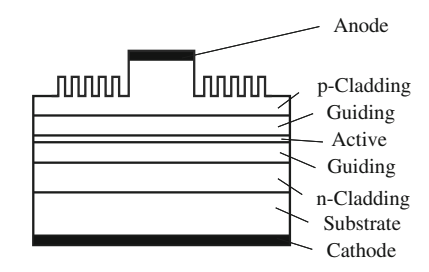


**Fig. 5.49** Horizontal near field patterns for the first-order horizontal transverse mode for a ridge LD with a transverse diffraction grating

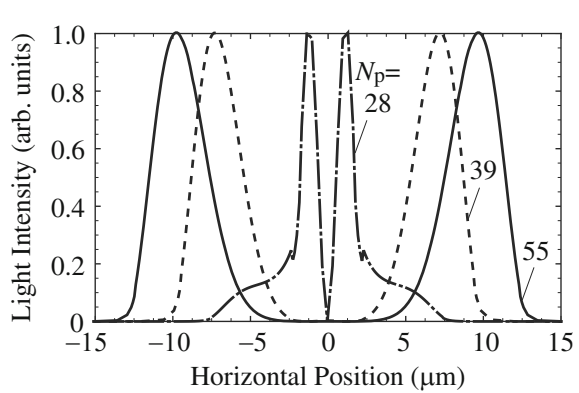


Figure 5.48 shows a cross-sectional view of a ridge LD with a transverse diffraction grating. Here, it is assumed that the structure in Fig. 5.48 has a phase-shifted transverse diffraction grating with a phase-shift  $-\Delta\Omega=\pi$ , a pitch of  $\Lambda=183\,\mathrm{nm}$ , and a depth of  $d=100\,\mathrm{nm}$ .

Figure 5.49 shows horizontal near field patterns for the first-order horizontal transverse mode with the number of pitches  $N_p$  as a parameter. The dash-dotted, broken, and solid lines correspond to  $N_p = 28$ , 39, and 55, respectively. With an increase in  $N_p$ , the peaks of the horizontal near field patterns for the first-order horizontal transverse mode move away from the center of the mesa. As a result, the optical gain for the first-order horizontal transverse mode decreases, leading to suppress laser oscillation of the first-order horizontal transverse mode.

# **5.11 Longitudinal Modes**

The *longitudinal modes*, or *axial modes*, which determine the resonance wavelengths of the cavity, show the light intensity distributions along the cavity axes. Figure 5.50 shows examples of oscillation spectra for (a) a *multimode operation* and (b) a *single-mode operation*.

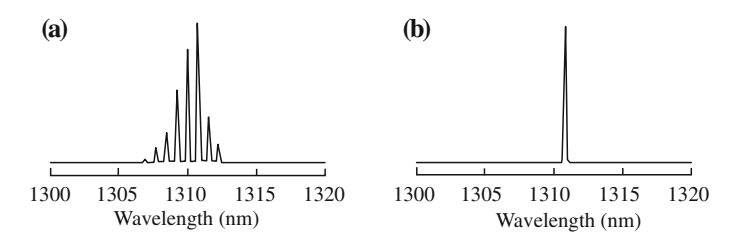


Fig. 5.50 Oscillation spectra of semiconductor lasers: a Multimode operation and b single-mode operation



Fig. 5.51 Light pulses in a a transmitter and b a receiver

Semiconductor lasers use *interband transitions* to obtain the optical gain, and the optical gain spectrum has a width of about 10 nm. Also, the Fabry-Perot cavities have a lot of resonance modes, which leads to low mode selectivity. For these two reasons, Fabry-Perot LDs tend to oscillate in multimodes. However, we do not need single-mode LDs for applications such as compact discs, laser printers, bar-code readers, laser pointers, or short-haul optical fiber communication systems, in which Fabry-Perot LDs are used.

In long-haul, large-capacity optical fiber communication systems, we need single-mode LDs because the optical fibers have *dispersions* that their refractive indexes depend on the wavelengths and modes of the lights. Due to the dispersions, the propagation speed of light changes according to the wavelengths and modes of the lights. If semiconductor lasers show multimode operations, the optical pulses broaden in a time domain while propagating the optical fibers. With an increase in the transmission distance and a decrease in the pulse spacing, adjacent optical pulses tend to overlap each other. As a result, the receivers cannot resolve sequentially transmitted optical pulses, as shown in Fig. 5.51.

To achieve single-longitudinal-mode operations, the DFB-LDs, DBR-LDs, surface emitting LDs, cleaved coupled cavity  $(C^3)$  LDs have been developed, in which the optical cavities select only one lasing mode. These single-longitudinal-mode LDs will be explained in Chap. 6; we focus on the longitudinal modes of Fabry-Perot LDs in this chapter.

Note that the longitudinal modes change with the transverse modes because the effective refractive indexes of the optical waveguides depend on the transverse modes. To achieve single-longitudinal-mode operations, we also have to obtain a single-transverse mode.

## 5.11.1 Static Characteristics of Fabry-Perot LDs

Spacing of the longitudinal modes in Fabry-Perot LDs is the same as the free spectral range  $\lambda_{FSR}$  in (4.15), which is written as

$$\lambda_{\text{FSR}} = \frac{{\lambda_0}^2}{2n_{\text{r}\lambda}L},\tag{5.80}$$

where  $\lambda_0$  is a center wavelength of a light, L is the cavity length, and  $n_{r\lambda}$  is the equivalent refractive index, which is the effective refractive index with dispersion, and is given by

$$n_{\rm r\lambda} = n_{\rm r} \left( 1 - \frac{\lambda_0}{n_{\rm r}} \, \frac{\mathrm{d}n_{\rm r}}{\mathrm{d}\lambda} \right). \tag{5.81}$$

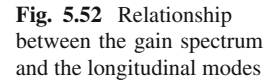
Here,  $n_{\rm r}$  is the effective refractive index of the optical waveguide for  $\lambda_0$ . Generally, we have  ${\rm d}n_{\rm r}/{\rm d}\lambda < 0$ , and the equivalent refractive index  $n_{\rm r}\lambda$  is larger than  $n_{\rm r}$ . For  $\lambda_0 = 1.55\,\mu{\rm m}$ ,  $n_{\rm r}\lambda = 3.5$ , and  $L = 300\,\mu{\rm m}$ ,  $\lambda_{\rm FSR}$  is  $11.4\,{\rm Å}$ .

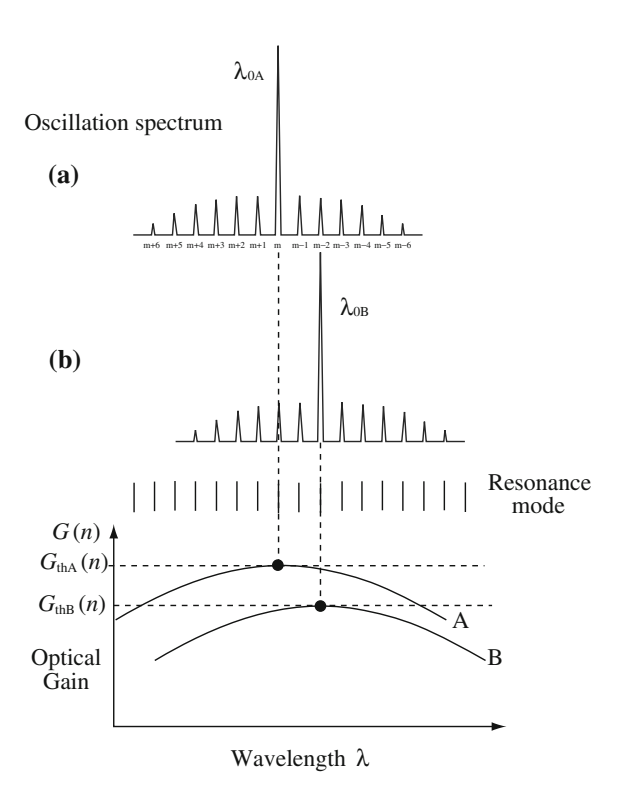
Figure 5.52 shows a relationship between the gain spectrum and the longitudinal modes. Fabry-Perot LDs oscillate at the resonance wavelength, which is closest to the gain peak. As a result, the oscillation wavelength for optical gain A is  $\lambda_{0A}$ , and that for optical gain B is  $\lambda_{0B}$ .

With an increase in the carrier concentration n, the *refractive index* decreases due to the free carrier plasma effect and increases due to Joule heating of the optical waveguide. Above the threshold, the carrier concentration in the active layer is almost constant. Therefore, above the threshold, the free carrier plasma effect does not change the refractive index, and Joule heating of the active layer enhances the refractive index with an increase in the injection current I. Hence, the resonance wavelength shifts to a longer wavelength with I ( $>I_{th}$ ) according to (5.5).

With an increase in n, the *optical gain spectrum* shifts to a shorter wavelength due to the band filling effect and to a longer wavelength due to Joule heating of the optical waveguide. The band filling effect is a phenomenon whereby the carriers fill the energy bands from the bottom, and with an increase in the carrier concentration n, the number of carriers with high energy increases. As a result, the optical gain peak shifts to a higher energy (a shorter wavelength) with an increase in n, as shown in Figs. 2.9 and 2.10. Above the threshold, the carrier concentration is almost constant, and the band filling effect is not dominant. Therefore, the gain peak shifts to a longer wavelength due to Joule heating of the optical waveguide with an increase in I.

As described earlier, with an increase in I above  $I_{th}$ , both the resonance wavelength and the gain peak shift to longer wavelengths due to Joule heating of the optical waveguide. Therefore, the oscillation wavelength increases with I. Here, it should be noted that the change rate of the resonance wavelength and that of the gain peak with a temperature  $T_j$  are different from each other. Hence, with an increase in I or  $I_j$ , the oscillation mode jumps, because the resonance wavelength closest to the gain





peak at the threshold departs from the gain peak, and other resonance wavelengths approach the gain peak.

Figure 5.53 shows dependence of the longitudinal modes on the injection current I. It is found that the longitudinal modes shift to a longer wavelength, and the mode jumps to the other mode at several values of I. Also, according to an increase or decrease in I, there exist *hysteresis loops*. Similar phenomena are observed when  $T_j$  is changed and I is kept constant. The cause of these hysteresis loops is that the optical gain concentrates on the oscillating longitudinal mode, and the optical gains for the other modes are suppressed due to coupling of modes as explained in Sect. 5.9.

The carriers, which interact in the oscillation mode, are consumed by the radiative recombination due to the stimulated emission. However, the *intraband relaxation time* of the carriers is of the order of  $10^{-12}$ – $10^{-13}$  s, and the other carriers promptly compensate the consumed carriers. Therefore, the number of carriers related to the unoscillating modes decreases, which reduces the optical gains for the unoscillating modes. Figure 5.54 schematically shows how the other carriers compensate the consumed carriers, which exist inside a rectangle.

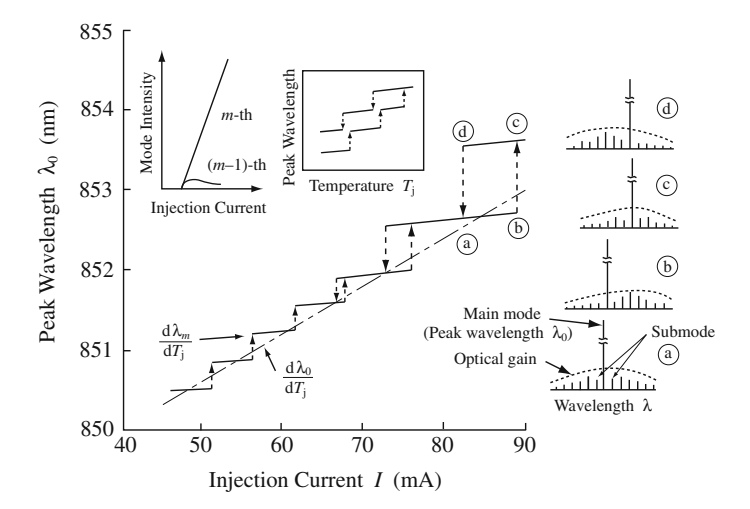
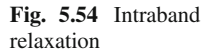
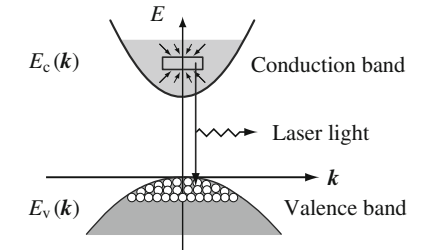


Fig. 5.53 Dependence of longitudinal modes on the injection current





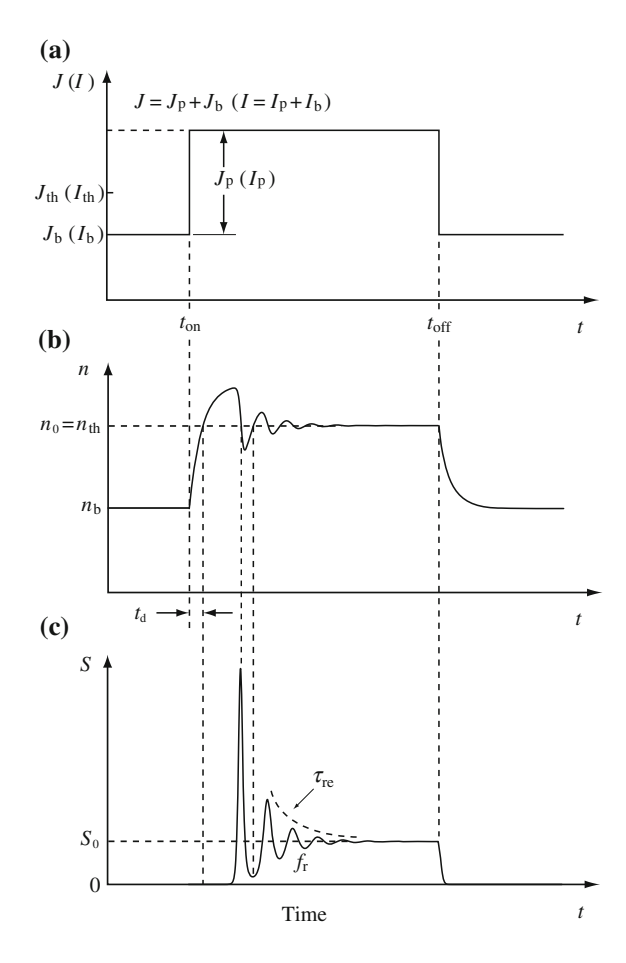
# 5.11.2 Dynamic Characteristics of Fabry-Perot LDs

#### 5.11.2.1 Turn-on Delay Time and Relaxation Oscillation

#### (i) Turn-on Delay Time

We assume that a step pulsed current is injected into a semiconductor laser. As shown in Fig. 5.55a, a bias current density  $J_b$  is below the threshold current density  $J_{th}$ , and a pulsed current density  $J_p$  is injected to the semiconductor laser at time  $t = t_{on} = 0$ . Note that the pulse width is much larger than the carrier lifetime  $\tau_n$ . The carrier concentration n increases from a bias value  $n_b$  with a time constant  $\tau_n$  and reaches the threshold carrier concentration  $n_{th}$  at  $t = t_d$ , as shown in Fig. 5.55b. This  $t_d$  is called the *turn-on delay time*, and at  $t = t_d$  laser oscillation starts. After the start of laser oscillation, the carrier concentration n and the photon density S show *relaxation oscillations*, as shown in Fig. 5.55b, c.

Fig. 5.55 Turn-on delay time and relaxation oscillation: a Current density, b carrier concentration, and c photon density



Let us calculate the turn-on delay time  $t_d$  using the rate equations. For simplicity, we neglect coupling of the spontaneous emission to the lasing mode. Therefore, when  $n < n_{th}$ , the photon density is S = 0. As a result, (5.20) reduces to

$$\frac{\mathrm{d}n}{\mathrm{d}t} = \frac{J}{ed} - \frac{n}{\tau_n}.\tag{5.82}$$

From the assumption, the current density J is given by

$$J = J_{p} \cdot u(t) + J_{b},$$

$$u(t) = \begin{cases} 0 & (t < 0), \\ 1 & (t \ge 0). \end{cases}$$
(5.83)

Substitution of (5.83) into (5.82) is followed by the *Laplace transform*. If we express a Laplace transform of n(t) as N(s) and let  $n(0) = n_b = \tau_n J_b/(ed)$ , we obtain

$$sN(s) - n(0) = sN(s) - \frac{\tau_n J_b}{ed} = \frac{J_p + J_b}{ed} \frac{1}{s} - \frac{1}{\tau_n} N(s).$$
 (5.84)

Hence, N(s) is written as

$$N(s) = \left(\frac{1}{s} - \frac{1}{s + \tau_n^{-1}}\right) \frac{\tau_n(J_p + J_b)}{ed} + \frac{\tau_n J_b}{ed} \frac{1}{s + \tau_n^{-1}}.$$
 (5.85)

When we take an *inverse Laplace transform* of N(s), we have

$$n(t) = \frac{\tau_n(J_p + J_b)}{ed} u(t) - \frac{\tau_n(J_p + J_b)}{ed} e^{-t/\tau_n} + \frac{\tau_n J_b}{ed} e^{-t/\tau_n}$$

$$= \frac{\tau_n(J_p + J_b)}{ed} u(t) - \frac{\tau_n J_p}{ed} e^{-t/\tau_n}.$$
(5.86)

In  $t \ge 0$ , we have u(t) = 1, and then (5.86) is expressed as

$$n(t) = \frac{\tau_n J}{ed} - \frac{\tau_n J_p}{ed} e^{-t/\tau_n},$$
(5.87)

where

$$J_{\rm p} + J_{\rm b} = J.$$
 (5.88)

At  $t = t_d$ , the carrier concentration n reaches the threshold carrier concentration  $n_{th}$ , and from (5.35) we have

$$n(t_{\rm d}) = n_{\rm th} = \frac{\tau_n J_{\rm th}}{ed}.$$
 (5.89)

Using (5.87)–(5.89), the turn-on delay time  $t_d$  is obtained as

$$t_{\rm d} = \tau_n \ln \frac{J - J_{\rm b}}{J - J_{\rm tb}}. (5.90)$$

For  $J_b = 0.8 J_{th}$ ,  $J = 1.2 J_{th}$ , and  $\tau_n = 2.5$  ns, we have  $t_d = 1.7$  ns.

To generate high speed optical signals by modulating the injection current into the semiconductor lasers, the turn-on delay time  $t_d$  should be short. From (5.90), it is found that a large bias current density  $J_b$ , a low threshold current density  $J_{th}$ , and a short carrier lifetime  $\tau_n$  are suitable for high-speed modulations.

It is also considered that (5.90) shows a relationship between  $t_d$  and  $\tau_n$ . Hence, by measuring  $t_d$  as a function of J or  $J_b$ , we can obtain the carrier lifetime  $\tau_n$  from (5.90). This measured result is shown in Fig. 5.56, where the bias current  $I_b$  is zero.

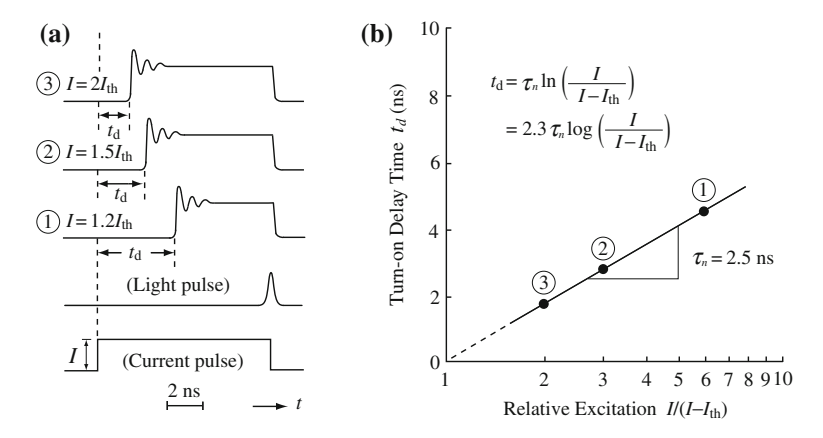


Fig. 5.56 Measurement of carrier lifetime: a Light pulses and a current pulse and b turn-on delay time as a function of relative excitation

#### (ii) Relaxation Oscillation

Let us calculate a decay coefficient and an oscillation frequency of the relaxation oscillation.

For brevity, by neglecting coupling of the spontaneous emission to the lasing mode, we solve the rate equations (5.20) and (5.21). Because there are no exact analytical solutions, Fig. 5.55 was drawn by numerically analyzing (5.20) and (5.21). However, if we use the *small-signal analysis*, we can obtain approximate analytical solutions, which clearly give us their physical meanings. To perform the small-signal analysis, we express the carrier concentration n, the photon density S, and the current density S as

$$n = n_{c0} + \delta n, \quad S = S_0 + \delta S, \quad J = J_0 + \delta J > J_{th},$$
  
 $n_{c0} \gg \delta n, \quad S_0 \gg \delta S, \quad J_0 \gg \delta J,$  (5.91)

where  $n_{c0}$ ,  $S_0$ ,  $J_0$  are the carrier concentration, the photon density, and the current density in a steady state, respectively, and  $\delta n$ ,  $\delta S$ , and  $\delta J$  are *deviations* from each steady-state value. If we assume  $J_b \gg J_p$  and exclude several initial sharp peaks in the relaxation oscillation, the conditions for the small-signal analysis are satisfied. Here, we put  $J_0 = J_b$  and  $\delta J = J_p$ .

Neglecting coupling of the spontaneous emission to the lasing mode, (5.20) and (5.21) reduce to

$$\frac{\mathrm{d}n}{\mathrm{d}t} = \frac{J}{ed} - G(n)S - \frac{n}{\tau_n},\tag{5.92}$$

$$\frac{\mathrm{d}S}{\mathrm{d}t} = G(n)S - \frac{S}{\tau_{\mathrm{ph}}}.\tag{5.93}$$

In a steady state (d/dt = 0), from (5.91) to (5.93), we have

$$\frac{J_0}{ed} - G(n_{c0})S_0 - \frac{n_{c0}}{\tau_n} = 0,$$

$$G(n_{c0}) = \frac{1}{\tau_{ph}}.$$
(5.94)

Substituting (5.91) into (5.22) results in

$$G(n) = G(n_{c0} + \delta n) = \Gamma_a g_0(n_{c0} + \delta n - n_0)$$
  
=  $\Gamma_a g_0(n_{c0} - n_0) + \Gamma_a g_0 \delta n = G(n_{c0}) + \frac{\partial G}{\partial n} \delta n,$  (5.95)

where we have introduced the differential gain, which is defined as

$$\Gamma_{a}g_{0} \equiv \frac{\partial G}{\partial n}.$$
 (5.96)

Inserting (5.91) into (5.92) and (5.93) with the help of (5.94) and (5.95) and then neglecting the second-order small term  $\delta n \cdot \delta S$ , we have the rate equations on the deviations  $\delta n$  and  $\delta S$  as

$$\frac{\mathrm{d}}{\mathrm{d}t}\delta n = \frac{\delta J}{ed} - \frac{\delta S}{\tau_{\mathrm{ph}}} - \frac{\partial G}{\partial n}S_0\delta n - \frac{\delta n}{\tau_n},\tag{5.97}$$

$$\frac{\mathrm{d}}{\mathrm{d}t}\delta S = \frac{\partial G}{\partial n}S_0\delta n. \tag{5.98}$$

From (5.98),  $\delta n$  is expressed as

$$\delta n = \frac{1}{(\partial G/\partial n)S_0} \frac{\mathrm{d}}{\mathrm{d}t} \delta S. \tag{5.99}$$

Substituting (5.97) and (5.99) into a time derivative of (5.98), we have

$$\frac{\mathrm{d}^2}{\mathrm{d}t^2}\delta S + \left(\frac{\partial G}{\partial n}S_0 + \frac{1}{\tau_n}\right)\frac{\mathrm{d}}{\mathrm{d}t}\delta S + \frac{\partial G}{\partial n}\frac{S_0}{\tau_{\mathrm{ph}}}\delta S = \frac{\partial G}{\partial n}\frac{S_0}{ed}\delta J. \tag{5.100}$$

This equation shows a relaxation oscillation on the deviation of the photon density  $\delta S$ . As a result, if we write the *decay coefficient* as  $\gamma_0$  and the *oscillation angular frequency* as  $\omega_r$ , we obtain

$$\gamma_0 = \frac{\partial G}{\partial n} S_0 + \frac{1}{\tau_n},\tag{5.101}$$

$$\omega_{\rm r}^2 = \frac{\partial G}{\partial n} \frac{S_0}{\tau_{\rm ph}}.\tag{5.102}$$

From (5.102), the relaxation oscillation frequency  $f_r$  is given by

$$f_{\rm r} = \frac{1}{2\pi} \sqrt{\frac{\partial G}{\partial n} \frac{S_0}{\tau_{\rm ph}}}.$$
 (5.103)

Note that the decay coefficient  $\gamma_0$  is related to the *decay time*  $\tau_{re}$  as

$$\gamma_0 = \frac{1}{\tau_{\rm re}}.\tag{5.104}$$

To generate high-speed optical signals by modulating the injection currents into the semiconductor lasers, the optical pulses have to quickly return to their steady-state values. Therefore, the decay coefficient  $\gamma_0$  and the relaxation oscillation frequency  $f_r$  have to be large. From (5.101) to (5.103), it is found that a large differential gain  $\partial G/\partial n$ , large photon density  $S_0$  in a steady state, short carrier lifetime  $\tau_n$ , and short photon lifetime  $\tau_{ph}$  are suitable for high-speed modulations.

Here, we consider a relationship between high-speed modulations and other characteristics. As found in (5.40) and (5.96), a large  $\partial G/\partial n$  leads to a low  $J_{th}$ , while short  $\tau_n$  and  $\tau_{ph}$  increase  $J_{th}$ . Hence, for simultaneous low-threshold and high-speed operations, we need to obtain a large  $\partial G/\partial n$ , which is achieved in the quantum well LDs (see Chap. 7). With regard to system applications, if  $S_0$  is large, light intensity is detected by a receiver even when optical pulses are not transmitted. As a result, an *extinction ratio* decreases and a *signal-to-noise* (S/N) *ratio* degrades. Therefore,  $S_0$  should be limited to satisfy specifications of applications.

The decay coefficient  $\gamma_0$  and the relaxation oscillation frequency  $f_r$  can also be expressed using the current density J. From (5.34), the threshold carrier concentration  $n_{th}$  and the transparent carrier concentration  $n_0$  are written as

$$n_{\rm th} = \frac{\tau_n}{ed} J_{\rm th}, \quad n_0 = \frac{\tau_n}{ed} J_0',$$
 (5.105)

where  $J'_0$  is the transparent current density, in which a material is transparent. From (5.39), we have

$$n_{\rm th} - n_0 = \frac{1}{\Gamma_{\rm a} g_0 \tau_{\rm ph}}. (5.106)$$

Substituting (5.96) and (5.105) into (5.106), we obtain

$$\frac{\partial G}{\partial n} = \frac{ed}{\tau_n \tau_{\text{ph}} \left( J_{\text{th}} - J_0' \right)}.$$
 (5.107)

Inserting (5.42) and (5.107) into (5.101) and (5.103), the decay coefficient  $\gamma_0$  and the relaxation oscillation frequency  $f_r$  are expressed as

$$\gamma_0 = \frac{1}{\tau_n} \frac{J - J_0'}{J_{\text{th}} - J_0'},\tag{5.108}$$

$$f_{\rm r} = \frac{1}{2\pi} \sqrt{\frac{1}{\tau_n \tau_{\rm ph}} \frac{J - J_{\rm th}}{J_{\rm th} - J_0'}}.$$
 (5.109)

# 5.11.2.2 Relationship Between the Relaxation Oscillation and the Longitudinal Modes

As shown in Fig. 5.55b, during the relaxation oscillation, the carrier concentration n deviates from  $n_{\rm th}$  by about  $\pm 10$  %. Due to this modulation in n, the optical gain and the refractive index simultaneously change, which alters the longitudinal modes.

First, we consider the optical gain. When the carrier concentration n is larger than  $n_{\rm th}$ , the optical gain g exceeds the threshold gain  $g_{\rm th}$  and the longitudinal modes with the optical gain  $g \geq g_{\rm th}$  show laser operations. Therefore, in the beginning of the relaxation oscillation, multimode laser oscillations are observed. With a decay in the relaxation oscillation, the number of the lasing longitudinal modes decreases.

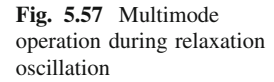
Secondly, we treat the refractive index. The refractive index is modulated by the free carrier plasma effect. When a deviation in the carrier concentration  $\delta n$  is  $2\times 10^{17}\,\mathrm{cm^{-3}}$ , the positions of the longitudinal modes shift to a shorter wavelength by about 4 Å from steady-state values. Such dynamic changes in the longitudinal modes due to modulations of n are called *chirping*. When the chirping takes place, the linewidth of the time-averaged light output spectra broaden, as shown in Fig. 5.57. Multimode laser operations and chirping are not suitable for long-haul, large-capacity optical fiber communication systems, because the optical fibers have dispersions, as described earlier.

It should be noted that the decay time of the relaxation oscillation is of the order of nanoseconds. Therefore, the effect of Joule heating with timescale longer than microseconds is negligible.

#### 5.12 Modulation Characteristics

# 5.12.1 Lightwave Transmission Systems and Modulation

From the viewpoint of light modulations in lightwave transmission systems, there are an *intensity-modulation/direct-detection* system and a *coherent* system. With regard to modulations of laser beams, there are a *direct modulation* of semiconductor lasers and an *external modulation* using optical modulators.



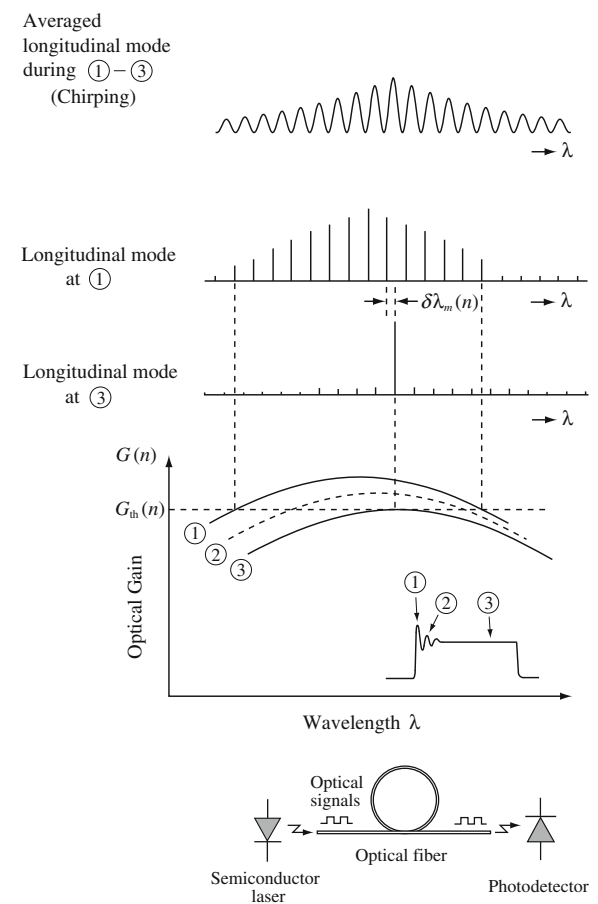


**Fig. 5.58** Intensity-modulation/direct-detection system

#### 5.12.1.1 Intensity-Modulation/Direct-Detection System

Figure 5.58 shows the intensity-modulation/direct-detection system. In this system, a transmitter sends optical signals by modulating the light intensity, while a receiver directly detects changes in the light intensity and transforms these optical signals into electric signals. This system is simpler and more cost-effective than the coherent one. Therefore, this intensity-modulation/direct-detection system is used in contemporary optical fiber communication systems. A problem with transmission distance, which was inferior to the coherent system, has been solved by the advent of *optical fiber amplifiers*.

## 5.12.1.2 Coherent System

In coherent systems, there are *amplitude shift keying* (ASK), *frequency shift keying* (FSK), and *phase shift keying* (PSK) systems according to modulations of the laser beam. As shown in Fig. 5.59, the modulated light from a master light source LD<sub>1</sub> and a light from a slave (local) light source LD<sub>2</sub> are simultaneously incident on a receiver. In the receiver, interference of these two laser beams generates an optical beat signal, which is converted to an electric signal.

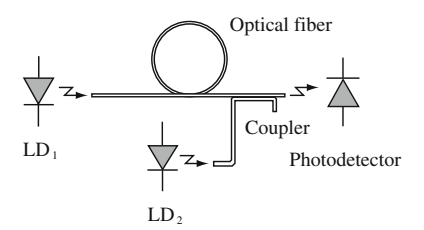
With increase in the light output of LD<sub>2</sub>, the *S/N* ratio is improved, which leads to long-haul optical fiber communication systems. However, to obtain the optical beat, we have to prepare two semiconductor lasers, whose laser lights have narrow spectral linewidths, almost common wavelengths, and the same polarizations. Moreover, we need *polarization controllers* to achieve the same polarizations, because the polarization of the lightwave changes with an increase in the propagation distance due to contortion of the laying optical fibers. Also, electronic circuits in the receiver are complicated. As a result, the cost of the coherent system is much higher than that of the intensity-modulation/direct-detection system.

#### 5.12.1.3 Direct Modulation

In direct modulation of semiconductor lasers, the injection currents into semiconductor lasers are modulated. During direct modulations, multimode operations, chirping, and changes in the turn-on delay time take place. In short-haul optical fiber communication systems, as in a building, these problems are not as serious, and the Fabry-Perot LDs can be used as light sources. In contrast, for long-haul optical fiber communication systems with a transmission distance of more than several tens of kilometers, Fabry-Perot LDs cannot satisfy the system specifications. Therefore, the DFB-LDs showing stable single-longitudinal-mode operations are used as light sources.

In the coherent system, we would like to modulate only one of the amplitude, frequency, or phase of light. However, they all simultaneously change, when conventional semiconductor lasers are directly modulated. To overcome these problems, semiconductor lasers containing phase-control regions have been developed.

Fig. 5.59 Coherent system



#### **5.12.1.4** External Modulation

In external modulation of laser beams, the injection currents into semiconductor lasers are kept constant, and the optical modulators modulate laser beams emitted from semiconductor lasers. Because the injection currents into semiconductor lasers are constant, relaxation oscillations do not exist, as opposed to direct modulation. Therefore, we can avoid multimode operations. Also, with a small change in the refractive index in the optical modulators, chirping is low. However, there are problems such as costs and optical coupling efficiencies between the optical modulators and semiconductor lasers. To overcome these problems, integrated light sources of the DFB-LDs and optical modulators have been developed and used in contemporary long-haul, large-capacity optical fiber communication systems.

Optical modulators often use Franz-Keldysh effect or quantum confined Stark effect (QCSE) as their operating principles. Franz-Keldysh effect is a shift of a fundamental absorption edge to a longer wavelength with an increase in the bias voltage of bulk semiconductors. Quantum confined Stark effect is a shift of an exciton absorption peak to a longer wavelength with an increase in the bias voltage of the semiconductor quantum structures.

In the following, we focus on direct modulation of semiconductor lasers, because it is helpful to understand peculiar characteristics of semiconductor lasers.

#### 5.12.2 Direct Modulation

#### **5.12.2.1** Dependence on Modulation Frequency

The relaxation oscillations of semiconductor lasers are analogous to a transient response theory of electric circuits, while dependence on modulation frequency corresponds to an alternating current theory.

When a deviation in the current density  $\delta J$  is related to the steady-state current density  $J_0$  as  $|\delta J| \ll J_0$ , we can use the small-signal analysis. We assume that a deviation from  $J_0$  is expressed as  $\delta J(\omega)e^{i\omega t}$ . As a result, a deviation in the carrier concentration  $\delta n$  and that in the photon density  $\delta S$  are expressed as  $\delta n = \delta n(\omega) e^{i\omega t}$ and  $\delta S = \delta S(\omega) e^{i\omega t}$ , respectively. Substituting these into (5.97) and (5.98), we have

$$\delta n(\omega) = -\frac{\mathrm{i}\,\omega}{D(\omega)} \, \frac{\delta J(\omega)}{ed},\tag{5.110}$$

$$\delta n(\omega) = -\frac{\mathrm{i}\,\omega}{D(\omega)} \frac{\delta J(\omega)}{ed}, \qquad (5.110)$$

$$\delta S(\omega) = -\frac{\tau_{\mathrm{ph}}\,\omega_{\mathrm{r}}^{2}}{D(\omega)} \frac{\delta J(\omega)}{ed}, \qquad (5.111)$$

where

$$D(\omega) = \omega^2 - \omega_r^2 - i\,\omega\gamma_0,\tag{5.112}$$

$$\gamma_0 = \frac{\partial G}{\partial n} S_0 + \frac{1}{\tau_n},\tag{5.113}$$

$$\omega_{\rm r}^2 = \frac{\partial G}{\partial n} \frac{S_0}{\tau_{\rm ph}}.\tag{5.114}$$

Note that (5.113) and (5.114) are equal to (5.101) and (5.102), respectively.

If we define a *modulation efficiency*  $\delta(\omega)$  as the number of photons generated per injected electron,  $\delta(\omega)$  is written as

$$\delta(\omega) = \left| \frac{\delta S(\omega)}{\delta J(\omega)/(ed)} \right| = \frac{\tau_{\text{ph}} \omega_{\text{r}}^2}{|D(\omega)|} = \frac{\tau_{\text{ph}} \omega_{\text{r}}^2}{\sqrt{(\omega^2 - \omega_{\text{r}}^2)^2 + \omega^2 \gamma_0^2}}, \tag{5.115}$$

where (5.111) and (5.112) were used. From (5.115), we obtain

$$\frac{\delta(\omega)}{\delta(0)} = \frac{\omega_{\rm r}^2}{\sqrt{(\omega^2 - \omega_{\rm r}^2)^2 + \omega^2 \gamma_0^2}}.$$
 (5.116)

As found in (5.116), the modulation efficiency  $\delta(\omega)$  shows resonance characteristics, and the *resonance angular frequency* is identical to the relaxation oscillation angular frequency  $\omega_r$ .

Figure 5.60 shows the modulation efficiency  $\delta(f)$  as a function of the modulation frequency  $f = \omega/2\pi$  with the injection current density J as a parameter. The modulation efficiency  $\delta(f)$  has a maximum value at a resonance frequency  $f_r$ , and  $\delta(f)$  drastically decreases with an increase in f over  $f_r$ . Therefore, the resonance frequency  $f_r$  indicates the highest limit in the modulation frequency. As shown in (5.109), with an increase in J,  $f_r$  is enhanced, which results in a large modulation bandwidth. It should be noted that electrical resistance and capacitance of semiconductor lasers also affect the modulation bandwidth.

#### **5.12.2.2** Analog Modulation and Digital Modulation

In the direct modulations of semiconductor lasers, there are *analog modulation* and *digital modulation*, as shown in Fig. 5.61.

Analog modulation transforms a change in the injection current into a change in light intensity and requires high linearity in the I-L curve. The upper limit in the modulation frequency is the resonance frequency  $f_{\rm r}$ , and the causes of high-frequency distortions are nonlinearity in the I-L curve and Joule heating during large amplitude modulations. Typical noises are optical feedback noises induced by the lights reflected from edges of the optical fibers and the modal noises generated in the optical fibers. Compared with digital modulation, analog modulation can transmit more information with lower modulation frequencies, but it is easily affected by distortions of optical signals during transmissions. As a result, analog modulation

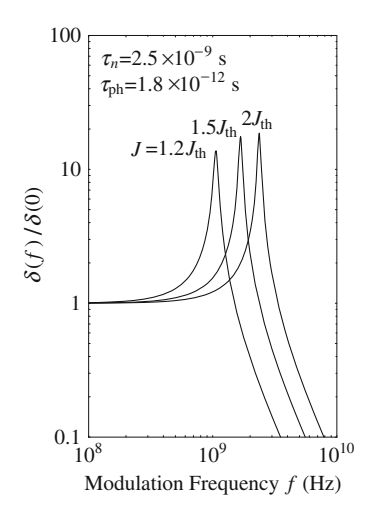


Fig. 5.60 Resonance phenomena

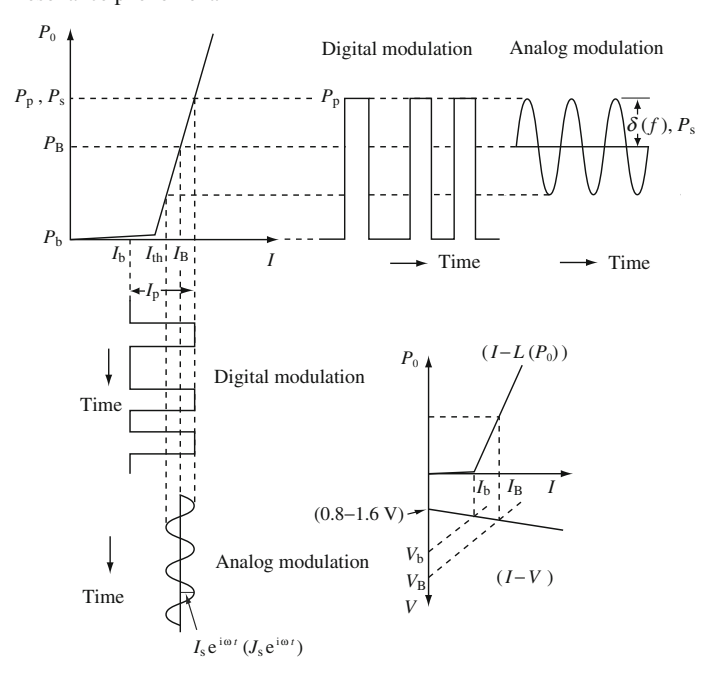


Fig. 5.61 Analog modulation and digital modulation

is used for short-haul, large-capacity optical fiber communication systems such as cable televisions (CATVs).

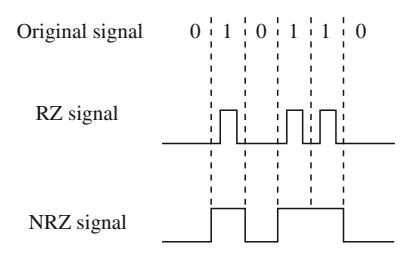


Fig. 5.62 RZ and NRZ signals

Digital modulation assigns the signal of 1/0 to ON/OFF of the light intensity. To obtain the optical pulses, which immediately follow the pulsed currents, DC bias currents are injected into semiconductor lasers to shorten the turn-on delay time. Compared with analog modulation, digital modulation is less affected by distortions of optical signals during transmission. As a result, digital modulation is used for long-haul, large-capacity optical fiber communication systems. However, to transmit a lot of information, such as motion pictures, higher modulation frequency than that of analog modulation is required.

In the following, we explain digital modulation in-depth. According to the original signals 1 and 0, there are *return-to-zero* (RZ) signal and *nonreturn-to-zero* (NRZ) signal, as shown in Fig. 5.62. In the RZ signal, a signal level is returned to zero after each signal is transmitted, which results in a large *S/N* ratio. However, we need a short pulse width, which leads to a high modulation frequency. In the NRZ signal, a signal level is not returned to zero after each signal is transmitted. Hence, if the original signal 1 continues, the signal level is kept high until the original signal 0 appears. Therefore, the *S/N* ratio is inferior to that of the RZ signal, but the modulation speed is not as high as that of the RZ signal.

Now we consider high-speed modulations to transmit large-capacity information. When the modulation speed is higher than 400 Mb/s, the pulse width is of the order of nanoseconds. In this case, the number of peaks in the relaxation oscillation for each optical pulse is at most two, and a steady state does not exist within each pulse. Hence, a decrease in average light intensity, pattern effect, and multimode operation takes place.

When the relaxation oscillation is sharp, the light intensity pulses have deep valleys and the averaged light intensity decreases, which restricts the transmission distance.

The carrier concentration in the active layer changes according to existence or nonexistence of a preceding optical pulse, which is referred to as the *pattern effect*. With a change in the remaining carrier concentration, the bias level is altered, which modifies the turn-on delay time, as shown in Fig. 5.63. In order to examine the changes in the optical pulses, an optical signal is formed by superimposing the optical pulses with the electrical pulses as the reference. This newly formed optical signal is called the *eye pattern*, because its waveform resembles an eye when a *duty* of the pulse is 50 %. When there are large deviations in the turn-on delay time, resolutions in the

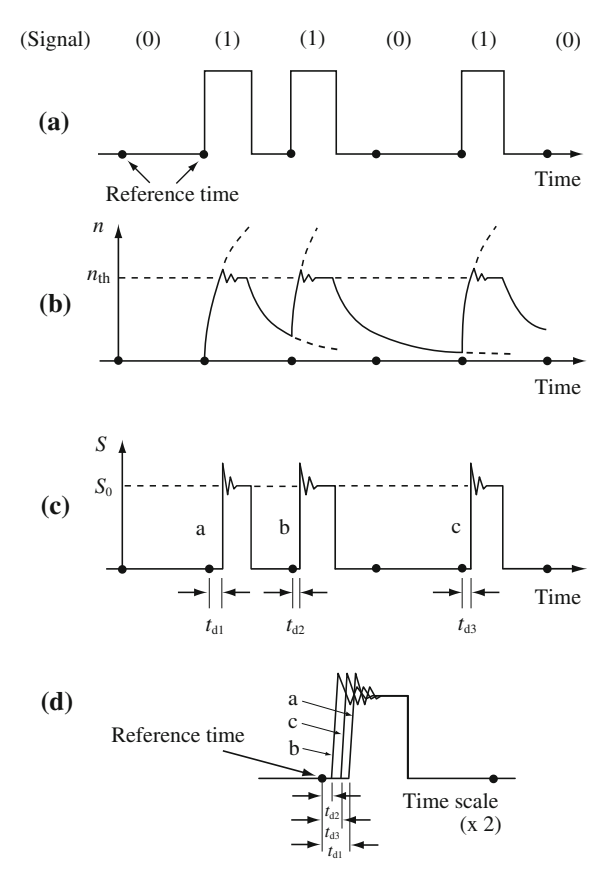


Fig. 5.63 Pattern effect: a Pulsed injection current, b injected carrier concentration, c pulsed light intensity, and d eye pattern

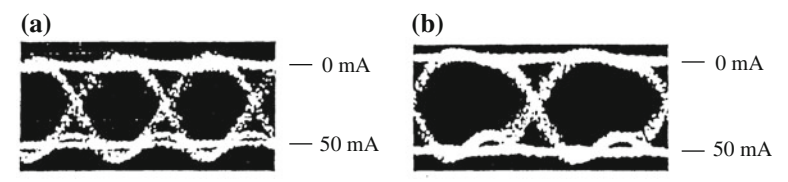


Fig. 5.64 Eye pattern: a 4 Gb/s and b 2.4 Gb/s

receiver degrade. In this case, the eye patterns collapse and a lot of jitters appear. When the deviations in the turn-on delay time are small, the eye patterns are wide open. Therefore, by observing the eye patterns, we can evaluate quality of the transmitted signals. Figure 5.64 shows examples of the eye patterns for modulation speeds of 4 and 2.4 Gb/s with a duty of 50 %. In these examples, the eye patterns are clearly open, and high-quality transmission characteristics are obtained.

**Table 5.2** Material dispersions and optical losses in glass optical fibers

Wavelength (µm)	Material dispersion (ps/Å/km)	Loss (dB/km)
0.85	9	2-3
1.30	~0	0.5
1.55	2	<0.2

When the relaxation oscillation takes place, Fabry-Perot LDs show multimode operations, which restrict the transmission distance due to the dispersions in the optical fibers. Here, we describe the dispersions in the optical fibers in detail and evaluate a relationship between the dispersions and the transmission distance.

The optical fibers have *mode dispersion*, *material dispersion*, and *structural dispersion*. Mode dispersion is a change in the effective refractive index of the optical fibers according to a mode, which corresponds to a distribution of light fields. Material dispersion, or *chromatic dispersion*, is a variation in the refractive index of the optical fibers with a wavelength of light. Structural dispersion is a change in the effective refractive index of the optical fibers with a wavelength of light for a common mode; it is caused because the refractive index of the core and that of the cladding of the optical fibers depend on a wavelength of light.

In long-haul, large-capacity optical fiber communication systems, a fundamental mode is used and the material dispersion is dominant. Table 5.2 shows the material dispersions and optical losses of the glass optical fibers for typical wavelengths of semiconductor lasers.

If five longitudinal modes lase during the relaxation oscillation, the difference in the longest and shortest wavelengths is approximately  $50\,\text{Å}$  for semiconductor lasers with a wavelength of  $1.55\,\mu\text{m}$ . When this optical signal is transmitted through the optical fibers by  $10\,\text{km}$ , the lights arrive at a receiver with a time difference of

$$2 \text{ ps/Å/km} \times 50 \text{ Å} \times 10 \text{ km} = 1 \text{ ns},$$
 (5.117)

and the optical pulse shape degrades.

Here, we summarize the key points for long-haul, large-capacity optical fiber communication systems.

For long-haul optical fiber communication systems, we need to use optical fibers with low material dispersions and low optical losses. A wavelength with the lowest dispersion is  $1.30\,\mu m$ , and a wavelength with the lowest optical loss is  $1.55\,\mu m$ . Hence, in the conventional optical fiber communication systems, wavelengths of 1.30 and  $1.55\,\mu m$  are used. In Japan, the dispersion-shifted optical fibers whose lowest dispersion wavelength is shifted from 1.30 to  $1.55\,\mu m$  are used in trunk-line systems. The light sources are required to show highly stable single-longitudinal-mode operations with low chirping and large average light output. Therefore, the DFB-LDs with excellent single-longitudinal-mode operations are adopted.

For large-capacity optical fiber communication systems, we need to shorten the turn-on delay time and enlarge the relaxation oscillation frequency (resonance fre-

quency). As a result, DC bias currents are injected into semiconductor lasers. Also, semiconductor laser structures are designed to reduce capacitance.

Finally, we briefly explain driving circuits of semiconductor lasers. The threshold current, light output, and oscillation wavelength of semiconductor lasers change with temperature. Hence, to prevent these changes in characteristics, temperature control circuits are used in the conventional optical fiber communication systems. Also, to keep the light output constant, a photodiode is placed at a rear facet of each semiconductor laser to monitor the light output, and *automatic power control* (APC) circuits are adopted.

#### 5.13 Noises

Noises related to semiconductor lasers are as follows.

- Noises Peculiar to Semiconductor Lasers
  - Ouantum noises:

AM noise (fluctuation in an amplitude of light) FM noise (fluctuation in a frequency of light)

- Noises on longitudinal modes:

Mode partition noise Mode hopping noise

- External Noises
  - Optical feedback noise
  - Noise due to fluctuations in temperature, driving current, and voltage.

## 5.13.1 Quantum Noises

#### **5.13.1.1 Fundamental Equations**

Amplitude modulating (AM) noise and frequency modulating (FM) noise are quantum noises. They are caused by spontaneous emission in a free space with random amplitudes, frequencies, and phases of the lights. Figure 5.65 shows a relationship between spontaneous emission and quantum noises such as AM noise and FM noise. In addition to spontaneous emission, FM noise is affected by AM noise as follows: Due to AM noise, the amplitude of the light field fluctuates, which modulates the carrier concentration in the active layer and leads to *carrier noise*. As a result, through the free carrier plasma effect, the refractive indexes of semiconductors fluctuate, which results in FM noise. Also, the carrier noise induced by AM noise generates *electric current noise*, which changes Joule heating in the active layer. Therefore,

5.13 Noises 157

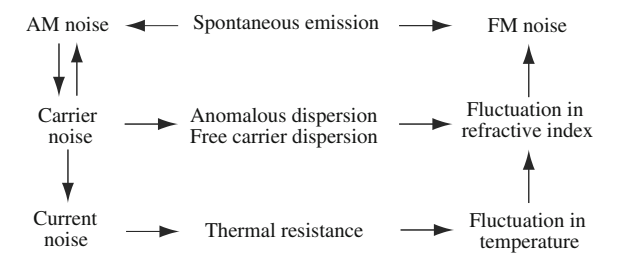


Fig. 5.65 Quantum noises

the refractive indexes of semiconductors fluctuate, which results in FM noise. AM noise is also altered by the carrier noise induced by AM noise itself.

To analyze the quantum noises, we use *semiclassical theory*, in which electromagnetic fields are treated classically and atomic systems in the fields are considered quantum mechanically [17].

From Maxwell's equations, we have an equation for the electric field E in an optical cavity for semiconductor lasers as

$$\nabla^2 \mathbf{E} - \mu \sigma \, \frac{\partial \mathbf{E}}{\partial t} - \mu \varepsilon \, \frac{\partial^2 \mathbf{E}}{\partial t^2} = \mu \, \frac{\partial^2}{\partial t^2} (\mathbf{P} + \mathbf{p}), \tag{5.118}$$

where  $\mu$  magnetic permeability;  $\sigma$  conductivity, which represents the optical losses;  $\varepsilon_0$  permittivity in a vacuum;  $n_{\rm r}$  a refractive index of the material ( $\varepsilon \equiv \varepsilon_0 \, n_{\rm r}^2$ ); P a polarization of a medium contributing to the laser transition; and p a polarization source for the spontaneous emission (Langevin source).

To derive (5.118), a vector formula

$$\nabla \times \nabla \times \mathbf{E} = \nabla(\nabla \cdot \mathbf{E}) - \nabla^2 \mathbf{E} \tag{5.119}$$

was used, and  $\nabla \cdot \mathbf{E} = 0$  was assumed.

We also suppose that the electric field  ${\it E}$  and the polarizations  ${\it P}$  and  ${\it p}$  are expressed as

$$E = \operatorname{Re}\left[\sum_{m} E_{m}(t)\boldsymbol{e}_{m}(\boldsymbol{r})\right],$$

$$P = \operatorname{Re}\left[\sum_{m} P_{m}(t)\boldsymbol{e}_{m}(\boldsymbol{r})\right],$$

$$p = \operatorname{Re}\left[\sum_{m} p_{m}(t)\boldsymbol{e}_{m}(\boldsymbol{r})\right].$$
(5.120)

Here, a spatial distribution function  $e_m(r)$  satisfies both the boundary conditions of the optical cavity and the following relation:

$$\nabla^2 \mathbf{e}_m(\mathbf{r}) + \omega_m^2 \mu \varepsilon \, \mathbf{e}_m(\mathbf{r}) = 0. \tag{5.121}$$

Also,  $e_m(r)$  is orthonormalized as

$$\int_{\text{all volume}} \mathbf{e}_m^* \cdot \mathbf{e}_n \, \mathrm{d}V = \delta_{mn} V_{\mathrm{m}}, \tag{5.122}$$

where  $V_{\rm m}$  is a *mode volume*. Substituting (5.120) into (5.118) with the help of (5.121), taking the inner product with  $e_n^*(r)$ , and using (5.122), we obtain

$$\ddot{E}_n + \frac{1}{\tau_{\text{ph}}} \dot{E}_n + \omega_n^2 E_n = -\frac{1}{\varepsilon} (\ddot{P}_n + \ddot{p}_n),$$
 (5.123)

where a dot and a double dot above  $E_n$ ,  $P_n$ , and  $p_n$  indicate a first derivative and a second derivative with respect to a time t, respectively;  $\omega_n$  is the resonance angular frequency of the nth mode; and  $\tau_{\rm ph} = \varepsilon/\sigma$  is the photon lifetime of the optical cavity. Here, we have also assumed  $\mu = \mu_0$ , which is usually satisfied in the optical materials.

The polarization of a medium  $P_n(t)$  is related to the electric field  $E_n(t)$  as

$$P_n(t) = \varepsilon_0 \left[ X^{(1)} + X^{(3)} |E_n(t)|^2 \right] E_n(t).$$
 (5.124)

Here,  $X^{(1)}$  and  $X^{(3)}$  are expressed as

$$X^{(1)} = \frac{\chi^{(1)}}{V_{\rm m}} \int_{\text{medium}} \mathbf{e}_n^* \cdot \mathbf{e}_n \, dV \approx \chi^{(1)} \, \frac{l}{L},$$

$$X^{(3)} = \frac{\chi^{(3)}}{V_{\rm m}} \int_{V_{\rm m}} (\mathbf{e}_n^* \cdot \mathbf{e}_n)^2 \, dV \approx \chi^{(3)} \, \frac{3l}{2L},$$
(5.125)

where  $\chi^{(1)}$  and  $\chi^{(3)}$  are the first and third optical susceptibilities, respectively; l is the crystal length; L is the cavity length; and  $V_{\rm m}$  is the mode volume.

Under the assumption of single-mode operation, we express the electric field  $E_n(t)$  and the polarization source for the spontaneous emission (Langevin source)  $p_n(t)$  as

$$E_n(t) = [A_0 + \delta(t)] e^{i[\omega_m t + \phi(t)]},$$
  
$$-\frac{1}{\varepsilon} \frac{\partial^2 p_n}{\partial t^2} = \Delta(t) e^{i[\omega_m t + \phi(t)]},$$
 (5.126)

5.13 Noises 159

where  $A_0$  an averaged amplitude of the electric field,  $\delta(t)$  a deviation in the amplitude of the electric field from  $A_0$ ,  $\phi(t)$  an instantaneous phase,  $\Delta(t)$  a random function representing spontaneous emission, and  $\omega_m$  an average angular frequency of laser light.

We also assume that  $\delta(t)$ ,  $\phi(t)$ , and  $\Delta(t)$  are slowly varying functions compared with  $\omega_m$ . For brevity, we neglect the carrier fluctuations. We further suppose that

$$\delta(t) \ll A_0, \quad \langle \delta(t) \rangle = \langle \phi(t) \rangle = \langle \Delta(t) \rangle = 0,$$
 (5.127)

where  $\langle \cdots \rangle$  shows a *time average* or an *ensemble average*. Substituting (5.124) and (5.126) into (5.123), we obtain

$$2 i \omega_{m} \left( \frac{\partial \delta}{\partial t} + i A_{0} \frac{\partial \phi}{\partial t} \right) + \frac{3A_{0}^{2} X^{(3)}}{n_{r}^{2}} \left( 2 i \omega_{m} \frac{\partial \delta}{\partial t} - \omega_{m}^{2} \delta \right) + \left[ \omega_{n}^{2} - \omega_{m}^{2} + i \frac{\omega_{m}}{\tau_{ph}} - (X^{(1)} + A_{0}^{2} X^{(3)}) \frac{\omega_{m}^{2}}{n_{r}^{2}} \right] A_{0} = \Delta(t), \quad (5.128)$$

where  $\varepsilon \equiv \varepsilon_0 n_{\rm r}^2$  ( $n_{\rm r}$ : a refractive index of the material) was used.

A real part and an imaginary part of the steady-state solution of (5.128) are given by

$$\omega_m^2 = \omega_n^2 \left[ 1 + \frac{X_r^{(1)} + A_0^2 X_r^{(3)}}{n_r^2} \right]^{-1}$$
: real, (5.129)

$$A_0^2 = -\frac{1}{X_i^{(3)}} \left( X_i^{(1)} + \frac{n_r^2}{\omega_m \tau_{\text{ph}}} \right)$$
: imaginary, (5.130)

where  $X^{(1,3)} = X_{\rm r}^{(1,3)} - i X_{\rm i}^{(1,3)}$ .

Therefore, (5.128) reduces to

$$A_0 \frac{\partial \phi}{\partial t} - \frac{3A_0^2 X_1^{(3)}}{n_r^2} \frac{\partial \delta}{\partial t} + \frac{3A_0^2 \omega_m X_r^{(3)}}{2n_r^2} \delta = -\frac{\Delta_r(t)}{2\omega_m} : \text{real},$$
 (5.131)

$$\left(1 + \frac{3A_0^2 X_{\rm r}^{(3)}}{n_{\rm r}^2}\right) \frac{\partial \delta}{\partial t} + \frac{3A_0^2 \omega_m X_{\rm i}^{(3)}}{2n_{\rm r}^2} \delta = \frac{\Delta_{\rm i}(t)}{2\omega_m} : \text{imaginary},$$
(5.132)

where  $\Delta(t) = \Delta_{\rm r}(t) + {\rm i}\,\Delta_{\rm i}(t)$ . These equations are the fundamental equations for noises in the laser light, when the carrier fluctuations are neglected. In (5.131), the second term on the left-hand side is usually neglected because it is smaller than the other terms. As a result, the amplitude fluctuation  $\delta$  and the phase fluctuation  $\phi$  are related to each other by the term including  $X_{\rm r}^{(3)}$ .

## 5.13.1.2 Spectra of a Laser Light

Among the spectra of laser lights, there are a *power fluctuation spectrum* expressing the AM noise, a *frequency fluctuation spectrum* indicating the FM noise, and a *field spectrum*. Figure 5.66 shows a measurement system for these spectra. It should be noted that a *spectral linewidth* of laser light usually represents a linewidth of the field spectrum.

To obtain the spectra of laser lights, we first calculate the *autocorrelation func*tions of the fluctuations using (5.131) and (5.132). Then, with the help of *Wiener-Khintchine theorem*, we have *spectral density functions*.

## (i) Autocorrelation Function of the Amplitude Fluctuation $\delta(t)$

For a usual laser field,  $A_0^2 X_{\rm r}^{(3)}/n_{\rm r}^2 \ll 1$  is satisfied. As a result, (5.132) reduces to

$$\frac{\partial \delta}{\partial t} + \omega_1 \delta = \frac{\Delta_i(t)}{2\omega_m}, \quad \omega_1 = \frac{3A_0^2 \omega_m X_i^{(3)}}{2n_r^2} > 0.$$
 (5.133)

Taking a Laplace transform of (5.133), we have

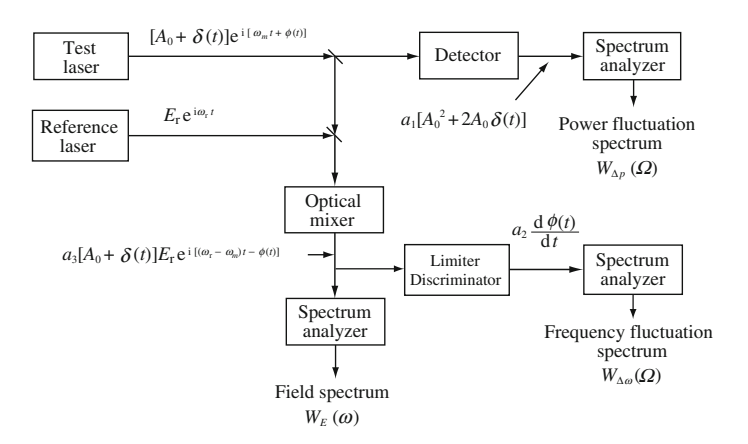


Fig. 5.66 Measurement system for spectra of a laser light

5.13 Noises 161

$$-\delta(0) + s\tilde{\delta}(s) + \omega_1 \tilde{\delta}(s) = \frac{\tilde{\Delta}_{i}(s)}{2\omega_m},$$

$$\tilde{\delta}(s) \equiv \int_{0}^{\infty} \delta(t) e^{-st} dt,$$

$$\tilde{\Delta}_{i}(s) \equiv \int_{0}^{\infty} \Delta_{i}(t) e^{-st} dt.$$
(5.134)

Supposing  $\delta(0) = 0$ , (5.134) results in

$$\tilde{\delta}(s) = \frac{\tilde{\Delta}_{i}(s)}{2\omega_{m}(s + \omega_{1})}.$$
(5.135)

Taking an inverse Laplace transform of (5.135), we obtain  $\delta(t)$  as

$$\delta(t) = \frac{1}{2\omega_m} \int_0^t \Delta_{\mathbf{i}}(\lambda) e^{-\omega_{\mathbf{i}}(t-\lambda)} d\lambda.$$
 (5.136)

From (5.136), the autocorrelation function  $\langle \delta(t+\tau)\delta(t)\rangle$  of the amplitude fluctuation  $\delta(t)$  is given by

$$\langle \delta(t+\tau)\delta(t)\rangle = \frac{1}{4\omega_m^2} \int_0^{t+\tau} d\lambda_1 \int_0^t d\lambda_2 \langle \Delta_i(\lambda_1)\Delta_i(\lambda_2)\rangle \times e^{-\omega_1(t+\tau-\lambda_1)} e^{-\omega_1(t-\lambda_2)}.$$
 (5.137)

Here, we assume that the correlation functions of the Langevin sources are written as

$$\langle \Delta_{\mathbf{i}}(\lambda_1) \Delta_{\mathbf{i}}(\lambda_2) \rangle = \langle \Delta_{\mathbf{r}}(\lambda_1) \Delta_{\mathbf{r}}(\lambda_2) \rangle = W \cdot D(\lambda_1 - \lambda_2),$$
  
$$\langle \Delta_{\mathbf{i}}(\lambda_1) \Delta_{\mathbf{r}}(\lambda_2) \rangle = \langle \Delta_{\mathbf{r}}(\lambda_1) \Delta_{\mathbf{i}}(\lambda_2) \rangle = 0,$$
  
(5.138)

where D(x) is a  $\delta$  function and W is a coefficient related to the spontaneous emission, which will be calculated later. Substituting (5.138) into (5.137), we obtain

$$\langle \delta(t+\tau)\delta(t)\rangle = \frac{W}{8\omega_m^2\omega_1} e^{-\omega_1|\tau|} (1 - e^{-2\omega_1 t}). \tag{5.139}$$

As a result, in a steady state where t is long enough, we have

$$\langle \delta(t+\tau)\delta(t)\rangle = \frac{W}{8\omega_m^2\omega_1} e^{-\omega_1|\tau|}.$$
 (5.140)

#### (ii) Autocorrelation Function of the Phase Fluctuation $\phi(t)$

The second term on the left-hand side of (5.131) is small enough compared with the other terms. Therefore, (5.131) reduces to

$$A_0 \frac{\partial \phi}{\partial t} + \frac{3A_0^2 \omega_m X_{\rm r}^{(3)}}{2n_{\rm r}^2} \delta = -\frac{\Delta_{\rm r}(t)}{2\omega_m}.$$
 (5.141)

When  $\phi(0) = 0$ , integration of (5.141) with respect to t results in

$$\phi(t) = -\frac{3}{4} \frac{X_{\rm r}^{(3)} A_0}{n_{\rm r}^2 \omega_1} \left[ \int_0^t \Delta_{\rm i}(\lambda) \, \mathrm{d}\lambda - \int_0^t \Delta_{\rm i}(\lambda) \mathrm{e}^{-\omega_1(t-\lambda)} \, \mathrm{d}\lambda \right]$$
$$-\frac{1}{2A_0 \omega_m} \int_0^t \Delta_{\rm r}(\lambda) \, \mathrm{d}\lambda, \tag{5.142}$$

where (5.136) was used.

From (5.133), (5.138), and (5.142), the autocorrelation function  $\langle \phi(t_1)\phi(t_2)\rangle$  of the phase fluctuation  $\phi(t)$  is given by

$$\langle \phi(t_1)\phi(t_2)\rangle = \frac{W}{4\omega_m^2 A_0^2} (1 + \alpha^2) \times \begin{cases} t_1 & (t_1 < t_2), \\ t_2 & (t_1 > t_2). \end{cases}$$
(5.143)

Here, we have introduced

$$\alpha \equiv \frac{X_{\rm r}^{(3)}}{X_{\rm i}^{(3)}},\tag{5.144}$$

which is called the  $\alpha$  parameter or the spectral linewidth enhancement factor. Using the following relation:

$$X = X_{r} - i X_{i},$$

$$X_{r} = X_{r}^{(1)} + X_{r}^{(3)} |E_{n}|^{2},$$

$$X_{i} = X_{i}^{(1)} + X_{i}^{(3)} |E_{n}|^{2},$$
(5.145)

we can rewrite (5.144) as

$$\alpha = \frac{X_{\rm r}^{(3)}}{X_{\rm i}^{(3)}} = \frac{\partial X_{\rm r}}{\partial |E_n|^2} \left(\frac{\partial X_{\rm i}}{\partial |E_n|^2}\right)^{-1} = \frac{\partial X_{\rm r}}{\partial n} \left(\frac{\partial X_{\rm i}}{\partial n}\right)^{-1},\tag{5.146}$$

5.13 Noises 163

where we have assumed that the light intensity, which is linearly proportional to  $|E_n|^2$ , is in proportion to the carrier concentration n. It should be noted that this  $\alpha$  parameter is important to characterize the spectral linewidth and the optical feedback noise in the semiconductor lasers.

#### (iii) Autocorrelation Function of the Angular Frequency Fluctuation $\Delta\omega(t)$

Using the averaged angular frequency  $\omega_m$  and the phase fluctuation  $\phi(t)$ , we can express the instantaneous angular frequency  $\omega(t)$  of a laser light as

$$\omega(t) = \omega_m + \frac{\partial \phi}{\partial t}.\tag{5.147}$$

As a result, the fluctuation in the angular frequency  $\Delta\omega(t)$  is written as

$$\Delta\omega(t) \equiv \omega(t) - \omega_m = \frac{\partial\phi}{\partial t}.$$
 (5.148)

Hence, the autocorrelation function  $\langle \Delta \omega(t_1) \Delta \omega(t_2) \rangle$  of the angular frequency fluctuation  $\Delta \omega(t)$  is obtained as

$$\langle \Delta\omega(t_1)\Delta\omega(t_2)\rangle = \langle \dot{\phi}(t_1)\dot{\phi}(t_2)\rangle$$

$$= \frac{W}{4\omega_m^2 A_0^2} \left[ D(t_1 - t_2) + \frac{\alpha^2}{2} \omega_1 e^{-\omega_1|t_1 - t_2|} \right], \quad (5.149)$$

where (5.140), (5.141), and (5.146) were used, and a dot above  $\phi$  represents a first derivative with respect to time.

#### (iv) Spectral Density Function

To obtain spectra of laser lights, we calculate the spectral density functions of the amplitude fluctuation  $\delta(t)$  and the angular frequency fluctuation  $\Delta\omega(t)$  using Wiener-Khintchine theorem.

From (5.140), the spectral density function  $W_{\delta}(\Omega)$  of the amplitude fluctuation  $\delta(t)$  is obtained as

$$W_{\delta}(\Omega) = \frac{1}{\pi} \int_{-\infty}^{\infty} \langle \delta(t+\tau)\delta(t) \rangle e^{-i\Omega\tau} d\tau$$
$$= \frac{W}{4\pi \omega_m^2 (\Omega^2 + \omega_1^2)}.$$
 (5.150)

From (5.149), the spectral density function  $W_{\Delta\omega}(\Omega)$  of the angular frequency fluctuation  $\Delta\omega(t)$  is given by

$$W_{\Delta\omega}(\Omega) = \frac{1}{\pi} \int_{-\infty}^{\infty} \langle \Delta\omega(t+\tau)\Delta\omega(t) \rangle e^{-i\Omega\tau} d\tau$$
$$= \frac{W}{4\pi\omega_m^2 A_0^2} \left( 1 + \frac{\alpha^2 \omega_1^2}{\Omega^2 + \omega_1^2} \right). \tag{5.151}$$

#### (v) Coefficient W

The generation rate of the spontaneous emission is expressed as  $E_{cv}\hbar\omega_m$  where  $E_{cv}$  is the number of photons spontaneously emitted to an oscillation mode per time. The dissipation rate of the spontaneous emission is given by  $\Psi_s/\tau_{ph}$  where  $\Psi_s$  is an energy of the spontaneous emission coupled to the oscillation mode and  $\tau_{ph}$  is the photon lifetime. In a steady state, the generation rate is balanced with the dissipation rate. As a result, we have

$$\Psi_{\rm s} = E_{\rm cv}\hbar\omega_m\tau_{\rm ph}.\tag{5.152}$$

The electric field of the spontaneous emission is given by a solution of the following equation:

$$\ddot{E}_n + \frac{1}{\tau_{\text{ph}}} \dot{E}_n + \omega_n^2 E_n = [\Delta_{\text{r}}(t) + i \, \Delta_{\text{i}}(t)] \, e^{i \, \omega_m t}, \qquad (5.153)$$

where the polarization due to stimulated emission in (5.123) is neglected and  $\omega_n \approx \omega_m$  is assumed.

If we suppose  $E(0) = \dot{E}(0)$ , as a solution of (5.153), we have

$$E(t) = \frac{1}{\omega_m} \int_{0}^{t} d\tau [\Delta_{\rm r}(\tau) + i \Delta_{\rm i}(\tau)] e^{i \omega_m \tau} e^{-(t-\tau)/(2\tau_{\rm ph})} \sin[\omega_m(t-\tau)]. \quad (5.154)$$

Hence,  $\langle E^*(t)E(t)\rangle$  is given by

$$\langle E^*(t)E(t)\rangle = \frac{1}{\omega_m^2} \int_0^t d\lambda_1 \int_0^t d\lambda_2 \, 2W D(\lambda_1 - \lambda_2) \, e^{-t/\tau_{\text{ph}}} \, e^{(\lambda_1 + \lambda_2)/(2\tau_{\text{ph}})}$$

$$\times \sin[\omega_m(t - \lambda_1)] \sin[\omega_m(t - \lambda_2)]$$

$$= \frac{W \tau_{\text{ph}}}{\omega_m^2}, \qquad (5.155)$$

5.13 Noises 165

where (5.138) was used.

With the help of (5.155), a steady-state spontaneous emission energy  $\Psi_s$  is expressed as

$$\Psi_{\rm S} = \varepsilon V_{\rm m} \langle E^*(t) E(t) \rangle = \frac{\varepsilon V_{\rm m} W \tau_{\rm ph}}{\omega_m^2},$$

$$V_{\rm m} \equiv \int |\boldsymbol{e}_n(\boldsymbol{r})|^2 \, \mathrm{d}V,$$
(5.156)

where  $\varepsilon$  is the dielectric constant of a material and  $V_{\rm m}$  is the mode volume.

From (5.152) and (5.156), W is obtained as

$$W = \frac{\hbar \omega_m^3 E_{\rm cv}}{\varepsilon V_{\rm m}}.$$
 (5.157)

## (vi) Intensity Fluctuation Spectrum (AM Noise)

To obtain the *intensity fluctuation spectrum*, we first clarify a relationship between the amplitude fluctuation  $\delta(t)$  and the intensity fluctuation.

The light emission rate  $\gamma$  from the optical cavity through the mirrors is given by

$$\gamma = \frac{c}{n_{\rm r}} \frac{1}{L} \ln \frac{1}{R},\tag{5.158}$$

where c is the speed of light in a vacuum,  $n_{\rm r}$  is the refractive index of a material, L is the cavity length, and R is the power reflectivity of a facet where both facets are assumed to have common reflectivity.

Let the electric field of the laser light be  $E_n$ ; then the light output P is expressed as

$$P = \varepsilon E_n^2 V_{\rm m} \gamma. \tag{5.159}$$

From (5.126) and (5.159), an averaged light output  $P_0$  and the fluctuation in the light output  $\Delta P = P - P_0$  are written as

$$P_0 = \varepsilon A_0^2 V_{\rm m} \gamma, \quad \Delta P = 2\varepsilon A_0 \delta V_{\rm m} \gamma.$$
 (5.160)

From (5.150), (5.157), (5.158), and (5.160), the spectral density function  $W_{\Delta P}(\Omega)$  of the light output fluctuation  $\Delta P$  is obtained as

$$\begin{split} W_{\Delta P}(\Omega) &= \frac{1}{\pi} \int_{-\infty}^{\infty} \langle \Delta P(t+\tau) \Delta P(t) \rangle \, \mathrm{e}^{-\mathrm{i}\Omega\tau} \, \mathrm{d}\tau \\ &= 4\varepsilon^2 A_0^2 V_\mathrm{m}^2 \gamma^2 W_\delta(\Omega) = \frac{\hbar \omega_m \varepsilon A_0^2 V_\mathrm{m} E_\mathrm{cv} \gamma^2}{\pi (\Omega^2 + \omega_1^2)} \\ &= \frac{\hbar \omega_m E_\mathrm{cv} P_0 \gamma}{\pi (\Omega^2 + \omega_1^2)} = \frac{\hbar \omega_m c E_\mathrm{cv} P_0 \ln(1/R)}{\pi (\Omega^2 + \omega_1^2) n_\mathrm{r} L}. \end{split} \tag{5.161}$$

#### (vii) Frequency Fluctuation Spectrum (FM Noise)

From (5.151), (5.157), (5.158), and (5.160), the spectral density function  $W_{\Delta\omega}(\Omega)$  of the angular frequency fluctuation  $\Delta\omega(t)$  is given by

$$W_{\Delta\omega}(\Omega) = \frac{\hbar\omega_m E_{\text{cv}}}{4\pi \varepsilon V_{\text{m}} A_0^2} \left( 1 + \frac{\alpha^2 \omega_1^2}{\Omega^2 + \omega_1^2} \right)$$
$$= \frac{\hbar\omega_m c E_{\text{cv}} \ln(1/R)}{4\pi P_0 n_{\text{r}} L} \left( 1 + \frac{\alpha^2 \omega_1^2}{\Omega^2 + \omega_1^2} \right). \tag{5.162}$$

#### (viii) Field Spectrum

The field spectrum is most frequently used as the laser light spectrum. Contribution of the amplitude fluctuation to the correlation function of the electric field is negligibly small, and the correlation function  $\langle E(t+\tau)E(t)\rangle$  is given by

$$\langle E(t+\tau)E(t)\rangle = \frac{1}{4} \langle [E(t+\tau) + E^*(t+\tau)][E(t) + E^*(t)]\rangle$$

$$= \frac{A_0^2}{4} [e^{-i\omega_m \tau} \langle e^{i\Delta\phi} \rangle + \text{c.c.}],$$

$$\Delta\phi \equiv \phi(t+\tau) - \phi(t).$$
(5.163)

The phase fluctuation  $\Delta \phi$ , which is important to determine the correlation function  $\langle E(t+\tau)E(t)\rangle$ , is related to many independent spontaneous emission processes. As a result, the distribution of  $\Delta \phi$  is given by the *Gaussian distribution function*  $g(\Delta \phi)$ , which is defined as

$$g(\Delta\phi) = \frac{1}{\sqrt{2\pi \langle (\Delta\phi)^2 \rangle}} e^{-\frac{(\Delta\phi)^2}{2\langle (\Delta\phi)^2 \rangle}}.$$
 (5.164)

Therefore, we obtain

5.13 Noises 167

$$\langle e^{i\Delta\phi} \rangle = \int_{-\infty}^{\infty} g(\Delta\phi) e^{i\Delta\phi} d(\Delta\phi) = e^{-\frac{1}{2}\langle (\Delta\phi)^2 \rangle}.$$
 (5.165)

Because  $(\Delta \phi)^2$  on the right-hand side of (5.165) is independent of a time t, we obtain

$$\langle (\Delta \phi)^2 \rangle = \frac{W}{4 \omega_m^2 A_0^2} (1 + \alpha^2) |\tau|,$$
 (5.166)

where we have assumed  $t_1 = t_2 = \tau$  in (5.143). Substituting (5.165) and (5.166) into (5.163) results in

$$\langle E(t+\tau)E(t)\rangle = \frac{A_0^2}{2} \exp\left[-\frac{W}{8\omega_m^2 A_0^2} (1+\alpha^2)|\tau|\right] \cos(\omega_m \tau).$$
 (5.167)

With the help of Wiener-Khintchine theorem, the spectral density function  $W_E(\omega)$  of the electric field is given by

$$W_E(\omega) = \frac{1}{\pi} \int_{-\infty}^{\infty} \langle E(t+\tau)E(t)\rangle e^{-i\omega\tau} d\tau$$

$$\approx \frac{A_0^2}{4\pi} \frac{\Delta\omega_0}{(\omega-\omega_m)^2 + (\Delta\omega_0/2)^2},$$
(5.168)

$$\Delta\omega_0 \equiv \frac{\hbar\omega_m c E_{\rm cv} \ln(1/R)}{4P_0 n_{\rm r} L} (1 + \alpha^2). \tag{5.169}$$

From (5.168), the field spectrum is *Lorentzian*, and the FWHM of the field spectrum  $\Delta\omega_0$  in (5.169), which is called *modified Schawlow-Townes linewidth formula*, gives the spectral linewidth for semiconductor lasers. In solid-state or gas lasers, the term  $\alpha^2$  can be neglected because  $\alpha^2 \ll 1$ . In contrast, in semiconductor lasers, the term  $\alpha^2$  is needed because  $\alpha^2 > 1$ . It should be noted that the fluctuation in the carrier concentration was neglected in the derivation of (5.168) and (5.169).

#### **5.13.1.3** Spectral Linewidth Enhancement Factor α

The spectral linewidth enhancement factor  $\alpha$  is an important parameter that differentiates semiconductor lasers from other lasers. As shown in (5.146),  $\alpha$  is given by

$$\alpha = \frac{\partial X_{\rm r}}{\partial n} \left( \frac{\partial X_{\rm i}}{\partial n} \right)^{-1}.$$
 (5.170)

Here, let us express  $\alpha$  using the refractive index and the optical gain. Using the complex refractive index  $\tilde{n} = n_r - i \kappa$ , the complex dielectric constant  $\tilde{\varepsilon}$  is written

as

$$\tilde{\varepsilon} = \varepsilon_0 \tilde{n}^2 = \varepsilon_0 [(n_r^2 - \kappa^2) - i \, 2n_r \kappa] = \varepsilon_0 (X_r - i \, X_i), \tag{5.171}$$

where

$$X_{\rm r} = n_{\rm r}^2 - \kappa^2, \quad X_{\rm i} = 2n_{\rm r}\kappa.$$
 (5.172)

In the vicinity of the bandgap in semiconductors  $n_r \gg \kappa$  is satisfied, and we obtain

$$\frac{\partial X_{\rm r}}{\partial n} = 2n_{\rm r} \frac{\partial n_{\rm r}}{\partial n} - 2\kappa \frac{\partial \kappa}{\partial n} \approx 2n_{\rm r} \frac{\partial n_{\rm r}}{\partial n},\tag{5.173}$$

$$\frac{\partial X_{\rm i}}{\partial n} = 2n_{\rm r} \frac{\partial \kappa}{\partial n} + 2\kappa \frac{\partial n_{\rm r}}{\partial n} \approx 2n_{\rm r} \frac{\partial \kappa}{\partial n}.$$
 (5.174)

Substituting (5.173) and (5.174) into (5.170) leads to

$$\alpha = \frac{\partial n_{\rm r}}{\partial n} \left( \frac{\partial \kappa}{\partial n} \right)^{-1}.$$
 (5.175)

Using the extinction coefficient  $\kappa$  in (5.171), we can express the optical power gain coefficient g as

$$g = -\frac{2\omega_m}{c} \,\kappa. \tag{5.176}$$

Also, g is related to G(n) in the rate equations as

$$G(n) = \frac{c}{n_r} g. ag{5.177}$$

Using (5.176) and (5.177), we have

$$\frac{\partial \kappa}{\partial n} = -\frac{n_{\rm r}}{2\omega_m} \frac{\partial G}{\partial n}.\tag{5.178}$$

Substituting (5.178) into (5.175) results in

$$\alpha = -\frac{2\omega_m}{n_r} \frac{\partial n_r}{\partial n} \left(\frac{\partial G}{\partial n}\right)^{-1}.$$
 (5.179)

When the optical gain increases with carrier injection  $(\partial G/\partial n > 0)$  and Joule heating of the active layer is negligibly small, the refractive index decreases  $(\partial n_{\rm T}/\partial n < 0)$  due to the free carrier plasma effect. Hence,  $\alpha$  defined in (5.179) is positive, and the measured values are between 1 and 7. From (5.179), it is found that we should increase  $\partial G/\partial n$  to reduce the value of  $\alpha$ , which is achieved in the quantum well LDs explained in Chap. 7.

5.13 Noises 169

## 5.13.1.4 Suppression of Quantum Noises

The quantum noises derived earlier are summarized as

AM Noise (Intensity Fluctuation Spectrum)

$$W_{\Delta P}(\Omega) = \frac{\omega_m c E_{\rm cv} P_0 \ln(1/R)}{\pi (\Omega^2 + \omega_1^2) n_{\rm r} L},$$
(5.180)

FM Noise (Frequency Fluctuation Spectrum)

$$W_{\Delta\omega}(\Omega) = \frac{\hbar \omega_m c E_{\rm cv} \ln(1/R)}{4\pi P_0 n_{\rm r} L} \left( 1 + \frac{\alpha^2 \omega_1^2}{\Omega^2 + \omega_1^2} \right), \tag{5.181}$$

Spectral Linewidth (of a Field Spectrum)

$$\Delta\omega_0 = \frac{\hbar\omega_m c E_{\rm cv} \ln(1/R)}{4P_0 n_{\rm r} L} (1 + \alpha^2). \tag{5.182}$$

From (5.180)–(5.182), to suppress all the quantum noises, we should reduce the mirror loss  $(1/L) \ln(1/R)$ , for which long cavity length L and large power reflectivity R are needed. However, the long cavities of the *external cavity lasers* are less stable than the cavities of ordinary semiconductor lasers. With a decrease in the spectral linewidth enhancement factor  $\alpha$ , which is achieved in the quantum well LDs, the FM noise and spectral linewidth are simultaneously reduced. To suppress the quantum noises, it is also important to stabilize driving circuits and environmental temperature.

# 5.13.2 Relative Intensity Noise (RIN)

When semiconductor lasers show two-mode operations, the rate equations on the photon densities  $S_1$  and  $S_2$  and the carrier concentration n are written as

$$\frac{\mathrm{d}S_1}{\mathrm{d}t} = (\alpha_1 - \beta_1 S_1 - \theta_{12} S_2) S_1 + \beta_{\mathrm{spl}} \frac{n}{\tau_n} + F_1(t), \tag{5.183}$$

$$\frac{\mathrm{d}S_2}{\mathrm{d}t} = (\alpha_2 - \beta_2 S_2 - \theta_{21} S_1) S_2 + \beta_{\mathrm{sp2}} \frac{n}{\tau_n} + F_2(t), \tag{5.184}$$

$$\frac{\mathrm{d}n}{\mathrm{d}t} = \frac{I}{eV_{\mathrm{A}}} - [G_1(n) - \beta_1 S_1 - \theta_{12} S_2] S_1 
- [G_2(n) - \beta_2 S_2 - \theta_{21} S_1] S_2 - \frac{n}{\tau_n} + F_n(t).$$
(5.185)

Here,  $\alpha_i \equiv G_i(n) - 1/\tau_{\text{ph}i}$  is the net amplification rate,  $G_i(n)$  the amplification rate,  $\tau_{\text{ph}i}$  the photon lifetime,  $\beta_i$  the self-saturation coefficient,  $\theta_{ij}$  the cross-saturation coefficient,  $\beta_{\text{sp}i}$  the spontaneous emission coupling factor (i, j = 1, 2),  $\tau_n$  the carrier lifetime, I the injection current, e the elementary charge, and  $V_A$  the volume of the active layer. Fluctuations are expressed by the Langevin noise sources  $F_1$ ,  $F_2$ , and  $F_n$ .

The amplification rate  $G_i(n)$  is given by

$$G_i(n) = \left[\frac{\partial G_i}{\partial n}\right]_{n=n_{0i}} (n - n_{0i}), \tag{5.186}$$

where  $n_{thi}$  is the threshold carrier concentration and  $n_{0i}$  is the transparent carrier concentration.

In a steady state with weak coupling (C < 1), there are free-running conditions where two modes exist simultaneously and a mode-inhibition condition where only one mode exists. In neutral and strong couplings, there exists only a mode-inhibition condition, where an oscillation mode suppresses the other mode.

As described earlier, stable simultaneous two-mode operations are obtained only in the weak coupling. In the following calculation:

$$\beta_1 = \beta_2 = \beta, \ \theta_{12} = \theta_{21} = \frac{2}{3}\beta$$
 (5.187)

is used as an example. Other typical physical parameters in the semiconductor lasers are as follows:  $[\partial G_i/\partial n]_{n=n_{\text{th}i}} = 10^{-6} \text{ cm}^3/\text{s}, n_{0i} = 6.0 \times 10^{17} \text{ cm}^3, \beta_{\text{sp}i} = 10^{-5}, \tau_n = 10^{-9} \text{ s}, \text{ and } \tau_{\text{ph}i} = 10^{-12} \text{ s}.$  It is supposed that the injection current I is kept constant but the carrier concentration n fluctuates.

#### 5.13.3 RIN with No Carrier Fluctuations

We express the photon densities  $S_1$  and  $S_2$  as

$$S_1 = S_{10} + \delta S_1(t), \quad S_2 = S_{20} + \delta S_2(t),$$
 (5.188)

where  $S_{10}$  and  $S_{20}$  are the average photon densities of mode 1 and mode 2 in a steady state, respectively; and  $\delta S_1$  and  $\delta S_2$  are the fluctuations of mode 1 and mode 2, respectively.

When the Fourier transform of  $\delta S_i(t)$  is written as  $\delta \tilde{S}_i(\omega)$ , the self-correlation functions  $\langle \delta \tilde{S}_1(\omega) \delta \tilde{S}_1^*(\omega') \rangle$  and  $\langle \delta \tilde{S}_2(\omega) \delta \tilde{S}_2^*(\omega') \rangle$  are given by

$$\langle \delta \tilde{S}_1(\omega) \delta \tilde{S}_1^*(\omega') \rangle = \tilde{S}_{\delta S_1}(\omega) \cdot 2\pi \delta(\omega - \omega'), \tag{5.189}$$

$$\langle \delta \tilde{S}_{2}(\omega) \delta \tilde{S}_{2}^{*}(\omega') \rangle = \tilde{S}_{\delta S_{2}}(\omega) \cdot 2\pi \delta(\omega - \omega'). \tag{5.190}$$

5.13 Noises 171

Using (5.189) and (5.190), we define the *relative intensity noises* (RINs) per unit bandwidth as

$$RIN_1 = \frac{2\tilde{S}_{\delta S_1}(\omega)}{S_{10}^2},\tag{5.191}$$

$$RIN_2 = \frac{2\tilde{S}_{\delta S_2}(\omega)}{{S_{20}}^2}. (5.192)$$

In the following, the RIN per unit bandwidth is expressed as the RIN for simplicity. On the derivation of the RIN, see Appendix G.

Figure 5.67 shows the RIN for single-mode operations as a function of the frequency with the light output P as a parameter for three different values of the self-saturation coefficient  $\beta$ . Here, the carrier fluctuations are neglected, that is,  $\delta n(t) = \delta \tilde{n}(\omega) = 0$ . With an increase in  $\beta$ , the RINs in a frequency range less than  $10^8$  Hz are drastically reduced. Also, with an increase in P, a frequency region with a flat RIN is expanded, because the self-saturation given by  $-\beta P$  cancels out a fluctuation in P.

Figure 5.68 shows the RINs for two-mode operations as a function of the frequency for three values of the light output  $P_1$  of a main mode when the carrier fluctuations are neglected. A parameter is the light extinction ratio  $P_2/P_1$  where  $P_2$  is the light output of a submode. With an increase in  $P_1$ , the RINs decrease similarly to single-mode operations. According to  $P_2/P_1$ , the RINs show complicated behaviors, because the cross saturation by  $P_2$  also affects a fluctuation in  $P_1$ . In a high frequency range over  $10^{10}$  Hz, however, all lines overlap each other in contrast to Fig. 5.67.

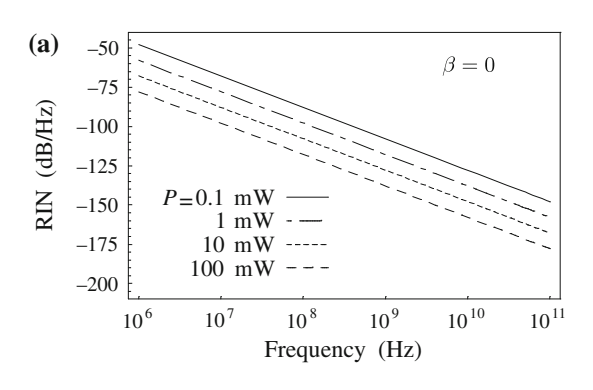
Comparing Fig. 5.67c with Fig. 5.68 where the self-saturation coefficient  $\beta$  is common, it can be said that single-mode operations have lower RINs than two-mode operations.

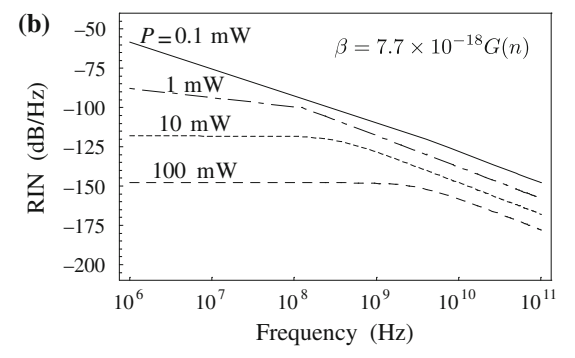
It should be noted that a peak in the RIN, which was already observed experimentally, does not exist when the carrier fluctuations are neglected. The effect of the carrier fluctuations on the RIN will be shown in the next section.

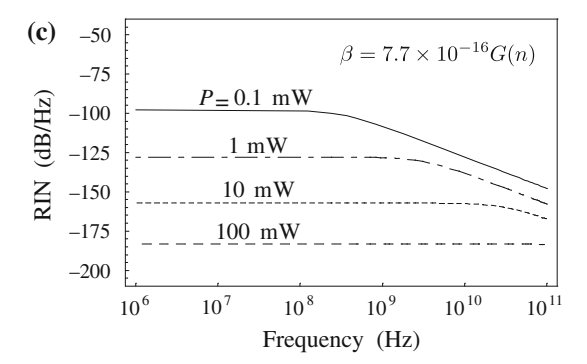
#### 5.13.4 RIN with Carrier Fluctuations

Figure 5.69 shows the RINs for single-mode operations as a function of the frequency with the light output P as a parameter for three values of  $\beta$  when the carrier fluctuations are included. It is found that the RIN has a peak, which has been experimentally observed, as opposed to Fig. 5.67. Thus, the carrier fluctuations are essential for a peak of the RIN. This resonance peak becomes dull when  $\beta$  increases. Therefore, by measuring resonance bandwidths of the RINs, we can determine a value of the self-saturation coefficient  $\beta$ . Comparing Fig. 5.69 with Fig. 5.67, it is also revealed that the RINs are reduced by the carrier fluctuations, and almost-constant RINs are obtained below the resonance frequency.

**Fig. 5.67** RIN per unit bandwidth for single-mode operations when the carrier fluctuations are neglected:  $\mathbf{a} \ \beta = 0$ ,  $\mathbf{b} \ \beta = 7.7 \times 10^{-18} G(n)$ , and  $\mathbf{c} \ \beta = 7.7 \times 10^{-16} G(n)$ 







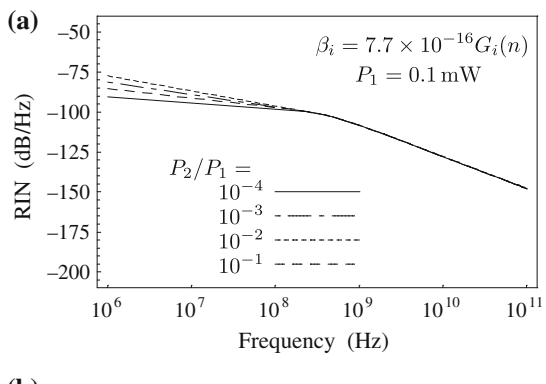
A resonance frequency  $f_r$  in the RIN for single-mode operations is given by

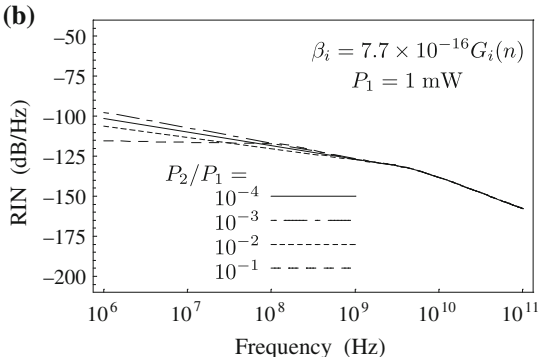
$$f_{\rm r} = \frac{1}{2\pi} \sqrt{\left[\frac{\partial G_1}{\partial n}\right]_{n=n_{\rm th}} \frac{S_{10}}{\tau_{\rm ph1}} + \beta S_{10} \left(\left[\frac{\partial G_1}{\partial n}\right]_{n=n_{\rm th}} S_{10} + \frac{1}{\tau_n}\right)}. \quad (5.193)$$

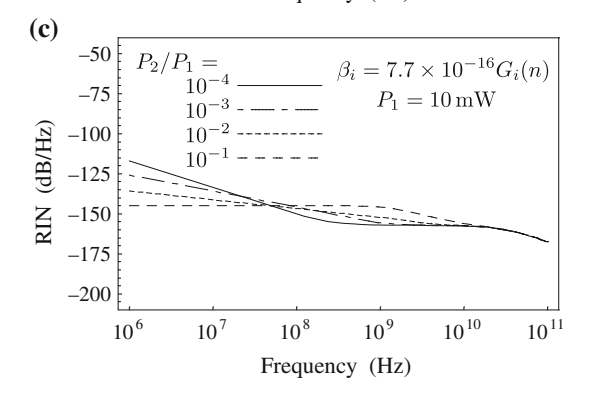
When the light output is low enough or the self-saturation is negligibly small, (5.193) reduces to

5.13 Noises 173

**Fig. 5.68** RIN per unit bandwidth for two-mode operations when the carrier fluctuations are neglected: **a**  $P_1 = 0.1 \,\text{mW}$ , **b**  $P_1 = 1 \,\text{mW}$ , and **c**  $P_1 = 10 \,\text{mW}$ 



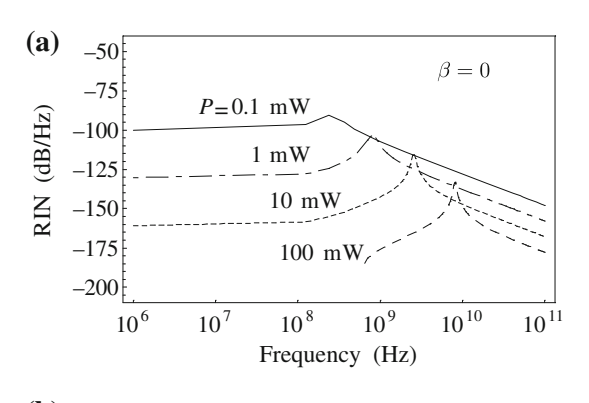


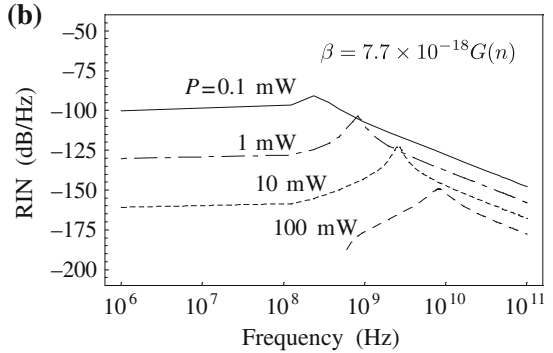


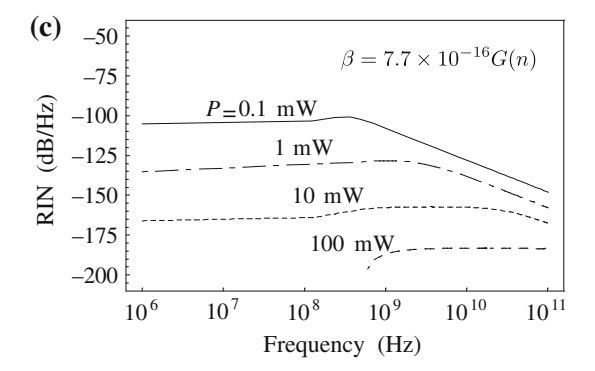
$$f_{\rm r} = \frac{1}{2\pi} \sqrt{\left[\frac{\partial G_1}{\partial n}\right]_{n=n_{\rm th}} \frac{S_{10}}{\tau_{\rm ph1}}},\tag{5.194}$$

which is the same as the resonance frequency of single-mode semiconductor lasers. Figure 5.70 shows the RINs for two-mode operations as a function of the frequency for three values of the light output  $P_1$  of a main mode when the carrier fluctuations are considered. A parameter is the light extinction ratio  $P_2/P_1$ , where  $P_2$  is the light

**Fig. 5.69** RIN per unit bandwidth for single-mode operations when the carrier fluctuations are included:  $\mathbf{a} \ \beta = 0$ ,  $\mathbf{b} \ \beta = 7.7 \times 10^{-18} G(n)$ , and  $\mathbf{c} \ \beta = 7.7 \times 10^{-16} G(n)$ 





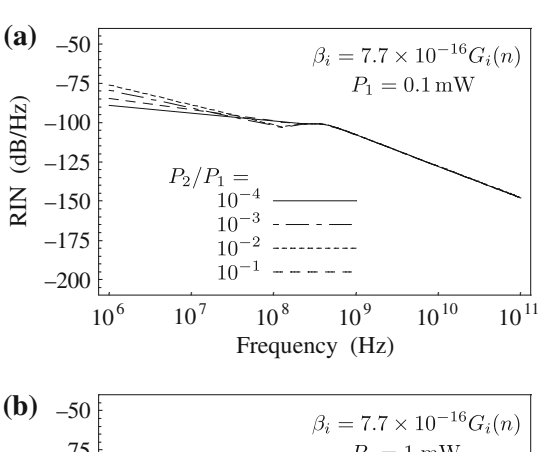


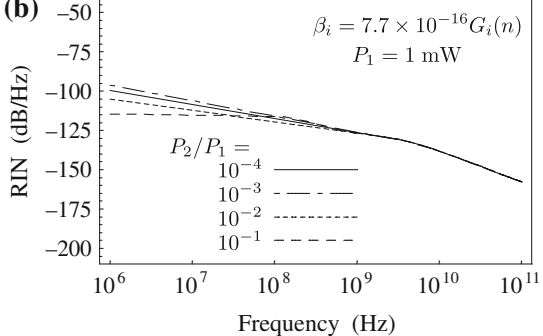
output of a submode. It is shown that a peak in the RIN is fairly vague in two-mode operations, compared with in single-mode operations. With an increase in  $P_1$ , the RINs decrease and show complicated behaviors according to  $P_2/P_1$  due to cross saturation.

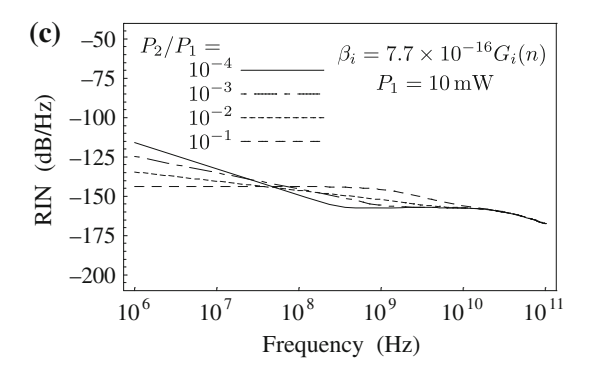
Comparing Fig. 5.69c with Fig. 5.70, where the self-saturation coefficient  $\beta$  is common, it is concluded that single-mode operations are superior to simultaneous two-mode operations from the viewpoint of the RINs.

5.13 Noises 175

**Fig. 5.70** RIN per unit bandwidth for two-mode operations when the carrier fluctuations are included: **a**  $P_1 = 0.1 \,\text{mW}$ , **b**  $P_1 = 1 \,\text{mW}$ , and **c**  $P_1 = 10 \,\text{mW}$ 







# 5.13.5 Noises on Longitudinal Modes

#### 5.13.5.1 Mode Partition Noise

The mode partition noise is observed when a longitudinal mode is selected during multimode operation. This noise is large in low frequencies, as explained in the RINs for two-mode operations. In multimode LDs, such as Fabry-Perot LDs under pulsed

operations or the gain guiding LDs, a noise for a total light intensity is comparable to the noise in single-mode LDs. However, a noise for each longitudinal mode in the multimode LDs is much larger than the noise in the single-mode LDs. As a result, the mode partition noise causes a serious problem in mode selective systems such as the optical fiber communication systems.

The cause of the mode partition noise is that the optical gain is randomly delivered to each mode during multimode operation. Therefore, to prevent the mode partition noise, we need single-mode LDs.

## 5.13.5.2 Mode Hopping Noise

The mode hopping noise is generated when a longitudinal mode in the single-mode LDs jumps to other modes. This mode hopping is closely related to driving conditions such as temperature and the injection current. At the time of the mode hopping, random oscillations between multiple modes are repeated and the noise increases due to a difference in light intensities between the relevant modes. When there are two competing modes, the noise is large in a low frequency range below 50 MHz; when there are three or more competing modes, the noise is large up to higher frequencies. Note that the mode partition noise is also large during mode hopping.

For analog systems, such as video discs, the RIN has to be lower than  $-140 \, \mathrm{dB/Hz}$ , and for digital systems, such as compact discs (CD-ROMs), the RIN should be lower than  $-120 \, \mathrm{dB/Hz}$ .

The causes of the mode hopping noise are fluctuations of the spontaneous emission and a propensity for the optical gain to concentrate on the oscillation mode. To avoid the mode hopping noise, two opposite ways, such as single-mode operations and multimode operations are used.

To achieve highly stable single-mode operations, *bistable LDs* or dynamic single-mode LDs are adopted. Bistable LDs containing *saturable absorbers* have hysteresis in *I–L* curves, which suppresses the mode competition. However, it is difficult for them to keep stable single-mode operations with large extinction ratio during modulation. Hence, the bistable LDs are not categorized in the dynamic single-mode LDs.

For systems without mode selectivity, such as video and compact disks, multimode operations are also used to reduce mode hopping noise. Multimode operations have a higher noise level than single-mode operations, but the noise level is stable with changes in temperature or the injection current. Therefore, the maximum noise level is lower than the mode hopping noise. To obtain multimode operations, *high frequency modulations* and *self-pulsations* are used. In high frequency modulation, electric current pulses with a frequency over 600 MHz are injected into Fabry-Perot LDs and the minimum current is set below the threshold current. The self-pulsations, which are the pulsed operations under DC bias, are obtained in the Fabry-Perot LDs with saturable absorbers or combined structures of the index and gain guidings. Due to the self-pulsations, multimode operations with low coherence take place, which results

5.13 Noises 177

in stable operations against the optical feedback noise. As a result, they are widely used as light sources for video disks and compact disks.

As described earlier, it is interesting that two contradictory methods, such as single-mode operation and multimode operation are used to suppress the mode hopping noise. In optical fiber communication systems, we need dynamic single-mode LDs, because the optical fibers have mode selectivity due to dispersions. In contrast, mode selectivity does not exist in video and compact disks. In these applications, we have to set up optical systems in a small volume, and we need to reduce optical feedback noise without using *optical isolators*. Therefore, multimode operations are suitable for video and compact disks.

# 5.13.6 Optical Feedback Noise

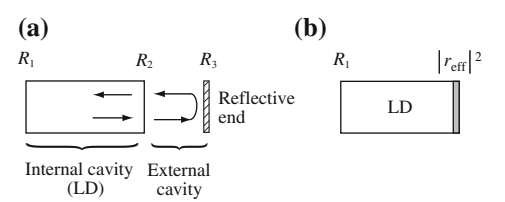
Optical feedback noise [18] is generated when a laser light emitted from a semiconductor laser is fed back to the semiconductor laser itself. A facet of semiconductor lasers forms *external cavities* with reflective external objects, such as optical components, optical fibers, and optical disks. These external cavities and the *internal cavity* of the semiconductor laser compose *coupled cavities*, which induce optical feedback noise.

The optical feedback noise is noticeable even when the relative feedback light intensity is of the order of  $10^{-6}$ . Due to optical feedback noise, the light output characteristics of the semiconductor laser change intricately, according to the distance between reflective external objects and the semiconductor laser, the feedback light intensity, and driving conditions. In static or time-averaged characteristics, the light intensity, the number of lasing modes, and the light output spectra are modified. In dynamic characteristics, a noise level and the shape of the light pulse are altered.

#### **5.13.6.1 Fundamental Equations**

We analyze the effect of the feedback lights on the characteristics of semiconductor lasers. Figure 5.71 shows (a) the coupled cavity and (b) its equivalent model. In the equivalent model, the effect of the external cavity is expressed by the equivalent amplitude reflectivity  $r_{\rm eff}$ .

**Fig. 5.71 a** Coupled cavity and **b** its equivalent model



First, we calculate  $r_{\rm eff}$ . We assume that the power reflectivities for the facets of the semiconductor laser are  $R_1$  and  $R_2$ , and the power reflectivity for the external reflector is  $R_3$ . Let an angular frequency of a laser light be  $\Omega$  and the roundtrip time in the external cavity be  $\tau$ ; then the electric field of the reflected light  $E_r e^{i\Omega t}$  is expressed as

$$E_{\rm r} e^{i\Omega t} = E_i e^{i\Omega t} \left[ \sqrt{R_2} + (1 - R_2) \sqrt{R_3} e^{-i\Omega \tau} + (1 - R_2) \sqrt{R_2} R_3 e^{-i2\Omega \tau} + \cdots \right],$$
 (5.195)

where  $E_i e^{i\Omega t}$  is the electric field of the incident light.

The third- and higher order terms in  $[\cdots]$  of (5.195) correspond to multireflections in the external cavity. Usually, the power reflectivity of the external reflector  $R_3$  is less than several percent. Therefore, we neglect multireflections in the external cavity. As a result,  $r_{\text{eff}}$  is obtained as

$$r_{\text{eff}} = \frac{E_{\text{r}}}{E_{i}} = \sqrt{R_{2}} \left( 1 + a e^{-i\Omega\tau} \right),$$

$$a = (1 - R_{2}) \sqrt{\frac{R_{3}}{R_{2}}} \ll 1.$$
(5.196)

For  $R_2 = 32 \%$ ,  $R_3 = 1 \%$ , we have a = 0.12.

Secondly, we consider the *decay rate* for the electric field. Let the power decay rate in the semiconductor laser itself be  $\gamma_0$ ; then the decay rate for the electric field  $\gamma_0/2$  is given by

$$\frac{1}{2}\gamma_0 = \frac{1}{2}\frac{c}{n_{\rm r0}}\left(\alpha_{\rm i} + \frac{1}{2L}\ln\frac{1}{R_1R_2}\right),\tag{5.197}$$

where c is the speed of light in a vacuum,  $n_{r0}$  is the effective refractive index of the semiconductor laser in a steady state,  $\alpha_i$  is the internal loss in the semiconductor laser, and L is the length of the internal cavity.

Using (5.197), we can write the decay rate for the coupled cavity  $\gamma$  as

$$\frac{1}{2} \gamma = \frac{1}{2} \frac{c}{n_{r0}} \left( \alpha_{i} + \frac{1}{2L} \ln \frac{1}{R_{1} r_{eff}^{2}} \right)$$

$$= \frac{1}{2} \gamma_{0} - \kappa e^{-i\Omega \tau},$$

$$\kappa = \frac{c}{2n_{r0}L} a = \frac{c}{2n_{r0}L} (1 - R_{2}) \sqrt{\frac{R_{3}}{R_{2}}}.$$
(5.198)

Here,  $\kappa$  is the *coupling rate of a feedback light to the semiconductor laser*, and for  $R_2 = 32\%$ ,  $R_3 = 1\%$ ,  $n_{r0} = 3.5$ , and  $L = 300 \,\mu\text{m}$ , we have  $\kappa = 1.7 \times 10^{10} \,\text{s}^{-1}$ . This value is between the decay rate for the carrier concentration  $1/\tau_n \sim 10^9 \,\text{s}^{-1}$ 

5.13 Noises 179

and that for the photon density  $1/\tau_{ph}\sim 10^{12}\,{\rm s}^{-1}$ . Using the decay rate  $\gamma$ , we can express an equation for the electric field E as

$$\frac{\mathrm{d}}{\mathrm{d}t}E\,\mathrm{e}^{\mathrm{i}\Omega t} = \left\{\mathrm{i}\,\omega_N(n) + \frac{1}{2}\left[G(n) - \gamma\right]\right\}E\,\mathrm{e}^{\mathrm{i}\Omega t},\tag{5.199}$$

where  $\omega_N(n)$  is an angular frequency for the Nth-order resonance mode when the carrier concentration is n. Substituting (5.198) into (5.199) results in

$$\frac{d}{dt}E(t) = \left\{ i \left[ \omega_N(n) - \Omega \right] + \frac{1}{2} \left[ G(n) - \gamma_0 \right] \right\} E(t) + \kappa E(t - \tau) e^{-i\Omega\tau}, \quad (5.200)$$

where the second term on the right-hand side shows a contribution of the feedback light. Note that this equation includes the phase of the laser light. Because the optical feedback noise is highly dependent on the phase of the feedback light, we use (5.200) instead of (5.21) to analyze the optical feedback noise.

A rate equation for the carrier concentration n is given by

$$\frac{d}{dt}n = \frac{J}{ed} - G(n)|E|^2 - \frac{n}{\tau_n}.$$
 (5.201)

#### 5.13.6.2 Effect of the Feedback Light on Static Characteristics

We assume that the electric field E takes a steady-state value. From a real part in (5.200), the amplification rate at the threshold  $G_{th}$  is given by

$$G_{\rm th} \equiv G(n_{\rm th}) = \gamma_0 - 2\kappa \cos(\Omega \tau). \tag{5.202}$$

From an imaginary part in (5.200), the oscillation angular frequency  $\Omega$  at the threshold is obtained as

$$\omega_N(n_{\rm th}) = \Omega + \kappa \sin(\Omega \tau). \tag{5.203}$$

Assuming that the steady-state values  $\omega_N(n_{c0})$ ,  $\Omega_0$ , and  $\kappa_0$  satisfy (5.202) and (5.203), we obtain

$$G(n_{c0}) = \gamma_0 - 2\kappa, \tag{5.204}$$

where we have supposed  $n_{\rm th}=n_{\rm c0}$  and  $\omega_N(n_{\rm c0})=\Omega_0$ . Because of the carrier lifetime  $\tau_n\sim 10^{-9}\,{\rm s}$  and the photon lifetime  $\tau_{\rm ph}\sim 10^{-12}\,{\rm s}$ , the carrier concentration n does not always take a steady-state value, even though the electric field E is in a steady state. Hence, if we place

$$n_{\rm th} = n_{\rm c0} + \Delta n,\tag{5.205}$$

then we can write  $G_{th}$  as

$$G_{\rm th} = G(n_{\rm c0}) + \frac{\partial G}{\partial n} \Delta n. \tag{5.206}$$

Substituting (5.206) into (5.202), and using (5.204) result in

$$\Delta n = 2\kappa \left(\frac{\partial G}{\partial n}\right)^{-1} [1 - \cos(\Omega \tau)], \tag{5.207}$$

where we have assumed  $\kappa = \kappa_0$  because  $1/\tau_n \sim 10^9 \, \rm s^{-1}$  and  $\kappa \sim 10^{10} \, \rm s^{-1}$ . The resonance angular frequency at the threshold  $\omega_N(n_{\rm th})$  is expressed as

$$\omega_N(n_{\rm th}) = \omega_N(n_{\rm c0}) - \frac{\omega_N(n_{\rm c0})}{n_{\rm r0}} \frac{\partial n_{\rm r}}{\partial n} \Delta n. \tag{5.208}$$

Inserting (5.179) and (5.207) into (5.208) leads to

$$\omega_N(n_{\rm th}) = \omega_N(n_{\rm c0}) + \alpha \kappa [1 - \cos(\Omega \tau)]. \tag{5.209}$$

From (5.209), it is found that the spectral linewidth enhancement factor  $\alpha$  plays an important role in the optical feedback noise, in addition to the spectral linewidth of the semiconductor lasers. Substituting (5.209) into (5.203), we obtain

$$\omega_N(n_{\rm c0}) = \Omega + \kappa \sin(\Omega \tau) - \alpha \kappa [1 - \cos(\Omega \tau)]. \tag{5.210}$$

These results are summarized as follows: When the electric field E takes a steady-state value, the amplification rate at the threshold  $G_{th}$  is given by

$$G_{\text{th}} \equiv G(n_{\text{th}}) = \gamma_0 - 2\kappa \cos(\Omega \tau), \tag{5.211}$$

and the oscillation angular frequency  $\Omega$  is obtained as

$$\omega_N(n_{c0}) = \Omega + \kappa \sin(\Omega \tau) - \alpha \kappa [1 - \cos(\Omega \tau)]. \tag{5.212}$$

The optical feedback noise in semiconductor lasers is larger than that in other lasers because semiconductor lasers have a larger  $\alpha$ , a lower  $R_2$ , and a shorter L than other lasers, which leads to a larger  $\kappa$ . For example, a gas laser with  $\alpha \ll 1$ ,  $R_2 = 98\%$ , and  $L \sim 1$  m has  $\kappa \sim 10^5 \, \mathrm{s}^{-1}$ , while a semiconductor laser with  $\alpha = 1-7$ ,  $R_2 = 32\%$ , and  $L \sim 300 \, \mu \mathrm{m}$  has  $\kappa \sim 10^{10} \, \mathrm{s}^{-1}$ .

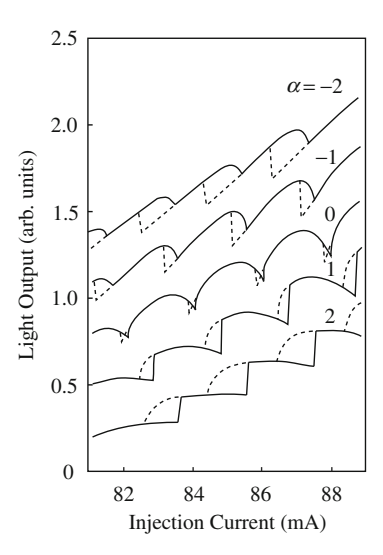
The terms including trigonometric functions in (5.211) and (5.212) indicate interference between the light in the semiconductor laser and the feedback light. Due to this interference, *hysteresis* accompanies the changes in both the oscillation angular frequency and the light intensity.

Figure 5.72 shows the resonance angular frequency  $\omega_N(n_{c0})$  as a function of the oscillation angular frequency  $\Omega$  for  $\kappa\tau=1$  and  $\alpha=3$ . Here, the arrows indicate

5.13 Noises 181

Fig. 5.72 Resonance angular frequency  $\omega_N(n_{\rm c0})$  versus oscillation angular frequency O

**Fig. 5.73** Current versus light output (I-L) characteristics



the points where  $\Omega$  jumps due to the nonlinear relationship between the interference condition and the oscillation angular frequency.

Figure 5.73 shows calculated I-L curves in DC operations with the spectral linewidth enhancement factor  $\alpha$  as a parameter. Here, Joule heating in the active layer is also considered. Hysteresis in the light intensity, which is shown in Fig. 5.73, is experimentally observed.

#### 5.13.6.3 Effect of Feedback Light on Dynamic Characteristics

Using (5.200) and (5.201), we can analyze the effect of the feedback light on the dynamic characteristics of semiconductor lasers. According to the phase of the feedback light, the dynamic characteristics show complicated behaviors, such as chaos and enhancement or suppression of the relaxation oscillation.

#### 5.13.6.4 Enhancement of Noise Due to Feedback Light

The most serious problem caused by feedback light is enhancement of noises. Due to the feedback light, the quantum noises increase in a certain frequency region. Moreover, laser oscillations become unstable, and the noise increases in a low frequency range, which is less than several hundred megahertz. The increase in this low frequency noise is caused by the random mode hopping between the longitudinal modes in the internal cavity and those in the external cavity.

### 5.13.6.5 Reducing Optical Feedback Noise

To stabilize a longitudinal mode in the internal cavity, we need single-mode LDs such as DFB-LDs and bistable LDs. To suppress the interference between the feedback light and the internal light, we should reduce the coherence of laser light by high frequency modulation or self-pulsation. To decrease the feedback light intensity, we require a low coupling rate  $\kappa$ , which is achieved by large facet reflectivity and a long cavity as shown in (5.198). However, a large reflectivity leads to a low light output, and a long cavity results in a large threshold current. Therefore, the optical isolators are used to decrease the feedback light intensity in optical fiber communication systems, but the cost and size of the optical systems increase.

# 5.14 Degradations and Lifetime

*Degradation* of semiconductor lasers means that the threshold currents increase and the external quantum efficiencies decrease, as shown in Fig. 5.74. If the degradation continues, CW laser operations stop.

The causes of the degradation, which depend on the properties of the materials, are propagation of the *crystal defects*, changes in the surface condition, destruction of facets, generation of the point defects, degradation of the *ohmic contacts* or the contact layers with the *heat sinks*, and so on. The speed of degradation is enhanced with increases in temperature, light output, and injection current.

In *automatic power control* (APC), the *lifetime* of semiconductor lasers is usually defined as a time when the operating current increases up to twice the initial value.

In InGaAsP/InP LDs used in trunk-line optical fiber communication systems, the expected lifetime is more than 27 years.

# 5.14.1 Classification of Degradations

#### 5.14.1.1 Catastrophic Optical Damage

When the temperature at a facet of a semiconductor laser increases up to a melting point, the light output from the melted facet rapidly falls, which is referred to as the *catastrophic optical damage* (COD). The destructed facet never returns to its original condition. Figure 5.75 schematically shows the catastrophic optical damage. In AlGaAs/GaAs LDs, the critical light output density of the COD in CW operations is of the order of  $10^6$  W/cm<sup>2</sup>. If the active layer is  $0.2 \,\mu m$  thick and  $5 \,\mu m$  wide, the critical light output of the COD is only  $10 \,mW$ .

The process of the catastrophic optical damage is as follows: Crystal surfaces have a lot of surface energy levels, which lead to nonradiative recombinations. As a result, the carrier concentration in the vicinity of the facet is too low to generate optical gain, and this region absorbs laser light. Due to absorption of the laser light, the temperature at the facet increases and the bandgap shrinks. Hence, the absorption coefficient at the facet further increases, which accelerates absorption of the laser light and Joule heating of the facet. Such positive feedback increases the temperature at the facet up to the melting point (about 1,500 °C in AlGaAs), and the facet melts.

To suppress the COD, the vicinity of the facet should be transparent for the laser light. Figure 5.76 shows *window structures*, which use a property that a bandgap in n-AlGaAs is larger than in p-AlGaAs. In CW operation, the critical light outputs of window structure LDs are several times higher than those of LDs without windows. In pulsed operations, the COD level is improved by a factor of ten.

In materials with low nonradiative recombination rate at the surface or high thermal conductivity, the COD levels are high. For example, in InGaAsP/InP LDs, the COD is not observed even in large light output over 100 mW.

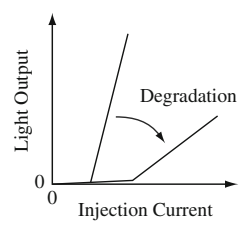


Fig. 5.74 Degradation of semiconductor lasers

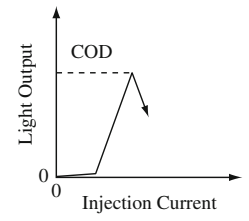


Fig. 5.75 Catastrophic optical damage

#### 5.14.1.2 Dark Line Defects

The dislocations cause dark line defects, which are named after the dark lines observed in light emission patterns. The dark line defects propagate by growth of the dislocations with repetitive emissions and absorptions of the point defects or extension of the dislocations due to movement of the slipped dislocations. Once the dark lines are generated, the nonradiative recombinations and the absorptions increase.

Among the dislocations, which are the sources of the dark lines, there exist the (1) penetration dislocations, that is, the dislocations in a substrate extended to the epitaxial layers; (2) dislocations generated at the interfaces of the heterojunctions; (3) dislocations based on some deposits, which were formed during epitaxial growth; (4) misfit dislocations generated above critical thickness due to lattice mismatching; and (5) dislocations induced by external stresses. To suppress these dislocations, we need to use high-quality substrates with few dislocations and optimize epitaxial growth conditions. It should be noted that in InGaAsP/InP LDs, the dislocations grow slowly and the dark lines do not appear frequently.

#### 5.14.1.3 Facet Degradation

In AlGaAs/GaAs LDs, even when they are placed in N<sub>2</sub>-ambient or air-proof packages, the facets are easily oxidized by a fraction of remaining oxygen. In contrast, the facets of InGaAsP/InP LDs are not readily oxidized. Figure 5.77 shows oxidization of the facets. If the facet is oxidized as shown in Fig. 5.77a, the laser light is

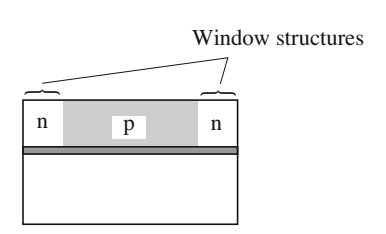


Fig. 5.76 Window-structure LD

scattered, which leads to a large radiation angle. Also, the oxidized region and its neighbor have many point defects and impurities, such as oxygen, which become nonradiative recombination centers. Hence, the threshold current increases, and the external quantum efficiency decreases. To avoid oxidization of the facets, dielectric thin films, such as SiO<sub>2</sub>, Al<sub>2</sub>O<sub>3</sub>, and Si<sub>3</sub>N<sub>4</sub>, are often coated on the facet, as illustrated in Fig. 5.77b. It should be noted that these dielectric thin films cannot reduce the dark lines, but the window structures can suppress oxidization of the facets.

**Fig. 5.77** Oxidation of a facet: **a** Degradation and **b** protection



# *5.14.2 Lifetime*

There are two definitions of the lifetime according to the driving conditions. In *automatic power control* (APC), the lifetime is a time in which a predetermined light output is not obtained. Considering the degradations in the longitudinal modes, transverse modes, and relaxation oscillation, the lifetime is often defined as a time when the operating current increases up to double the initial value. In *automatic current control* (ACC), the lifetime is frequently defined as a time when the light output decreases down to half of the initial value.

In manufacturing processes of semiconductor lasers, *intentionally accelerating degradation tests* called the *screening tests* are widely used. It is experimentally confirmed that after the screening tests low degradation LDs have long lifetimes.

#### References

- Alferov, Z.I., Andreev, V.M., Portnoy, E.L., et al.: AlAs-GaAs heterojunction injection lasers with a low room-temperature threshold. Sov. Phys. Semicond. 3, 1107 (1970)
- 2. Hayashi, I., Panish, M.B., Foy, P.W., et al.: Junction lasers which operate continuously at room temperature. Appl. Phys. Lett. 17, 109 (1970)
- 3. Lamb Jr, W.E.: Theory of an optical maser. Phys. Rev. **134**, A1429 (1964)
- Louisell, W.H.: Quantum Statistical Properties of Radiation. John Wiley and Sons, New York (1973)
- 5. Sargent III, M., Scully, M.O., Lamb, W.E. Jr.,: Laser Physics. Addison-Wesley, Reading (1974)
- 6. Haken, H.: Laser Theory. Springer, Berlin (1984)
- 7. Shimoda, K.: Introduction to Laser Physics, 2nd edn. Springer, Berlin (1986)
- 8. Siegman, A.E.: Lasers. University Science Books, Mill Valley (1986)
- Shomura, N., Fujimoto, M., Numai, T.: Fiber pump semiconductor lasers with optical antiguiding layers for horizontal transverse modes. IEEE J. Quantum Electron 44, 819 (2008)

- Shomura, N., Fujimoto, M., Numai, T.: Fiber-pump semiconductor lasers with optical antiguiding layers for horizontal transverse modes: dependence on mesa width. Jpn. J. Appl. Phys. 48, 042103 (2009)
- Shomura, N., Numai, T.: Ridge-type semiconductor lasers with optical antiguiding layers for horizontal transverse modes: dependence on step positions. Jpn. J. Appl. Phys. 48, 042104 (2009)
- Takada, H., Numai, T.: Ridge-type semiconductor lasers with antiguiding cladding layers for horizontal transverse modes. IEEE J. Quantum Electron 45, 917 (2009)
- Yoshida, H., Numai, T.: Ridge-type semiconductor lasers with antiguiding layers for horizontal transverse modes: dependence on space in the antiguiding layers. Jpn. J. Appl. Phys. 48, 082105 (2009)
- Yoshida, H., Numai, T.: Simulation of ridge-type semiconductor lasers with selectively protonimplanted cladding layers. Jpn. J. Appl. Phys. 49, 012101 (2010)
- Kato, H., Yoshida, H., Numai, T.: Simulation of a ridge-type semiconductor laser for separate confinement of horizontal transverse modes and carriers. Opt. Quantum Electron 45, 573 (2013)
- 16. Chai, G., Numai, T.: Simulation of a ridge-type semiconductor laser with horizontal coupling of lateral modes. Opt. Quantum Electron (2013). doi:10.1007/s11082-013-9821-y
- 17. Yariv, A.: Quantum Electronics, 3rd edn. John Wiley and Sons, New York (1989)
- Lang, R., Kobayashi, K.: External optical feedback effects on semiconductor injection laser properties. IEEE J. Quantum Electron QE-16, 347 (1980)

# Chapter 6 Dynamic Single-Mode LDs

#### **6.1 Introduction**

In order to transmit signals, we modulate a laser light by direct modulation or external modulation. Note that direct modulation is superior to external modulation in terms of cost.

Dynamic single-mode LDs are semiconductor lasers, which show single longitudinal mode operations in direct modulation. Because the optical fibers have dispersions, dynamic single-mode LDs are key devices for long-haul, large-capacity optical fiber communication systems. Therefore, the DFB-LDs, the DBR-LDs, the surface emitting LDs, and the cleaved coupled cavity (C³) LDs have been developed. Because the optical gain spectra of semiconductor lasers have a linewidth on the order of 10 nm, the optical cavities play important roles to select only one resonance mode for dynamic single-mode operations. It should be noted that the bistable LDs with saturable absorbers are not categorized into dynamic single-mode LDs, because they show single-mode operations only in a steady state and lead to multimode operation in direct modulation.

#### 6.2 DFB-LDs and DBR-LDs

Distributed feedback (DFB) LDs and distributed Bragg reflector (DBR) LDs have diffraction gratings in the optical waveguides to achieve high-mode selectivity. As shown in Fig. 6.1, the DFB-LDs have the active layers in the corrugated regions, and the DBR-LDs do not have the active layers in the corrugated regions.

The DFB-LDs and DBR-LDs periodically modulate their complex refractive indexes to achieve optical feedback. The reflection points of the Fabry-Perot LDs are only the facets, while those of the DFB-LDs and the DBR-LDs are distributed all over the corrugated regions.

#### 6.2.1 DFB-LDs

#### 6.2.1.1 Index-Coupled DFB-LDs

In an *index-coupled grating*, only a real part of the complex refractive index is periodically modulated and an imaginary part is uniform. The real part  $n_r(z)$  is expressed as

$$n_{\rm r}(z) = n_{\rm r0} + n_{\rm r1}\cos(2\beta_0 z + \Omega).$$
 (6.1)

Here, z is a position,  $\Omega$  is the grating phase at z = 0, and  $\beta_0$  is written as

$$\beta_0 = \frac{\pi}{4},\tag{6.2}$$

where  $\Lambda$  is the grating pitch.

Figure 6.2 shows the index-coupled grating. If we form corrugations on the interfaces of two layers with refractive indexes  $n_A$  and  $n_B \neq n_A$ , we can periodically modulate the refractive index. Due to this periodical modulation of the refractive index, a forward running wave and a backward running wave are coupled to each other, which is indicated by the grating coupling coefficient  $\kappa$  given by

$$\kappa = \frac{\pi n_{\rm rl}}{\lambda_0}.\tag{6.3}$$

Here, we put  $\alpha_1=0$  in (4.34). The grating coupling coefficient  $\kappa$  is an important parameter, which represents resonance characteristics of the DFB-LDs and the DBR-LDs.

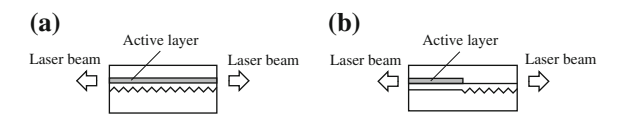
#### (i) Uniform Grating

We consider the oscillation condition of the DFB-LD with a uniform grating, in which both the depth and the pitch are constant all over the corrugated region. As shown in Fig. 6.3, we assume that both facets are antireflection (AR) coated, and reflections at both facets are negligibly low.

When the transmissivity in (4.48) is infinity, the DFB-LD starts to lase. As a result, from (4.45) and (4.47), the threshold condition of the DFB-LD with a uniform grating is obtained as

$$\cosh(\gamma L) - \frac{\alpha_0 - i \delta}{\gamma} \sinh(\gamma L) = 0, \tag{6.4}$$

Fig. 6.1 a DFB-LD and b DBR-LD



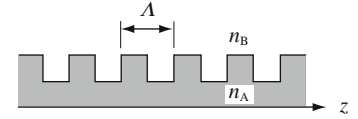


Fig. 6.2 Index-coupled grating

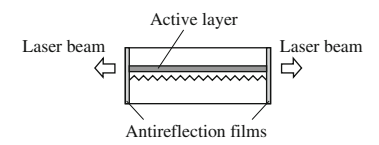


Fig. 6.3 DFB-LD with a uniform grating

where  $\alpha_0$  is the amplitude gain coefficient, L is the cavity length, and

$$\gamma^2 = (\alpha_0 - i \delta)^2 + \kappa^2, \tag{6.5}$$

$$\delta = \frac{\beta^2 - {\beta_0}^2}{2\beta_0} \simeq \beta - \beta_0. \tag{6.6}$$

Here,  $\beta$  is the propagation constant of a light.

Figure 6.4 shows transmission spectra of a uniform grating for four values of the optical gain, where  $\alpha_{th}$  is the threshold gain. As found in Fig. 6.4, the DFB-LD with a uniform grating oscillates in two modes when the reflectivities of both facets are negligibly low.

When the reflectivities of both facets are not negligible as in the cleaved facets, the oscillation modes show complicated behaviors according to the grating phases  $\Omega$  at the facets. For a certain grating phase, single-mode operations are obtained. However, the grating pitch is as short as about  $0.2\,\mu\text{m}$ , and it is almost impossible to control the cleaved position of the gratings in manufacturing. Therefore, it is difficult to obtain single-mode operations in the DFB-LDs with a uniform grating, and a yield for single-mode operations is less than several percent.

To achieve stable single-mode operations with a high yield, the phase-shifted DFB-LDs and the gain-coupled DFB-LDs have been developed.

#### (ii) Phase-Shifted Grating

As shown in Fig. 6.5, the corrugations of the phase-shifted grating are shifted, whereas the corrugations of the uniform gratings continue as indicated by a broken line. Here, the phase shift is expressed as  $-\Delta\Omega$  according to the definition of the refractive index in (6.1).

Let us consider an analytical model that consists of two regions and includes the phase shift as a phase jump at the interface, as shown in Fig. 6.6. We express a transfer matrix for region 1 with length of  $L_1$  as  $F_1$ , and that for region 2 with length of  $L_2$ 

**Fig. 6.4** Transmission spectrum for a uniform grating

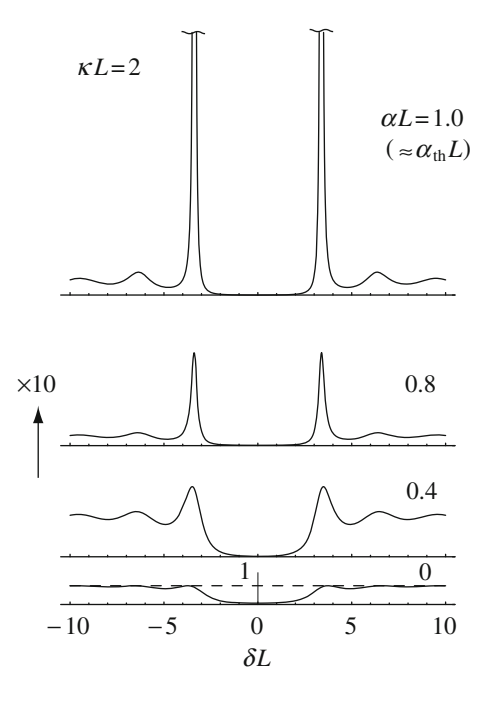


**Fig. 6.5** Phase-shifted grating

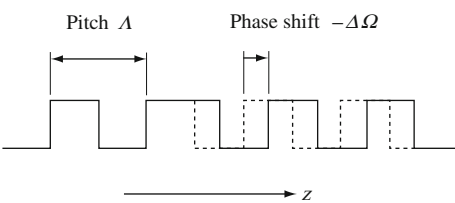
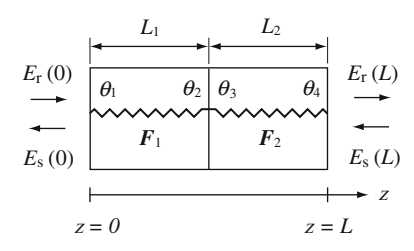


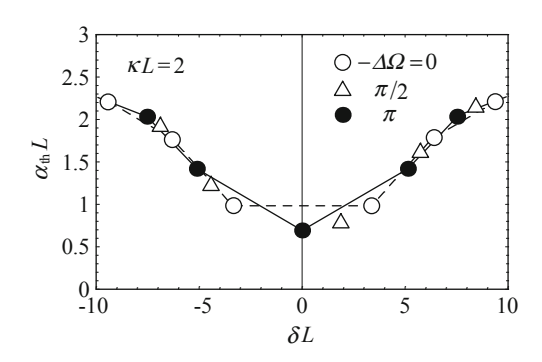
**Fig. 6.6** Analytical model for the phase-shifted grating



as  $F_2$ . Here, we assume that both the pitch and the depth of the corrugations are constant except in the phase-shifted region, and the optical gain is uniform all over the grating.

We suppose that both facet reflectivities are negligibly low. If we write the grating phase  $\Omega$  at the left edge of region 1 as  $\theta_1$ , the grating phase  $\theta_2$  at the right edge of region 1 is given by

Fig. 6.7 Calculated amplitude threshold gain  $\alpha_{\rm th}L$  as a function of  $\delta L = \delta \times L$  for three phase-shift values



$$\theta_2 = \theta_1 + 2\beta_0 L_1. \tag{6.7}$$

Because of the phase shift  $\Delta\Omega$  at the interface of regions 1 and 2, the grating phase  $\theta_3$  at the left edge of region 2 is expressed as

$$\theta_3 = \theta_2 + \Delta\Omega = \theta_1 + 2\beta_0 L_1 + \Delta\Omega. \tag{6.8}$$

The threshold condition is given by  $F_{11} = 0$ , where  $F_{11}$  is a matrix element of  $\mathbf{F} = \mathbf{F}_1 \times \mathbf{F}_2$  and is written as

$$\left[\cosh(\gamma L_1) - \frac{\alpha_0 - i \delta}{\gamma} \sinh(\gamma L_1)\right] \left[\cosh(\gamma L_2) - \frac{\alpha_0 - i \delta}{\gamma} \sinh(\gamma L_2)\right] + \frac{\kappa^2}{\gamma^2} \sinh(\gamma L_1) \sinh(\gamma L_2) e^{i\Delta\Omega} = 0.$$
(6.9)

When the phase-shifted position is located at a center of the optical cavity ( $L_1 = L_2 = L/2$ ), (6.9) reduces to

$$\left[\cosh(\gamma L) - \frac{\alpha_0 - i \delta}{\gamma} \sinh(\gamma L)\right] + \frac{\kappa^2}{\gamma^2} \left(e^{i\Delta\Omega} - 1\right) \left[\sinh\left(\frac{\gamma L}{2}\right)\right]^2 = 0.$$
 (6.10)

The first term in (6.10) is the same as the left-hand side in (6.4) for the DFB-LD with a uniform grating. The second term in (6.10) represents an effect of the phase shift. Figure 6.7 shows calculated results of the amplitude threshold gain  $\alpha_{\rm th}L$  as a function of  $\delta L = \delta \times L$  for three phase-shift values.

Laser oscillation starts at a mode with the lowest  $\alpha_{th}L$ . If a difference in the threshold gain of the oscillation mode and that of other modes is large enough, highly stable single-mode operations are obtained. For the phase shift  $\Delta\Omega = 0$  as

in the uniform grating, two modes have a common lowest threshold gain  $\alpha_{\rm th}L$ , as indicated by open circles. Therefore,  $\Delta\Omega=0$  results in two-mode operations. For the phase shift  $-\Delta\Omega=\pi/2$  shown by open triangles, there is only one mode whose threshold gain is the lowest, and a single-mode operation is expected. For the phase shift  $-\Delta\Omega=\pi$  represented by closed circles, there exists only one mode whose threshold gain is the lowest at Bragg wavelength. Note that the difference in the lowest threshold gain and the second-lowest one is largest for  $-\Delta\Omega=\pi$ , which leads to the most stable single-mode operations.

From (4.41), Bragg wavelength  $\lambda_B$  in a vacuum, which satisfies  $\delta=0$ , is given by

$$\lambda_{\rm B} = \frac{2n_{\rm r0}\Lambda}{m},\tag{6.11}$$

where  $\Lambda$  is the grating pitch and m is a positive integer, which is called *order of diffraction*.

When the phase shift  $-\Delta\Omega$  is  $\pi$  in the first-order gratings (m=1), the corrugations are shifted by  $\Lambda/2$ . From (6.11), we have

$$\frac{\Lambda}{2} = \frac{\lambda_{\rm B}}{4n_{\rm r0}} = \frac{\lambda_m}{4}, \quad \lambda_m = \frac{\lambda_{\rm B}}{n_{\rm r0}},\tag{6.12}$$

where  $\lambda_m$  is a wavelength in a material. From (6.12), the phase shift of  $\pi$  corresponds to a quarter of a wavelength in a material. Therefore, the phase-shifted grating with  $-\Delta\Omega = \pi$  is often called a  $\lambda/4$ -shifted grating or a quarter-wavelength-shifted grating.

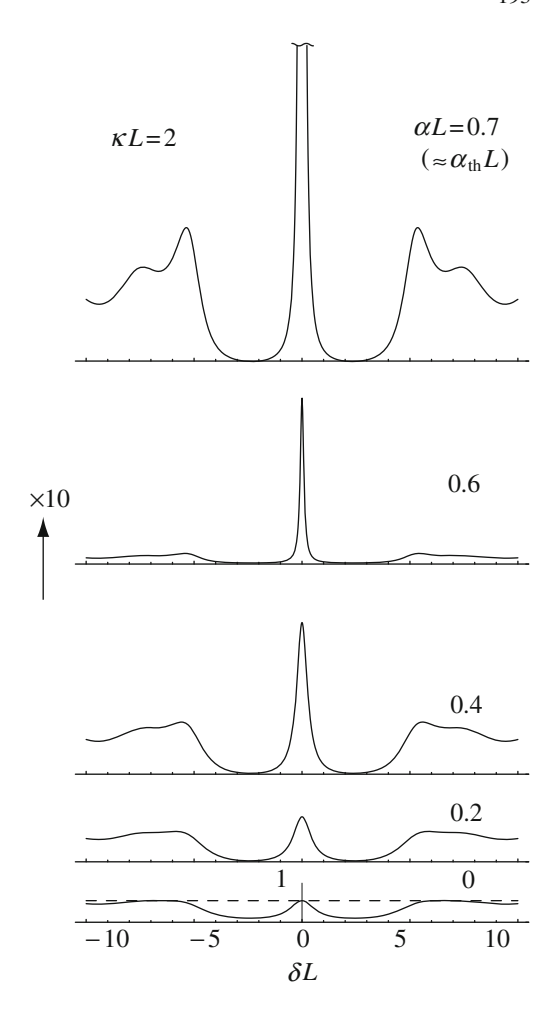
Figure 6.8 shows transmission spectra of the  $\lambda/4$ -shifted grating for four values of the optical gain. As found in Fig. 6.8, the  $\lambda/4$ -shifted DFB-LD oscillates at Bragg wavelength located at the center of the stop band and shows highly stable single-mode operations when the reflectivities at both facets are negligibly low.

According to the light intensity distribution along the cavity axis, the radiative recombinations are altered and spatial distribution of the carrier concentration is modified. This phenomenon is designated as the *spatial hole burning*, and the distribution of the refractive index changes with that of the carrier concentration, which may lead to a change in the phase shift. Therefore, a grating with a phase shift slightly altered from  $\pi$  is used to achieve  $-\Delta\Omega = \pi$  at the operating condition, or the chirped grating is adopted to reduce the spatial hole burning.

When there are lections at both facets, as in the cleaved facets, the oscillation modes of the phase-shifted DFB-LDs show complicated behaviors according to the grating phases at the facets, which is similar to the DFB-LD with a uniform grating. In addition, stability of single-mode operations is lower than that of the phase-shifted DFB-LD without reflections at the facets. Therefore, to achieve highly stable single-mode operations in the phase-shifted DFB-LD, we need antireflection-coated facets or window structures to reduce reflections at the facets.

Due to the high stability of single-mode operations, the index-coupled DFB-LDs are used in long-haul, large-capacity optical fiber communication systems such as

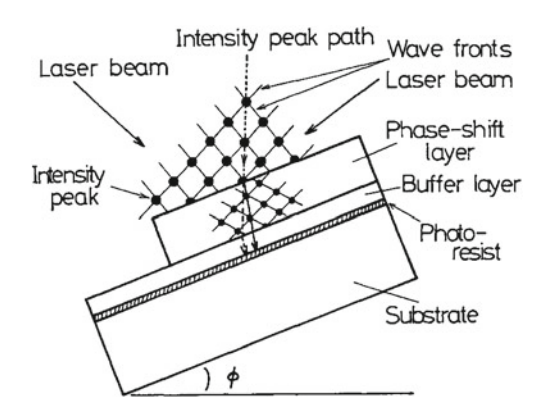
**Fig. 6.8** Transmission spectrum for a  $\lambda/4$ -shifted grating



trunk-line optical fiber cable systems in Japan and submarine optical fiber cable systems between Japan and the United States. Because the phase-shifted DFB-LD has been developed after the DFB-LD with a uniform grating, both DFB-LDs have been practically used. However, it is needless to say that stability and reproducibility of single-mode operations in the phase-shifted DFB-LD are better than those in the DFB-LD with a uniform grating.

In the following, the first mass-produced phase-shifted DFB-LDs [1] are briefly explained. Figure 6.9 shows the principle of the fabrication method for the phase-shifted grating. The dashed arrow represents the path of the intensity peak through the air. At the interface between the air and the phase-shift layer, the laser beam is refracted due to Snell's law. As a result, the path of the intensity peak goes through the phase-shift layer, as indicated by the solid arrow.

Fig. 6.9 Principle of the fabrication method of a phase-shifted grating [1] (Copyright © 1987 The Japan Society of Applied Physics)



The grating pitch  $\Lambda$  and the phase-shift  $-\Delta\Omega$  are given by

$$\Lambda = \frac{\lambda_{\text{ex}}}{2\sin\theta\cos\phi},\tag{6.13}$$

$$-\Delta\Omega = \frac{2\pi t}{\Lambda} \left[ \tan\phi - \tan\left(\frac{\sin(\theta + \phi) - \sin(\theta - \phi)}{n_{\rm r}}\right) \right],\tag{6.14}$$

where  $\lambda_{\rm ex}$  is the wavelength of the incident laser beam for the holographic lithography,  $\theta$  is the incident angle,  $\phi$  is the angle of incline, t is the thickness of the phase-shift layer, and  $n_{\rm r}$  is the refractive of the phase-shift layer.

Figure 6.10 draws the fabrication process of the phase-shifted gratings. Initially, a novolak-type photoresist whose thickness is 130 nm, is coated onto an InP substrate using a spin coater. After prebaking of the novolak-type photoresist, the buffer layer, which is a base compound of a photoresist without light sensitivity, is coated onto the novolak-type photoresist. Then, the phase-shift layer, which is a photoresist with the refractive index of  $n_r = 1.75$  for the light with  $\lambda_{\rm ex} = 325$  nm, is coated onto the buffer layer. The phase-shift layer is exposed using a conventional Hg lamp. By controlling the exposure time, the novolak-type photoresist is not exposed, because the phase-shift layer absorbs the UV light emitted from the Hg lamp. After developing the phase-shift layer, the novolak-type photoresist is exposed using a holographic exposure whose light source is a He-Cad laser with  $\lambda_{\rm ex}=325\,{\rm nm}.$  The phase-shift layer absorbs only 20 % of the power of the incident laser beam with  $\lambda_{\rm ex} = 325\,{\rm nm}$ , the novolak-type photoresist is exposed regardless of the existence of the phase-shift layer. The incident angle  $\theta$  is 44.5° and the angle of incline  $\phi$  is 15.0°. From (6.13), the grating pitch  $\Lambda$  is 240 nm. From (6.14), the thickness of the phase-shift layer t is 0.4  $\mu$ m for the  $\lambda/8$ -shifted grating with  $-\Delta\Omega = \pi/2$ ; and 0.8  $\mu$ m for the  $\lambda/4$ shifted grating with  $-\Delta\Omega = \pi$ . After the holographic exposure, the phase-shift layer and the buffer layer are removed, and then the novolak-type photoresist is developed. When the InP substrate is patterned by wet etching, a phase-shifted grating is formed.

Fig. 6.10 Fabrication process of a phase-shifted grating [1] (Copyright © 1987 The Japan Society of Applied Physics)

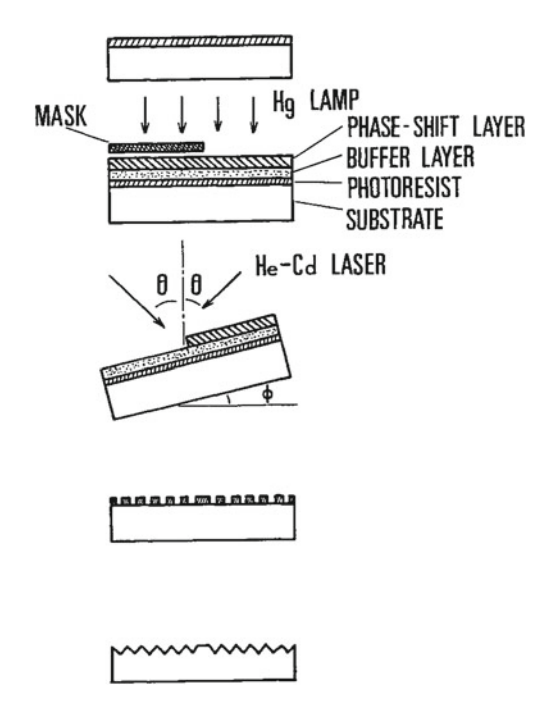


Fig. 6.11 SEM photograph of a phase-shifted grating [1] (Copyright © 1987 The Japan Society of Applied Physics)

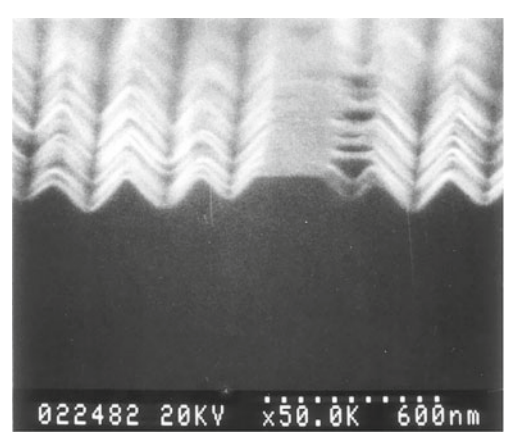


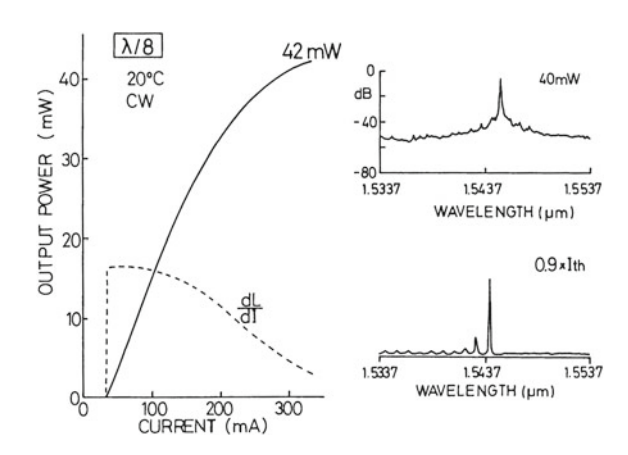
Figure 6.11 shows a scanning electron micrograph (SEM) of the phase-shifted grating, which was fabricated for the first time by using the fabrication process shown in Fig. 6.9. The grating pitch  $\Lambda$  is 240 nm and the depth is 150 nm. The shape of the corrugation is triangular with  $\langle 111 \rangle A$  crystal surfaces.

Figure 6.12 shows a schematic of the structure of a phase-shifted DFB-DC-PBH laser diode (LD). The cavity length is  $300\,\mu$ m and the phase-shift position is located at the center of the cavity. Both facets are antireflection (AR) coated by using SiN<sub>x</sub> and

Fig. 6.12 Schematic of the structure of a phase-shifted DFB-DC-PBH laser diode [1] (Copyright © 1987 The Japan Society of Applied Physics)

PHS CONTACT SIO2
SIN AMB
ACT GUIDE SUBSTRATE
CONTACT
SIN 3/4 SHIFT POSITION

Fig. 6.13 Light output as a function of an injection current [1] (Copyright © 1987 The Japan Society of Applied Physics)



the residual power reflectivity is estimated to be 1%. In the data book of the photonic semiconductor devices for 1993 in NEC Corporation [2], which was published in 1992, the phase-shifted DFB-LDs occupy about 20% of the lineups.

In Fig. 6.13, cw I-L characteristics and the light output spectra are shown for a  $\lambda/8$ -shifted DFB-LD. The slope efficiency is 0.20 mW/mA, and the maximum light output is 42 mW. The sub-mode suppression ratio (SMSR) is larger than 35 dB. It should be noted that  $\lambda/8$ -shifted DFB-LDs are superior to  $\lambda/4$ -shifted DFB-LDs with regard to the stability of the single-mode operation. Since the phase-shift  $-\Delta\Omega$  increases with an increase in the injection current due to the spatial hole burning during laser operation,  $-\Delta\Omega$  in the  $\lambda/8$ -shifted DFB-LDs comes up to  $\pi$ ;  $-\Delta\Omega$  in the  $\lambda/4$ -shifted DFB-LDs goes away from  $\pi$ . Therefore, single longitudinal mode operations in the  $\lambda/8$ -shifted DFB-LDs are more stable than those in the  $\lambda/4$ -shifted DFB-LDs.

Finally, we briefly explain the polarizations of the laser lights in the DFB-LDs. Because the grating coupling coefficient  $\kappa_{TE}$  for the TE mode is larger than that for the TM mode  $\kappa_{TM}$ , the threshold gain for the TE mode is lower than that for the TM mode. Therefore, the DFB-LDs start to lase in the TE mode. However, a difference in the threshold gains between the TE and TM modes is smaller than that of the Fabry-Perot LDs if the reflectivities at both facets are negligibly low. Hence, to stabilize the polarization of a laser light, quantum well-active layers are frequently

**Fig. 6.14** DBR-LDs: **a** DBR and cleaved facets and **b** two DBRs

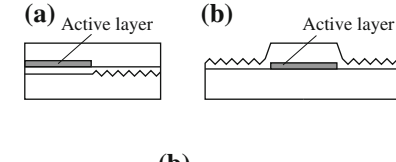
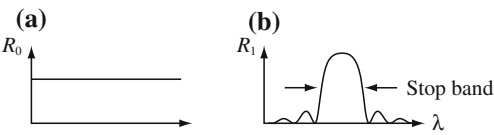


**Fig. 6.15** Reflectivities of the **a** cleaved facet and **b** DBR



adopted to obtain polarization-dependent optical gains, which will be described in Chap. 7.

### 6.2.1.2 Gain-Coupled DFB-LDs

In gain-coupled DFB-LDs [3], the optical gain or optical loss is periodically modulated along the cavity axis. They are characterized by stable single-mode operations even without the phase-shifted gratings and antireflection films coated on the facets. Also, they are less sensitive to feedback lights than the index-coupled DFB-LDs. However, there are still problems in fabrication methods and reliability of the devices.

When only the optical gain or loss is periodically modulated, the grating coupling coefficient  $\kappa$  is given by

$$\kappa = i \frac{\alpha_1}{2},\tag{6.15}$$

where  $\alpha_1$  is a deviation from a steady-state amplitude gain coefficient  $\alpha_0$ . If both the real and imaginary parts of the complex refractive index are periodically modulated with the same phase,  $\kappa$  is given by (4.34).

# 6.2.2 DBR-LDs

In DBR-LDs, the optical gain regions and corrugated regions are separated from each other. The corrugated regions function as reflectors. As a result, a DBR-LD with a DBR and cleaved facets and one with two DBRs have been developed, as shown in Fig. 6.14.

Figure 6.15 shows the reflectivities of the cleaved facet and the DBR. The reflectivity  $R_0$  for the cleaved facet is considered to be almost independent of a light wavelength, although  $R_0$  is slightly modified by the material dispersion. In contrast, the reflectivity  $R_1$  for the DBR is high only within the stop band. Because the resonance condition is not always satisfied at Bragg wavelengths, the DBR-LDs do not always lase at Bragg wavelengths.

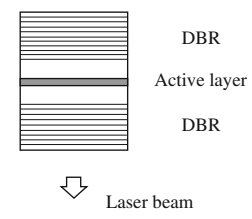


Fig. 6.16 Vertical cavity surface emitting LD

Note that the DFB-LDs are superior to the DBR-LDs in both stability of single-mode operations and light-output intensity.

As wavelength tunable LDs, DFB- or DBR-LDs with phase-control sections have been demonstrated. If these LDs are biased just below the threshold, they function as wavelength tunable resonant optical amplifiers (optical filters).

# **6.3 Surface Emitting LDs**

# 6.3.1 Vertical Cavity Surface Emitting LDs

Figure 6.16 shows the schematic structure of a *vertical cavity surface emitting LD* (VCSEL) [4], in which the active layers and the cladding layers are sandwiched by the reflectors with multilayers.

A laser light propagates along a normal to the surface of the epitaxial layers. Therefore, the length of the optical gain region is equal to the active layer thickness, which is of the order of ten nanometers to several micrometers. In contrast, the length of the optical gain region in conventional Fabry-Perot LDs or DFB-LDs is on the order of  $300\,\mu m$ . As a result, to achieve a low threshold in VCSELs, we need high reflective reflectors, for example, with the power reflectivity of  $99.5\,\%$ . Such a high reflectivity is achieved by multilayer reflectors, which consist of alternately stacked layers with different refractive indexes. As explained in Chap. 4, the operating principles behind the multilayer reflectors and the waveguide DBRs are common, and the multilayer reflectors used in the VCSELs are also called DBRs.

Note that the optical cavities of the VCSELs are short enough to obtain dynamic single-mode operations. For example, when the refractive index is 3.5 and the cavity length is 4  $\mu$ m, the oscillation wavelength is 1  $\mu$ m and the free spectral range is 36 nm from (4.15). This value is larger than the linewidth of the optical gain spectra such as 10 nm. As a result, there exists only one longitudinal mode in the gain spectrum.

Compared with other dynamic single-mode LDs, the VCSELs have the following additional features:

 It is possible to fabricate monolithic optical cavities, for which cleaving is not needed.

- 2. It is easy to test devices on wafers before pelletizing.
- 3. It is easy to couple a laser light to optical components, because circular beams with small radiation angles are obtained.
- 4. It is possible to integrate devices by stacking.
- 5. Because horizontal sizes can be less than several tens of micrometers,
  - (a) extremely low threshold currents are expected and
  - (b) the structures are suitable for high-density two-dimensional arrays.

Based on these features, the VCSELs take a lot of attention as key devices for parallel optical information processing and parallel lightwave transmissions. Also, optical functional devices based on the VCSELs have been demonstrated.

# 6.3.2 Horizontal Cavity Surface Emitting LDs

In the horizontal cavity surface emitting LDs [5, 6], some structures are added to conventional edge-emitting semiconductor lasers to emit laser lights along a normal to the epitaxial layer planes. Figure 6.17a and b show the structures where a part of the epitaxial layers is etched off to form reflection surfaces to emit laser lights. However, fabrication methods to form low-damage reflectors have yet not been established. Figure 6.17c has a second-order grating, and a first-order diffracted laser beam is emitted upward. However, the beam divergence angle is wide, and the diffraction efficiency of the second-order grating is low.

# **6.4 Coupled Cavity LDs**

The coupled cavity LDs use optical feedback to achieve single-mode operations. As shown in Fig. 6.18, the external cavity LD with a mirror and with a diffraction grating and the cleaved coupled cavity  $(C^3)$  LD have been developed.

The external cavity LDs have long cavities, 10 cm or more, and their cavities are sensitive to mechanical vibrations. Also, only a part of the optical cavity contributes to modulation of laser lights, which leads to low modulation efficiency. The C<sup>3</sup> LDs, in which the Fabry-Perot LDs are placed in series, have solved all the problems in the external cavity LDs. However, we need precise control of the injection currents

**Fig. 6.17** Horizontal cavity surface emitting LDs with **a** an inclined etched facet, **b** an inclined etched groove, and **c** a second-order grating





**Fig. 6.18** Coupled cavity LDs: **a** external cavity LD (mirror), **b** external cavity LD (grating), and **c** cleaved coupled cavity LD

into the two constituent Fabry-Perot LDs to obtain stable single-mode operations, and complicated driving electronic circuits are required.

Among dynamic single-mode LDs, only the DFB-LDs are widely used in practical applications for the reasons described earlier. There are various approaches to solve problems. However, we should keep in mind that practically used technologies work for a reason.

#### References

- Numai, T., Yamaguchi, M., Mito, I., et al.: A new grating fabrication method for phase-shifted DFB LDs. Jpn. J. Appl. Phys. Part 2 26, L1910 (1987)
- NEC Corporation: Data Book, Hikari Handoutai Devices (Photonic Semiconductor Devices) 1993 (in Japanese) NEC Corporation, Tokyo (1992)
- Nakano, Y., Luo, Y., Tada, K.: Facet reflection independent, single longitudinal mode oscillation in a GaAlAs/GaAs distributed feedback laser equipped with a gain-coupling mechanism. Appl. Phys. Lett. 55, 1606 (1989)
- 4. Iga, K., Koyama, F., Kinoshita, S.: Surface emitting semiconductor lasers. IEEE J. Quantum Electron. **QE-24**, 1845 (1988)
- Liau, Z.L., Walpole, J.N.: Large monolithic two-dimensional arrays of GaInAsP/InP surfaceemitting lasers. Appl. Phys. Lett. 50, 528 (1987)
- Carlson, N.W., Evans, G.A., Bour, D.P., et al.: Demonstration of a grating-surface-emitting diode laser with low-threshold current density. Appl. Phys. Lett. 56, 16 (1990)

# Chapter 7 **Quantum Well LDs**

#### 7.1 Introduction

Quantum well (QW) LDs [1, 2] are semiconductor lasers whose active layers take quantum well structures. A QW-LD with one potential well is called the *single quantum well* (SQW) LD, and that with plural QWs is named the *multiple quantum well* (MQW) LD.

As explained in Chap. 1, the density of states of the QW is a step function of the energy. Therefore, excellent characteristics, such as a low threshold current, high differential quantum efficiency, high-speed modulation, low chirping, and narrow spectral linewidth are simultaneously obtained in the QW-LDs.

# 7.2 Features of Quantum Well LDs

# 7.2.1 Configurations of Quantum Wells

Figure 7.1 shows the configurations of various QWs at the band edge. Figure 7.1a illustrates the SQW, in which the optical confinement factor  $\Gamma_a$  is reduced with a decrease in the active layer thickness  $L_z$ , as shown in Fig. 5.9. This reduction in  $\Gamma_a$  leads to a drastic increase in the threshold current density  $J_{th}$  as illustrated in Fig. 5.10. Therefore, to obtain a larger  $\Gamma_a$  than that of the SQW, structures (b)–(e) have been developed.

Figure 7.1b shows the MQW, in which the optical confinement factor  $\Gamma_a$  is enlarged by forming multiple QWs in the optical confinement region. However, due to the energy barriers between the adjacent QWs, the carrier injection efficiency decreases with an increase in the propagation distance of the carriers. Hence, it is difficult to achieve uniform carrier distribution all over the QWs.

To improve the carrier injection efficiency and the uniformity of the carrier distribution in the MQW, the *modified MQW* in Fig. 7.1c has been developed. The energy

barriers between the adjacent QWs are lower than those in the cladding layers, which results in a high carrier injection efficiency and uniform carrier distribution all over the OWs.

The separate confinement heterostructure (SCH) exhibited in Fig. 7.1d has been demonstrated to increase the optical confinement factor  $\Gamma_a$  in the SQW. In the materials conventionally used for semiconductor lasers, the refractive index increases with a decrease in the bandgap energy. Using this property, the energy potential is modified by two steps in the SCH structure. The outer potential confines a light to the QW active layer by the refractive index distribution, while the inner potential confines the carriers by the energy barriers. Because the potentials to confine the light and the carriers are separate, this structure is called the SCH.

Figure 7.1e illustrates the *graded index* SCH (GRIN-SCH) whose potential and refractive index distributions of the outer region are parabolic. In the GRIN-SCH, the optical confinement factor  $\Gamma_a$  is proportional to the active layer thickness  $L_z$  with a small  $L_z$ , while  $\Gamma_a$  in the SQW is in proportion to  $L_z^2$ . Therefore, when the active layer is thin, a relatively large  $\Gamma_a$  is obtained in the GRIN-SCH.

# 7.2.2 Characteristics of QW-LDs

#### 7.2.2.1 Low Threshold Current

It is important to achieve a low threshold current  $I_{th}$  in semiconductor lasers, because a low  $I_{th}$  leads to low power consumption. The density of states  $\rho(E)$  per unit energy per unit area in the SQW is written as

$$\rho(E) = \sum_{n=1}^{\infty} \frac{m^*}{\pi \hbar^2} H(E - \epsilon_n), \tag{7.1}$$

where E is the energy of the carrier,  $m^*$  is the effective mass of the carrier,  $\hbar$  is the Dirac's constant, and H(x) is the *Heaviside function* or a *step function* given by

$$H(x) = \begin{cases} 0 : x < 0, \\ 1 : x \ge 0. \end{cases}$$
 (7.2)

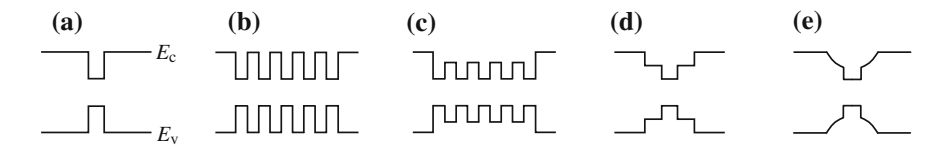


Fig. 7.1 Configurations of quantum wells: a SQW, b MQW, c modified MQW, d SCH, and e GRIN-SCH

If the barrier height or barrier thickness is too large for each QW to be independent of each other, the energy level of the *n*th subband  $\epsilon_n$  is expressed as

$$\epsilon_n = \frac{(n\pi\hbar)^2}{2m^*L_z^2}. (7.3)$$

When the barrier height or barrier thickness is large enough to separate each QW, the density of states  $\rho(E)$  per unit energy per unit area in the MQW is obtained as

$$\rho(E) = N \sum_{n=1}^{\infty} \frac{m^*}{\pi \hbar^2} H(E - \epsilon_n), \tag{7.4}$$

where N is the number of QWs.

When the barrier height or barrier thickness is small, the wave functions for the carriers penetrate into the adjacent QWs. Therefore, the QWs are coupled to each other, and degeneracy is removed to generate N quantum levels per degenerated quantum level. In this case, the density of states  $\rho(E)$  is given by

$$\rho(E) = \sum_{n=1}^{\infty} \sum_{k=1}^{N} \frac{m^*}{\pi \hbar^2} H(E - \epsilon_{nk}), \tag{7.5}$$

where  $\epsilon_{nk}$  (k = 1, 2, ..., N) is the energy of the quantum level, which is produced by the removal of degeneracy.

As described earlier, the densities of states in the QW-LDs are step functions, which results in narrow optical gain spectra. Hence, the optical gain concentrates on a certain energy, and the peak gain is enhanced. As a result, a threshold current density  $J_{\rm th}$  as low as 1/3 of that of a bulk double heterostructure (DH) LD was obtained in a QW-LD.

Here, we consider the linear optical gains of the QW-LDs. We assume that the nonradiative recombinations are negligibly low. Under the k-selection rule, the linear optical gain g (in units of cm<sup>-1</sup>) is written as

$$\frac{c}{n_{\rm r}}g(E,n) = \frac{\omega}{n_{\rm r}^2}\chi_{\rm I}(E,n),$$

$$\frac{\omega}{n_{\rm r}^2}\chi_{\rm I}(E,n) = \int \sum_{n=0}^{\infty} \sum_{j=l,h} \rho_{{\rm red},n}^j [f_{\rm c}(E_{{\rm c},n}) - f_{\rm v}(E_{{\rm v},n}^j)]\hat{\chi}_{\rm I}^{n,j}(E,\epsilon) \,\mathrm{d}\epsilon, \qquad (7.6)$$

$$\hat{\chi}_{\rm I}^{n,j}(E,\epsilon) = \frac{e^2h}{2m^2\varepsilon_0 n_{\rm r}^2 E_{\rm g}} |M_{n,j}(\epsilon)|_{\rm ave}^2 \frac{\hbar/\tau_{\rm in}}{(E-\epsilon)^2 + (\hbar/\tau_{\rm in})^2},$$

where c is the speed of light in a vacuum;  $n_r$  is the effective refractive index of the semiconductor laser; E is the photon energy;  $\omega$  is the angular frequency of a light;  $\chi_I$  is an imaginary part of the *relative electric susceptibility*, and j = h, l represents

the heavy hole (h) and the light hole (l), respectively. In the second equation of (7.6),  $\hat{\chi}_{\mathrm{I}}^{n,j}(E,\epsilon)$  is the imaginary part of the relative electric susceptibility for a photon with the energy E and an electron-hole pair with the energy  $\epsilon$ . In the third equation of (7.6), e is the elementary charge, h is Planck's constant, m is the electron mass in a vacuum,  $\varepsilon_0$  is permittivity in a vacuum,  $E_{\mathrm{g}}$  is the bandgap energy,  $|M_{n,j}(\epsilon)|_{\mathrm{ave}}^2$  is a square of the momentum matrix element, and  $\tau_{\mathrm{in}}$  is the *intraband relaxation time*. The reduced density of states for the nth subband  $\rho_{\mathrm{red},n}^j$  is given by

$$\rho_{\text{red},n}^{j} = \left(\frac{1}{\rho_{\text{c},n}} + \frac{1}{\rho_{\text{v},n}^{j}}\right)^{-1},\tag{7.7}$$

where  $\rho_{c,n}$  and  $\rho_{v,n}^j$  are the density of states for the *n*th subband in the conduction band and that in the valence bands, respectively;  $f_c(E_{c,n})$  and  $f_v(E_{v,n}^j)$  are the Fermi-Dirac distribution function of the conduction band and that of the valence bands, respectively. Here,  $E_{c,n}$  and  $E_{v,n}^j$  are the energy of the conduction band and that of the valence bands, respectively, and are expressed as

$$E_{c,n} = \frac{m_c \epsilon_{v,n}^j + m_v^j E + m_v^j \epsilon_{c,n}}{m_c + m_v^j},$$
(7.8)

$$E_{v,n}^{j} = \frac{m_{c}\epsilon_{v,n}^{j} - m_{c}E + m_{v}^{j}\epsilon_{c,n}}{m_{c} + m_{v}^{j}},$$
(7.9)

where  $m_c$  and  $m_v^j$  are the effective mass of the electron and that of the holes, respectively; and  $\epsilon_{c,n}$  and  $\epsilon_{v,n}^j$  are the energy of the *n*th subband in the conduction band and that in the valence bands, respectively. Figure 7.2a shows the *modal gain*  $g_{\text{mod}} = \Gamma_a g$  as a function of the injection current density J with the number of QWs N as a parameter. Here,  $\Gamma_a$  is the optical confinement factor of the active layer.

It is found that  $g_{\text{mod}}$  takes a different value according to N for a common current density. Hence, the number of QWs to minimize  $J_{\text{th}}$  depends on the optical loss in the optical cavity, which is equal to the threshold gain. Also, in the SQW (N=1), gain flattening is observed with an increase in the injection current. As shown in Fig. 7.2b, the cause of the gain flattening is that the density of states is a step function. Here,  $E_{\text{L}}$  is a lasing photon energy.

#### 7.2.2.2 Characteristic Temperature

Because the densities of states in the QWs are step functions, changes in the characteristics of the QW-LDs with the temperature are expected to be small. However,

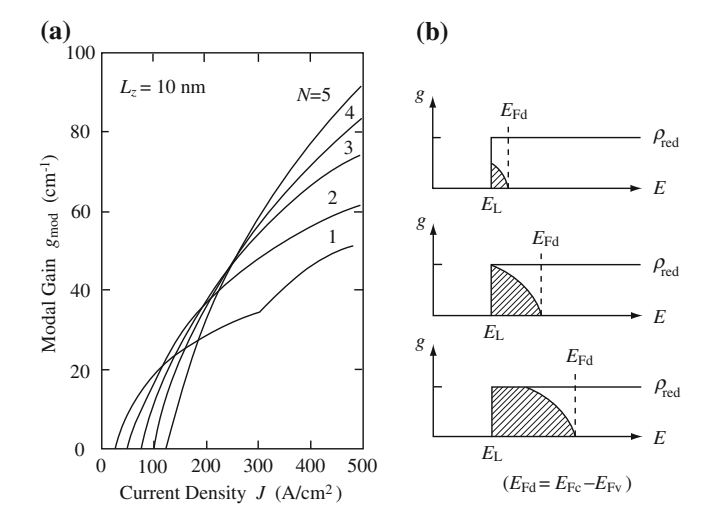


Fig. 7.2 a Modal gain and b gain flattening

even in a bulk DH-LD, a characteristic temperature  $T_0$  as high as 200 K is obtained, and an advantage of the OW-LDs over the bulk DH-LDs has not been proved yet.

### 7.2.2.3 Anisotropic Optical Gain

A difference in the optical gains for the TE and TM modes is about  $20\,\mathrm{cm}^{-1}$  in the bulk DH-LDs, while it is as large as  $\sim 140\,\mathrm{cm}^{-1}$  in the QW-LDs. In the bulk DH-LDs, an *anisotropic optical gain* is generated by the configurations of the optical waveguides, because the optical confinement factor  $\Gamma_a$  of the TE mode is larger than that of the TM mode. In the QW-LDs, the anisotropic optical gain is produced by the selection rule of the optical transitions, which will be explained in the following.

As described in Chap. 1, in the bulk structures, the heavy hole (hh) band with  $m_j = 3/2$ , and the light hole (lh) band with  $m_j = 1/2$  are degenerate at k = 0, while in the QWs this degeneracy is removed. Figure 7.3 schematically shows the energies of the valence band. Here,  $E_{\rm hh1}$  and  $E_{\rm hh2}$  (solid lines) represent the heavy hole bands;  $E_{\rm lh1}$  and  $E_{\rm lh2}$  (broken lines) indicate the light hole bands where a subscript 1 or 2 is a principal quantum number n.

It should be noted that the effective masses of the holes in the QWs are dependent on directions. As shown in Fig. 7.4, if we select a quantization axis as the z-axis, the effective mass along the z-axis of the heavy hole  $m_{z,hh}^*$  is larger than that of the light hole  $m_{z,hh}^*$ , while the effective mass on the xy-plane of the heavy hole  $m_{xy,hh}^*$  is smaller than that of the light hole  $m_{xy,hh}^*$ . This result is summarized as

```
along the z-axis: m_{z,hh}^* > m_{z,lh}^*, on the xy-plane: m_{xy,hh}^* < m_{xy,lh}^*.
```

206 7 Quantum Well LDs

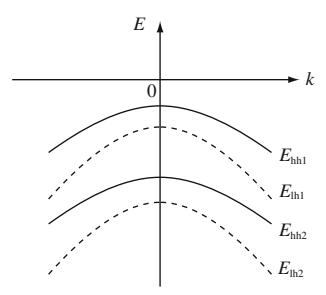


Fig. 7.3 Valence band in a one-dimensional QW

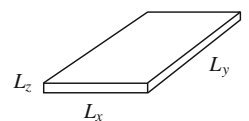


Fig. 7.4 Quantum well

Because a wave function of the heavy hole distributes in the xy-plane corresponding to the  $p_x$ - or  $p_y$ -like orbital, the heavy hole moves on the xy-plane more easily than along the z-axis, which leads to  $m_{xy,hh}^* < m_{z,hh}^*$ . In contrast, a wave function of the light hole distributes along the z-axis corresponding to the  $p_z$ -like orbital, the light hole moves along the z-axis more easily than on the xy-plane, which results in  $m_{z,hh}^* < m_{xy,hh}^*$ . For example, in GaAs, we have  $m_{z,hh}^* = 0.377 \, m$ ,  $m_{z,hh}^* = 0.09 \, m$ ,  $m_{xy,hh}^* = 0.11 \, m$ , and  $m_{xy,hh}^* = 0.21 \, m$ , where m is the electron mass in a vacuum.

#### 7.2.2.4 Wave Function and Momentum Matrix Element

We assume that a wave vector k is directed toward the z-axis and contribution of the split-off band is negligible. Hence, we consider the heavy hole band and the light hole band as the valence bands. If we express the up-spin and down-spin as  $\alpha$  and  $\beta$ , respectively, the wave functions of the conduction band are written as

$$|s\alpha\rangle, |s\beta\rangle.$$
 (7.10)

Quantum states of the valence bands are indicated by j, which is a sum of the angular momentum operator l and the spin operator s when the spin-orbit interaction is considered. We can express the wave function  $|j, m_j\rangle$  as

For the heavy hole

$$\left| \frac{3}{2}, \frac{3}{2} \right\rangle = \frac{1}{\sqrt{2}} |(x + iy)\alpha\rangle,$$

$$\left| \frac{3}{2}, -\frac{3}{2} \right\rangle = \frac{1}{\sqrt{2}} |(x - iy)\beta\rangle,$$
(7.11)

For the light hole

$$\left| \frac{3}{2}, \frac{1}{2} \right\rangle = \frac{1}{\sqrt{6}} |2z\alpha + (x + iy)\beta\rangle,$$

$$\left| \frac{3}{2}, -\frac{1}{2} \right\rangle = \frac{1}{\sqrt{6}} |2z\beta - (x - iy)\alpha\rangle,$$
(7.12)

where j is the eigenvalue of j and  $m_i$  is the eigenvalue of  $j_z$ .

In the following, we will consider the optical transitions between the conduction band and the valence bands. As shown in (2.41), the optical power gain coefficient g is in proportion to a square of the momentum matrix element  $\langle 1|p|2\rangle^2$ . Therefore, to examine the anisotropic optical gain, we compare the momentum matrix elements for the optical transitions.

Along each axis, the momentum matrix elements between the conduction band and the heavy hole band are given by

x-axis: 
$$\frac{1}{\sqrt{2}}\sqrt{3}M$$
,  
y-axis:  $\pm i \frac{1}{\sqrt{2}}\sqrt{3}M$ ,  
z-axis: 0.

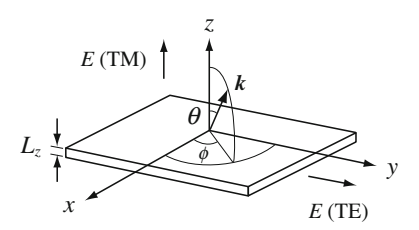
Here, from (1.6) and (1.42), M is defined as

$$\sqrt{3}M \equiv \langle s|p_x|x\rangle = \langle s|p_y|y\rangle = \langle s|p_z|z\rangle 
= m \left[ \frac{1}{2m_e^*} \frac{E_g(E_g + \Delta_0)}{E_g + \frac{2}{3}\Delta_0} \right]^{1/2},$$
(7.13)

where m is the electron mass in a vacuum,  $m_e^*$  is the effective mass of the electron in the conduction band,  $E_g$  is the bandgap energy, and  $\Delta_0$  is the split-off energy due to the spin-orbit interaction. A coefficient  $\sqrt{3}$  is introduced so that a matrix element averaged over all directions of the wave vector k may be M.

208 7 Quantum Well LDs

**Fig. 7.5** Direction of a wave vector k



# 7.2.2.5 Optical Transitions in QWs

As shown in Fig. 7.5, we assume that a quantization axis is the z-axis and a QW layer is placed on the xy-plane. If a light is supposed to propagate along a positive direction of the x-axis, an electric field E along the y-axis is the TE mode, and an electric field E along the z-axis is the TM mode. Because the wave vector k can take various directions, we express a direction of k in a spherical polar coordinate system, as shown in Fig. 7.5. In this QW, the z-component of k is discrete, whereas the x- and y-components of k are continuous. For example, if the energy barrier is infinite, we have  $k_z = n\pi/L_z$  with an integer n.

According to the directions of k, the momentum matrix elements between the conduction band and the heavy hole band are given by

x-axis: 
$$\frac{1}{\sqrt{2}}\sqrt{3}M(\cos\theta\cos\phi\mp i\sin\phi)$$
,  
y-axis:  $\frac{1}{\sqrt{2}}\sqrt{3}M(\cos\theta\sin\phi\pm i\cos\phi)$ ,  
z-axis:  $-\frac{1}{\sqrt{2}}\sqrt{3}M\sin\theta$ .

The square of the optical transition matrix elements is proportional to  $(1|E \cdot p|2)^2$ , where E is the electric field. Therefore, only the momentum matrix element with a component parallel to E contributes to the optical transitions. We consider a wave vector  $k_n$  for a quantum number n, and we average the square of the momentum matrix element all over the directions on the xy-plane by fixing the z-component  $k_{nz}$  of  $k_n$ .

# 7.2.2.6 Momentum Matrix Elements Between the Conduction Band and the Heavy Hole Band in QWs

An average of the squared momentum matrix element  $\langle M^2 \rangle_{hh,TE}$  for the TE mode (E//y) is expressed as

$$\langle M^{2} \rangle_{hh,TE} = \frac{3M^{2}}{2} \cdot \frac{1}{2\pi} \int_{0}^{2\pi} (\cos^{2}\theta \sin^{2}\phi + \cos^{2}\phi) \, D\phi$$

$$= \frac{3M^{2}}{4} (1 + \cos^{2}\theta) = \frac{3M^{2}}{4} \left(1 + \frac{k_{z}^{2}}{k^{2}}\right)$$

$$= \frac{3M^{2}}{4} \left(1 + \frac{E_{z,n}}{E_{n}}\right), \tag{7.14}$$

where  $E_{z,n}$  is the quantized energy of the *n*th subband and  $E_n$  is the total energy of the *n*th subband.

At the subband edge,  $E_{z,n} = E_n$  is satisfied; then we have

$$\langle M^2 \rangle_{\text{hh,TE}} = \frac{3M^2}{2}.\tag{7.15}$$

An average of the squared momentum matrix element  $\langle M^2 \rangle_{hh,TM}$  for the TM mode (E//z) is given by

$$\langle M^2 \rangle_{\text{hh,TM}} = \frac{3M^2}{2} \sin^2 \theta = \frac{3M^2}{2} (1 - \cos^2 \theta)$$
$$= \frac{3M^2}{2} \left( 1 - \frac{k_z^2}{k^2} \right) = \frac{3M^2}{2} \left( 1 - \frac{E_{z,n}}{E_n} \right). \tag{7.16}$$

As a result, at the subband edge, we obtain

$$\langle M^2 \rangle_{\text{hh,TM}} = 0. \tag{7.17}$$

As shown in (7.15) and (7.17), there is a *selection rule* between the conduction band and the heavy hole band at the subband edge, that is, only the optical transition for the TE mode is allowed; that for the TM mode is inhibited.

# 7.2.2.7 Momentum Matrix Elements Between the Conduction Band and the Light Hole Band in QWs

An average of the squared momentum matrix element  $\langle M^2 \rangle_{lh,TE}$  for the TE mode  $(E/\!/y)$  is obtained as

$$\langle M^2 \rangle_{\text{lh,TE}} = \frac{M^2}{4} (1 + \cos^2 \theta) + M^2 \sin^2 \theta$$
$$= \frac{M^2}{4} \left( 1 + \frac{E_{z,n}}{E_n} \right) + M^2 \left( 1 - \frac{E_{z,n}}{E_n} \right). \tag{7.18}$$

210 7 Quantum Well LDs

Hence, at the subband edge, we have

$$\langle M^2 \rangle_{\text{lh,TE}} = \frac{M^2}{2}.\tag{7.19}$$

An average of the squared momentum matrix element  $\langle M^2 \rangle_{lh,TM}$  for the TM mode (E//z) is written as

$$\langle M^2 \rangle_{\text{lh,TM}} = \frac{M^2}{2} \sin^2 \theta + 2M^2 \cos^2 \theta$$
  
=  $\frac{M^2}{2} \left( 1 - \frac{E_{z,n}}{E_n} \right) + 2M^2 \frac{E_{z,n}}{E_n}.$  (7.20)

Therefore, at the subband edge, we obtain

$$\langle M^2 \rangle_{\text{lh,TM}} = 2M^2. \tag{7.21}$$

#### 7.2.2.8 Optical Gains in QW-LDs

In Fig. 7.3, the vertical line shows the electron energy, and the hole energy decreases with an increase in the height. As a result, the concentration of the heavy hole is larger than that of the light hole. Thus, among the polarization-dependent optical gain  $g_{e-hh,TE}$ ,  $g_{e-lh,TE}$ , and  $g_{e-lh,TM}$ , we have the following relation

$$g_{\text{e-hh.TE}} > g_{\text{e-lh.TM}} > g_{\text{e-lh.TE}}$$

where subscripts e-hh and e-lh show the recombination of the electron and the heavy hole and of the electron and the light hole, respectively. As shown earlier, the optical gain for the TE mode has a maximum value in the optical transition between the conduction band and the heavy hole band in the QW-LDs.

#### 7.2.2.9 Low-Loss Optical Waveguides

In the QWs, the densities of states are step functions, and the absorption coefficient at the band edge changes sharply with wavelength. Therefore, the absorption loss in the optical waveguides with the QWs is lower than that with the bulk DHs.

#### 7.2.2.10 High-Speed Modulation

As shown in (5.103), the relaxation oscillation frequency  $f_r$  is given by

$$f_{\rm r} = \frac{1}{2\pi} \sqrt{\frac{\partial G}{\partial n} \frac{S_0}{\tau_{\rm ph}}} \ . \tag{7.22}$$

In the QW-LDs, based on the step-like densities of states, the differential optical gain  $\partial G/\partial n$  is larger than that in the bulk DH-LDs. Hence,  $f_r$  in the QW-LDs is larger than that in the bulk DH-LDs, which leads to high-speed modulations in the QW-LDs. Figure 7.6 shows a calculated differential optical gain  $(n_r/c)\partial G/\partial n$  as a function of the quasi-Fermi level of the conduction band  $E_{Fc}$ . It is clearly revealed that the differential optical gain in the QW-LDs is larger than that in the bulk DH-LDs.

From (7.6), the optical gain is simplified as

$$g = |M|_{\text{ave}}^2 \rho [f_c - f_v]. \tag{7.23}$$

The QWs modify the density of states  $\rho$  in (7.23), while the intentionally doped active layers can change  $[f_c - f_v]$ . For example, p-doped active layers reduce  $f_v$ , and a relaxation oscillation frequency of about 30 GHz has been reported.

#### 7.2.2.11 Narrow Spectral Linewidth

From (5.169), the spectral linewidth  $\Delta\omega_0$  of a laser light is expressed as

$$\Delta\omega_0 = \frac{\hbar\omega_m c E_{\rm cv} \ln(1/R)}{4P_0 n_{\rm r} L} (1 + \alpha^2), \tag{7.24}$$

where the spectral linewidth enhancement factor  $\alpha$ , which is also called  $\alpha$  parameter, is given by

$$\alpha = -\frac{2\omega_m}{n_r} \frac{\partial n_r}{\partial n} \left(\frac{\partial G}{\partial n}\right)^{-1},\tag{7.25}$$

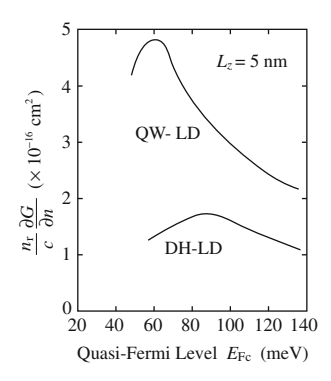


Fig. 7.6 Differential optical gain

as shown in (5.179). Here,  $n_{\rm r}$  is the refractive index, n is the carrier concentration, and G is the amplification rate. As illustrated in Fig. 7.6, the differential optical gain  $\partial G/\partial n$  in the QW-LDs is larger than that in the bulk DH-LDs. As a result, from (7.25), the absolute value of  $\alpha$  in the QW-LDs is small, which leads to a narrow spectral line width  $\Delta\omega_0$ . Figure 7.7 shows calculated  $\alpha$  values as a function of the quasi-Fermi level of the conduction band  $E_{\rm Fc}$ . It is found that  $\alpha$  in the QW-LDs is smaller than that in the bulk DH-LDs. Moreover, a small  $\alpha$  leads to low chirping during modulation, which is suitable for long-haul, large-capacity optical fiber communication systems.

### 7.3 Strained Quantum Well LDs

# 7.3.1 Effect of Strains

According to *group theory*, with a decrease in symmetry of the crystals, degeneracy of the energy band is removed. In the bulk structures for semiconductor lasers, due to their high symmetry, the heavy hole band and the light hole band are degenerate at  $\Gamma$  point (k = 0). In the QWs, due to their lower symmetry than that of the bulk structures, degeneracy at k = 0 is removed, as shown in Fig. 7.3.

When the *strains* are applied to semiconductor crystals, symmetry of the crystals is reduced, and degeneracy of the energy bands is removed. According to the compressive or tensile strains, the band structures change in different ways. Based on this principle, *band-structure engineering*, which modifies the band structures by intentionally controlling the strains, has been developed. By introducing the strains into the active layers, we can obtain excellent characteristics, such as a low threshold current, a high differential quantum efficiency, high-speed modulation, low chirping, and a narrow spectral linewidth in semiconductor lasers, as in the QW-LDs. With regard to the optical gain for the TE mode  $g_{TE}$  and that for the TM mode  $g_{TM}$ , the

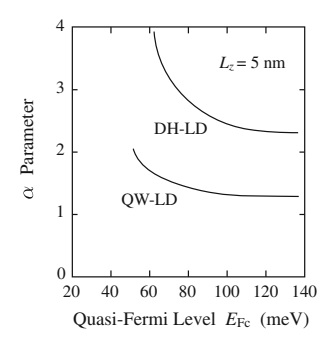


Fig. 7.7 Spectral linewidth enhancement factor

compressive strains in the active layer plane lead to  $g_{\rm TE} > g_{\rm TM}$ , while the tensile strains result in  $g_{\rm TE} < g_{\rm TM}$ .

To induce the strains in semiconductor crystals, an external *stress*, a difference in the thermal expansion coefficients of the materials, and a difference in the lattice constants are used. Especially, a difference in the lattice constants, which is referred to as *lattice mismatching*, is frequently adopted, because the most stable strains are obtained. The lattice mismatching takes place when a semiconductor layer is epitaxially grown on the substrate with a different lattice constant from that of the grown layer. If thickness of the grown layer exceeds the *critical thickness*, the dislocations are generated in the grown layer. If the layer thickness further increases up to about 1  $\mu$  m, which is much larger than the critical thickness, the dislocations are sometimes reduced, and such a thick grown layer can be used as the *buffer layer*. However, this thick layer is not suitable for active layers, because the threshold current is large. When the grown layer is thinner than the critical thickness as in the QWs, the dislocations are not generated. Hence, the *strained QWs* are suitable for band-structure engineering.

#### 7.3.2 Band-Structure Engineering

#### 7.3.2.1 Epitaxial Growth and Strains

When the epitaxially grown layers are thinner than the critical thickness, the epitaxial layers are grown on the substrate with their lattice constants matched to that of the substrate. Therefore, the *elastic strains* are induced in the epitaxial layers. We assume that the lattice constant of an epitaxial layer itself is a(x) and the lattice constant of the substrate is  $a_0$ . For  $a(x) > a_0$ , the *compressive strain* is generated in the grown layer, while for  $a(x) < a_0$ , the *tensile strain* is produced in the grown layer.

The strain *tensors* are expressed by matrixes using their symmetrical properties. The matrix elements of the strains  $\varepsilon_{ij}$  consist of the *diagonal elements*  $\varepsilon_{ii}$  called the *hydrostatic strains* and the *nondiagonal elements*  $\varepsilon_{ij}$  ( $i \neq j$ ) named the *shear strains*.

#### 7.3.2.2 Low Threshold Current

The radii of the curvature of the energy bands, that is, the effective masses of the carriers, are modified by the strains. With decreases in the effective masses of the carriers, the carrier concentration to achieve the population inversion decreases. Therefore, a low threshold current is obtained, as in the following.

When the electric currents are injected in semiconductor lasers, many electrons are generated in the conduction band, and many holes are simultaneously produced in the valence bands. In this case, the carrier distributions are far from thermal equilibrium. Therefore, we cannot express the distribution functions of the electron

and the hole with a single Fermi level,  $E_{\rm F}$ . As a result, regarding the electrons in the conduction band and the holes in the valence band independently take the Fermi-Dirac distributions, and we introduce the quasi-Fermi levels  $E_{\rm Fc}$  and  $E_{\rm Fv}$ , which are defined as

$$n \equiv N_{\rm c} \exp\left(-\frac{E_{\rm c} - E_{\rm Fc}}{k_{\rm B}T}\right),$$

$$p \equiv N_{\rm v} \exp\left(-\frac{E_{\rm Fv} - E_{\rm v}}{k_{\rm B}T}\right),$$

$$N_{\rm c} = 2\left(\frac{2\pi m_{\rm e} * k_{\rm B}T}{h^2}\right)^{3/2},$$

$$N_{\rm v} = 2\left(\frac{2\pi m_{\rm h} * k_{\rm B}T}{h^2}\right)^{3/2},$$

$$(7.26)$$

where n and p are the concentrations of the electron and the hole, respectively;  $E_c$  and  $E_v$  are the energies of the bottom of the conduction band and the top of the valence band, respectively;  $k_B$  is the Boltzmann constant; T is absolute temperature;  $N_c$  and  $N_v$  are the effective densities of states for the electron and the hole, respectively;  $m_e^*$  and  $m_h^*$  are the effective masses of the electron and the hole, respectively; and h is Planck's constant.

From (7.26),  $E_{Fc}$  and  $E_{Fv}$  are expressed as

$$E_{Fc} = E_{c} + k_{B}T \ln\left(\frac{n}{N_{c}}\right),$$

$$E_{Fv} = E_{v} - k_{B}T \ln\left(\frac{p}{N_{v}}\right).$$
(7.27)

Hence, we obtain

$$E_{\rm Fc} - E_{\rm Fv} = E_{\rm g} + k_{\rm B}T \ln \frac{np}{N_{\rm c}N_{\rm v}}, \quad E_{\rm g} = E_{\rm c} - E_{\rm v}.$$
 (7.28)

As shown in (2.9), the condition for the population inversion is given by

$$E_{\rm Fc} - E_{\rm Fv} > E_{\rm g},\tag{7.29}$$

which reduces to

$$np > N_{\rm c}N_{\rm v} = 4\left(\frac{2\pi k_{\rm B}T}{h^2}\right)^3 (m_{\rm e}^*m_{\rm h}^*)^{3/2},$$
 (7.30)

where (7.26) and (7.28) were used. From (7.30), the transparent carrier concentration  $n_0$  is obtained as

$$n_0 = 2\left(\frac{2\pi k_{\rm B}T}{h^2}\right)^{3/2} (m_{\rm e}^* m_{\rm h}^*)^{3/4}.$$
 (7.31)

Therefore, to achieve a low  $n_0$  leading to a low threshold,  $m_e^*$  and  $m_h^*$  should be light.

As shown in (1.11), the effective mass tensor  $m_{ij}$  of the carrier is written as

$$\left(\frac{1}{m}\right)_{ij} = \frac{1}{\hbar^2} \frac{\partial^2 E}{\partial k_i \partial k_j},\tag{7.32}$$

which is related to the radius of the curvature of the band energy. The compressive strains in the active layer decrease the radius of the curvature of the heavy hole band in the vicinity of the band edge, which reduces the effective mass of the heavy hole. As a result, the threshold carrier concentration decreases, and therefore the Auger recombination rate in (5.52) is also reduced. Furthermore, from the momentum conservation law and the energy conservation law, the Auger transitions are going to be inhibited. Hence, the Auger processes are drastically reduced. As a result, a high light emission efficiency and a low threshold current density are simultaneously obtained. The strains in the active layers also enhance the differential optical gain  $\partial G/\partial n$ , which further reduces the threshold carrier concentration.

### 7.3.2.3 Anisotropic Optical Gain

The tensile strains make the energy of the light hole lower than that of the heavy hole. When we draw the energy bands with the vertical line as the energy of the electron, the band edge of the light hole is above that of the heavy hole. As a result, concentration of the light hole is larger than that of the heavy hole, and the optical gain for the TM mode is larger than that for the TE mode, which results in laser oscillation in the TM mode. By optimizing the tensile strains so that the optical gain for the TE mode and that for the TM mode may take a common value, polarization-independent semiconductor optical amplifiers have been demonstrated.

#### 7.3.2.4 High-Speed Modulation

The strains in the active layers enhance the differential optical gain  $\partial G/\partial n$ , which leads to high-speed modulations. The compressive strains result in large gain saturation, while the tensile strains lead to low gain saturation with a large optical gain. Hence, the tensile strains are expected to improve high-speed modulation characteristics.

#### 7.3.2.5 Narrow Spectral Linewidth

The strains increase the differential optical gain  $\partial G/\partial n$  and decrease  $\alpha$ . Therefore, a narrow spectral linewidth such as 3.6 kHz has been obtained in a strained QW  $\lambda/4$ -shifted DFB-LD [3].

#### 7.3.3 Analysis

#### 7.3.3.1 Fundamental Equations

We introduce the effect of strains into the Schrödinger equation as the perturbation, where the unperturbed Hamiltonian is assumed to include the  $k \cdot p$  perturbation and the spin-orbit interaction. This unperturbed Hamiltonian whose base wave function is  $|j, m_j\rangle$  is known as *Luttinger-Kohn Hamiltonian* [4], while the perturbation Hamiltonian representing the effect of the strains is called *Pikus-Bir Hamiltonian* [5–7].

#### 7.3.3.2 Luttinger-Kohn Hamiltonian

In Chap. 1, to obtain the eigenenergies of the valence bands, we used the following Hamiltonian

$$\mathcal{H} = \mathcal{H}_0 + \mathcal{H}_{kp} + \mathcal{H}_{so}, \tag{7.33}$$

where  $\mathcal{H}_0$  is the unperturbed Hamiltonian,  $\mathcal{H}_{kp}$  is the  $\mathbf{k} \cdot \mathbf{p}$  perturbation Hamiltonian, and  $\mathcal{H}_{so}$  is the spin-orbit interaction Hamiltonian. Using this Hamiltonian  $\mathcal{H}$ , we consider a  $6 \times 6$  matrix expressed as

$$\begin{bmatrix} \mathcal{H}_{11} \ \mathcal{H}_{12} \ \mathcal{H}_{13} \ \mathcal{H}_{14} \ \mathcal{H}_{15} \ \mathcal{H}_{16} \\ \mathcal{H}_{21} \ \mathcal{H}_{22} \ \mathcal{H}_{23} \ \mathcal{H}_{24} \ \mathcal{H}_{25} \ \mathcal{H}_{26} \\ \mathcal{H}_{31} \ \mathcal{H}_{32} \ \mathcal{H}_{33} \ \mathcal{H}_{34} \ \mathcal{H}_{35} \ \mathcal{H}_{36} \\ \mathcal{H}_{41} \ \mathcal{H}_{42} \ \mathcal{H}_{43} \ \mathcal{H}_{44} \ \mathcal{H}_{45} \ \mathcal{H}_{46} \\ \mathcal{H}_{51} \ \mathcal{H}_{52} \ \mathcal{H}_{53} \ \mathcal{H}_{54} \ \mathcal{H}_{55} \ \mathcal{H}_{56} \\ \mathcal{H}_{61} \ \mathcal{H}_{62} \ \mathcal{H}_{63} \ \mathcal{H}_{24} \ \mathcal{H}_{65} \ \mathcal{H}_{66} \end{bmatrix},$$

$$(7.34)$$

where  $\mathcal{H}_{ij} = \langle i | \mathcal{H} | j \rangle$  and  $\langle i |$  and  $| j \rangle$  are written as

$$\langle 1| = \left\langle \frac{3}{2}, \frac{3}{2} \right|, \quad \langle 2| = \left\langle \frac{3}{2}, \frac{1}{2} \right|, \quad \langle 3| = \left\langle \frac{3}{2}, -\frac{1}{2} \right|, \quad \langle 4| = \left\langle \frac{3}{2}, -\frac{3}{2} \right|,$$

$$\langle 5| = \left\langle \frac{1}{2}, \frac{1}{2} \right|, \quad \langle 6| = \left\langle \frac{1}{2}, -\frac{1}{2} \right|, \quad |1\rangle = \left| \frac{3}{2}, \frac{3}{2} \right\rangle, \quad |2\rangle = \left| \frac{3}{2}, \frac{1}{2} \right\rangle, \quad (7.35)$$

$$|3\rangle = \left| \frac{3}{2}, -\frac{1}{2} \right\rangle, \quad |4\rangle = \left| \frac{3}{2}, -\frac{3}{2} \right\rangle, \quad |5\rangle = \left| \frac{1}{2}, \frac{1}{2} \right\rangle, \quad |6\rangle = \left| \frac{1}{2}, -\frac{1}{2} \right\rangle.$$

Equation (7.34) shows Luttinger-Kohn Hamiltonian for the valence bands, and this Hamiltonian is used as the unperturbed Hamiltonian to analyze the strains. When the split-off energy  $\Delta_0$  is larger than 0.3 eV as in GaAs, contribution of the split-off band can be neglected. In this case, Luttinger-Kohn Hamiltonian for the valence bands  $\mathcal{H}_{LK}$  results in a 4 × 4 matrix, which is given by

$$\mathcal{H}_{LK} = \begin{bmatrix} \mathcal{H}_{11} & \mathcal{H}_{12} & \mathcal{H}_{13} & \mathcal{H}_{14} \\ \mathcal{H}_{21} & \mathcal{H}_{22} & \mathcal{H}_{23} & \mathcal{H}_{24} \\ \mathcal{H}_{31} & \mathcal{H}_{32} & \mathcal{H}_{33} & \mathcal{H}_{34} \\ \mathcal{H}_{41} & \mathcal{H}_{42} & \mathcal{H}_{43} & \mathcal{H}_{44} \end{bmatrix} = \begin{bmatrix} a_{+} & b & c & 0 \\ b^{*} & a_{-} & 0 & c \\ c^{*} & 0 & a_{-} & -b \\ 0 & c^{*} & -b^{*} & a_{+} \end{bmatrix},$$
(7.36)

where

$$a_{\pm} = \frac{\hbar^2}{2m} \left[ -(\gamma_1 \mp 2\gamma_2)k_z^2 - (\gamma_1 \pm \gamma_2)(k_x^2 + k_y^2) \right],$$

$$b = \frac{\hbar^2}{m} \sqrt{3} \gamma_3 (k_x - i k_y) k_z,$$

$$c = \frac{\hbar^2}{2m} \sqrt{3} \left[ \gamma_2 (k_x^2 - k_y^2) - i 2\gamma_3 k_x k_y \right].$$
(7.37)

Here,  $\gamma_1$ ,  $\gamma_2$ , and  $\gamma_3$  are *Luttinger parameters*, and they are related to the effective masses  $m_{\text{hh}}^*$  and  $m_{\text{lh}}^*$  of the heavy hole and the light hole as

$$\frac{1}{m}(\gamma_1 - 2\gamma_2) = \frac{1}{m_{\rm bh}^*}$$
 (heavy hole), (7.38)

$$\frac{1}{m}(\gamma_1 + 2\gamma_2) = \frac{1}{m_{1h}^*}$$
 (light hole), (7.39)

where *m* is the electron mass in a vacuum.

We can also express (7.36) as

$$\mathcal{H}_{LK} = \frac{\hbar^2}{2m} \left[ -\left(\gamma_1 + \frac{5}{2}\gamma_2\right) k^2 + 2\gamma_2 (k_x^2 J_x^2 + k_y^2 J_y^2 + k_z^2 J_z^2) + 4\gamma_3 \left[ \{k_x k_y\} \{J_x J_y\} + \{k_y k_z\} \{J_y J_z\} + \{k_z k_x\} \{J_z J_x\} \right] \right],$$
 (7.40)

where  $J_x$ ,  $J_y$ , and  $J_z$  are the matrixes represented as

218 7 Quantum Well LDs

$$J_{x} = \frac{1}{2} \begin{bmatrix} 0 & \sqrt{3}i & 0 & 0 \\ -\sqrt{3}i & 0 & 2i & 0 \\ 0 & -2i & 0 & \sqrt{3}i \\ 0 & 0 & -\sqrt{3}i & 0 \end{bmatrix},$$

$$J_{y} = \frac{1}{2} \begin{bmatrix} 0 & \sqrt{3} & 0 & 0 \\ \sqrt{3} & 0 & 2 & 0 \\ 0 & 2 & 0 & \sqrt{3} \\ 0 & 0 & \sqrt{3} & 0 \end{bmatrix},$$

$$J_{z} = \frac{1}{2} \begin{bmatrix} 3 & 0 & 0 & 0 \\ 0 & 1 & 0 & 0 \\ 0 & 0 & -1 & 0 \\ 0 & 0 & 0 & -3 \end{bmatrix}.$$

$$(7.41)$$

In (7.40),  $\{k_x k_y\}$  and  $\{J_x J_y\}$  are defined as

$$\{k_x k_y\} \equiv \frac{1}{2} (k_x k_y + k_y k_x), \quad \{J_x J_y\} \equiv \frac{1}{2} (J_x J_y + J_y J_x).$$
 (7.42)

#### 7.3.3.3 Pikus-Bir Hamiltonian

Pikus-Bir Hamiltonian  $\mathcal{H}_s$  is given by a sum of the *orbit-strain interaction Hamiltonian*  $\mathcal{H}_{os}$  and the *strain-dependent spin-orbit interaction Hamiltonian*  $\mathcal{H}_{ss}$ . In the valence bands of the zinc-blende structure, the orbit-strain interaction Hamiltonian  $\mathcal{H}_{os}$  at  $\Gamma$  point (k=0) is written as

$$\mathcal{H}_{os} = -a_{1}(\varepsilon_{xx} + \varepsilon_{yy} + \varepsilon_{zz})$$

$$-3b_{1} \left[ \left( L_{x}^{2} - \frac{L^{2}}{3} \right) \varepsilon_{xx} + \left( L_{y}^{2} - \frac{L^{2}}{3} \right) \varepsilon_{yy} + \left( L_{z}^{2} - \frac{L^{2}}{3} \right) \varepsilon_{zz} \right]$$

$$-\sqrt{3}d_{1} \left( L_{x}L_{y} + L_{y}L_{x} \right) \varepsilon_{xy} - \sqrt{3}d_{1} \left( L_{y}L_{z} + L_{z}L_{y} \right) \varepsilon_{yz}$$

$$-\sqrt{3}d_{1} \left( L_{z}L_{x} + L_{x}L_{z} \right) \varepsilon_{zx}. \tag{7.43}$$

The strain-dependent spin-orbit interaction Hamiltonian  $\mathcal{H}_{\text{ss}}$  is expressed as

$$\mathcal{H}_{ss} = -a_{2}(\varepsilon_{xx} + \varepsilon_{yy} + \varepsilon_{zz})(\boldsymbol{L} \cdot \boldsymbol{s})$$

$$-3b_{2}\left(L_{x}s_{x} - \frac{\boldsymbol{L} \cdot \boldsymbol{s}}{3}\right)\varepsilon_{xx} - 3b_{2}\left(L_{y}s_{y} - \frac{\boldsymbol{L} \cdot \boldsymbol{s}}{3}\right)\varepsilon_{yy}$$

$$-3b_{2}\left(L_{z}s_{z} - \frac{\boldsymbol{L} \cdot \boldsymbol{s}}{3}\right)\varepsilon_{zz}$$

$$-\sqrt{3}d_{2}\left(L_{x}s_{y} + L_{y}s_{x}\right)\varepsilon_{xy} - \sqrt{3}d_{2}\left(L_{y}s_{z} + L_{z}s_{y}\right)\varepsilon_{yz}$$

$$-\sqrt{3}d_{2}\left(L_{z}s_{x} + L_{x}s_{z}\right)\varepsilon_{zx},$$

$$(7.44)$$

where  $L_x$ ,  $L_y$ ,  $L_z$ , and L are the *orbital angular momentum operators*;  $s_x$ ,  $s_y$ ,  $s_z$ , and s are the *spin angular momentum operators*;  $\varepsilon_{ij}(i, j = x, y, z)$  is a matrix element for the strain tensor; and  $a_i$ ,  $b_i$ , and  $d_i$  (i = 1, 2) are the *deformation potentials*.

Because the orbit-strain interaction Hamiltonian  $\mathcal{H}_{os}$  is larger than the strain-dependent spin-orbit interaction Hamiltonian  $\mathcal{H}_{ss}$ , the strained QWs are often analyzed by considering only  $\mathcal{H}_{os}$ .

#### 7.3.3.4 Relationship Between Strain and Stress

The strains  $\varepsilon$  and stresses  $\sigma$  are both tensors, which are related by

$$\sigma_{ij} = \sum_{k,l} c_{ijkl} \varepsilon_{kl} = c_{ijkl} \varepsilon_{kl}, \tag{7.45}$$

where  $c_{ijkl}$  is the elastic stiffness constant. Also, on the right-hand side,  $\sum$  is omitted by promising that we take a sum with regard to a subscript appearing twice, which is referred to as the *Einstein summation convention*.

It is useful to express the tensors by the matrixes, because of symmetry in the tensors. As a coordinate system for the tensors, we use 1, 2, and 3 as indexes. For example, 1, 2, and 3 correspond to x, y, and z, respectively. Here, we relate indexes 1, 2, and 3 of the tensors to indexes 1, 2, 3, 4, 5, and 6 of the matrixes as follows:

Therefore, we can rewrite (7.45) as

$$\sigma_i = \sum_j c_{ij} \varepsilon_j = c_{ij} \varepsilon_j \quad (i, j = 1, 2, 3, 4, 5, 6), \tag{7.46}$$

220 7 Quantum Well LDs

where

$$\begin{bmatrix} \sigma_{11} & \sigma_{12} & \sigma_{13} \\ \sigma_{21} & \sigma_{22} & \sigma_{23} \\ \sigma_{31} & \sigma_{32} & \sigma_{33} \end{bmatrix} = \begin{bmatrix} \sigma_{11} & \sigma_{12} & \sigma_{31} \\ \sigma_{12} & \sigma_{22} & \sigma_{23} \\ \sigma_{31} & \sigma_{23} & \sigma_{33} \end{bmatrix} = \begin{bmatrix} \sigma_{1} & \sigma_{6} & \sigma_{5} \\ \sigma_{6} & \sigma_{2} & \sigma_{4} \\ \sigma_{5} & \sigma_{4} & \sigma_{3} \end{bmatrix},$$
(7.47)

$$\begin{bmatrix} \varepsilon_{11} \ \varepsilon_{12} \ \varepsilon_{13} \\ \varepsilon_{21} \ \varepsilon_{22} \ \varepsilon_{23} \\ \varepsilon_{31} \ \varepsilon_{32} \ \varepsilon_{33} \end{bmatrix} = \begin{bmatrix} \varepsilon_{11} \ \varepsilon_{12} \ \varepsilon_{23} \\ \varepsilon_{12} \ \varepsilon_{22} \ \varepsilon_{23} \\ \varepsilon_{31} \ \varepsilon_{23} \ \varepsilon_{33} \end{bmatrix} = \frac{1}{2} \begin{bmatrix} 2\varepsilon_{1} \ \varepsilon_{6} \ \varepsilon_{5} \\ \varepsilon_{6} \ 2\varepsilon_{2} \ \varepsilon_{4} \\ \varepsilon_{5} \ \varepsilon_{4} \ 2\varepsilon_{3} \end{bmatrix}.$$
(7.48)

In the zinc-blende structures with symmetry of  $\bar{4}3m$  or  $T_d$ , (7.45) reduces to [8, 9]

$$\begin{bmatrix} \sigma_{1} \\ \sigma_{2} \\ \sigma_{3} \\ \sigma_{4} \\ \sigma_{5} \\ \sigma_{6} \end{bmatrix} = \begin{bmatrix} c_{11} c_{12} c_{12} & 0 & 0 & 0 \\ c_{12} c_{11} c_{12} & 0 & 0 & 0 \\ c_{12} c_{12} c_{11} & 0 & 0 & 0 \\ 0 & 0 & 0 c_{44} & 0 & 0 \\ 0 & 0 & 0 & 0 c_{44} & 0 \\ 0 & 0 & 0 & 0 & 0 c_{44} \end{bmatrix} \begin{bmatrix} \varepsilon_{1} \\ \varepsilon_{2} \\ \varepsilon_{3} \\ \varepsilon_{4} \\ \varepsilon_{5} \\ \varepsilon_{6} \end{bmatrix}.$$
(7.49)

#### 7.3.3.5 Bulk Structures

Here, we consider a semiconductor crystal in which *biaxial stresses* are applied to the crystal plane due to the lattice mismatching. We assume that the epitaxial layers are grown along the z-axis, and the layer plane is on the xy-plane. When the lattice constant of the substrate is  $a_0$  and that of the epitaxially grown layer itself is a(x), the strains due to lattice mismatching are given by

$$\varepsilon_{xx} = \varepsilon_{yy} = \frac{a_0 - a(x)}{a(x)} = \varepsilon, \quad \varepsilon_{zz} \neq 0,$$

$$\varepsilon_{xy} = \varepsilon_{yz} = \varepsilon_{zx} = 0,$$
(7.50)

where  $\varepsilon < 0$  corresponds to the compressive strain and  $\varepsilon > 0$  shows the tensile strain.

When the biaxial stresses are induced in the layer plane (xy-plane) due to lattice mismatching, neither the stress along the growth axis (z-axis) nor the shear stresses are imposed to the epitaxial layer. Therefore, the biaxial stresses are expressed as

$$\sigma_{xx} = \sigma_{yy} = \sigma, \quad \sigma_{zz} = 0,$$

$$\sigma_{xy} = \sigma_{yz} = \sigma_{zx} = 0.$$
(7.51)

If we relate indexes 1, 2, and 3 of the tensors to x, y, and z, respectively, and substitute (7.50) and (7.51) into (7.49), we have

$$\begin{bmatrix} \sigma \\ \sigma \\ 0 \\ 0 \\ 0 \\ 0 \\ 0 \end{bmatrix} = \begin{bmatrix} c_{11} & c_{12} & c_{12} & 0 & 0 & 0 \\ c_{12} & c_{11} & c_{12} & 0 & 0 & 0 \\ c_{12} & c_{12} & c_{11} & 0 & 0 & 0 \\ 0 & 0 & 0 & c_{44} & 0 & 0 \\ 0 & 0 & 0 & 0 & c_{44} & 0 \\ 0 & 0 & 0 & 0 & 0 & c_{44} \end{bmatrix} \begin{bmatrix} \varepsilon \\ \varepsilon \\ \varepsilon_{zz} \\ 0 \\ 0 \\ 0 \end{bmatrix}.$$
 (7.52)

From (7.52), we obtain

$$\sigma = (c_{11} + c_{12})\varepsilon + c_{12}\varepsilon_{zz},$$

$$0 = 2c_{12}\varepsilon + c_{11}\varepsilon_{zz},$$
(7.53)

which leads to

$$\varepsilon_{zz} = -\frac{2c_{12}}{c_{11}} \varepsilon,$$

$$\sigma = \left(c_{11} + c_{12} - \frac{2c_{12}^2}{c_{11}}\right) \varepsilon.$$
(7.54)

Substituting (7.54) into (7.43) results in

$$\mathcal{H}_{os} = -2a_1 \left( 1 - \frac{c_{12}}{c_{11}} \right) \varepsilon + 3b_1 \left( L_z^2 - \frac{1}{3} L^2 \right) \left( 1 + \frac{2c_{12}}{c_{11}} \right) \varepsilon. \tag{7.55}$$

Here, we consider a matrix  $\mathcal{H}_{sv}$  such as

$$\mathcal{H}_{sv} = \begin{bmatrix} \langle 1|\mathcal{H}_{os}|1\rangle & \langle 1|\mathcal{H}_{os}|2\rangle & \langle 1|\mathcal{H}_{os}|3\rangle & \langle 1|\mathcal{H}_{os}|4\rangle \\ \langle 2|\mathcal{H}_{os}|1\rangle & \langle 2|\mathcal{H}_{os}|2\rangle & \langle 2|\mathcal{H}_{os}|3\rangle & \langle 2|\mathcal{H}_{os}|4\rangle \\ \langle 3|\mathcal{H}_{os}|1\rangle & \langle 3|\mathcal{H}_{os}|2\rangle & \langle 3|\mathcal{H}_{os}|3\rangle & \langle 3|\mathcal{H}_{os}|4\rangle \\ \langle 4|\mathcal{H}_{os}|1\rangle & \langle 4|\mathcal{H}_{os}|2\rangle & \langle 4|\mathcal{H}_{os}|3\rangle & \langle 4|\mathcal{H}_{os}|4\rangle \end{bmatrix}$$

$$= \begin{bmatrix} \delta E_{hy} - \zeta & 0 & 0 & 0 \\ 0 & \delta E_{hy} + \zeta & 0 & 0 \\ 0 & 0 & \delta E_{hy} + \zeta & 0 \\ 0 & 0 & 0 & \delta E_{hy} - \zeta \end{bmatrix}, (7.56)$$

where

$$\delta E_{\text{hy}} = -2a_1 \left( 1 - \frac{c_{12}}{c_{11}} \right) \varepsilon,$$

$$\zeta = -b_1 \left( 1 + \frac{2c_{12}}{c_{11}} \right) \varepsilon,$$
(7.57)

and (7.35) were used. Equations (7.56) and (7.57) represent the energy shifts at k = 0, which indicates that degeneracy of the valence bands is removed.

222 7 Quantum Well LDs

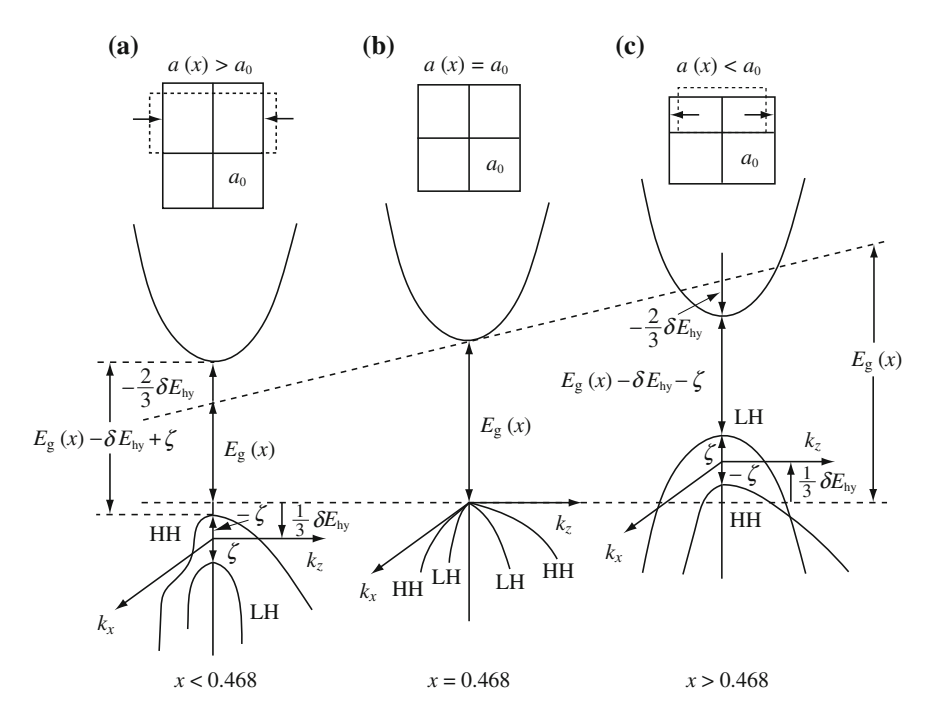


Fig. 7.8 Band structures for the bulk  $In_{1-x}Ga_x$  As layers grown on an InGaAsP layer, which is lattice-matched to an InP substrate: **a** compressive, **b** lattice matching, and **c** tensile

The orbit-strain interaction Hamiltonian for the conduction band  $\mathcal{H}_{sc}$  is given by

$$\mathcal{H}_{\text{sc}} = C_1(\varepsilon_{xx} + \varepsilon_{yy} + \varepsilon_{zz}), \tag{7.58}$$

where  $C_1$  is the deformation potential of the conduction band. The energies of the heavy hole band and the light hole band are given by the eigenvalues of  $\mathcal{H}_{LK} + \mathcal{H}_{sv}$  with the help of (7.36) and (7.56). The energy of the conduction band is obtained as the eigenvalue of  $\mathcal{H}_{LK} + \mathcal{H}_{sc}$  by using (7.36) and (7.58).

Figure 7.8 shows the band structures for the strained bulk  $In_{1-x}Ga_xAs$  layers grown on an InGaAsP layer, which is lattice-matched to an InP substrate. Here,  $C_1 = -2a_1$  is assumed, and the dislocations are neglected. From Fig. 7.8, it is found that the compressive strains lower the energy of the heavy hole more than that of the light hole, and the tensile strains lower the energy of the light hole more than that of the heavy hole. It should be noted that the energy of the hole is low with an increase in the height, because the vertical axis represents the energy of the electron.

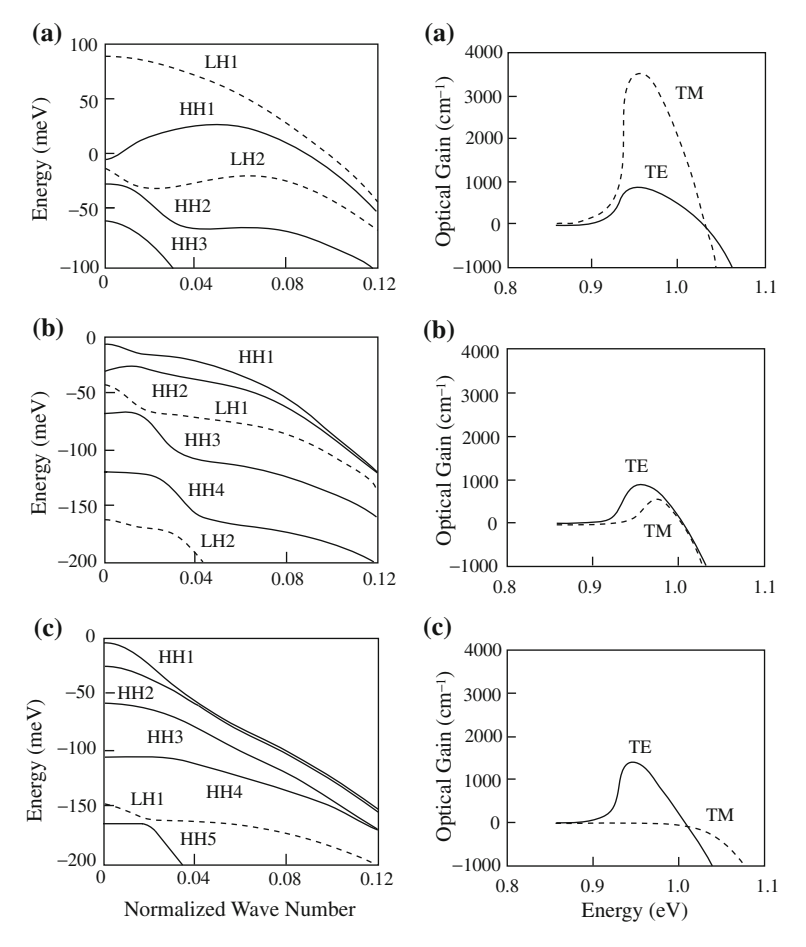


**Fig. 7.9** Energy bands and optical gains in the strained QWs. Here, the oscillation wavelength is  $1.3\,\mu\text{m}$ , and the InGaAsP well is  $10\,\text{nm}$  thick for a  $1.9\,\%$  tensile strain, b lattice matching, and c a  $1.4\,\%$  compressive strain

#### 7.3.3.6 Strained QWs

In the strained QWs, the Hamiltonian for the valence bands is given by

$$\mathcal{H}_{LK} + \mathcal{H}_{sv} + V(z), \tag{7.59}$$

where V(z) represents a potential of the QWs, which is expressed as

$$V(z) = \begin{cases} 0 & \text{(well),} \\ \Delta E_{\text{v}} - \delta E_{\text{hy}} & \text{(barrier).} \end{cases}$$
 (7.60)

If the quantization axis is the z-axis, Schrödinger equation can be solved by replacing  $k_z \to -\mathrm{i}\,\partial/\partial z$ , under the effective mass approximations. The obtained results for the energy bands and the optical gains for the heavy hole (HH) and light hole (LH) are illustrated in Fig. 7.9. Here, the oscillation wavelength is 1.3  $\mu$ m, and the InGaAsP well is 10 nm thick for a 1.9% tensile strain, lattice matching, and a 1.4% compressive strain. As found in Fig. 7.9, the tensile strains enhance the optical gain for the TM mode, and the compressive strains increase the optical gain for the TE mode.

# 7.4 Requirements for Fabrication

The QW-LDs have been in practical use. However, the quantum wire LDs and the quantum box LDs, whose quantum effects are more significant than those of the QW-LDs, are still under research because these quantum structures require highly sophisticated fabrication technologies, which can produce

- 1. highly uniform,
- 2. highly integrated,
- 3. various shaped,
- 4. nanostructures whose quantum effects are significant,
- 5. with low damage,
- 6. in a short time.

Fluctuations in size obscure the density of states, and the quantum effects are degraded. Therefore, uniform quantum structures are needed. When we use quantum wires or quantum boxes in the active layers, the optical gain length is short, because of their tiny size. However, as shown in (5.11), to obtain a low threshold gain, we need long optical gain length L, which is only achieved by highly integrated quantum structures. The fourth requirement is indispensable to quantum structures; the others are common to all devices.

To satisfy these requirements, selective epitaxial growth and self-organized epitaxial growth have attracted a lot of interest.

#### References

- Arakawa, Y., Yariv, A.: Quantum well lasers—gain, spectra, dynamics. IEEE J. Quantum Electron. QE-22, 1887 (1986).
- 2. Zory Jr, P.S. (ed.): Quantum Well Lasers. Academic Press, San Diego (1993)
- Okai, M., Suzuki, M., Taniwatari, T.: Strained multiquantum-well corrugation-pitch-modulated distributed feedback laser with ultranarrow (3.6 kHz) spectral linewidth. Electron. Lett. 29, 1696 (1993)

References 225

4. Luttinger, J.M., Kohn, W.: Motion of electrons and holes in perturbed periodic fields. Phys. Rev. 97, 869 (1955)

- 5. Pikus, G.E., Bir, G.L.: Effect of deformation on the energy spectrum and the electrical properties of imperfect germanium and silicon. Sov. Phys. Solid State 1, 136 (1959)
- 6. Yu, P.Y., Cardona, M.: Fundamentals of Semiconductors, Physics and Materials Properties, 2nd edn. Springer, Berlin (1999)
- Adachi, S.: Physical Properties of III-V Semiconductor Compounds. John Wiley and Sons, New York (1992)
- 8. Kittel, C.: Introduction to Solid State Physics, 7th edn. John Wiley and Sons, New York (1996)
- 9. Nye, J.F.: Physical Properties of Crystals. Oxford University Press, New York (1985)

# **Chapter 8 Control of Spontaneous Emission**

#### 8.1 Introduction

High energy states are unstable. As a result, the electrons in high energy states transit to low energy states in a certain lifetime. The radiation associated with this transition is referred to as spontaneous emission.

Figure 8.1 schematically shows spontaneous emission in semiconductors, which is the radiative recombination of electrons in the conduction band and holes in the valence band. It should be noted that spontaneous emission takes place regardless of incident light, whereas stimulated emission and absorption are induced by incident light.

According to quantum mechanics, spontaneous emission takes place due to interactions of atomic systems and the vacuum field. Therefore, spontaneous emission is considered to be the stimulated emission induced by fluctuations in the vacuum field (zero-point vibrations). It should be noted that the term *stimulated emission* usually represents the stimulated emission induced by incident light.

As described earlier, spontaneous emission is caused by the interactions of atomic systems and the vacuum field. As a result, the mode and lifetime of the spontaneous emission can be modified by controlling the vacuum field with optical cavities, which is referred to as *cavity quantum electrodynamics* (QED).

# **8.2 Spontaneous Emission**

#### 8.2.1 Fermi's Golden Rule

With regard to the spontaneous emission rate, we explain *Fermi's golden rule*. As shown in Fig. 8.2, we consider a two-level system, which consists of a *ground state*  $|gr\rangle$  with an energy  $E_{gr}$  and an *excited state*  $|ex\rangle$  with an energy  $E_{ex}$ . Here, we assume that a resonance spectral linewidth of the optical cavity in units of angular frequency  $\Delta\omega_c$  is much larger than that of the atomic system  $\Delta\omega_a$ . When the spectrum is

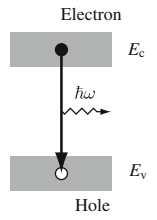


Fig. 8.1 Spontaneous emission in semiconductors

Lorentzian, the spectral linewidth is inversely proportional to the lifetime. Hence, the assumption  $\Delta\omega_c\gg\Delta\omega_a$  indicates  $\tau_c\ll\tau_a$ , where  $\tau_c=\tau_{ph}$  is the photon lifetime and  $\tau_a$  is the lifetime of the atomic transition. Therefore, during the transitions of atoms from the excited state to the ground state, lights are readily emitted outward from the optical cavity. Hence, this transition is irreversible, and absorptions do not take place.

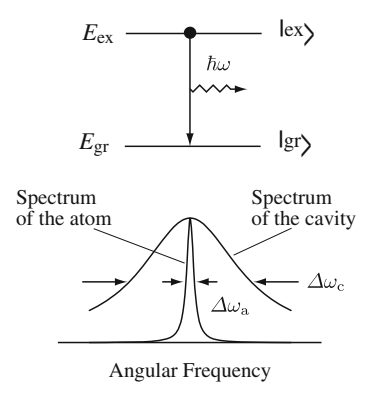
From perturbation theory in quantum mechanics, the transition rate W of an atom is given by

$$W = \frac{2\pi}{\hbar} \sum_{l} \mu_l^2 \left( \frac{\hbar \omega_l}{2V \varepsilon} \right) \sin^2(\mathbf{k}_l \cdot \mathbf{r}) (n_l + 1) F(E_{\text{ex}} - E_{\text{gr}} - \hbar \omega_l), \tag{8.1}$$

where  $\hbar = h/2 \pi$  is Dirac's constant and h is Planck's constant;  $\mu_l$  is the electric dipole moment for the lth cavity mode;  $\omega_l$  is the angular frequency of the lth cavity mode; V is the volume of the optical cavity;  $\varepsilon$  is the dielectric constant of a material in the optical cavity;  $k_l$  is the wave vector of the lth cavity mode;  $n_l$  is the photon density; and  $F(E_{\rm ex} - E_{\rm gr} - \hbar \omega_l)$  is a normalized spectral function.

From (8.1), it is found that W > 0 is obtained even when photons do not exist in the optical cavity  $(n_l = 0)$ . A transition rate for  $n_l = 0$  in (8.1) is the spontaneous emission rate  $W_{\rm sp}$ , which is expressed as

Fig. 8.2 Fermi's golden rule



$$W_{\rm sp} = \frac{2\pi}{\hbar} \sum_{l} \mu_l^2 \left( \frac{\hbar \omega_l}{2V\varepsilon} \right) \sin^2(\mathbf{k}_l \cdot \mathbf{r}) F(E_{\rm ex} - E_{\rm gr} - \hbar \omega_l). \tag{8.2}$$

## 8.2.2 Spontaneous Emission in a Free Space

A *free space* can be regarded as an optical cavity whose size is much larger than the wavelength of a light. Therefore, a spectral distribution of the resonance modes in the free space is (quasi-)continuous. In this case, a sum with respect to a resonance mode l in (8.2) is replaced by integration with respect to k. Hence, the spontaneous emission rate in the free space  $W_{\rm sp, free}$  is written as

$$W_{\rm sp,free} = \frac{\omega_0^3 n_{\rm rc}^3}{3 \pi c^3 \hbar \varepsilon} \bar{\mu}^2, \tag{8.3}$$

where  $n_{\rm rc}$  is the refractive index of a material in the optical cavity,  $\bar{\mu}^2$  is the squared electric dipole moment averaged over all directions of polarizations,  $\omega_0 = (E_{\rm ex} - E_{\rm gr})/\hbar$  is the angular frequency of a light, and  $\sin^2(k_l \cdot r)$  is replaced by the averaged value 1/2.

In this case, a transition rate for each mode is small, and it is inversely proportional to the volume of the optical cavity V. The number of modes N contributing to the optical transitions is proportional to V, and the value of N for usual waveguide-type LDs is about  $10^5$ . As a result, the spontaneous emission rate in the free space  $W_{\rm sp,free}$  is independent of V. Moreover,  $W_{\rm sp,free}$  is not affected by the positions of the atoms. Therefore, the spontaneous emission in the free space seems to be governed by the properties of the atoms themselves.

# 8.2.3 Spontaneous Emission in a Microcavity

The microcavity [1] is the optical cavity whose size is of the order of a light wavelength. Hence, the resonance modes in the microcavity are discrete. From (8.2), when the spontaneous emission coupling factor is  $\beta_{\rm sp}=1$ , the spontaneous emission rate in the microcavity  $W_{\rm sp,micro}$  is given by

$$W_{\text{sp,micro}} = \frac{\pi}{\hbar} \mu_l^2 \left( \frac{\hbar \omega_l}{V \varepsilon} \right) \left( \frac{1}{\hbar \Delta \omega_c} \right) \sin^2(\mathbf{k}_l \cdot \mathbf{r}), \tag{8.4}$$

where  $\Delta\omega_c$  is the spectral linewidth of the resonance mode of the optical cavity in units of angular frequency.

From (8.3) and (8.4), when the angular frequency of the light  $\omega_0$  is equal to that of the *l*th optical cavity mode  $\omega_l$  ( $\omega_0 = \omega_l$ ), the spontaneous emission rate in the

microcavity  $W_{\text{sp,micro}}$ , and the spontaneous emission rate in the free space  $W_{\text{sp,free}}$  are related as

$$\frac{W_{\rm sp,micro}}{W_{\rm sp,free}} = \frac{3}{8\pi} \frac{\lambda_l^3}{n_{\rm rc}^3} \frac{1}{V} \left(\frac{\omega_l}{\Delta \omega_c}\right) \sin^2(\mathbf{k}_l \cdot \mathbf{r}), \tag{8.5}$$

where  $\lambda_l$  is the resonance wavelength in a vacuum for the lth optical cavity mode.

From (8.5), it is found that enhancement of the spontaneous emission ( $W_{\rm sp,micro} > W_{\rm sp,free}$ ) happens when the following three conditions are satisfied: (1) The optical cavity is the microcavity whose size is of the order of a light wavelength ( $V \approx \lambda_l^3/n_{\rm rc}^3$ ), (2) the Q-value of the optical cavity is extremely large ( $\omega_l/\Delta\omega_c\gg 1$ ), and (3) excited atoms are placed at antinodes of the standing wave in the optical cavity where  $\sin^2(k_l \cdot r) = 1$ .

In contrast, the spontaneous emission is suppressed when the angular frequency of the light  $\omega_0$  and that of the *l*th optical cavity mode  $\omega_l$  are different from each other  $(\omega_0 \neq \omega_l)$ . If the excited atoms exist at nodes of the standing wave where  $\sin^2(\mathbf{k}_l \cdot \mathbf{r}) = 0$ , spontaneous emission is prohibited because  $W_{\rm sp,micro} = 0$ .

#### 8.2.4 Fluctuations in the Vacuum Field

In a system consisting of bosons, such as photons and phonons, the fluctuations in the vacuum field are generated due to Heisenberg's uncertainty principle, even when the bosons do not exist  $(n_l = 0)$ . As a result, there exists a zero-point energy  $\hbar\omega_l/2$  in a resonance mode. The spontaneous emission is induced by these fluctuations in the vacuum field, and a theory of Cohen-Tannoudji and others [2] will be briefly explained in the following.

When atoms in the excited state interact with fluctuations in the vacuum field, optical transitions take place from the excited state to the ground state. The state of an atom (electron)  $|\Psi\rangle$  is given by a linear combination of the two eigenstates  $|\text{ex}\rangle$  and  $|\text{gr}\rangle$ , which is written as

$$|\Psi\rangle = C_{\rm ex}|\exp\left(-i\frac{E_{\rm ex}}{\hbar}t\right) + C_g|gr\rangle\exp\left(-i\frac{E_{\rm gr}}{\hbar}t\right).$$
 (8.6)

The expectation value of the electric dipole moment is expressed as

$$\langle \Psi | e \mathbf{r} | \Psi \rangle = C_{\text{ex}}^* C_g \langle \text{ex} | e \mathbf{r} | \text{gr} \rangle \exp(i \omega_0 t) + \text{h.c.},$$
 (8.7)

where e is the elementary charge and h.c. shows the Hermite conjugate.

The electric dipole moment, which vibrates with the angular frequency  $\omega_0$ , emits an electromagnetic wave with  $\omega_0$ . Also, the emitted electromagnetic wave reacts on the electric dipole moment. When the atom is in the excited state, the fluctuations in the vacuum field and the electromagnetic wave interact with the same phase, which

induces spontaneous emission. While the atom is in the ground state, the interaction takes place with the antiphase and *spontaneous absorption* never happens.

## 8.3 Microcavity LDs

From (2.27), a low mode density and a large spontaneous emission rate result in a large stimulated emission rate. Hence, a low threshold current is expected in the microcavity LDs. As shown in (8.5), to enhance spontaneous emission, we need microcavities with high Q-values. From this viewpoint, the vertical cavity surface emitting LDs (VCSELs) explained in Sect. 6.3 are suitable for microcavity LDs.

From (5.20) and (5.21), the rate equations for the carrier concentration n and the photon density S are expressed as

$$\frac{\mathrm{d}n}{\mathrm{d}t} = \frac{J}{ed} - G(n)S - \frac{n}{\tau_n},\tag{8.8}$$

$$\frac{\mathrm{d}S}{\mathrm{d}t} = G(n)S - \frac{S}{\tau_{\mathrm{ph}}} + \beta_{\mathrm{sp}} \frac{n}{\tau_{n}},\tag{8.9}$$

where J is the injection current density, e is the elementary charge, d is the active layer thickness, G(n) is the amplification rate due to the stimulated emission,  $\tau_n$  is the carrier lifetime,  $\tau_{\rm ph}$  is the photon lifetime, and  $\beta_{\rm sp}$  is the spontaneous emission coupling factor. It should be noted that G(n) includes an effect of enhancement or suppression of the spontaneous emission caused by the microcavities, and  $\tau_{\rm r}=\tau_n$  is assumed.

When the mode distribution is continuous, from (5.32), the spontaneous emission coupling factor  $\beta_{sp}$  for a wavelength in a vacuum  $\lambda_0$  is given by

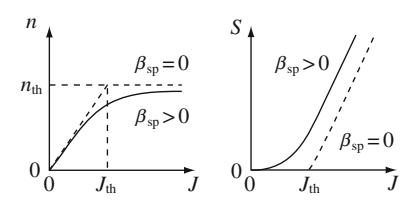
$$\beta_{\rm sp} = \frac{1}{4 \,\pi^2 \, n_{\rm r}^3 \, V_{\rm m}} \, \frac{\lambda_0^4}{\Delta \lambda} = \frac{\Gamma_{\rm a}}{4 \,\pi^2 \, n_{\rm r}^3 \, V_{\rm a}} \, \frac{\lambda_0^4}{\Delta \lambda},\tag{8.10}$$

where  $\Gamma_{\rm a}=V_{\rm a}/V_{\rm m}$  is the optical confinement factor of the active layer,  $V_{\rm a}$  is the volume of the active layer,  $V_{\rm m}$  is the mode volume, and  $\Delta\lambda$  is the FWHM of the light emission spectrum in a wavelength region. From (8.10), a small mode volume  $V_{\rm m}$  and a narrow FWHM  $\Delta\lambda$  lead to a large  $\beta_{\rm sp}$ . In microcavities, the mode distribution is discrete, and  $\beta_{\rm sp}$  has a different form from (8.10), but it is no change that  $\beta_{\rm sp}$  increases with a decrease in  $V_{\rm m}$ .

Figure 8.3 shows the carrier concentration n and the photon density S in microcavity LDs as a function of the injection current density J. With an increase in  $\beta_{\rm sp}$ , the threshold current density  $J_{\rm th}$  decreases and becomes indistinct.

In microcavity LDs, due to enhancement of spontaneous emission, the carrier lifetime  $\tau_n$  decreases and the stimulated emission rate increases, which enhances  $\partial G/\partial n$ . As shown in (5.103) and (5.109), the resonance frequency  $f_r$  is given by

**Fig. 8.3** Characteristics of microcavity LDs



$$f_{\rm r} = \frac{1}{2\,\pi} \sqrt{\frac{1}{\tau_n \tau_{\rm ph}}} \frac{J - J_{\rm th}}{J_{\rm th} - J_0'} = \frac{1}{2\,\pi} \sqrt{\frac{\partial G}{\partial n}} \frac{S_0}{\tau_{\rm ph}}.$$
 (8.11)

Therefore, a large  $f_r$ , which leads to high-speed modulation, is obtained in microcavity LDs. Note that in optical cavities with high Q-values, the photon lifetime  $\tau_{ph}$  is large, which reduces  $f_r$ . Hence, we have to design microcavity LDs according to the required modulation speed in application systems.

From the preceding explanations, it might be assumed that microcavity LDs have only benefits. However, they have serious problems in electrical resistance and light output. Because the size of microcavity LDs is of the order of a wavelength of a light, their electrical resistances are extremely high. Therefore, with increase in injection current, large Joule's heat is generated, which suppresses CW operations at room temperature. Even though the threshold current is low, due to large electrical resistance, the power consumptions are not always low, and sometimes they are large. Also, due to small light emission regions, the light outputs are low.

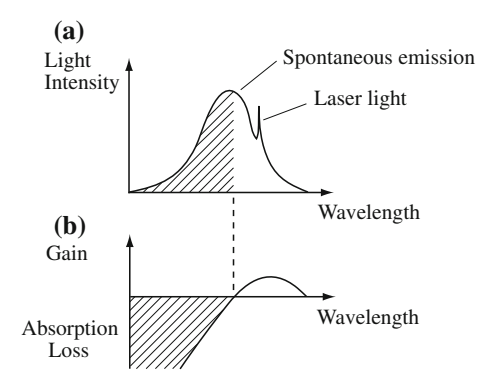
# **8.4 Photon Recycling**

When electric current is injected into semiconductor lasers, spontaneous emission takes place. A fraction of this spontaneous emission is used as the seed of a laser light; this seed is repeatedly amplified in optical cavities by stimulated emission. When the optical gains exceed the optical losses in the optical cavities, laser oscillations start.

In contrast, spontaneous emission other than the seed of laser light is readily emitted outward from optical cavities. Therefore, the injected carriers consumed for such spontaneous emission do not contribute to laser oscillations. In *photon recycling*, this wasted spontaneous emission is absorbed, and the carriers are generated [3–6]. Using photon recycling, the carrier concentration in the active layer is larger than that without photon recycling at the same current level, which results in low threshold current. This concept of photon recycling resembles the *confinement of resonant radiation* in gas lasers.

Figure 8.4a, b schematically shows the light emission spectra and the optical gain spectra of semiconductor lasers. A peak wavelength in the optical gain spectra is longer than that in the spontaneous emission spectra. Therefore, the active layer can absorb the spontaneous emission located in a shorter wavelength region, which is indicated with slanted lines. Consequently, to achieve efficient photon recycling,

Fig. 8.4 a Light emission spectrum and b optical gain spectrum



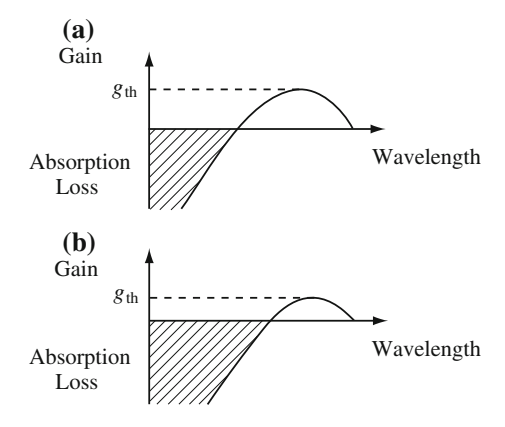
we should confine the spontaneously emitted lights to the optical cavities. To avoid wasting the injected carriers, we should also reduce the nonradiative recombination rates and suppress Joule heating in the active layers so that the carriers may not overflow to the cladding layers.

From Fig. 8.4, it is found that a large absorption region in a wavelength leads to efficient photon recycling. As shown in Fig. 8.5, with a decrease in the threshold gain  $g_{th}$ , the absorption wavelength region increases. Therefore, semiconductor lasers with low threshold gain as in Fig. 8.5b are suitable for efficient photon recycling.

Figure 8.6 schematically shows the structure of a vertical cavity surface emitting LD, which uses photon recycling. To efficiently confine the spontaneous emission in the optical cavity, the sidewalls of the optical cavity are covered with highly reflective materials.

In photon recycling, limitations to the size of the optical cavities do not exist, as opposed to in microcavity LDs. Consequently, when we use photon recycling, we can avoid an increase in electrical resistance and a decrease in the light output, as shown in microcavity LDs.

Fig. 8.5 Threshold gain and photon recycling: a Large threshold gain and b low threshold gain



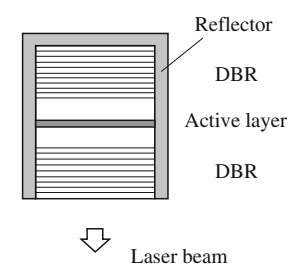


Fig. 8.6 Vertical cavity surface emitting LD with photon recycling

#### References

- Yokoyama, H., Ujihara, K. (eds.): Spontaneous Emission and Laser Oscillation in Microcavities. CRC Press, New York (1995)
- Dalibard, J., Dupont-Roc, J., Cohen-Tannoudji, C.: Vacuum fluctuations and radiation reaction: identification of their respective contributions. J. Phys. 43, 1617 (1982)
- Stern, F., Woodall, J.M.: Photon recycling in semiconductor lasers. J. Appl. Phys. 45, 3904 (1974)
- Numai, T., Kosaka, H., Ogura, I., et al.: Indistinct threshold laser operation in a pnpn vertical to surface transmission electro-photonic device with a vertical cavity. IEEE J. Quantum Electron. 29, 403 (1993)
- Numai, T., Kurihara, K., Ogura, I., et al.: Effect of sidewall reflector on current versus lightoutput in a pnpn vertical to surface transmission electro-photonic device with a vertical cavity. IEEE J. Quantum Electron. 29, 2006 (1993)
- Numai, T.: Analysis of photon recycling in semiconductor ring lasers. Jpn. J. Appl. Phys., Part 1. 39, 6535 (2000)

# Appendix A Cyclotron Resonance

# A.1 Fundamental Equations

Let us consider the motion of an electron in a magnetic field. As shown in Fig. A.1, we assume that a uniform magnetic field is applied along the z-axis, and a magnetic flux density is  $B(|B| = B_z)$ . The *Lorentz force* acting on the electron in this magnetic field has only x- and y-components and does not have a z-component.

When the relaxation term is neglected, an equation of motion for the electron in the magnetic field is given by

$$m\frac{\mathrm{d}\boldsymbol{v}}{\mathrm{d}t} = -e\left(\boldsymbol{v}\times\boldsymbol{B}\right),\tag{A.1}$$

where m, v, and e are the electron mass, velocity, and elementary charge, respectively. From (A.1), we obtain

$$\ddot{x} = -\omega_{\rm c}\dot{y}, \quad \ddot{y} = \omega_{\rm c}\dot{x},\tag{A.2}$$

where a double dot above x and y shows a second derivative with respect to time, and

$$\omega_{\rm c} = \frac{eB_z}{m} \tag{A.3}$$

is the cyclotron angular frequency.

Assuming x=0,  $y=-v_0/\omega_c$ ,  $\dot{x}=v_0$ , and  $\dot{y}=0$  at t=0 as an initial condition, and then integrating (A.2) with respect to time result in

$$\dot{x} = -\omega_{\rm c} y, \quad \dot{y} = \omega_{\rm c} x, \tag{A.4}$$

where a dot above x and y shows a first derivative with respect to time. Substituting (A.4) into (A.2), we have

© Springer Japan 2015

<sup>235</sup> 

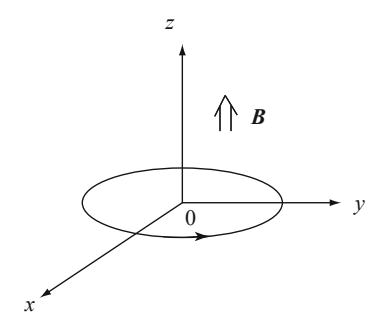


Fig. A.1 Cyclotron motion

$$\ddot{x} = -\omega_c^2 x, \quad \ddot{y} = -\omega_c^2 y. \tag{A.5}$$

As a result, the solutions are obtained as

$$x = \frac{v_0}{\omega_c} \sin \omega_c t, \quad y = -\frac{v_0}{\omega_c} \cos \omega_c t. \tag{A.6}$$

These solutions show the *cyclotron motion* that is a circular motion with a radius  $R = v_0/\omega_c$  about the origin.

When an electromagnetic wave whose electric field is in the xy-plane and the angular frequency  $\omega_c$  is incident on the semiconductors, the electromagnetic wave is resonantly absorbed by the electrons with cyclotron motions. This phenomenon is called the *cyclotron resonance*.

We assume that the effective mass of the carrier is  $m^*$ , the velocity of the carrier is v, the charge of the carrier is q (q=-e<0 for the electron and q=+e>0 for the hole), the electric field is E, the magnetic flux density is B, and the relaxation time is  $\tau$ . Then the equation of motion for the carrier is written as

$$m^* \frac{\mathrm{d}\mathbf{v}}{\mathrm{d}t} = q \left( \mathbf{E} + \mathbf{v} \times \mathbf{B} \right) - \frac{m^* \mathbf{v}}{\tau}. \tag{A.7}$$

Using the carrier concentration n, we can express the x- and y-components of the current density as  $J_i = nqv_i$  (i = x, y). From the Joule losses formula, the absorbed energy density per unit time P is obtained as

$$P = \overline{\text{Re}(\boldsymbol{J}) \cdot \text{Re}(\boldsymbol{E})} = \frac{1}{2} \text{Re}(\boldsymbol{J} \cdot \boldsymbol{E}^*), \tag{A.8}$$

where Re indicates a real part. In the following, we consider a right-handed circularly polarized wave, a left-handed circularly polarized wave, and a linearly polarized wave. These electromagnetic waves are assumed to propagate along the z-axis and to have the angular frequency  $\omega$ .

# A.2 Right-Handed Circularly Polarized Wave

The right-handed circularly polarized wave is expressed as

$$E_x = E_0 \exp(i \omega t), \quad E_y = i E_x = i E_0 \exp(i \omega t).$$
 (A.9)

Substituting (A.9) into (A.7) and using (A.8) results in

$$P = \frac{\sigma_0 E_0^2}{(\omega - \omega_c)^2 \tau^2 + 1},$$
 (A.10)

where

$$\omega_{\rm c} = \frac{qB_z}{m^*}, \quad \sigma_0 = \frac{nq^2\tau}{m^*}.\tag{A.11}$$

# A.3 Left-Handed Circularly Polarized Wave

The left-handed circularly polarized wave is written as

$$E_x = E_0 \exp(i \omega t), \quad E_y = -i E_x = -i E_0 \exp(i \omega t).$$
 (A.12)

Substituting (A.12) into (A.7) and using (A.8) leads to

$$P = \frac{\sigma_0 E_0^2}{(\omega + \omega_c)^2 \tau^2 + 1}.$$
 (A.13)

# A.4 Linearly Polarized Wave

When the *linearly polarized wave* has an electric field with only an *x*-component, which is given by

$$E_x = E_0 \exp(i \omega t), \tag{A.14}$$

the absorbed energy density per unit time P is represented as

$$P = \frac{1}{4} \sigma_0 E_0^2 \left[ \frac{1}{(\omega - \omega_c)^2 \tau^2 + 1} + \frac{1}{(\omega + \omega_c)^2 \tau^2 + 1} \right].$$
 (A.15)

Here, the first and second terms correspond to the right-handed circularly polarized wave and the left-handed circularly polarized wave, respectively.

# A.5 Relationship Between Polarization of a Wave and an Effective Mass

From (A.11), it is found that we can obtain the effective mass of the carrier by measuring the cyclotron angular frequency  $\omega_c$ . The right-handed circularly polarized wave is resonantly absorbed by the carrier, which has a positive effective mass with a positive  $\omega_c$ , such as the electron in the conduction band in the vicinity of the band edge. The left-handed circularly polarized wave is resonantly absorbed by the carrier, which has a negative effective mass with a negative  $\omega_c$ , such as the hole in the valence bands in the vicinity of the band edge.

Finally, we show an example of a value for the cyclotron angular frequency  $\omega_c$ . When the observed effective mass in a magnetic field with the magnetic flux density of  $1\,\mathrm{G} = 10^{-4}\,\mathrm{T}$  is  $0.1\,m$ , where m is the electron mass in a vacuum,  $\omega_c$  is  $1.76\times10^8\,\mathrm{rad/s}$ , and the cyclotron frequency  $f_c = \omega_c/2\pi$  is  $2.80\times10^7\,\mathrm{Hz}$ .

# Appendix B

# **Time-Independent Perturbation Theory**

We consider the following Schrödinger equation expressed as

$$\mathcal{H}\psi = W\psi, \quad \mathcal{H} = \mathcal{H}_0 + \mathcal{H}', \quad \mathcal{H}_0 u_k = E_k u_k, \tag{B.1}$$

where  $\mathcal{H}_0$  is an *unperturbed Hamiltonian* whose solutions are already obtained;  $\mathcal{H}'$  is a *perturbation* to  $\mathcal{H}_0$ ;  $\psi$  and W are an eigenfunction (wave function) and an energy eigenvalue for a perturbed steady state, respectively; and  $u_k$  and  $E_k$  are an orthonormalized eigenfunction and an energy eigenvalue for the unperturbed Hamiltonian  $\mathcal{H}_0$ , respectively.

# **B.1 Nondegenerate Case**

The perturbed eigenfunction and the perturbed energy eigenvalue are assumed to be expanded in power series of  $\mathcal{H}'$ . Here, we replace  $\mathcal{H}'$  by  $\lambda \mathcal{H}'$  where  $\lambda$  is a parameter, and we express  $\psi$  and W with the power series of  $\lambda$ . In obtaining the final results, we set  $\lambda = 1$ . Under this assumption,  $\psi$  and W are written as

$$\psi = \psi_0 + \lambda \, \psi_1 + \lambda^2 \psi_2 + \lambda^3 \psi_3 + \cdots, 
W = W_0 + \lambda W_1 + \lambda^2 W_2 + \lambda^3 W_3 + \cdots.$$
(B.2)

Substituting (B.2) into (B.1) and replacing  $\mathcal{H}'$  by  $\lambda \mathcal{H}'$ , we have

$$(\mathcal{H}_{0} + \lambda \mathcal{H}')(\psi_{0} + \lambda \psi_{1} + \lambda^{2} \psi_{2} + \lambda^{3} \psi_{3} + \cdots)$$

$$= (W_{0} + \lambda W_{1} + \lambda^{2} W_{2} + \lambda^{3} W_{3} + \cdots)(\psi_{0} + \lambda \psi_{1} + \lambda^{2} \psi_{2} + \lambda^{3} \psi_{3} + \cdots).$$
(B.3)

If we assume that (B.3) is satisfied for any value of  $\lambda$ , the terms with the common power series of  $\lambda$  on both sides have to be the same, which is expressed as

$$\lambda^{0} : (\mathcal{H}_{0} - W_{0})\psi_{0} = 0,$$

$$\lambda^{1} : (\mathcal{H}_{0} - W_{0})\psi_{1} = (W_{1} - \mathcal{H}')\psi_{0},$$

$$\lambda^{2} : (\mathcal{H}_{0} - W_{0})\psi_{2} = (W_{1} - \mathcal{H}')\psi_{1} + W_{2}\psi_{0},$$

$$\lambda^{3} : (\mathcal{H}_{0} - W_{0})\psi_{3} = (W_{1} - \mathcal{H}')\psi_{2} + W_{2}\psi_{1} + W_{3}\psi_{0},$$

$$\vdots$$

$$(B.4)$$

From (B.1) and the first equation in (B.4), it is found that  $\psi_0$  is one of the unperturbed eigenfunctions  $u_k$ s. Therefore, in the nondegenerate case, we put

$$\psi_0 = u_m, \quad W_0 = E_m.$$
 (B.5)

As an eigenfunction  $\psi_s(s > 0)$  in a perturbed steady state, we consider a solution satisfying the dot product given by

$$(\psi_0, \psi_s) = \int \psi_0^* \psi_s \, \mathrm{d}^3 \mathbf{r} = 0.$$
 (B.6)

Under this condition, multiplying both sides of (B.4) by  $\psi_0^*$  from the left and then integrating with respect to all the space results in

$$W_s = \frac{(\psi_0, \mathcal{H}'\psi_{s-1})}{(\psi_0, \psi_0)} = (u_m, \mathcal{H}'\psi_{s-1}), \tag{B.7}$$

where we have used that  $u_k$ s are orthonormal functions. From (B.5) and (B.7), we have

$$W_1 = (u_m, \mathcal{H}'\psi_0) = (u_m, \mathcal{H}'u_m) = \langle m|\mathcal{H}'|m\rangle, \tag{B.8}$$

from which it is revealed that the first-order perturbation energy  $W_1$  is the expectation value of  $\mathcal{H}'$  for the unperturbed state  $|m\rangle$ .

Here, by expanding with respect to  $u_n$ , we write the first-order perturbed eigenfunction  $\psi_1$  as

$$\psi_1 = \sum_n a_n^{(1)} u_n, \tag{B.9}$$

where  $a_n^{(1)}$  is the expansion coefficient. If we calculate  $a_n^{(1)}$ , an eigenfunction in the first-order perturbation is obtained. First, let us consider a dot product of  $u_m$  and (B.9). Because  $u_n$  is an orthonormal function, we have the following relation

$$\langle m|n\rangle = \delta_{mn},\tag{B.10}$$

where  $\delta_{mn}$  is the Kronecker delta. Using (B.6), we obtain

$$(u_m, \psi_1) = \langle m | \sum_n a_n^{(1)} | n \rangle = \sum_n a_n^{(1)} \langle m | n \rangle$$
  
=  $a_m^{(1)} = (\psi_0, \psi_1) = 0.$  (B.11)

Substituting (B.9) into the second equation in (B.4) results in

$$\sum_{n} a_n^{(1)} (\mathcal{H}_0 - E_m) u_n = (W_1 - \mathcal{H}') u_m, \tag{B.12}$$

where (B.5) was used. Taking a dot product of  $u_k$  and (B.12) with the help of (B.1) leads to

$$a_k^{(1)}(E_k - E_m) = -\langle k|\mathcal{H}'|m\rangle,$$

$$\therefore a_k^{(1)} = \frac{\langle k|\mathcal{H}'|m\rangle}{E_m - E_k} \quad (k \neq m).$$
(B.13)

As a result,  $\psi_1$  is written as

$$\psi_1 = \sum_n \frac{\langle n|\mathcal{H}'|m\rangle}{E_m - E_n} u_n. \tag{B.14}$$

Therefore, to the first-order perturbation, the eigenfunction  $\psi$  is given by

$$\psi = \psi_0 + \psi_1 = u_m + \sum_n \frac{\langle n|\mathcal{H}'|m\rangle}{E_m - E_n} u_n, \tag{B.15}$$

where we have set  $\lambda = 1$ .

Putting s = 2 in (B.7), the second-order perturbation energy is obtained as

$$W_2 = (u_m, \mathcal{H}'\psi_1) = \sum_n \frac{\langle m|\mathcal{H}'|n\rangle\langle n|\mathcal{H}'|m\rangle}{E_m - E_n}, \qquad (B.16)$$

where (B.14) was used. From (B.5), (B.8), and (B.16), to the second-order perturbation, the energy eigenvalue is expressed as

$$W = W_0 + W_1 + W_2$$
  
=  $E_m + \langle m|\mathcal{H}'|m\rangle + \sum_n \frac{\langle m|\mathcal{H}'|n\rangle\langle n|\mathcal{H}'|m\rangle}{E_m - E_n}.$  (B.17)

Finally, let us calculate an eigenfunction in the second-order perturbation. The second-order perturbed eigenfunction  $\psi_2$  is expanded with  $u_n$  as

$$\psi_2 = \sum_n a_n^{(2)} u_n, \tag{B.18}$$

where  $a_m^{(2)} = 0$ . Substituting (B.5), (B.9), and (B.18) into the third equation in (B.4) gives

$$\sum_{n} a_n^{(2)} (\mathcal{H}_0 - W_0) u_n = \sum_{n} a_n^{(1)} (W_1 - \mathcal{H}') u_n + W_2 u_m.$$
 (B.19)

Taking a dot product of  $u_k (k \neq m)$  and (B.19) with the help of (B.1) results in

$$a_k^{(2)}(E_k - E_m) = a_k^{(1)}W_1 - \sum_n a_n^{(1)} \langle k|\mathcal{H}'|n\rangle.$$
 (B.20)

From (B.8), (B.13), and (B.20), we obtain

$$a_k^{(2)} = \sum_{n} \frac{\langle k|\mathcal{H}'|n\rangle\langle n|\mathcal{H}'|m\rangle}{(E_m - E_k)(E_m - E_n)} - \frac{\langle k|\mathcal{H}'|m\rangle\langle m|\mathcal{H}'|m\rangle}{(E_m - E_k)^2}.$$
 (B.21)

As a result, to the second-order perturbation with  $\lambda=1$ , the eigenfunction  $\psi$  is written as

$$\psi = \psi_0 + \psi_1 + \psi_2$$

$$= u_m + \sum_k u_k \left[ \frac{\langle k | \mathcal{H}' | m \rangle}{E_m - E_k} \left( 1 - \frac{\langle m | \mathcal{H}' | m \rangle}{E_m - E_k} \right) + \sum_n \frac{\langle k | \mathcal{H}' | n \rangle \langle n | \mathcal{H}' | m \rangle}{(E_m - E_k)(E_m - E_n)} \right].$$
(B.22)

In summary, the eigenfunction and the energy eigenvalue in the nondegenerate case are expressed as

to the first-order perturbation

$$\psi = u_m + \sum_n \frac{\langle n|\mathcal{H}'|m\rangle}{E_m - E_n} u_n, \tag{B.23}$$

$$W = W_0 + W_1 = E_m + \langle m | \mathcal{H}' | m \rangle, \tag{B.24}$$

to the second-order perturbation

$$\psi = u_m + \sum_{k} u_k \left[ \frac{\langle k | \mathcal{H}' | m \rangle}{E_m - E_k} \left( 1 - \frac{\langle m | \mathcal{H}' | m \rangle}{E_m - E_k} \right) + \sum_{n} \frac{\langle k | \mathcal{H}' | n \rangle \langle n | \mathcal{H}' | m \rangle}{(E_m - E_k)(E_m - E_n)} \right],$$
(B.25)

$$W = E_m + \langle m|\mathcal{H}'|m\rangle + \sum_n \frac{\langle m|\mathcal{H}'|n\rangle\langle n|\mathcal{H}'|m\rangle}{E_m - E_n}.$$
 (B.26)

### **B.2** Degenerate Case

In the perturbation theory in the degenerate case, only the zeroth-order eigenfunction  $\psi_0$  is different from that of the perturbation theory in the nondegenerate case; other processes are common.

Here, we assume that the unperturbed eigenfunctions  $u_l$  and  $u_m$  ( $l \neq m$ ) have the same unperturbed energy  $W_0$ . As a result, we can write  $\psi_0$  and  $W_0$  as

$$\psi_0 = a_l u_l + a_m u_m, \quad W_0 = E_l = E_m.$$
 (B.27)

Substituting (B.27) into the second equation in (B.4) and then taking dot products with  $u_l$  and  $u_m$ , we have

$$(\langle l|\mathcal{H}'|l\rangle - W_1) a_l + \langle l|\mathcal{H}'|m\rangle a_m = 0,$$

$$\langle m|\mathcal{H}'|l\rangle a_l + (\langle m|\mathcal{H}'|m\rangle - W_1) a_m = 0.$$
(B.28)

In order that (B.28) may have solutions other than  $a_l = a_m = 0$ , the determinant for the coefficients of  $a_l$  and  $a_m$  must be zero, which is expressed as

$$(\langle l|\mathcal{H}'|l\rangle - W_1)(\langle m|\mathcal{H}'|m\rangle - W_1) - \langle l|\mathcal{H}'|m\rangle \langle m|\mathcal{H}'|l\rangle = 0.$$
 (B.29)

Solving (B.29) with respect to  $W_1$ , we have

$$W_{1} = \frac{1}{2} \left( \langle l | \mathcal{H}' | l \rangle + \langle m | \mathcal{H}' | m \rangle \right)$$

$$\pm \frac{1}{2} \left[ \left( \langle l | \mathcal{H}' | l \rangle - \langle m | \mathcal{H}' | m \rangle \right)^{2} + 4 \langle l | \mathcal{H}' | m \rangle \langle m | \mathcal{H}' | l \rangle \right]^{1/2}. \tag{B.30}$$

From (B.30), it is found that degeneracy is removed in the first-order perturbation, so long as the terms in  $[\cdots]$  do not vanish. When degeneracy is removed and  $W_1$  has two solutions,  $a_l$  and  $a_m$  are obtained from (B.28), and they are used to calculate the

wave functions. Substituting (B.9) and (B.27) into the second equation in (B.4) and then taking a dot product with  $u_k (k \neq l, m)$ , we obtain

$$a_k^{(1)}(E_k - E_m) = -\langle k|\mathcal{H}'|m\rangle a_m - \langle k|\mathcal{H}'|l\rangle a_l.$$
 (B.31)

If we assume that  $a_l^{(1)} = a_m^{(1)} = 0$ , (B.6) with s = 1 is satisfied. Using  $a_k^{(1)}$  in (B.31), we can obtain the eigenfunction to the first-order perturbation.

To the second-order perturbation, substituting (B.27) into the third equation in (B.4) and then taking dot products with  $u_l$  and  $u_m$ , we have

$$\sum_{n} \langle l | \mathcal{H}' | n \rangle a_n^{(1)} - W_2 a_l = 0,$$

$$\sum_{n} \langle m | \mathcal{H}' | n \rangle a_n^{(1)} - W_2 a_m = 0.$$
(B.32)

Substituting (B.31) into (B.32) leads to

$$\left(\sum_{n} \frac{\langle l|\mathcal{H}'|n\rangle\langle n|\mathcal{H}'|l\rangle}{E_{m} - E_{n}} - W_{2}\right) a_{l} + \sum_{n} \frac{\langle l|\mathcal{H}'|n\rangle\langle n|\mathcal{H}'|m\rangle}{E_{m} - E_{n}} a_{m} = 0,$$

$$\sum_{n} \frac{\langle m|\mathcal{H}'|n\rangle\langle n|\mathcal{H}'|l\rangle}{E_{m} - E_{n}} a_{l} + \left(\sum_{n} \frac{\langle m|\mathcal{H}'|n\rangle\langle n|\mathcal{H}'|m\rangle}{E_{m} - E_{n}} - W_{2}\right) a_{m} = 0.$$
(B.33)

By solving (B.33), we can obtain the energy eigenvalues to the second-order perturbation.

# Appendix C

# **Time-Dependent Perturbation Theory**

#### **C.1 Fundamental Equation**

We consider a time-dependent Schrödinger equation such as

$$i\hbar \frac{\partial \psi}{\partial t} = \mathcal{H}\psi, \quad \mathcal{H} = \mathcal{H}_0 + \mathcal{H}'(t), \quad \mathcal{H}_0 u_k = E_k u_k,$$
 (C.1)

where  $\mathcal{H}_0$  is an unperturbed steady-state Hamiltonian whose solutions are already obtained,  $\mathcal{H}'(t)$  is a time-dependent perturbation to  $\mathcal{H}_0$ ,  $\psi$  is a perturbed eigenfunction (wave function), and  $u_k$  and  $E_k$  are an orthonormal eigenfunction and an energy eigenvalue for  $\mathcal{H}_0$ , respectively. When  $\mathcal{H}'(t) \neq 0$ , transitions take place between the eigenstates of  $\mathcal{H}_0$ .

Using a solution for an unperturbed wave equation given by

$$u_n e^{-i E_n t/\hbar}, (C.2)$$

we can expand a solution  $\psi$  as

$$\psi = \sum_{n} a_n(t) u_n e^{-i E_n t/\hbar}, \qquad (C.3)$$

where  $a_n(t)$  is a time-dependent expansion coefficient. Substituting (C.3) into (C.1) results in

$$\sum_{n} i \hbar \dot{a}_{n} u_{n} e^{-i E_{n} t/\hbar} + \sum_{n} a_{n} E_{n} u_{n} e^{-i E_{n} t/\hbar}$$

$$= \sum_{n} a_{n} \left[ \mathcal{H}_{0} + \mathcal{H}'(t) \right] u_{n} e^{-i E_{n} t/\hbar}$$

$$= \sum_{n} \left( a_{n} E_{n} u_{n} e^{-i E_{n} t/\hbar} + a_{n}(t) \mathcal{H}'(t) u_{n} e^{-i E_{n} t/\hbar} \right), \qquad (C.4)$$

<sup>©</sup> Springer Japan 2015

<sup>245</sup> 

T. Numai, Fundamentals of Semiconductor Lasers,

where a dot above the expansion coefficient  $a_n$  denotes a first derivative with respect to time. From (C.4), we have

$$\sum_{n} i \hbar \dot{a}_{n} u_{n} e^{-i E_{n} t/\hbar} = \sum_{n} a_{n}(t) \mathcal{H}'(t) u_{n} e^{-i E_{n} t/\hbar}. \tag{C.5}$$

Taking a dot product of (C.5) and  $u_k$  leads to

$$i \hbar \dot{a}_k e^{-i E_k t/\hbar} = \sum_n \langle k | \mathcal{H}'(t) | n \rangle a_n e^{-i E_n t/\hbar}.$$
 (C.6)

When we define the Bohr angular frequency  $\omega_{kn}$  as

$$\omega_{kn} \equiv \frac{E_k - E_n}{\hbar},\tag{C.7}$$

we can rewrite (C.6) as

$$\dot{a}_{k} = \frac{1}{\mathrm{i}\,\hbar} \sum_{n} \langle k | \mathcal{H}'(t) | n \rangle a_{n} \mathrm{e}^{\mathrm{i}\,\omega_{kn}t}. \tag{C.8}$$

Replacing  $\mathcal{H}'(t)$  in (C.8) by  $\lambda \mathcal{H}'(t)$ , we expand  $a_n$  with  $\lambda$  as

$$a_n = a_n^{(0)} + \lambda a_n^{(1)} + \lambda^2 a_n^{(2)} + \cdots$$
 (C.9)

Substituting (C.9) into (C.8) gives

$$\dot{a}_{k}^{(0)} + \lambda \dot{a}_{k}^{(1)} + \lambda^{2} \dot{a}_{k}^{(2)} + \cdots 
= \frac{1}{\mathrm{i} \, \hbar} \sum_{n} \langle k | \lambda \mathcal{H}'(t) | n \rangle (a_{n}^{(0)} + \lambda a_{n}^{(1)} + \lambda^{2} a_{n}^{(2)} + \cdots) \, \mathrm{e}^{\mathrm{i} \, \omega_{kn} t}.$$
(C.10)

In order that any value of  $\lambda$  may satisfy (C.10), we need

$$\dot{a}_k^{(0)} = 0, \quad \dot{a}_k^{(s+1)} = \frac{1}{\mathrm{i}\,\hbar} \sum_n \langle k|\mathcal{H}'(t)|n\rangle a_n^{(s)} \,\mathrm{e}^{\,\mathrm{i}\,\omega_{kn}t}.$$
 (C.11)

From the first equation in (C.11), it is revealed that  $a_k$  is independent of time in the zeroth-order perturbation. From the second equation in (C.11), once a lower order  $a_k^{(s)}$  is obtained, a next higher order  $a_k^{(s+1)}$  can be calculated. Here, we assume

$$a_k^{(0)} = \langle k | m \rangle = \delta_{km}, \tag{C.12}$$

which means that the initial state  $|m\rangle$  is a definite unperturbed energy state. Using (C.11) and (C.12), we obtain

$$\dot{a}_k^{(1)} = \frac{1}{\mathrm{i}\,\hbar} \langle k | \mathcal{H}'(t) | m \rangle \,\mathrm{e}^{\,\mathrm{i}\,\omega_{km}t}. \tag{C.13}$$

Assuming that  $a_k^{(1)}$  is zero before perturbation is applied, that is,  $a_k^{(1)} = 0$  at  $t = -\infty$ , integrating (C.13) with respect to time results in

$$a_k^{(1)} = \frac{1}{\mathrm{i}\,\hbar} \int_{-\infty}^t \langle k|\mathcal{H}'(t')|m\rangle \,\mathrm{e}^{\,\mathrm{i}\,\omega_{km}t'} \,\mathrm{d}t', \tag{C.14}$$

which is the expansion coefficient for the first-order perturbation.

#### **C.2 Harmonic Perturbation**

When a harmonic perturbation is applied at t = 0 and removed at  $t = t_0$ , we have

$$\langle k|\mathcal{H}'(t')|m\rangle = 2\langle k|\mathcal{H}'|m\rangle \sin \omega t', \tag{C.15}$$

where  $\langle k|\mathcal{H}'|m\rangle$  is independent of time. Substituting (C.15) into (C.14) leads to

$$a_{k}^{(1)}(t \ge t_{0}) = \frac{2}{\mathrm{i}\,\hbar} \langle k|\mathcal{H}'|m\rangle \int_{0}^{t_{0}} \sin\omega t' \,\mathrm{e}^{\mathrm{i}\,\omega_{km}t'} \,\mathrm{d}t'$$

$$= -\frac{\langle k|\mathcal{H}'|m\rangle}{\mathrm{i}\,\hbar} \left[ \frac{\mathrm{e}^{\mathrm{i}\,(\omega_{km}+\omega)t_{0}} - 1}{\omega_{km}+\omega} - \frac{\mathrm{e}^{\mathrm{i}\,(\omega_{km}-\omega)t_{0}} - 1}{\omega_{km}-\omega} \right]. \tag{C.16}$$

On the right-hand side of (C.16), the first term is dominant for  $\omega_{km} \approx -\omega$ , that is,  $E_k \approx E_m - \hbar \omega$ , and the second term is dominant for  $\omega_{km} \approx \omega$ , that is,  $E_k \approx E_m + \hbar \omega$ . In other words, to the first-order perturbation, due to the harmonic perturbation (C.15), Planck's quantum energy  $\hbar \omega$  is transferred to or received from the system.

When the initial state is  $|m\rangle$  and the final state is  $|k\rangle$ , let us calculate the probability that the system is in the final state  $|k\rangle$  after the perturbation is removed.

For  $E_k < E_m$ , the first term in (C.16) is dominant, which results in

$$|a_k^{(1)}(t \ge t_0)|^2 = \frac{4|\langle k|\mathcal{H}'|m\rangle|^2}{\hbar^2(\omega_{km} + \omega)^2} \sin^2\left[\frac{1}{2}(\omega_{km} + \omega)t_0\right]. \tag{C.17}$$

For  $E_k > E_m$ , the second term in (C.16) is dominant, which leads to

$$|a_k^{(1)}(t \ge t_0)|^2 = \frac{4|\langle k|\mathcal{H}'|m\rangle|^2}{\hbar^2(\omega_{km} - \omega)^2} \sin^2\left[\frac{1}{2}(\omega_{km} - \omega)t_0\right]. \tag{C.18}$$

#### **C.3** Transition Probability

Figure C.1 shows a plot of (C.18). Here, we assume that there is a group of final states  $|k\rangle$  whose energy  $E_k$  is nearly equal to  $E_m + \hbar \omega$ , and  $\langle k|\mathcal{H}'|m\rangle$  is roughly independent of  $|k\rangle$ . In this case, the probability of finding the system in one of these states  $|k\rangle$  is obtained by integrating (C.18) with respect to  $\omega_{km}$ . This integration is shown by an area enclosed by the horizontal line and the curve in Fig. C.1. The height of the main peak is proportional to  $t_0^2$ , and the spectral linewidth is in proportion to  $t_0^{-1}$ . As a result, the probability of finding the system in one of these states  $|k\rangle$  is proportional to  $t_0$ .

It should be noted that the uncertainty principle is satisfied, because the spectral linewidth, which represents uncertainty in the energy, is in proportion to  $t_0^{-1}$ . In addition, because of  $E_k \approx E_m + \hbar \omega$ , the energy conservation law is also satisfied. It is interesting that the uncertainty principle and the energy conservation law are automatically obtained without particular assumptions.

The transition probability per unit time w is given by

$$w = \frac{1}{t_0} \int |a_k^{(1)}(t \ge t_0)|^2 \rho(k) \, dE_k, \tag{C.19}$$

where  $\rho(k)$  d $E_k$  is the number of the final states with the energy between  $E_k$  and  $E_k + dE_k$ . With an increase in  $t_0$ , the spectral linewidth decreases, and  $\langle k|\mathcal{H}'|m\rangle$  and  $\rho(k)$  are considered to be approximately independent of  $E_k$ . In this case,  $\langle k|\mathcal{H}'|m\rangle$  and  $\rho(k)$  can be taken outside the integral in (C.19). Therefore, the transition probability per unit time w is obtained as

$$w = \frac{4|\langle k|\mathcal{H}'|m\rangle|^2}{\hbar^2 t_0} \rho(k) \int_{-\infty}^{\infty} \frac{\sin^2\left[\frac{1}{2}(\omega_{km} - \omega)t_0\right]}{(\omega_{km} - \omega)^2} \hbar \,\mathrm{d}\omega_{km}$$
$$= \frac{2\pi}{\hbar} \rho(k) |\langle k|\mathcal{H}'|m\rangle|^2. \tag{C.20}$$

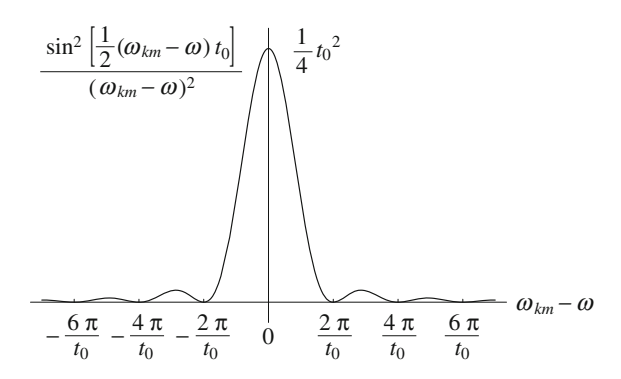


Fig. C.1 Transition probability

#### **C.4 Electric Dipole Interaction (Semiclassical Treatment)**

A classical Hamiltonian  $\mathcal{H}_c$  for a particle, which has a mass m and an electric charge -e in an electromagnetic field, is written as

$$\mathcal{H}_{c} = \frac{1}{2m} (\mathbf{p} + e\mathbf{A})^{2} - e\phi,$$

$$\mathbf{E} = -\frac{\partial \mathbf{A}}{\partial t} - \nabla \phi,$$
(C.21)

where E is the electric field, A is the *vector potential*, and  $\phi$  is the *scalar potential*. First, before calculating the transition probability, we will derive (C.21). The *Lagrangian* L for a particle with the mass m and the electric charge -e in an electromagnetic field is given by

$$L = \frac{1}{2}m\dot{q}^2 + e\phi(q) - e\dot{q}\cdot A(q), \qquad (C.22)$$

where q is a generalized coordinate. Validity of (C.22) will be shown in the following. The *Lagrange equation* is expressed as

$$\frac{\mathrm{d}t}{\mathrm{d}t}\frac{\partial L}{\partial \dot{q}} - \frac{\partial L}{\partial q} = 0. \tag{C.23}$$

As an example, we consider an x-component in the xyz-coordinate system. From (C.22), we have

$$\frac{\partial L}{\partial \dot{x}} = m\dot{x} - eA_x,\tag{C.24}$$

$$\frac{\mathrm{d}t}{\mathrm{d}t}\frac{\partial L}{\partial \dot{x}} = m\ddot{x} - e\left(\frac{\partial A_x}{\partial t} + \dot{x}\frac{\partial A_x}{\partial x} + \dot{y}\frac{\partial A_x}{\partial y} + \dot{z}\frac{\partial A_x}{\partial z}\right),\tag{C.25}$$

$$\frac{\partial L}{\partial x} = e \frac{\partial \phi}{\partial x} - e \left( \dot{x} \frac{\partial A_x}{\partial x} + \dot{y} \frac{\partial A_y}{\partial x} + \dot{z} \frac{\partial A_z}{\partial x} \right). \tag{C.26}$$

Substituting (C.24)–(C.26) into (C.23) results in

$$m\ddot{x} - e\frac{\partial\phi}{\partial x} - e\left[\frac{\partial A_x}{\partial t} + \dot{y}\left(\frac{\partial A_x}{\partial y} - \frac{\partial A_y}{\partial x}\right) + \dot{z}\left(\frac{\partial A_x}{\partial z} - \frac{\partial A_z}{\partial x}\right)\right] = 0 \quad (C.27)$$

or

$$m\frac{\mathrm{d}^{2}x}{\mathrm{d}t^{2}} = -eE_{x} - e(\mathbf{v} \times \mathbf{B})_{x},$$

$$E_{x} = -\frac{\partial \phi}{\partial x} - \frac{\partial A_{x}}{\partial t}, \quad \mathbf{B} = \text{rot}\mathbf{A},$$
(C.28)

which is known as the *Lorentz equation*, and validity of (C.22) has been proved. Similar results are obtained for the y- and z-components.

Using the Lagrangian L, a momentum p of the particle is defined as

$$p \equiv \frac{\partial L}{\partial \dot{q}} = m\dot{q} - eA. \tag{C.29}$$

As a result, the Hamiltonian  $\mathcal{H}$  for the particle is obtained as

$$\mathcal{H}(\mathbf{p}, \mathbf{q}) \equiv \mathbf{p} \cdot \dot{\mathbf{q}} - L$$

$$= m\dot{q}^2 - e\,\dot{\mathbf{q}} \cdot \mathbf{A} - \frac{1}{2}\,m\dot{q}^2 - e\phi + e\,\dot{\mathbf{q}} \cdot \mathbf{A}$$

$$= \frac{1}{2}\,m\dot{q}^2 - e\phi$$

$$= \frac{1}{2m}\,(\mathbf{p} + e\mathbf{A})^2 - e\phi,$$
(C.30)

which is the same as (C.21).

When  $\nabla \cdot \mathbf{A} = 0$  and  $\phi = 0$ , the Schrödinger equation is written as

$$i \hbar \frac{\partial \psi}{\partial t} = [\mathcal{H}_0 + \mathcal{H}'(t)] \psi,$$

$$\mathcal{H}_0 = -\frac{\hbar^2}{2m} \nabla^2 + V(\mathbf{r}), \quad \mathcal{H}'(t) = -\frac{i e \hbar}{m} \mathbf{A} \cdot \nabla,$$
(C.31)

where (C.21) was used. If we express an electric field E as

$$E = \hat{x} E_0 \exp[i(\omega t - kz)], \tag{C.32}$$

where  $\hat{x}$  is a unit vector along the x-axis, the vector potential A is written as

$$A = \hat{x} \frac{i E_0}{\omega} \exp[i(\omega t - kz)], \qquad (C.33)$$

which leads to

$$|A|^2 = |A^* \cdot A| = \frac{E_0^2}{\omega^2}.$$
 (C.34)

To consider the energy flow, we calculate the *Poynting vector S*. Using

$$\mathbf{B} = \text{rot}\mathbf{A} = \mu_0 \mathbf{H},\tag{C.35}$$

where B is the magnetic flux density and H is the magnetic field, we have

$$|S| = |E \times H| = \frac{1}{2} E_0^2 \frac{k}{\mu_0 \omega} = \frac{1}{2} E_0^2 \frac{n_r}{\mu_0 c} = \frac{1}{2} \varepsilon_0 E_0^2 n_r c.$$
 (C.36)

Here,  $n_r$  is the refractive index of a material. Because (C.36) is equal to the energy flow of  $n_{\rm ph}\hbar\omega \, c/n_{\rm r}$ , we obtain

$$E_0^2 = \frac{2n_{\rm ph}\hbar\omega}{\varepsilon_0 n_{\rm r}^2},\tag{C.37}$$

where  $n_{\rm ph}$  is the photon density. From (C.34) and (C.37), we obtain

$$|A|^2 = \frac{2n_{\rm ph}\hbar}{\varepsilon_0 n_{\rm r}^2 \omega}.$$
 (C.38)

Also, (C.31) gives

$$\langle k|\mathcal{H}'|m\rangle = -\frac{\mathrm{i}\,e\hbar}{m}\mathbf{A}\,\langle k|\nabla|m\rangle = \frac{e}{m}\mathbf{A}\,\langle k|\mathbf{p}|m\rangle$$
$$= e\mathbf{A}\,\frac{\mathrm{d}}{\mathrm{d}t}\,\langle k|\mathbf{r}|m\rangle = \mathrm{i}\,\omega_{km}\mathbf{A}\,\langle k|e\mathbf{r}|m\rangle,\tag{C.39}$$

where the matrix element includes the *electric dipole moment er*. Therefore, the transition due to this perturbation is referred to as the *electric dipole transition*.

When the perturbation is applied at t = 0 and removed at  $t = t_0$ , substituting (C.33) and (C.39) into (C.14) results in

$$a_k^{(1)}(t \ge t_0) = -\frac{eE_0}{\hbar \omega m} \langle k | \mathbf{p} | m \rangle e^{-ikz} \frac{e^{i(\omega_{km} + \omega)t_0} - 1}{\omega_{km} + \omega}.$$
 (C.40)

When there is a flow of a photon per unit volume, by substituting (C.40) into (C.19), we can obtain the transition probability per unit time w as

$$w = \frac{e^2 h}{2m^2 \varepsilon_0 n_r^2 E_{km}} |\langle k | \boldsymbol{p} | m \rangle|^2 \quad (E_{km} \equiv \hbar \omega_{km}), \tag{C.41}$$

where the spectral linewidth of  $|A|^2$  is assumed to be narrow.

It should be noted that the transition probability per unit time w in (C.41) is the transition rate for the stimulated emission B in (2.35).

# Appendix D

## TE Mode and TM Mode

#### **D.1 Fundamental Equation**

Figure D.1 shows a two-dimensional optical waveguide in which the guiding layer is sandwiched between the cladding layer and the substrate. We assume that each layer is uniform and the refractive indexes of the guiding layer, the cladding layer, and the substrate are  $n_f$ ,  $n_c$ , and  $n_s$ , respectively, where  $n_f > n_s \ge n_c$  is satisfied to confine a light in the guiding layer. In usual optical waveguides,  $n_f - n_s$  is  $10^{-3} - 10^{-1}$ .

When the electric current does not flow, Maxwell's equations are written as

$$rot \mathbf{E} = \nabla \times \mathbf{E} = -\mu_0 \frac{\partial \mathbf{H}}{\partial t}, \quad rot \mathbf{H} = \nabla \times \mathbf{H} = \varepsilon_0 n_{\rm r}^2 \frac{\partial \mathbf{E}}{\partial t}, \tag{D.1}$$

where E is the electric field, H is the magnetic field,  $\mu_0$  is magnetic permeability in a vacuum,  $\varepsilon_0$  is permittivity in a vacuum, and  $n_r$  is the refractive index of a material. We can also express (D.1) with each component as

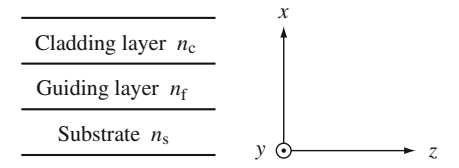
$$\frac{\partial E_{z}}{\partial y} - \frac{\partial E_{y}}{\partial z} = -\mu_{0} \frac{\partial H_{x}}{\partial t}, \quad \frac{\partial H_{z}}{\partial y} - \frac{\partial H_{y}}{\partial z} = \varepsilon_{0} n_{r}^{2} \frac{\partial E_{x}}{\partial t}, 
\frac{\partial E_{x}}{\partial z} - \frac{\partial E_{z}}{\partial x} = -\mu_{0} \frac{\partial H_{y}}{\partial t}, \quad \frac{\partial H_{x}}{\partial z} - \frac{\partial H_{z}}{\partial x} = \varepsilon_{0} n_{r}^{2} \frac{\partial E_{y}}{\partial t}, 
\frac{\partial E_{y}}{\partial x} - \frac{\partial E_{x}}{\partial y} = -\mu_{0} \frac{\partial H_{z}}{\partial t}, \quad \frac{\partial H_{y}}{\partial x} - \frac{\partial H_{x}}{\partial y} = \varepsilon_{0} n_{r}^{2} \frac{\partial E_{z}}{\partial t}.$$
(D.2)

We assume that a light propagates toward a positive direction on the z-axis with a propagation constant  $\beta$ , and its electric field E and magnetic field H are written as

$$E = E(x, y) \exp[i(\omega t - \beta z)],$$
  

$$H = H(x, y) \exp[i(\omega t - \beta z)].$$
(D.3)

**Fig. D.1** Cross-sectional view of a two-dimensional optical waveguide



In a two-dimensional optical waveguide with an abrupt index profile as shown in Fig. D.1, the lightwave along the y-axis is uniform, which results in  $\partial/\partial y = 0$ . Also, from (D.3), we have  $\partial/\partial t = \mathrm{i}\,\omega$  and  $\partial/\partial z = -\mathrm{i}\,\beta$ . Therefore, (D.2) reduces to

$$i\beta E_{y} = -i\omega\mu_{0}H_{x}, \quad i\beta H_{y} = i\varepsilon_{0}n_{r}^{2}\omega E_{x},$$

$$-i\beta E_{x} - \frac{\partial E_{z}}{\partial x} = -i\omega\mu_{0}H_{y}, \quad -i\beta H_{x} - \frac{\partial H_{z}}{\partial x} = i\varepsilon_{0}n_{r}^{2}\omega E_{y},$$

$$\frac{\partial E_{y}}{\partial x} = -i\omega\mu_{0}H_{z}, \quad \frac{\partial H_{y}}{\partial x} = i\varepsilon_{0}n_{r}^{2}\omega E_{z}.$$
(D.4)

If there are no electric charges,  $\nabla \cdot \mathbf{E} = 0$  is satisfied. Hence, with the help of the vector analysis formula, we obtain

$$\nabla \times \nabla \times \mathbf{E} = \nabla(\nabla \cdot \mathbf{E}) - \nabla^2 \mathbf{E} = -\nabla^2 \mathbf{E}.$$
 (D.5)

Substituting (D.1) and (D.3) into (D.5) leads to

$$-\nabla^{2}\mathbf{E} = -\mu_{0}\frac{\partial}{\partial t}\left(\nabla \times \mathbf{H}\right) = -\varepsilon_{0}\mu_{0}n_{r}^{2}\frac{\partial^{2}}{\partial t^{2}}\mathbf{E} = \frac{n_{r}^{2}\omega^{2}}{c^{2}}\mathbf{E},\tag{D.6}$$

where c is the speed of light in a vacuum.

#### **D.2** TE Mode

The electromagnetic wave whose electric field E does not have a component  $E_z$  along the propagation direction is called the transverse electric (TE) wave. For a TE wave with  $E_z = 0$ , (D.4) reduces to

$$i \beta E_{y} = -i \omega \mu_{0} H_{x}, \quad i \beta H_{y} = i \varepsilon_{0} n_{r}^{2} \omega E_{x},$$

$$-i \beta E_{x} = -i \omega \mu_{0} H_{y}, \quad -i \beta H_{x} - \frac{\partial H_{z}}{\partial x} = i \varepsilon_{0} n_{r}^{2} \omega E_{y},$$

$$\frac{\partial E_{y}}{\partial x} = -i \omega \mu_{0} H_{z}, \quad \frac{\partial H_{y}}{\partial x} = 0.$$
(D.7)

For brevity, if we put  $H_y = 0$ , (D.7) results in

$$E_x = 0$$
,  $H_x = -\frac{\beta}{\omega\mu_0} E_y$ ,  $H_z = -\frac{1}{\mathrm{i}\,\omega\mu_0} \frac{\partial E_y}{\partial x}$ . (D.8)

Substituting the first equation in (D.8) into (D.6) leads to

$$\frac{\partial^2}{\partial x^2} E_y + \left(\frac{n_r^2 \omega^2}{c^2} - \beta^2\right) E_y = \frac{\partial^2}{\partial x^2} E_y + (k_0^2 n_r^2 - \beta^2) E_y = 0,$$
 (D.9)

where  $k_0 = \omega/c$ .

In summary, the electric field and the magnetic field for the TE mode obey the following equations given by

$$E_x = E_z = 0, \quad \frac{\partial^2}{\partial x^2} E_y + (k_0^2 n_r^2 - \beta^2) E_y = 0,$$

$$H_x = -\frac{\beta}{\omega \mu_0} E_y, \quad H_y = 0, \quad H_z = -\frac{1}{\mathrm{i} \omega \mu_0} \frac{\partial E_y}{\partial x}.$$
(D.10)

We select a coordinate system, as illustrated in Fig. D.2, and assume that the angle of incidence is  $\theta_f$ , which is the same as the angle of reflection. If we express the amplitudes of the electric fields in the cladding layer, the guiding layer, and the substrate as  $E_c$ ,  $E_f$ , and  $E_s$ , respectively, the electric field  $E_y$  is written as

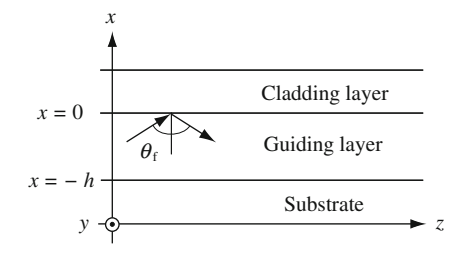
$$E_y = E_c \exp(-\gamma_c x)$$
 : cladding layer,  
 $E_y = E_f \cos(k_x x + \phi_c)$  : guiding layer,  
 $E_y = E_s \exp[\gamma_s (x + h)]$  : substrate,

where

$$\beta = k_0 N, \quad N = n_f \sin \theta_f, \tag{D.12}$$

$$\gamma_{\rm c} = k_0 \sqrt{N^2 - n_{\rm c}^2}, \quad k_x = k_0 \sqrt{n_{\rm f}^2 - N^2}, \quad \gamma_{\rm s} = k_0 \sqrt{N^2 - n_{\rm s}^2}.$$
 (D.13)

**Fig. D.2** Cross-sectional view of a two-dimensional optical waveguide



At each interface, the tangent of the electric field  $E_y$  and that of the magnetic field  $H_z$  are continuous. Therefore, we obtain

$$E_{\rm c} = E_{\rm f} \cos \phi_{\rm c}, \quad \tan \phi_{\rm c} = \frac{\gamma_{\rm c}}{k_x} : x = 0,$$
 (D.14)

$$E_{\rm s} = E_{\rm f} \cos(k_x h - \phi_{\rm c}), \quad \tan(k_x h - \phi_{\rm c}) = \frac{\gamma_{\rm s}}{k_x} : x = -h.$$
 (D.15)

From (D.14) and (D.15), the eigenvalue equation is expressed as

$$k_x h = m\pi + \tan^{-1} \frac{\gamma_c}{k_x} + \tan^{-1} \frac{\gamma_s}{k_x},$$
 (D.16)

where m is a nonnegative integer. Because the following relation

$$k_x = k_0 n_f \cos \theta_f$$
,  $\tan^{-1} \frac{\gamma_c}{k_x} = \phi_c$ ,  $\tan^{-1} \frac{\gamma_s}{k_x} = \phi_s$  (D.17)

is satisfied, (D.16) is the same as (3.16).

#### **D.3 TM Mode**

The electromagnetic wave whose magnetic field H does not have a component  $H_z$  along the propagation direction is called the transverse magnetic (TM) wave. For the TM wave with  $H_z = 0$ , (D.4) reduces to

$$i \beta E_{y} = -i \omega \mu_{0} H_{x}, \quad i \beta H_{y} = i \varepsilon_{0} n_{r}^{2} \omega E_{x},$$

$$-i \beta E_{x} - \frac{\partial E_{z}}{\partial x} = -i \omega \mu_{0} H_{y}, \quad -i \beta H_{x} = i \varepsilon_{0} n_{r}^{2} \omega E_{y},$$

$$\frac{\partial E_{y}}{\partial x} = 0, \quad \frac{\partial H_{y}}{\partial x} = i \varepsilon_{0} n_{r}^{2} \omega E_{z}.$$
(D.18)

For brevity, if we put  $E_y = 0$ , (D.18) results in

$$H_x = 0, \quad E_x = \frac{\beta}{\varepsilon_0 n_{\rm r}^2 \omega} H_y, \quad E_z = \frac{1}{\mathrm{i} \varepsilon_0 n_{\rm r}^2 \omega} \frac{\partial H_y}{\partial x},$$
 (D.19)

$$H_y = \frac{\beta}{\omega \mu_0} E_x + \frac{1}{\mathrm{i} \omega \mu_0} \frac{\partial E_z}{\partial x}.$$
 (D.20)

Substituting (D.19) into (D.20) leads to

$$\frac{\partial^2}{\partial x^2} H_y + (k_0^2 n_r^2 - \beta^2) H_y = 0.$$
 (D.21)

In summary, the electric field and the magnetic field for the TM mode obey the following equation given by

$$E_{x} = \frac{\beta}{\varepsilon_{0}n_{r}^{2}\omega} H_{y}, \quad E_{y} = 0, \quad E_{z} = \frac{1}{\mathrm{i}\,\varepsilon_{0}n_{r}^{2}\omega} \frac{\partial H_{y}}{\partial x},$$

$$H_{x} = H_{z} = 0, \quad \frac{\partial^{2}}{\partial x^{2}} H_{y} + (k_{0}^{2}n_{r}^{2} - \beta^{2})H_{y} = 0.$$
(D.22)

If we express the amplitudes of the magnetic fields in the cladding layer, the guiding layer, and the substrate as  $H_c$ ,  $H_f$ , and  $H_s$ , the magnetic field  $H_y$  is written as

$$H_y = H_c \exp(-\gamma_c x)$$
 : cladding layer,  
 $H_y = H_f \cos(k_x x + \phi_c)$  : guiding layer,  
 $H_y = H_s \exp[\gamma_s (x + h)]$  : substrate. (D.23)

At each interface, the tangent of the magnetic field  $H_y$  and that of the electric field  $E_z$  are continuous, respectively. Therefore, we obtain

$$H_{\rm c} = H_{\rm f} \cos \phi_{\rm c}, \quad \frac{\gamma_{\rm c}}{n_{\rm c}^2} H_{\rm c} = \frac{k_x}{n_{\rm f}^2} H_{\rm f} \sin \phi_{\rm c} : \ x = 0, \quad (D.24)$$

$$H_{\rm s} = H_{\rm f} \cos(k_x h - \phi_{\rm c}), \quad \frac{\gamma_{\rm s}}{n_{\rm s}^2} H_{\rm s} = \frac{k_x}{n_{\rm f}^2} H_{\rm f} \sin(k_x h - \phi_{\rm c}) : x = -h.$$
 (D.25)

From (D.24) and (D.25), we obtain the following eigenvalue equation

$$k_x h = m\pi + \tan^{-1} \left[ \left( \frac{n_f}{n_c} \right)^2 \frac{\gamma_c}{k_x} \right] + \tan^{-1} \left[ \left( \frac{n_f}{n_s} \right)^2 \frac{\gamma_s}{k_x} \right], \tag{D.26}$$

where m is a nonnegative integer.

# Appendix E

# **Characteristic Matrix in Discrete Approach**

#### E.1 Fundamental Equation

When the electric current does not flow, *Maxwell's equations* in a uniform optical material with the refractive index  $n_r$  and magnetic permeability in a vacuum  $\mu_0$  are written as

$$\nabla \times \mathbf{E} = -\mu_0 \frac{\partial \mathbf{H}}{\partial t}, \quad \nabla \times \mathbf{H} = \varepsilon_0 n_{\rm r}^2 \frac{\partial \mathbf{E}}{\partial t}, \tag{E.1}$$

where E is the electric field, H is the magnetic field, and  $\varepsilon_0$  is permittivity in a vacuum. We can also express (E.1) with each component as

$$\frac{\partial E_z}{\partial y} - \frac{\partial E_y}{\partial z} = -\mu_0 \frac{\partial H_x}{\partial t}, \quad \frac{\partial H_z}{\partial y} - \frac{\partial H_y}{\partial z} = \varepsilon_0 n_r^2 \frac{\partial E_x}{\partial t}, 
\frac{\partial E_x}{\partial z} - \frac{\partial E_z}{\partial x} = -\mu_0 \frac{\partial H_y}{\partial t}, \quad \frac{\partial H_x}{\partial z} - \frac{\partial H_z}{\partial x} = \varepsilon_0 n_r^2 \frac{\partial E_y}{\partial t}, 
\frac{\partial E_y}{\partial x} - \frac{\partial E_x}{\partial y} = -\mu_0 \frac{\partial H_z}{\partial t}, \quad \frac{\partial H_y}{\partial x} - \frac{\partial H_x}{\partial y} = \varepsilon_0 n_r^2 \frac{\partial E_z}{\partial t}.$$
(E.2)

We assume that a light propagates toward a positive direction on the z-axis, and dependence of the electric field E and the magnetic field H on time is expressed as  $\exp(i \omega t)$ . In this case, we obtain  $\partial/\partial t = i \omega$ . Therefore, (E.2) reduces to

$$\frac{\partial E_z}{\partial y} - \frac{\partial E_y}{\partial z} = -ik_0 Z_0 H_x, \quad \frac{\partial H_z}{\partial y} - \frac{\partial H_y}{\partial z} = i\frac{k_0}{Z_0} n_r^2 E_x, 
\frac{\partial E_x}{\partial z} - \frac{\partial E_z}{\partial x} = -ik_0 Z_0 H_y, \quad \frac{\partial H_x}{\partial z} - \frac{\partial H_z}{\partial x} = i\frac{k_0}{Z_0} n_r^2 E_y, 
\frac{\partial E_y}{\partial x} - \frac{\partial E_x}{\partial y} = -ik_0 Z_0 H_z, \quad \frac{\partial H_y}{\partial x} - \frac{\partial H_x}{\partial y} = i\frac{k_0}{Z_0} n_r^2 E_z,$$
(E.3)

<sup>©</sup> Springer Japan 2015

<sup>259</sup> 

where  $k_0 = \omega/c$  is a wave number in a vacuum,  $c = 1/\sqrt{\varepsilon_0\mu_0}$  is the speed of light in a vacuum, and  $Z_0 = \sqrt{\mu_0/\varepsilon_0}$  is the *impedance of vacuum*.

#### E.2 TE Mode

We consider the optical waveguide shown in Fig. D.1. Because the lightwave is uniform along the y-axis, we have  $\partial/\partial y = 0$ , which results in  $E_x = E_z = 0$  and  $H_y = 0$  for the TE wave from (D.10). Therefore, (E.3) reduces to

$$\frac{\partial E_y}{\partial z} = ik_0 Z_0 H_x, \quad \frac{\partial E_y}{\partial x} = -ik_0 Z_0 H_z, 
\frac{\partial H_x}{\partial z} - \frac{\partial H_z}{\partial x} = i\frac{k_0}{Z_0} n_r^2 E_y.$$
(E.4)

From (E.4), we obtain a wave equation as

$$\frac{\partial^2 E_y}{\partial x^2} + \frac{\partial^2 E_y}{\partial z^2} = ik_0 Z_0 \left( \frac{\partial H_x}{\partial z} - \frac{\partial H_z}{\partial x} \right) = -k_0^2 n_r^2 E_y.$$
 (E.5)

Here, we assume a *separation-of-variables procedure*. Substituting  $E_y = X(x)U(z)$  into (E.5) and then dividing both sides by  $E_y$  lead to

$$\frac{1}{X}\frac{\partial^2 X}{\partial x^2} + \frac{1}{U}\frac{\partial^2 U}{\partial z^2} = -k_0^2 n_r^2.$$
 (E.6)

From (E.6), if we put

$$\frac{1}{X}\frac{\partial^2 X}{\partial x^2} = -k_0^2 n_r^2 \sin^2 \theta, \quad \frac{1}{U}\frac{\partial^2 U}{\partial z^2} = -k_0^2 n_r^2 \cos^2 \theta, \tag{E.7}$$

where  $\theta$  is defined in Fig. E.1, we can express  $E_y$  as

$$E_y = U(z) \exp[i(\omega t - k_0 n_r x \sin \theta)]. \tag{E.8}$$

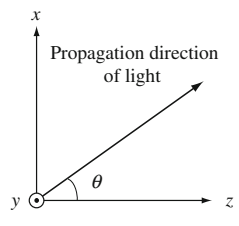


**Fig. E.1** Definition of  $\theta$ 

Similarly, we have

$$Z_0 H_x = V(z) \exp[i(\omega t - k_0 n_r x \sin \theta)],$$
  

$$Z_0 H_z = W(z) \exp[i(\omega t - k_0 n_r x \sin \theta)].$$
(E.9)

Substituting (E.8) and (E.9) into (E.4) results in

$$\frac{\mathrm{d}U}{\mathrm{d}z} = \mathrm{i}\,k_0V,\tag{E.10}$$

$$n_{\rm r}\sin\theta \cdot U = W,\tag{E.11}$$

$$\frac{\mathrm{d}V}{\mathrm{d}z} + \mathrm{i} k_0 n_{\mathrm{r}} \sin \theta \cdot W = \mathrm{i} k_0 n_{\mathrm{r}}^2 U. \tag{E.12}$$

From (E.11) and (E.12), we obtain

$$\frac{\mathrm{d}V}{\mathrm{d}z} = \mathrm{i}\,k_0 n_\mathrm{r}^2 \cos^2\theta \cdot U. \tag{E.13}$$

Differentiating (E.13) with respect to z with the help of (E.10), we have

$$\frac{d^2V}{dz^2} + k_0^2 n_r^2 \cos^2 \theta \cdot V = 0.$$
 (E.14)

In summary, a relationship between U and V is written as

$$\frac{d^2 U}{dz^2} + k_0^2 n_r^2 \cos^2 \theta \cdot U = 0, \quad \frac{d^2 V}{dz^2} + k_0^2 n_r^2 \cos^2 \theta \cdot V = 0, \tag{E.15}$$

$$\frac{\mathrm{d}U}{\mathrm{d}z} = \mathrm{i}\,k_0 V, \quad \frac{\mathrm{d}V}{\mathrm{d}z} = \mathrm{i}\,k_0 n_{\mathrm{r}}^2 \cos^2\theta \cdot U. \tag{E.16}$$

From (E.15) and (E.16), solutions for U and V are expressed as

$$U = A\cos(k_0 n_r z \cos\theta) + B\sin(k_0 n_r z \cos\theta), \tag{E.17}$$

$$V = i n_r \cos \theta [A \sin(k_0 n_r z \cos \theta) - B \cos(k_0 n_r z \cos \theta)]. \tag{E.18}$$

Because (E.15) is a linear differential equation of the second order, we can express U and V as

$$\begin{bmatrix} U(z) \\ V(z) \end{bmatrix} = \begin{bmatrix} F(z) & f(z) \\ G(z) & g(z) \end{bmatrix} \begin{bmatrix} U(0) \\ V(0) \end{bmatrix},$$
 (E.19)

where

$$U_1 = f(z), U_2 = F(z), V_1 = g(z), V_2 = G(z).$$
 (E.20)

Also, from (E.16), we have the following relation

$$\frac{dU_1}{dz} \equiv U_1' = i k_0 V_1, \quad \frac{dU_2}{dz} \equiv U_2' = i k_0 V_2,$$
 (E.21)

$$\frac{dV_1}{dz} \equiv V_1' = i k_0 n_r^2 \cos^2 \theta \cdot U_1, \quad \frac{dV_2}{dz} \equiv V_2' = i k_0 n_r^2 \cos^2 \theta \cdot U_2, \quad (E.22)$$

from which we obtain

$$U_1V_2' - V_1'U_2 = 0, \quad V_1U_2' - U_1'V_2 = 0.$$
 (E.23)

As a result, we have

$$\frac{d}{dz}(U_1V_2 - V_1U_2) = 0. (E.24)$$

Therefore, the following determinant is satisfied:

$$\begin{vmatrix} U_1 & U_2 \\ V_1 & V_2 \end{vmatrix} = \text{constant.} \tag{E.25}$$

As the matrix elements satisfying (E.25), we consider

$$f(0) = G(0) = 0, \quad F(0) = g(0) = 1,$$
  
 $F(z)g(z) - f(z)G(z) = 1.$  (E.26)

From (E.19) and (E.26), we define the transfer matrix M as

$$\begin{bmatrix} U(0) \\ V(0) \end{bmatrix} = \mathbf{M} \begin{bmatrix} U(z) \\ V(z) \end{bmatrix}, \quad \mathbf{M} = \begin{bmatrix} g(z) & -f(z) \\ -G(z) & F(z) \end{bmatrix}.$$
 (E.27)

Also, from (E.17), (E.18), and (E.26), we put

$$f(z) = \frac{i}{n_r \cos \theta} \sin(k_0 n_r z \cos \theta),$$

$$F(z) = \cos(k_0 n_r z \cos \theta),$$

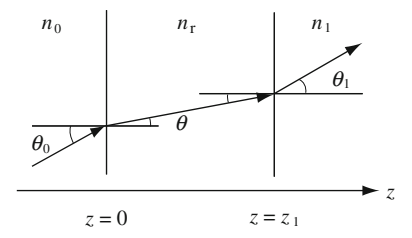
$$g(z) = \cos(k_0 n_r z \cos \theta),$$
(E.28)

$$G(z) = i n_{\rm r} \cos \theta \cdot \sin(k_0 n_{\rm r} z \cos \theta).$$

If we place

$$\beta_i = k_0 n_{\rm r} z \cos \theta, \quad p_i = n_{\rm r} \cos \theta, \tag{E.29}$$

Fig. E.2 Propagation of light in a region with different refractive indexes



and substitute (E.28) and (E.29) into (E.27), we can express the transfer matrix M as

$$\mathbf{M} = \begin{bmatrix} \cos \beta_i & -\frac{\mathrm{i}}{p_i} \sin \beta_i \\ -\mathrm{i} \ p_i \sin \beta_i & \cos \beta_i \end{bmatrix} = \begin{bmatrix} m_{11} \ m_{12} \\ m_{21} \ m_{22} \end{bmatrix}. \tag{E.30}$$

As shown in Fig. E.2, we consider a light propagating along the arrow in sequentially placed layers with different refractive indexes. The tangent of the electric field  $E_y$  and that of the magnetic field  $H_x$  are continuous at each interface. Therefore, if we write the tangent components of the electric fields for the incident wave, the reflected wave, and the transmitted wave as A, R, and T, respectively, the boundary condition is expressed as

$$A + R = U(0), T = U(z_1),$$
 (E.31)

$$p_0(A - R) = V(0), \quad p_1 T = V(z_1),$$
 (E.32)

where

$$p_0 = n_0 \cos \theta, \quad p_1 = n_1 \cos \theta.$$
 (E.33)

Here,  $n_0$  and  $n_1$  are the refractive indexes of the first and last media, respectively. From (E.27) and (E.30)–(E.33), we obtain

$$A + R = (m_{11} + m_{12}p_1)T, (E.34)$$

$$p_0(A - R) = (m_{21} + m_{22}p_1)T.$$
 (E.35)

From (E.34) and (E.35), the amplitude reflectivity r and the amplitude transmissivity t are given by

$$r = \frac{R}{A} = \frac{(m_{11} + m_{12}p_1)p_0 - (m_{21} + m_{22}p_1)}{(m_{11} + m_{12}p_1)p_0 + (m_{21} + m_{22}p_1)},$$

$$t = \frac{T}{A} = \frac{2p_0}{(m_{11} + m_{12}p_1)p_0 + (m_{21} + m_{22}p_1)}.$$
(E.36)

$$t = \frac{T}{A} = \frac{2p_0}{(m_{11} + m_{12}p_1)p_0 + (m_{21} + m_{22}p_1)}.$$
 (E.37)

Using the amplitude reflectivity r and the amplitude transmissivity t, the power reflectivity R and the power transmissivity T are expressed as

$$R = r^* r, \quad T = \frac{p_1}{p_0} t^* t.$$
 (E.38)

#### E.3 TM Mode

For the TM wave, we have  $E_y = 0$  and  $H_x = H_z = 0$  from (D.22). Other components of the TM wave are written as

$$Z_0 H_y = U(z) \exp[i(\omega t - k_0 n_r x \sin \theta)],$$

$$E_x = -V(z) \exp[i(\omega t - k_0 n_r x \sin \theta)],$$

$$E_z = -W(z) \exp[i(\omega t - k_0 n_r x \sin \theta)].$$
(E.39)

Also, from (E.3), we have

$$\frac{\partial H_y}{\partial z} = -i \frac{k_0}{Z_0} n_r^2 E_x, 
\frac{\partial H_y}{\partial x} = i \frac{k_0}{Z_0} n_r^2 E_z, 
\frac{\partial E_x}{\partial z} - \frac{\partial E_z}{\partial x} = -i k_0 Z_0 H_y.$$
(E.40)

Therefore, we obtain a wave equation

$$\frac{\partial^2 H_y}{\partial x^2} + \frac{\partial^2 H_y}{\partial z^2} = -i \frac{k_0 n_r^2}{Z_0} \left( \frac{\partial E_x}{\partial z} - \frac{\partial E_z}{\partial x} \right) = -k_0^2 n_r^2 H_y.$$
 (E.41)

Substituting (E.39) into (E.41) gives

$$\frac{d^2 U}{dz^2} + (k_0 n_r \cos \theta)^2 U = 0.$$
 (E.42)

Inserting (E.39) into (E.40) results in

$$\frac{\mathrm{d}U}{\mathrm{d}z} = \mathrm{i}\,k_0 n_{\mathrm{r}}^2 V,\tag{E.43}$$

$$\sin \theta \cdot U = n_{\rm r} W,\tag{E.44}$$

$$\frac{\mathrm{d}V}{\mathrm{d}z} + \mathrm{i}\,k_0 n_\mathrm{r}\sin\theta \cdot W = \mathrm{i}\,k_0 U. \tag{E.45}$$

From (E.44) and (E.45), we obtain

$$\frac{\mathrm{d}V}{\mathrm{d}z} = \mathrm{i}\,k_0\cos^2\theta \cdot U. \tag{E.46}$$

Differentiating (E.46) with respect to z with the help of (E.43) results in

$$\frac{d^2V}{dz^2} + (k_0 n_r \cos \theta)^2 V = 0.$$
 (E.47)

In summary, a relationship between U and V for the TM mode is written as

$$\frac{d^2 U}{dz^2} + k_0^2 n_r^2 \cos^2 \theta \cdot U = 0, \quad \frac{d^2 V}{dz^2} + k_0^2 n_r^2 \cos^2 \theta \cdot V = 0, \tag{E.48}$$

$$\frac{\mathrm{d}U}{\mathrm{d}z} = \mathrm{i}\,k_0 n_\mathrm{r}^2 V, \quad \frac{\mathrm{d}V}{\mathrm{d}z} = \mathrm{i}\,k_0 \cos^2\theta \cdot U. \tag{E.49}$$

For the TM mode, the transfer matrix M, the amplitude reflectivity r, the amplitude transmissivity t, the power reflectivity R, and the power transmissivity T are obtained by replacing  $p_i$  for the TE mode with

$$q_i = \frac{\cos \theta}{n_{\rm r}}.\tag{E.50}$$

# Appendix F

# Free Carrier Absorption and Plasma Effect

An equation of motion for the electron in a crystal without a magnetic field is given by

$$m^* \frac{\mathrm{d}^2 x}{\mathrm{d}t^2} + \frac{1}{\tau} m^* \frac{\mathrm{d}x}{\mathrm{d}t} = -eE,$$
 (F.1)

where  $m^*$  is the effective mass of the electron,  $\tau$  is the relaxation time such as the mean free time of collision, e is the elementary charge, and E is the electric field. If we assume dependence of x and E on time t is expressed as  $\exp(i \omega t)$  where  $\omega$  is the angular frequency of a light, a position x of the electron is obtained as

$$x = \frac{eE}{m^* \left(\omega^2 - i\,\omega/\tau\right)}. ag{F.2}$$

The polarization P of a material is written as

$$P = P_0 + P_1; P_1 = -nex,$$
 (F.3)

where  $P_0$  is the polarization caused by ionization of atoms constituting the crystal, and  $P_1$  is the polarization induced by the motion of the electrons. Here, we express the electric flux density D as

$$D = \varepsilon_0 E + P = (\varepsilon_0 E + P_0) + P_1 = \varepsilon \varepsilon_0 E + P_1 = \varepsilon' \varepsilon_0 E, \tag{F.4}$$

where  $\varepsilon_0$  is permittivity in a vacuum and  $\varepsilon$  is the dielectric constant of the crystal based on ionization of the atoms. The dielectric constant  $\varepsilon'$ , which is modified by the motion of the electrons, is written as

$$\varepsilon' = \varepsilon_{\rm r} - i\,\varepsilon_{\rm i} = \varepsilon - \frac{nex}{\varepsilon_0 E},$$
 (F.5)

where  $\varepsilon_r$  and  $\varepsilon_i$  are real and imaginary parts of  $\varepsilon'$ , respectively. Substituting (F.2) into (F.5) leads to

$$\varepsilon_{\rm r} - \varepsilon \simeq -\frac{ne^2}{m^*\omega^2\varepsilon_0},$$
 (F.6)

$$\varepsilon_{\rm i} \simeq \frac{ne^2}{m^* \omega^3 \varepsilon_0 \tau},$$
(F.7)

where  $\omega \gg 1/\tau$  was used.

Using the complex refractive index  $n_r - i \kappa$ , we can express  $\varepsilon_r$  and  $\varepsilon_i$  as

$$\varepsilon_{\rm r} = n_{\rm r}^2 - \kappa^2,\tag{F.8}$$

$$\varepsilon_{\rm i} = 2n_{\rm r}\kappa.$$
 (F.9)

Therefore, the optical power absorption coefficient  $\alpha$  due to free carrier absorption is obtained as

$$\alpha = \frac{2\omega}{c}\kappa = \frac{\omega}{c}\frac{\varepsilon_{\rm i}}{n_{\rm r}} = \frac{ne^2}{m^*\omega^2\varepsilon_0 n_{\rm r}c\tau},\tag{F.10}$$

where *c* is the speed of light in a vacuum.

When the carrier concentration increases by n, we assume that  $\varepsilon_{\rm r}$  and  $n_{\rm r}$  change to  $\varepsilon_{\rm r} + \Delta \varepsilon_{\rm r}$  and  $n_{\rm r} + \Delta n_{\rm r}$ , respectively. In this case, we have

$$2n_{\rm r}\Delta n_{\rm r} = \Delta\varepsilon_{\rm r}.\tag{F.11}$$

Hence, we obtain

$$\Delta n_{\rm r} = \frac{\Delta \varepsilon_{\rm r}}{2n_{\rm r}} = \frac{\varepsilon_{\rm r} - \varepsilon}{2n_{\rm r}} = -\frac{e^2}{2m^*\omega^2\varepsilon_0 n_{\rm r}} n,\tag{F.12}$$

which is referred to as the free carrier plasma effect.

# Appendix G

# **Relative Intensity Noise (RIN)**

#### **G.1 Rate Equations with Fluctuations**

When semiconductor lasers show two-mode operations, the rate equations on the photon densities  $S_1$  and  $S_2$  and the carrier concentration n are expressed as

$$\frac{dS_1}{dt} = (\alpha_1 - \beta_1 S_1 - \theta_{12} S_2) S_1 + \beta_{\text{sp1}} \frac{n}{\tau_n} + F_1(t), \tag{G.1}$$

$$\frac{dS_2}{dt} = (\alpha_2 - \beta_2 S_2 - \theta_{21} S_1) S_2 + \beta_{\text{sp2}} \frac{n}{\tau_n} + F_2(t), \tag{G.2}$$

$$\frac{dn}{dt} = \frac{I}{eV_{A}} - [G_{1}(n) - \beta_{1}S_{1} - \theta_{12}S_{2}] S_{1}$$

$$-\left[G_2(n) - \beta_2 S_2 - \theta_{21} S_1\right] S_2 - \frac{n}{\tau_n} + F_n(t). \tag{G.3}$$

Here,  $\alpha_i \equiv G_i(n) - 1/\tau_{\text{ph}i}$  is the net amplification rate,  $G_i(n)$  is the amplification rate,  $\tau_{\text{ph}i}$  is the photon lifetime,  $\beta_i$  is the self-saturation coefficient,  $\theta_{ij}$  is the cross-saturation coefficient,  $\beta_{\text{sp}i}$  is the spontaneous emission coupling factor (i, j = 1, 2),  $\tau_n$  is the carrier lifetime, I is the injection current, e is the elementary charge, and  $V_A$  is a volume of the active layer.

Fluctuations are expressed by the Langevin noise sources  $F_1$ ,  $F_2$ , and  $F_n$ . In Markoffian approximation, time averages of  $F_1$ ,  $F_2$ , and  $F_n$  satisfy

$$\langle F_k(t) \rangle = 0, \tag{G.4}$$

$$\langle F_k(t)F_l(t')\rangle = 2D_{kl}\delta(t-t'),$$
 (G.5)

where k, l = 1, 2, and n. The diffusion coefficients  $D_{kl}$  are given by

$$D_{11} = \beta_{\text{sp1}} \frac{n}{\tau_n} S_{10}, \ D_{22} = \beta_{\text{sp2}} \frac{n}{\tau_n} S_{20}, \ D_{12} = D_{21} = 0,$$

$$D_{nn} = \beta_{\text{sp1}} \frac{n}{\tau_n} S_{10} + \beta_{\text{sp2}} \frac{n}{\tau_n} S_{20} + \frac{n}{\tau_n},$$

$$D_{1n} = -\beta_{\text{sp1}} \frac{n}{\tau_n} S_{10}, \ D_{2n} = -\beta_{\text{sp2}} \frac{n}{\tau_n} S_{20},$$
(G.6)

where  $S_{10}$  and  $S_{20}$  are the average photon densities of mode 1 and mode 2, respectively.

The amplification rate  $G_i(n)$  is given by

$$G_i(n) = \left[\frac{\partial G_i}{\partial n}\right]_{n=n_{thi}} (n - n_{0i}), \tag{G.7}$$

where  $n_{\text{th}i}$  is the threshold carrier concentration and  $n_{0i}$  is the transparent carrier concentration.

#### **G.2 RIN Without Carrier Fluctuations**

We express the photon densities  $S_1$  and  $S_2$  as

$$S_1 = S_{10} + \delta S_1(t), \quad S_2 = S_{20} + \delta S_2(t),$$
 (G.8)

where  $S_{10}$  and  $S_{20}$  are the average photon densities in a steady state, and  $\delta S_1$  and  $\delta S_2$  are the fluctuations of mode 1 and mode 2, respectively. Substituting Fourier transforms

$$\delta S_i(t) = \frac{1}{2\pi} \int_{-\infty}^{\infty} \delta \tilde{S}_i(\omega) \exp(i\omega t) d\omega, \qquad (G.9)$$

$$\delta \tilde{S}_{i}(\omega) = \int_{-\infty}^{\infty} \delta S_{i}(t) \exp(-i \omega t) dt, \qquad (G.10)$$

$$F_i(t) = \frac{1}{2\pi} \int_{-\infty}^{\infty} \tilde{F}_i(\omega) \exp(i\omega t) d\omega, \qquad (G.11)$$

$$\tilde{F}_{i}(\omega) = \int_{-\infty}^{\infty} F_{i}(t) \exp(-i\omega t) dt,$$
(G.12)

into (G.1)–(G.3), and then neglecting  $F_n(t)$ , we have

$$i\omega\delta\tilde{S}_{1}(\omega) = -A_{1}\delta\tilde{S}_{1}(\omega) - B_{1}\delta\tilde{S}_{2}(\omega) + \tilde{F}_{1}(\omega), \tag{G.13}$$

$$i \omega \delta \tilde{S}_{2}(\omega) = -A_{2} \delta \tilde{S}_{2}(\omega) - B_{2} \delta \tilde{S}_{1}(\omega) + \tilde{F}_{2}(\omega), \tag{G.14}$$

where

$$A_1 = \beta_1 S_{10}, \quad A_2 = \beta_2 S_{20},$$
 (G.15)

$$B_1 = \theta_{12} S_{10}, \quad B_2 = \theta_{21} S_{20}.$$
 (G.16)

From (G.13) and (G.14), the self-correlation functions  $\langle \delta \tilde{S}_1(\omega) \delta \tilde{S}_1^*(\omega') \rangle$  and  $\langle \delta \tilde{S}_2(\omega) \delta \tilde{S}_2^*(\omega') \rangle$  are given by

$$\langle \delta \tilde{S}_1(\omega) \delta \tilde{S}_1^*(\omega') \rangle = \tilde{S}_{\delta S_1}(\omega) \cdot 2\pi \delta(\omega - \omega'), \tag{G.17}$$

$$\tilde{S}_{\delta S_1}(\omega) = \frac{(\omega^2 + A_2^2)W_1 - 2A_2B_1W_{12} + B_1^2W_2}{(A_1A_2 - B_1B_2 - \omega^2)^2 + \omega^2(A_1 + A_2)^2},$$
 (G.18)

$$\langle \delta \tilde{S}_{2}(\omega) \delta \tilde{S}_{2}^{*}(\omega') \rangle = \tilde{S}_{\delta S_{2}}(\omega) \cdot 2\pi \delta(\omega - \omega'), \tag{G.19}$$

$$\tilde{S}_{\delta S_2}(\omega) = \frac{(\omega^2 + A_1^2)W_2 - 2A_1B_2W_{21} + B_2^2W_1}{(A_1A_2 - B_1B_2 - \omega^2)^2 + \omega^2(A_1 + A_2)^2},$$
 (G.20)

where

$$W_1 = \langle \tilde{F}_1(\omega) \tilde{F}_1^*(\omega) \rangle, \tag{G.21}$$

$$W_2 = \langle \tilde{F}_2(\omega) \tilde{F}_2^*(\omega) \rangle, \tag{G.22}$$

$$W_{12} = \langle \tilde{F}_1(\omega) \tilde{F}_2^*(\omega) \rangle. \tag{G.23}$$

In the shot noise Langevin model, the correlation strengths  $\langle \tilde{F}_k(\omega) \tilde{F_k}^*(\omega) \rangle$  and  $\langle \tilde{F}_k(\omega) \tilde{F}_l^*(\omega) \rangle$  are given by

$$\langle \tilde{F}_k(\omega) \tilde{F}_k^*(\omega) \rangle, = \sum R_k^+ + \sum R_k^-$$
 (G.24)

$$\langle \tilde{F}_k(\omega) \tilde{F}_l^*(\omega) \rangle = -\left(\sum R_{kl} + \sum R_{lk}\right),$$
 (G.25)

where  $R_k^+$  and  $R_k^-$  (k=1,2) are the rate for the photon to enter the photon reservoirs and to leave them, respectively;  $R_k^+$  and  $R_k^-$  (k=n) are the rate for the electron to enter the electron reservoirs and to leave them, respectively; and  $R_{kl}$  and  $R_{lk}$  are the exchange rates.

As a result, the correlation strength  $\langle \tilde{F}_1(\omega) \tilde{F}_1^*(\omega) \rangle$  is obtained as

$$W_{1} = \langle \tilde{F}_{1}(\omega) \tilde{F}_{1}^{*}(\omega) \rangle$$

$$= \frac{1}{V_{A}} \left[ \left( \alpha_{1} + \frac{1}{\tau_{\text{ph}1}} + \beta_{1} S_{10} + \theta_{12} S_{20} \right) S_{10} + \beta_{\text{sp}1} \frac{n}{\tau_{n}} \right]$$

$$\simeq 2 \left( \alpha_{1} + \frac{1}{\tau_{\text{ph}1}} \right) \frac{S_{10}}{V_{A}}.$$
(G.26)

Similarly, we have

$$W_2 = \langle \tilde{F}_2(\omega) \tilde{F}_2^*(\omega) \rangle \simeq 2 \left( \alpha_2 + \frac{1}{\tau_{\text{ph}2}} \right) \frac{S_{20}}{V_{\text{A}}},$$
 (G.27)

$$W_{12} = \langle \tilde{F}_1(\omega) \tilde{F}_2^*(\omega) \rangle \simeq (\theta_{12} + \theta_{21}) \frac{S_{10} S_{20}}{V_A} = W_{21}.$$
 (G.28)

Using (G.18) and (G.20), we define the *relative intensity noises* (RINs) per unit bandwidth as

$$RIN_{1} = \frac{2\tilde{S}_{\delta S_{1}}(\omega)}{S_{10}^{2}} = \frac{2}{S_{10}^{2}} \frac{(\omega^{2} + A_{2}^{2})W_{1} - 2A_{2}B_{1}W_{12} + B_{1}^{2}W_{2}}{(A_{1}A_{2} - B_{1}B_{2} - \omega^{2})^{2} + \omega^{2}(A_{1} + A_{2})^{2}}, \quad (G.29)$$

$$RIN_2 = \frac{2\tilde{S}_{\delta S_2}(\omega)}{S_{20}^2} = \frac{2}{S_{20}^2} \frac{(\omega^2 + A_1^2)W_2 - 2A_1B_2W_{21} + B_2^2W_1}{(A_1A_2 - B_1B_2 - \omega^2)^2 + \omega^2(A_1 + A_2)^2}.$$
 (G.30)

#### **G.3 RIN with Carrier Fluctuations**

We express the carrier concentration n as

$$n = n_{c0} + \delta n(t), \tag{G.31}$$

where  $n_{c0}$  is the carrier concentration in a steady state and  $\delta n$  is the fluctuation in the carrier concentration. Their Fourier transforms are written as

$$\delta n(t) = \frac{1}{2\pi} \int_{-\infty}^{\infty} \delta \tilde{n}(\omega) \exp(i\omega t) d\omega, \qquad (G.32)$$

$$\delta \tilde{n}(\omega) = \int_{-\infty}^{\infty} \delta n(t) \exp(-i\omega t) dt, \qquad (G.33)$$

$$F_n(t) = \frac{1}{2\pi} \int_{-\infty}^{\infty} \tilde{F}_n(\omega) \exp(i\omega t) d\omega, \qquad (G.34)$$

$$\tilde{F}_n(\omega) = \int_{-\infty}^{\infty} F_n(t) \exp(-i\omega t) dt.$$
 (G.35)

Substituting (G.9)–(G.12) and (G.32)–(G.35) into (G.1)–(G.3), we have

$$i \omega \delta \tilde{S}_{1}(\omega) = -A_{1} \delta \tilde{S}_{1}(\omega) - B_{1} \delta \tilde{S}_{2}(\omega) + C_{1} \delta \tilde{n}(\omega) + \tilde{F}_{1}(\omega), \tag{G.36}$$

$$i\omega\delta\tilde{S}_{2}(\omega) = -A_{2}\delta\tilde{S}_{2}(\omega) - B_{2}\delta\tilde{S}_{1}(\omega) + C_{2}\delta\tilde{n}(\omega) + \tilde{F}_{2}(\omega), \tag{G.37}$$

$$i \omega \delta \tilde{n}(\omega) = -G_1(n_{c0}) \delta \tilde{S}_1(\omega) - G_2(n_{c0}) \delta \tilde{S}_2(\omega) + C_3 \delta \tilde{n}(\omega) + \tilde{F}_n(\omega),$$
(G.38)

where

$$C_1 = \left[\frac{\partial G_1}{\partial n}\right]_{n=n_{\text{th}}} S_{10} + \frac{\beta_{\text{sp1}}}{\tau_n},\tag{G.39}$$

$$C_2 = \left[\frac{\partial G_2}{\partial n}\right]_{n=n_{\text{th}}} S_{20} + \frac{\beta_{\text{sp2}}}{\tau_n},\tag{G.40}$$

$$C_3 = C_1 + C_2 + \frac{1}{\tau_n}. ag{G.41}$$

From (G.36)–(G.38), the self-correlation functions  $\langle \delta \tilde{S}_1(\omega) \delta \tilde{S}_1^*(\omega') \rangle$  and  $\langle \delta \tilde{S}_2(\omega) \delta \tilde{S}_2^*(\omega') \rangle$  are given by

$$\langle \delta \tilde{S}_{1}(\omega) \delta \tilde{S}_{1}^{*}(\omega') \rangle = \tilde{S}_{\delta S_{1}}(\omega) \cdot 2\pi \delta(\omega - \omega'), \tag{G.42}$$

$$\tilde{S}_{\delta S_{1}}(\omega) = \frac{1}{|X_{1}X_{2} - Y_{1}Y_{2}|^{2}} \times \{|X_{2}|^{2}W_{1} - (X_{2}^{*}Y_{1} + X_{2}Y_{1}^{*})W_{12} + |Y_{1}|^{2}W_{2} + |Z_{1}X_{2} - Z_{2}Y_{1}|^{2}W_{n} + [X_{2}^{*}(Z_{1}X_{2} - Z_{2}Y_{1}) + X_{2}(Z_{1}X_{2} - Z_{2}Y_{1})^{*}]W_{1n} - [Y_{1}^{*}(Z_{1}X_{2} - Z_{2}Y_{1}) + Y_{1}(Z_{1}X_{2} - Z_{2}Y_{1})^{*}]W_{2n}\}, \tag{G.43}$$

$$\langle \delta \tilde{S}_{2}(\omega) \delta \tilde{S}_{2}^{*}(\omega') \rangle = \tilde{S}_{\delta S_{2}}(\omega) \cdot 2\pi \delta(\omega - \omega'), \tag{G.44}$$

$$\tilde{S}_{\delta S_{2}}(\omega) = \frac{1}{|X_{1}X_{2} - Y_{1}Y_{2}|^{2}} \times \{|Y_{2}|^{2}W_{1} - (X_{1}^{*}Y_{2} + X_{1}Y_{2}^{*})W_{12} + |X_{1}|^{2}W_{2} + |Z_{2}X_{1} - Z_{1}Y_{2}|^{2}W_{n} - [Y_{2}^{*}(Z_{2}X_{1} - Z_{1}Y_{2}) + Y_{2}(Z_{2}X_{1} - Z_{1}Y_{2})^{*}]W_{1n} + [X_{1}^{*}(Z_{2}X_{1} - Z_{1}Y_{2}) + X_{1}(Z_{2}X_{1} - Z_{1}Y_{2})^{*}]W_{2n}\}, \tag{G.45}$$

where

$$X_1 = i\omega + A_1 + \frac{C_1 G_1(n_{c0})}{i\omega + C_3},$$
 (G.46)

$$X_2 = i\omega + A_2 + \frac{C_2 G_2(n_{c0})}{i\omega + C_3},$$
 (G.47)

$$Y_1 = B_1 + \frac{C_1 G_2(n_{c0})}{i \omega + C_3},$$
 (G.48)

$$Y_2 = B_2 + \frac{C_2 G_1(n_{c0})}{i\omega + C_3},\tag{G.49}$$

$$Z_1 = \frac{C_1}{\mathrm{i}\,\omega + C_3},\tag{G.50}$$

$$Z_2 = \frac{C_2}{i\,\omega + C_3},\tag{G.51}$$

$$W_n = \langle \tilde{F}_n(\omega) \tilde{F}_n^*(\omega) \rangle = \frac{2I_0}{eV_A^2}, \tag{G.52}$$

$$W_{1n} = \langle \tilde{F}_1(\omega) \tilde{F}_n^*(\omega) \rangle = -W_1, \tag{G.53}$$

$$W_{2n} = \langle \tilde{F}_2(\omega) \tilde{F}_n^*(\omega) \rangle = -W_2. \tag{G.54}$$

Using (G.43) and (G.45), we obtain the RINs per unit bandwidth as

$$RIN_{1} = \frac{2\tilde{S}_{\delta S_{1}}(\omega)}{S_{10}^{2}}$$

$$= \frac{2}{S_{10}^{2}} \frac{1}{|X_{1}X_{2} - Y_{1}Y_{2}|^{2}}$$

$$\times \{|X_{2}|^{2}W_{1} - (X_{2}^{*}Y_{1} + X_{2}Y_{1}^{*})W_{12}$$

$$+ |Y_{1}|^{2}W_{2} + |Z_{1}X_{2} - Z_{2}Y_{1}|^{2}W_{n}$$

$$+ [X_{2}^{*}(Z_{1}X_{2} - Z_{2}Y_{1}) + X_{2}(Z_{1}X_{2} - Z_{2}Y_{1})^{*}]W_{1n}$$

$$- [Y_{1}^{*}(Z_{1}X_{2} - Z_{2}Y_{1}) + Y_{1}(Z_{1}X_{2} - Z_{2}Y_{1})^{*}]W_{2n}\}, \qquad (G.55)$$

$$RIN_{2} = \frac{2\tilde{S}_{\delta S_{2}}(\omega)}{S_{20}^{2}}$$

$$= \frac{2}{S_{20}^{2}} \frac{1}{|X_{1}X_{2} - Y_{1}Y_{2}|^{2}} \times \{|Y_{2}|^{2}W_{1} - (X_{1}^{*}Y_{2} + X_{1}Y_{2}^{*})W_{12} + |X_{1}|^{2}W_{2} + |Z_{2}X_{1} - Z_{1}Y_{2}|^{2}W_{n} - [Y_{2}^{*}(Z_{2}X_{1} - Z_{1}Y_{2}) + Y_{2}(Z_{2}X_{1} - Z_{1}Y_{2})^{*}]W_{1n} + [X_{1}^{*}(Z_{2}X_{1} - Z_{1}Y_{2}) + X_{1}(Z_{2}X_{1} - Z_{1}Y_{2})^{*}]W_{2n}\}.$$
 (G.56)

# Appendix H

# **Rate Equations: Comparison of Two Definitions** of the Photon Density

## H.1 Rate Equations for the Number of the Photons $N_{\rm ph}$

Prior to comparing two definitions of the *photon density*, we show the rate equations for *the number of the carriers* and *the number of the photons*, because they are the bases of the rate equations for the *carrier concentration* and the *photon density*.

If we assume that the number of the electrons N is equal to the number of the holes P, the rate equations for the number of the carriers N and the number of the photons  $N_{\rm ph}$  of the laser light are given by

$$\begin{split} \frac{\mathrm{d}N}{\mathrm{d}t} &= \frac{I}{e} - G(n)N_{\mathrm{ph}} - \frac{N}{\tau_n} \\ &= \frac{I}{e} - g(n)\Gamma_{\mathrm{a}}N_{\mathrm{ph}} - \frac{N}{\tau_n}, \\ \frac{\mathrm{d}N_{\mathrm{ph}}}{\mathrm{d}t} &= G(n)N_{\mathrm{ph}} - \frac{N_{\mathrm{ph}}}{\tau_{\mathrm{ph}}} + \beta_{\mathrm{sp}} \frac{N}{\tau_{\mathrm{r}}} \\ &= g(n)\Gamma_{\mathrm{a}}N_{\mathrm{ph}} - \frac{N_{\mathrm{ph}}}{\tau_{\mathrm{ph}}} + \beta_{\mathrm{sp}} \frac{N}{\tau_{\mathrm{r}}}. \end{split} \tag{H.1}$$

Here, I is the injection current flowing through the active layer; e is the elementary charge;  $G(n) = g(n)\Gamma_a$  is the mode amplification rate due to the stimulated emission; g(n) is the amplification rate in the active layer due to the stimulated emission; n is the carrier concentration;  $\Gamma_a$  is the optical confinement factor of the active layer;  $\tau_n$  is the carrier lifetime;  $\tau_{ph}$  is the photon lifetime;  $\beta_{sp}$  is the spontaneous emission coupling factor; and  $\tau_r$  is the radiative recombination lifetime due to the spontaneous emission.

In (H.1), I/e is an increased rate of the number of the carriers in the active layer;  $-G(n)N_{\rm ph} = -g(n)\Gamma_{\rm a}N_{\rm ph}$  shows a consumption rate of the number of the carriers due to the stimulated emission. It should be noted that only the photons existing in the active layer contribute to the stimulated emission; the number of the photons

existing in the active layer is denoted by  $\Gamma_a N_{\rm ph}$ . The third term in the right-hand side in (H.1),  $-N/\tau_n$ , expresses a decay rate of the number of the carriers in the carrier lifetime  $\tau_n$ .

In (H.2),  $G(n)N_{\rm ph}=g(n)\Gamma_{\rm a}N_{\rm ph}$  shows an increased rate of the number of the photons  $N_{\rm ph}$  due to the stimulated emission;  $-N_{\rm ph}/\tau_{\rm ph}$  is a decreased rate of the number of the photons inside the optical cavity due to the absorption and light emission toward the outside of the optical cavity; and  $\beta_{\rm sp} N/\tau_{\rm r}$  represents a coupling rate of spontaneously emitted photons to the lasing mode, which is a resonance mode of the cavity.

## H.2 Rate Equations for the Photon Density $S = N_{\rm ph}/V_{\rm a}$

The carrier concentration n is defined as  $n = N/V_a$ ; the *photon density* S is defined as  $S = N_{\rm ph}/V_a$  where N is the number of the carriers in the active layer,  $N_{\rm ph}$  is the number of the photons, and  $V_a$  is the volume of the active layer.

Dividing the both sides of (H.1) by the volume of the active layer  $V_a$ , the left-hand side and the right-hand side are written as

Left-hand side 
$$= \frac{1}{V_a} \frac{dN}{dt} = \frac{d(N/V_a)}{dt} = \frac{dn}{dt},$$
(H.3)
$$\text{Right-hand side} = \frac{1}{V_a} \left[ \frac{I}{e} - G(n)N_{\text{ph}} - \frac{N}{\tau_n} \right]$$

$$= \frac{I/V_a}{e} - G(n)\frac{N_{\text{ph}}}{V_a} - \frac{N/V_a}{\tau_n}$$

$$= \frac{J}{ed} - G(n)S - \frac{n}{\tau_n}.$$
(H.4)

Here, J = I/A is the injection current density, which is an electric current flowing through a unit area in the active layer, A is the area of the active layer,  $d = V_a/A$  is the thickness of the active layer.

Dividing the both sides of (H.2) by the volume of the active layer  $V_a$ , the left-hand side and the right-hand side are expressed as

Left-hand side 
$$= \frac{1}{V_a} \frac{dN_{ph}}{dt} = \frac{d(N_{ph}/V_a)}{dt} = \frac{dS}{dt},$$
(H.5)  
Right-hand side 
$$= \frac{1}{V_a} \left[ G(n)N_{ph} - \frac{N_{ph}}{\tau_{ph}} + \beta_{sp} \frac{N}{\tau_r} \right]$$

$$= G(n)\frac{N_{ph}}{V_a} - \frac{N_{ph}/V_a}{\tau_{ph}} + \beta_{sp} \frac{N/V_a}{\tau_r}$$

$$= G(n)S - \frac{S}{\tau_{ph}} + \beta_{sp} \frac{n}{\tau_r}.$$
(H.6)

From (H.3)–(H.6), we obtain the following rate equations

$$\frac{\mathrm{d}n}{\mathrm{d}t} = \frac{J}{ed} - G(n)S - \frac{n}{\tau_n},\tag{H.7}$$

$$\frac{\mathrm{d}S}{\mathrm{d}t} = G(n)S - \frac{S}{\tau_{\mathrm{ph}}} + \beta_{\mathrm{sp}} \frac{n}{\tau_{\mathrm{r}}},\tag{H.8}$$

which are shown in (5.20) and (5.21), respectively.

## H.3 Rate Equations for the Photon Density $s = N_{\rm ph}/V_{\rm m}$

The carrier concentration n is defined as  $n = N/V_a$ ; the *photon density s* is defined as  $s = N_{\rm ph}/V_{\rm m}$  where N is the number of the carriers in the active layer,  $N_{\rm ph}$  is the number of the photons,  $V_a$  is the volume of the active layer, and  $V_{\rm m}$  is the mode volume. The optical confinement factor of the active layer  $\Gamma_a$  is given by  $\Gamma_a = V_a/V_{\rm m}$ .

Dividing the both sides of (H.1) by the volume of the active layer  $V_a$ , the left-hand side and the right-hand side are written as

Left-hand side 
$$= \frac{1}{V_{a}} \frac{dN}{dt} = \frac{d(N/V_{a})}{dt} = \frac{dn}{dt}, \tag{H.9}$$
Right-hand side 
$$= \frac{1}{V_{a}} \left[ \frac{I}{e} - g(n) \Gamma_{a} N_{ph} - \frac{N}{\tau_{n}} \right]$$

$$= \frac{I/V_{a}}{e} - g(n) \frac{V_{a}}{V_{m}} \frac{N_{ph}}{V_{a}} - \frac{N/V_{a}}{\tau_{n}}$$

$$= \frac{J}{ed} - g(n)s - \frac{n}{\tau_{n}}. \tag{H.10}$$

Here, J = I/A is the injection current density, which is an electric current flowing through a unit area in the active layer, A is the area of the active layer,  $d = V_a/A$  is the thickness of the active layer.

Dividing the both sides of (H.2) by the mode volume  $V_{\rm m}$ , the left-hand side and the right-hand side are expressed as

Left-hand side 
$$= \frac{1}{V_{\rm m}} \frac{\mathrm{d}N_{\rm ph}}{\mathrm{d}t} = \frac{\mathrm{d}(N_{\rm ph}/V_{\rm m})}{\mathrm{d}t} = \frac{\mathrm{d}s}{\mathrm{d}t}, \tag{H.11}$$
Right-hand side 
$$= \frac{1}{V_{\rm m}} \left[ g(n) \Gamma_{\rm a} N_{\rm ph} - \frac{N_{\rm ph}}{\tau_{\rm ph}} + \beta_{\rm sp} \frac{N}{\tau_{\rm r}} \right]$$

$$= g(n) \Gamma_{\rm a} \frac{N_{\rm ph}}{V_{\rm m}} - \frac{N_{\rm ph}/V_{\rm m}}{\tau_{\rm ph}} + \beta_{\rm sp} \frac{N/V_{\rm m}}{\tau_{\rm r}}$$

$$= \Gamma_{\rm a} g(n) s - \frac{s}{\tau_{\rm ph}} + \Gamma_{\rm a} \beta_{\rm sp} \frac{n}{\tau_{\rm r}}, \tag{H.12}$$

where  $N/V_{\rm m} = (N/V_{\rm a}) \cdot (V_{\rm a}/V_{\rm m}) = n\Gamma_{\rm a}$  was used.

From (H.9)–(H.12), we obtain the following rate equations

$$\frac{\mathrm{d}n}{\mathrm{d}t} = \frac{J}{ed} - g(n)s - \frac{n}{\tau_n},\tag{H.13}$$

$$\frac{\mathrm{d}s}{\mathrm{d}t} = \Gamma_{\mathrm{a}}g(n)s - \frac{s}{\tau_{\mathrm{ph}}} + \Gamma_{\mathrm{a}}\beta_{\mathrm{sp}}\frac{n}{\tau_{\mathrm{r}}}.\tag{H.14}$$

Using the transparent carrier concentration  $n_0$ , in which a semiconductor is transparent, the amplification rate due to the stimulated emission g(n) can be approximately written as

$$g(n) = g_0(n - n_0), (H.15)$$

where  $g_0$  is the differential gain coefficient, which is defined as

$$g_0 \equiv \frac{\partial g}{\partial n}.\tag{H.16}$$

By using the *small-signal analysis*, approximate analytical solutions can be obtained from (H.13) and (H.14). To proceed the small-signal analysis, we put the carrier concentration n, the photon density s, and the current density J as follows:

$$n = n_{c0} + \delta n, \quad s = s_0 + \delta s, \quad J = J_0 + \delta J > J_{th},$$
  

$$n_{c0} \gg \delta n, \quad s_0 \gg \delta s, \quad J_0 \gg \delta J,$$
(H.17)

where  $n_{c0}$ ,  $s_0$ ,  $J_0$  are steady state values of the carrier concentration, the photon density, and the current density, respectively;  $\delta n$ ,  $\delta s$ , and  $\delta J$  are the deviations from each steady-state value.

Neglecting coupling of the spontaneous emission to the lasing mode, (H.13) and (H.14) are reduced to

$$\frac{\mathrm{d}n}{\mathrm{d}t} = \frac{J}{ed} - g(n)s - \frac{n}{\tau_n},\tag{H.18}$$

$$\frac{\mathrm{d}s}{\mathrm{d}t} = \Gamma_{\mathrm{a}}g(n)s - \frac{s}{\tau_{\mathrm{ph}}}.\tag{H.19}$$

In a steady state (d/dt = 0), substituting (H.17) into (H.18) and (H.19) leads to

$$\frac{J_0}{ed} - g(n_{c0})s_0 - \frac{n_{c0}}{\tau_n} = 0, (H.20)$$

$$\Gamma_{\rm a}g(n_{\rm c0}) = \frac{1}{\tau_{\rm ph}}.\tag{H.21}$$

Substituting (H.17) into (H.15) results in

$$g(n) = g(n_{c0} + \delta n) = g_0(n_{c0} + \delta n - n_0)$$
  
=  $g_0(n_{c0} - n_0) + g_0\delta n = g(n_{c0}) + \frac{\partial g}{\partial n}\delta n$ , (H.22)

where (H.16) was used.

Inserting (H.17) into (H.18) and (H.19) with the help of (H.20)–(H.22) and then neglecting the second-order small term  $\delta n \cdot \delta s$ , the rate equations on the deviations  $\delta n$  and  $\delta s$  are written as

$$\frac{\mathrm{d}}{\mathrm{d}t}\delta n = \frac{\delta J}{ed} - \frac{\delta s}{\Gamma_{\mathrm{a}}\tau_{\mathrm{ph}}} - \frac{\partial g}{\partial n}s_{0}\delta n - \frac{\delta n}{\tau_{n}},\tag{H.23}$$

$$\frac{\mathrm{d}}{\mathrm{d}t}\delta s = \Gamma_{\mathrm{a}} \frac{\partial g}{\partial n} s_0 \delta n. \tag{H.24}$$

By removing  $\delta n$  from (H.23) and (H.24), we have

$$\frac{\mathrm{d}^2}{\mathrm{d}t^2}\delta s + \left(\frac{\partial g}{\partial n}s_0 + \frac{1}{\tau_n}\right)\frac{\mathrm{d}}{\mathrm{d}t}\delta s + \frac{\partial g}{\partial n}\frac{s_0}{\tau_{\mathrm{ph}}}\delta s = \Gamma_{\mathrm{a}}\frac{\partial g}{\partial n}\frac{s_0}{ed}\delta J. \tag{H.25}$$

From (H.25), the decay coefficient  $\gamma_0$ , the decay time  $\tau_{\rm re}$ , and the oscillation angular frequency  $\omega_{\rm r}$  are written as

$$\gamma_0 = \frac{\partial g}{\partial n} s_0 + \frac{1}{\tau_n} = \frac{1}{\tau_{\text{re}}},\tag{H.26}$$

$$\omega_{\rm r}^2 = \frac{\partial g}{\partial n} \frac{s_0}{\tau_{\rm ph}}.\tag{H.27}$$

From (H.27) and (H.21), the relaxation oscillation frequency  $f_r$  is given by

$$f_{\rm r} = \frac{1}{2\pi} \sqrt{\frac{\partial g}{\partial n} \frac{s_0}{r_{\rm ph}}} = \frac{1}{2\pi} \sqrt{\Gamma_{\rm a} g(n_{\rm c0}) \frac{\partial g}{\partial n} s_0}.$$
 (H.28)

A	Bandgap, I
Absorption, 1, 26, 31	Base function, 15
induced, 26	Beam waist, 120
rate, 31	Bernard-Duraffourg relation, 35
Absorption loss, 81	BH, see buried heterostructure (BH)
ACC, see automatic current control (ACC)	Bias, 141
$\alpha$ parameter, 162	Biaxial stress, 220
Alternating current theory, 150	Biot-Savart's law, 6
AM noise, see amplitude modulating (AM)	Bistable LD, 176
noise	Blackbody radiation theory, 32
Amplitude modulating (AM) noise, 156	Bloch function, 3
Amplitude shift keying (ASK), 149	Bloch oscillation, 21
Analog modulation, 151	Bloch theorem, 3
Angle of incidence, 44	Bohr angular frequency, 246
Anisotropic optical gain, 205	Bohr magneton, 7
Antiguiding, 123	Boltzmann constant, 29
-effect, 119	Bra vector, 4
Antiguiding effect, 119	Bragg wavelength, 70, 192
Antireflection (AR), 188, 195	Brillouin zone, 2
Anti-Stokes luminescence, 25	bending of, 21
APC, see automatic power control (APC)	Buffer layer, 213
Aspect ratio, 57	Bulk, 2
Astigmatism, 120	Buried heterostructure (BH), 122
Asymmetry measure, 49	
Auger process, 23, 105	
Autocorrelation function, 160	C
Automatic current control (ACC), 185	(C <sup>3</sup> ) LD, see cleaved coupled cavity (C <sup>3</sup> )
Automatic power control (APC), 156, 182,	LD
185	Carrier concentration, 97
Axial mode, 137	threshold, 100
	Carrier distribution, 28
	Carrier lifetime, 90, 97
B	Carrier noise, 156
Band edge emission, 26	Catastrophic optical damage (COD), 183
Band filling effect, 37	Cathodoluminescence, 25
Band offset, 14, 91	Cavity, 61
Band-structure engineering, 212	distributed feedback (DFB), 61
© Springer Japan 2015	283
T. Numai, Fundamentals of Semiconductor Laser	rs,
Springer Series in Optical Sciences 93, DOI 10.1	007/978-4-431-55148-5

Fabry-Perot, 61	light output, 107, 108
optical, 27, 61	measurement, 107
ring, 61	Deviation, 144
Cavity quantum electrodynamics (QED),	DFB, see distributed feedback (DFB)
227	DFB-LD, see distributed feedback (DFB)
Characteristic matrix, 73	LD
Characteristic temperature, 104	Diagonal element, 213
Chemiluminescence, 25	Diamond structure, 4
Chirped grating, 76	Dielectric film, 62
Chirping, 147	Differential gain, 145
Chromatic dispersion, 77, 155	Diffracted pattern, 114
Cladding layer, 43	Diffraction grating, 61, 187
Cleaved coupled cavity (C <sup>3</sup> ) LD, 199	Diffusion length, 121
Cleaved facet, 61	Digital modulation, 151, 153
COD, see catastrophic optical damage	Dipole moment, 36
(COD)	Dirac's constant, 3
Coherent, 147	Direct modulation, 147, 149
Complex refractive index, 41	Direct transition, 11, 23
Compressive strain, 213	Discrete, 1
Confinement of resonant radiation, 232	Discrete approach, 72
Coupled cavity, 177	Dislocation, 22, 184
Coupled wave equation, 70	Dispersion, 81, 138
Coupled wave theory, 70	chromatic, 77, 155
Coupling coefficient, 69	material, 155
Coupling rate of a feedback light to the semi-	mode, 155
conductor laser, 178	structual, 155
Critical angle, 43	Dispersion curve, 49
Critical thickness, 22, 213	Distributed bragg reflector (DBR), 61
Crystal defect, 182	Distributed Bragg reflector (DBR), 61  Distributed Bragg reflector (DBR) LD, 187
Current versus light output $(I-L)$ , 97	Distributed feedback (DFB), 61
Cutoff, 44	Distributed feedback (DFB), 01  Distributed feedback (DFB) LD, 187
condition, 50	Double heterostructure, 21, 91
Cyclotron angular frequency, 235	Duty, 153
Cyclotron motion, 236	Dynamic single-mode LD, 187
	Dynamic single-mode LD, 187
Cyclotron resonance, 11, 236	
	E
D	Effective density of states, 29
Dark line defect, 184	Effective mass, 4
	approximation, 4
DBR, see distributed Bragg reflector (DBR)	Effective mass approximation, 15
DBR-LD, see distributed Bragg reflector (DBR) LD	Effective refractive index, 48
Decay coefficient, 145	method, 57
Decay rate, 178	Eigenvalue equation, 49
Decay time, 146	1
Deformation potential, 219	Einstein summation convention, 219
	Einstein's <i>A</i> coefficient, 32 Einstein's <i>B</i> coefficient, 32
Degenerate, 4	· · · · · · · · · · · · · · · · · · ·
Degradation, 182	Einstein's relation, 32
$\delta$ function, 161 Density of states, 15	Elastic strain, 22, 213
effective, 29	Electric current noise, 156
	Electric dipole moment, 251
Derivative	Electric dipole transition, 251
electrical resistance, 107, 109	Electroluminescence, 25

injection-type, 25 Electron-beam exposure, 82 Emission, 1	Fresnel formulas, 45, 110 Full width at half maximum (FWHM), 66 Fundamental mode, 117
induced, 26	FWHM, see full width at half maximum
spontaneous, 26	(FWHM)
stimulated, 26	
Energy band, 1	
Energy barrier, 91	G
Energy barrier layer, 14	Gain
Energy eigenvalue, 3	optical, 27
Energy level, 1	Gain flattening, 204
Ensemble average, 159	Gain guiding, 41, 118
Envelope function, 15	Gaussian distribution function, 166
Equivalent refractive index, 139	Goos-Hänchen shift, 47
Etching mask, 82	Graded index SCH (GRIN-SCH), 202
Evanescent wave, 47	Grating
Excitation, 23	chirped, 76
Excited state, 227	phase-shifted, 76
Exciton, 25, 150	tapered, 76
Exciton recombination, 26	uniform, 76
External cavity, 177	GRIN-SCH, see graded index SCH (GRIN-
External cavity laser, 169	SCH)
External cavity LD, 199	Ground state, 227
External differential quantum efficiency, 95	Group theory, 212
External modulation, 147, 150	Guiding effect, 120
Extinction coefficient, 42	anti-, 119
Extinction ratio, 146	Guiding layer, 43
Eye pattern, 153	
	Н
	Half width at half maximum (HWHM), 66
F	Harmonic perturbation, 247
Fabry-Perot cavity, 61	Heat sink, 182
Facet, 50	Heaviside function, 202
Far-field pattern, 114	Heavy hole band, 10
Feedback, 27	Heterojunction, 91
Fermi level, 28	Heterostructure, 21
quasi-, 29	double, 21, 91
Fermi's golden rule, 227	High frequency modulation, 176
Fermi-Dirac distribution, 29	Holographic exposure, 82
Field spectrum, 160	Homojunction, 91
Finesse, 67	Horizontal cavity surface emitting LD, 199
Fluorescence, 25	Horizontal transverse mode, 114, 118
FM noise, see amplitude modulating (FM) noise	HWHM, see half width at half maximum (HWHM)
Forward bias, 90	Hybrid orbital, 4
Franz-Keldysh effect, 150	Hydrostatic strain, 213
Free carrier absorption, 105	Hysteresis, 180
Free carrier plasma effect, 119	Hysteresis loop, 140
Free space, 41, 229	
Free spectral range, 65	<b>*</b>
Frequency fluctuation spectrum, 160	I
Frequency modulating (FM) noise, 156 Frequency shift keying (FSK), 149	<i>I–L</i> , see current versus light output ( <i>I–L</i> ) Impedance of vacuum, 52, 73, 260

259
259
259
259
259
259
259
259
239
for-
well
WCII
11
)1
8
-
C

0	Plane wave, 44
Ohmic contacts, 182	Pn-junction, 121
Optical cavity, 27, 61	Pnpn structure, 121
Optical confinement factor, 49	Point defect, 184
Optical fiber, 41	Polarization, 44
Optical fiber amplifier, 148	Polarization controller, 149
Optical gain, 27	Population inversion, 26
Optical isolator, 177	Potential well, 14
Optical resonator, 27, 61	Power fluctuation spectrum, 160
Optical transition, 1	Poynting vector, 250
Optical waveguide, 41	Propagate, 41
planar, 42	Propagation constant, 46
strip, 42	Propagation mode, 43
three-dimensional, 42, 56	1.8
two-dimensional, 42	
Orbit-strain interaction Hamiltonian, 218	O
Orbital angular momentum, 7	Quantum box, 18
Orbital angular momentum operator, 219	Quantum confined stark effect (QCSE), 150
Order of diffraction, 71, 192	
Orthonormalize, 158	Quantum noise, 156
Oscillation, 92	Quantum number, 3
Overflow, 105	Quantum structures, 12
Overnow, 103	Quantum well (QW), 4, 14
	one-dimensional, 15
_	three-dimensional, 18
P	two-dimensional, 17
Pattern effect, 153	Quantum well (QW) LD, 201
Pauli exclusion principle, 1	Quantum wire, 17
Pauli's spin matrices, 7	Quarter wavelength shifted grating, 192
Penetration depth, 47	Quasi-Fermi level, 29
Periodic multilayer, 72	QW, see quantum well (QW)
Periodic potential, 13	strained, 213
Perturbation, 239	QW-LD, see quantum well (QW) LD
Perturbation parameter, 2	
Perturbation theory	
$k \cdot p, 2$	R
first-order, 3	Radiation, 26
second-order, 4	Radiative recombination, 23
Phase shift, 45	Radiative recombination lifetime, 97
Phase shift keying (PSK), 149	Radiative transition, 1
Phase velocity, 46	Rate
Phase-shifted grating, 76	absorption, 31
Phonon, 23	spontaneous emission, 31
Phosphorescence, 25	stimulated emission, 30
Photoluminescence, 25	transition, 30
Photon, 23	Rate equations, 97, 277
Photon density, 97	Reciprocal effective mass tensor, 4
Photon lifetime, 97	Recombination, 23
Photon recycling, 232	impurity, 25
Photoresist, 82	nonradiative, 23
Pikus-Bir Hamiltonian, 216, 218	radiative, 23
Planar optical waveguide, 42	Reflected light, 44
Planck's constant, 3	Reflector, 27
Plane of incidence, 44	Refracted light, 44

Refractive index, 41	Hamiltonian, 7
complex, 41	Split-off band, 10
Relative electric susceptibility, 203	Split-off energy, 10
Relative intensity noise (RIN), 171, 272	Spontaneous emission, 26, 31
Relaxation, 23	rate, 31
Relaxation oscillation, 141	Spontaneous emission coupling factor, 97
Resonance angular frequency, 151	SQW-LD, see single quantum well (SQW)
Resonance condition, 65, 92	LD
Resonant tunneling effect, 21	Standing wave, 68
Resonator, 27	Steady state, 99
Return-to-zero (RZ), 153	Step function, 202
Rib waveguide, 121	Stimulated emission, 26, 30
Ridge, 57	rate, 30
Ridge-waveguide, 122	Stokes luminescence, 25
Right-handed circularly polarized wave, 237	Stop band, 72
Ring cavity, 61	Strain, 212
Running wave, 68	compressive, 213
RZ, see return-to-zero (RZ)	elastic, 22
	hydrostatic, 213
	shear, 213
S	tensile, 213
S/N ratio, see signal-to-noise (S/N) ratio	Strain-dependent spin-orbit interaction
Saturable absorber, 176	Hamiltonian, 218
Scalar potential, 249	Strained QW, 213
SCH, see separate confinement heterostruc-	Stress, 213
ture (SCH)	Strip optical waveguide, 42
Schrödinger equation, 2	Structural dispersion, 155
Screening tests, 185	Sub-mode suppression ratio (SMSR), 196
Selection rule, 209	Substrate, 43
Self-pulsation, 176	Super lattice, 19
Semiclassical theory, 157	Type I, 20
Semimetal, 20	Type II, 20
Separate confinement heterostructure	Type III, 20
(SCH), 202	Surface emitting LD
Separation-of-variables procedure, 260	horizontal cavity, 199
Shear strain, 213	vertical cavity, 198
Signal-to-noise (S/N) ratio, 146	Synchrotron radiation, 84
Single crystal, 3	
Single quantum well (SQW) LD, 201	
Single-mode operation, 137	T
Slope efficiency, 94	Tapered grating, 76
Small-signal analysis, 144	TE mode, 44
Snell's law, 43	Tensile strain, 213
Spatial hole burning, 119, 192	Tensor, 213
Spectral density functions, 160	Thermal equilibrium, 26
Spectral linewidth, 66, 160	Thermoluminescence, 25
Spectral linewidth enhancement factor, 162	Three-dimensional optical waveguide, 42,
Spherical polar coordinate systems, 8	56
Spin	Threshold
angular momentum, 7	carrier concentration, 100
magnetic moment, 7	Threshold current
Spin angular momentum operator, 219	density, 99
Spin-orbit interaction, 6	Thyristor, 121

Time-average, 159	$\mathbf{U}$
Time-dependent quantum mechanical per-	Undoped, 90
turbation theory, 36	Uniform grating, 76
Time-dependent Schrödinger equation, 245	Unperturbed Hamiltonian, 239
TM mode, 44	
Total reflection, 43	
Transfer matrix, 71, 262	V
Transient response theory, 150	Valence band absorption, 105
Transition	VCSEL, see vertical cavity surface emitting
direct, 11, 23	LD (VCSEL)
indirect, 11, 24	Vector potential, 249
nonradiative, 1	Vertical cavity surface emitting LD, 198
optical, 1	Vertical transverse mode, 114, 115
radiative, 1	
Transition rate, 30	W
Transmission characteristics, 62	Wave function, 2
Transverse electric (TE) mode, 44	Wave vector, 2
Transverse magnetic (TM) mode, 44	Wiener-Khintchine theorem, 160
Transverse mode, 114	Window structure, 183
horizontal, 114, 118	Window Structure, 188
vertical, 114, 115	
Transverse resonance condition, 47	X
Triboluminescence, 25	X-ray exposure, 82
Tunneling effect, 21	
resonant, 21	
Turn-on delay time, 141	${f z}$
Two-dimensional optical waveguide, 42	Zinc-blende structure, 4